

Lecture Notes in Mechanical Engineering

Ramesh K. Agarwal *Editor*

# Recent Advances in Manufacturing Engineering and Processes


Proceedings of ICMEP 2022

 Springer

# Lecture Notes in Mechanical Engineering


## Series Editors

Fakher Chaari, National School of Engineers, University of Sfax, Sfax, Tunisia

Francesco Gherardini , Dipartimento di Ingegneria “Enzo Ferrari”, Università di Modena e Reggio Emilia, Modena, Italy

Vitalii Ivanov, Department of Manufacturing Engineering, Machines and Tools, Sumy State University, Sumy, Ukraine

## Editorial Board

Francisco Cavas-Martínez , Departamento de Estructuras, Construcción y Expresión Gráfica Universidad Politécnica de Cartagena, Cartagena, Murcia, Spain

Francesca di Mare, Institute of Energy Technology, Ruhr-Universität Bochum, Bochum, Nordrhein-Westfalen, Germany

Mohamed Haddar, National School of Engineers of Sfax (ENIS), Sfax, Tunisia

Young W. Kwon, Department of Manufacturing Engineering and Aerospace Engineering, Graduate School of Engineering and Applied Science, Monterey, CA, USA

Justyna Trojanowska, Poznan University of Technology, Poznan, Poland

**Lecture Notes in Mechanical Engineering (LNME)** publishes the latest developments in Mechanical Engineering—quickly, informally and with high quality. Original research reported in proceedings and post-proceedings represents the core of LNME. Volumes published in LNME embrace all aspects, subfields and new challenges of mechanical engineering.

To submit a proposal or request further information, please contact the Springer Editor of your location: **Europe, USA, Africa:** Leontina Di Cecco at [Leontina.dicecco@springer.com](mailto:Leontina.dicecco@springer.com) **China:** Ella Zhang at [ella.zhang@springer.com](mailto:ella.zhang@springer.com) **India:** Priya Vyas at [priya.vyas@springer.com](mailto:priya.vyas@springer.com) **Rest of Asia, Australia, New Zealand:** Swati Meherishi at [swati.meherishi@springer.com](mailto:swati.meherishi@springer.com) Topics in the series include:

- Engineering Design
- Mechanical Structures and Stress Analysis
- Engine Technology
- Nanotechnology and Microengineering
- Control, Robotics, Mechatronics
- MEMS
- Theoretical and Applied Mechanics
- Fluid Mechanics
- Engineering Thermodynamics, Heat and Mass Transfer
- Manufacturing
- Precision Engineering, Instrumentation, Measurement
- Tribology and Surface Technology

**Indexed by SCOPUS and EI Compendex.** All books published in the series are submitted for consideration in Web of Science.

To submit a proposal for a monograph, please check our Springer Tracts in Mechanical Engineering at <https://link.springer.com/bookseries/11693>

Ramesh K. Agarwal  
Editor

# Recent Advances in Manufacturing Engineering and Processes

Proceedings of ICMEP 2022

 Springer



*Editor*

Ramesh K. Agarwal  
Department of Mechanical Engineering  
and Material Science  
Washington University in St. Louis  
St. Louis, MO, USA

ISSN 2195-4356

ISSN 2195-4364 (electronic)

Lecture Notes in Mechanical Engineering

ISBN 978-981-19-6840-2

ISBN 978-981-19-6841-9 (eBook)

<https://doi.org/10.1007/978-981-19-6841-9>

© The Editor(s) (if applicable) and The Author(s), under exclusive license to Springer Nature Singapore Pte Ltd. 2023

This work is subject to copyright. All rights are solely and exclusively licensed by the Publisher, whether the whole or part of the material is concerned, specifically the rights of translation, reprinting, reuse of illustrations, recitation, broadcasting, reproduction on microfilms or in any other physical way, and transmission or information storage and retrieval, electronic adaptation, computer software, or by similar or dissimilar methodology now known or hereafter developed.

The use of general descriptive names, registered names, trademarks, service marks, etc. in this publication does not imply, even in the absence of a specific statement, that such names are exempt from the relevant protective laws and regulations and therefore free for general use.

The publisher, the authors, and the editors are safe to assume that the advice and information in this book are believed to be true and accurate at the date of publication. Neither the publisher nor the authors or the editors give a warranty, expressed or implied, with respect to the material contained herein or for any errors or omissions that may have been made. The publisher remains neutral with regard to jurisdictional claims in published maps and institutional affiliations.

This Springer imprint is published by the registered company Springer Nature Singapore Pte Ltd.

The registered company address is: 152 Beach Road, #21-01/04 Gateway East, Singapore 189721, Singapore

# Organization

## Conference Chairs

Prof. Ramesh K. Agarwal, Washington University in St. Louis, USA  
Prof. Omar S. Es-Said, Loyola Marymount University, USA

## Program Chairs

Assoc. Prof. Ken Mao, Warwick University, UK  
Prof. Rong Liu, Carleton University, Canada

## Student Program Chair

Prof. Yong Suk Yang, Pusan National University, Korea

## International Technical Committees

Francisco Velasco, Universidad Carlos III de Madrid, España  
Jingdong Wang, Changchun University of Science and Technology, China  
Kazem Abhary, University of South Australia, Australia  
Waa'il Mahmud Lafta, Martinus Rail Pty Ltd, Australia  
Cherng-Yuan Lin, National Taiwan Ocean University, Taiwan  
Eka Lutfi Septiani, Universitas Internasional Semen Indonesia, Indonesia  
Chitphong Ketthanom, Vongchavalitkul University, Thailand  
Jing YU, Dalian Maritime University, China

Rahul Chhibber, Indian Institute of Technology, India  
 Saiful Amri Mazlan, Universiti Teknologi Malaysia, Malaysia  
 Chih-Yuan Chen, National Taipei University of Technology, Taiwan  
 Zaini Ahmad, Universiti Teknologi Malaysia, Malaysia  
 Mohd Sukri Mustapa, Universiti Tun Hussein Onn Malaysia, Malaysia  
 S. Eiamsa-ard, Mahanakorn University of Technology, Thailand  
 Ivitskiy Igor, National Technical University of Ukraine, Ukraine  
 Mohd Rasidi Bin Ibrahim, Universiti Tun Hussein Onn Malaysia, Malaysia  
 Shiau Wei Chan, Universiti Tun Hussein Onn Malaysia, Malaysia  
 Kowit Piyamongkala, King Mongkut's University of Technology North Bangkok, Thailand  
 Tien-Dat Hoang, Thai Nguyen University of Technology, Vietnam  
 Jayavel S., Indian Institute of Information Technology, Design and Manufacturing, Kanchipuram, Melakottaiyur, India  
 Dhaneshwar Mishra, Manipal University Jaipur, India  
 Gobinda Gopal Khan, Tripura University (A Central University), India  
 Deepa Prabhu, Manipal Institute of Technology, India  
 Nuchnapa Tangboriboon, Kasetsart University, Thailand  
 Minh Tuan Pham, Ho Chi Minh City University of Technology, Vietnam  
 Thitipong Wutisart, Dhonburi Rajabhat University, Thailand  
 Rafail Apakashev, Ural State Mining University, Russia  
 Mark Khazin, Ural State Mining University, Russia  
 Marina Menshykova, University of Aberdeen, UK  
 Zartasha Mustansar, NICHE-NUST Interdisciplinary Cluster for Higher Education, Pakistan  
 Mohammad Junaid Iqbal Khan, NICHE-NUST Interdisciplinary Cluster for Higher Education, Pakistan  
 Nuchanaporn Pijarn, Ubon Ratchathani University, Thailand  
 Rifky Ismail, Universitas Diponegoro, Indonesia  
 Shoroog Alraddadi, Umm Al-Qura University, Saudi Arabia  
 Menandro Marquez, Mapua University, Philippines  
 Krit Jiamjiroch, Thammasat University, Thailand  
 Hassan A. El-Hofy, Egypt Japan University of Science and Technology, Egypt  
 Mohanad Alabdullah, Deakin University, Australia  
 Pham Son Minh, Ho Chi Minh City University of Technology and Education, Vietnam  
 Wahyu Dwi Lestari, University of Pembangunan Nasional Veteran Jawa Timur, Indonesia  
 Mehmet Karakose, Firat University, Turkey  
 Silviu-Mihai Petrisor, Land Forces Academy from Sibiu, Romania  
 Constantin Dulucheanu, University "Stefan cel Mare" of Suceava, Romania  
 Radu Godina, NOVA University Lisbon, Portugal  
 Panarat Rattanaphanee, Suranaree University of Technology, Thailand  
 Markus Brillinger, Graz University of Technology, Austria  
 Samet AKAR, Çankaya University, Turkey

İlhan Asiltürk, Selcuk University, Turkey  
Izirwan Bin Izhab, Universiti Malaysia Pahang, Lebuhraya  
Zafer Bingül, Kocaeli University, Turkey  
Vesna Spasojevic Brkic, University of Belgrade, Serbia  
Mehmet Savsar, Kuwait University, Kuwait  
Pirat Khunkitti, Khon Kaen University, Thailand  
Elisha D. Markus, Central University of Technology, South Africa  
Nguyen Dinh Ngoc, Thai Nguyen University of Technology, Vietnam  
Abbas Amini, Western Sydney University, Australia  
Baris Burak Kanbur, Nanyang Technological University, Singapore

## **International Reviewer Committees**

Anh Van Nguyen, Cranfield University, UK  
Ajeng Yulianti Dwi Lestari, Universitas Islam Indonesia, Indonesia  
Sukangkana Talangkun, Khon Kaen University Thailand, Thailand  
Naruebodee Srisang, Prince of Chumphon Campus, Thailand  
Lu-Lin Li, National United University, Taiwan  
Mohammed H. Rady, Universiti Tun Hussein Onn Malaysia, Malaysia  
Mohd Azhar Harimon, Universiti Tun Hussein Onn Malaysia  
Manjunath Shettar, Manipal Institute of Technology, India  
Achmad Chafidz Mas Sahid, Universitas Islam Indonesia, Indonesia  
Shazarel Shamsudin, Universiti Tun Hussein Onn Malaysia, Malaysia  
Wahyu Dwi Lestari, Universitas Pembangunan Nasional Veteran Jawa Timur, Indonesia  
Thanh-Hai Nguyen, Ho Chi Minh City University of Technology (HCMUT), Vietnam  
Ali Mamedov, American University of the Middle East, Kuwait  
Pham Quang Trung, Ho Chi Minh City University of Technology, Vietnam  
Rhoert Endozo Alvarez, Batangas State University, Philippines  
Inoka Manthilake, University of Moratuwa, Sri Lanka

# Preface

During June 6–8, 2022, the 12th International Conference on Manufacturing Engineering and Processes (ICMEP 2022) was successfully held via web platform.

Since 2021, ICMEP has been successfully held for 11 years. It always aims at providing international and excellent platform for scholars and researchers from all over the world to exchange ideas in the field of manufacturing engineering and process and so on.

All delegates from all over the world communicated thoughts, shared experience, etc., again with this form. It is great memories. All of them were active and positive.

After a fair and rigorous review by technical committees, 21 papers from Morocco, Egypt, Indonesia, Vietnam, Thailand and so on were selected as a volume and presented during the conference. We sincerely hope that all scholars of the related research areas will benefit from it.

We are so appreciated to acknowledge all those who supported ICMEP2022. And, especially thanks to technical committees and reviewers for taking time to help us review papers rigorously. And, thanks for all participants' support. We will try our best to make ICMEP a more influential and professional platform. And, we look forward to meeting you all physically next year!

St. Louis, USA

Ramesh K. Agarwal

# Contents

|  |    |
|--|----|
| <b>Electromechanical System and Engineering Design</b>   |    |
| <b>Finite Element Analysis of Ankle Foot Design Based on Indonesian Anthropometry</b> .....  | 3  |
| W. D. Lestari, N. Adyono, L. Z. Faiza, P. Bagas, and G. D. Widagda   |    |
| <b>Automated Disinfection System for Polyethylene Terephthalate Bottles for Bacteria, Fungi, and Viruses Using UVC LED Camera</b> .....            | 11 |
| Gerson Orihuela, Esleiter Reyes, and Deyby Huamanchahua  |    |
| <b>Design of the CNC Router Structure for Machining Wood Materials Using Reliability-Based Design Optimization Method</b> .....                    | 25 |
| Huu Loc Nguyen and Van Thuy Tran   |    |
| <b>Development of Intelligent Drone for Cassava Farming</b> .....  | 37 |
| Orapadee Joochim, Kridtat Satharanond, and Wirachat Kumkun   |    |
| <b>Calculation and Optimization of the Two Stage Worm-Gear Reducers Speed Ratio</b> .....  | 47 |
| Le Thuy Anh and Nguyen Huu Loc   |    |
| <b>Project-Based Learning in Product Design Engineering: A Case Study of External Gear Pump Design</b> .....                                       | 59 |
| Muhammad Izzuddin Sabaruddin,<br>Mohammad Habib Fadillah Mohammad Mazni Latiff,<br>Nur Saidah Awang Abdullah, Wahyu Caesarendra, and Juliana Zaini |    |
| <b>Machining and Manufacturing</b>   |    |
| <b>Tool Wear Analysis on Time-Domain and Frequency-Domain Data of Machining S45C Using Signal Processing Technique</b> .....                       | 69 |
| P. Jirapipattanaporn, A. Chanpariyavatevong, W. Lawanont,<br>and W. Boongsod   |    |

**Optimization of the Weight and Size Characteristics of the Power Bracket for Additive Manufacturing Based on Topological Optimization Algorithms** ..... 79  
A. V. Zhdanov, S. A. Baranov, and L. V. Belyaev

**Identification and Active Control of the Chatter Phenomenon in the Milling Process Using a Pneumatic Actuator** ..... 87  
Peyman Enteshari Najafabadi, Reza Nosouhi, Milad Soleimani, and Mahmood Mirkhanzadeh

**SHS Extrusion of a Composite Material Based on Aluminum-Magnesium Spinel** ..... 99  
Andrey Chizhikov, Alexander Konstantinov, Pavel Bazhin, and Mikhail Antipov

**Fluid Mechanical Engineering and Engineering Thermodynamics**

**Visual Observation of the Vortex Flow from the Same Diameter Circular Cylinders Which Sandwiched a Partition Disk** ..... 109  
Yoshifumi Yokoi

**Experimental Study of the Porous Emitter Installed in a Gas Porous Burner** ..... 119  
Panuwat Chanmak, Wapee Sripunya, and Bundit Krittacom

**Experimental and Numerical Investigations of Effects of Wall Friction and Vibrational Amplitude on Convection Phenomena in Granular Materials Under Vertical Vibrations** ..... 127  
Tanapon Yachai, Itthichai Preechawuttipong, and Pawarut Jongchansitto

**Comparative Study of Radiative Flux from Mushroom BLEVE Model** ..... 135  
Anas Mbarki, Aziz Ettahir, and Abderraouf Guelzim

**Applied Mechanics and Engineering Mechanics**

**Belt Layer Effects on Non-pneumatic Tire Performance by Finite Element Analysis** ..... 149  
Juthanee Phromjan and Chakrit Suvanjumrat

**Analysis of Hybrid Viscoelastic Sheets Adhered to the Hull of a GFRP Vessel to Reduce Impact Damage** ..... 159  
Patrick Townsend, Juan C. Suárez Bermejo, and Alvaro Rodríguez-Ortíz

**On the Contact Between Viscoelastic Tube with Inner Nonuniform Coating and Several Rigid Inserts** ..... 167  
Kirill E. Kazakov and Svetlana P. Kurdina

**Failure Modes of Skull Bone of a Dog Head Under Impact Loading** .... 177  
Reda M. Othman, M. A. Hassan, and Wael M. Khierldeen

**Seismic Retrofit of RC Building with Elastic Stage of Buckling-Restrain Braces** ..... 187  
Thanawat Thipprapan, Amphon Jarasjarungkiat, Panumas Saingam, and Arthit Petchsasithon

**Response and Damage Identification by Long-Gauge Strain Sensor of Beam-Like Bridges Under the Loads of Vehicle: A Comparison of the Analytical Model and in Situ Measurement** ..... 197  
Pham-Truong Son, Tien Hoang, Denis Duhamel, Gilles Foret, Franziska Schmidt, François-Baptiste Cartiaux, and Véronique Le Corvec

**Metallic Materials and Corrosion Protection**

**Relation Between Binding Energy, Isothermal Bulk Modulus, and Surface Tension of Liquid Metals** ..... 211  
Yu. N. Starodubtsev and V. S. Tsepelev

**Corrosion Protection Method with Sacrificial Anode for Steel Members in Boundary with Ground Using Water Swelling Rubber** .... 219  
J. Xu, S. Kainuma, K. Takaki, M. Yang, and T. Tomoda



# **Electromechanical System and Engineering Design**

# Finite Element Analysis of Ankle Foot Design Based on Indonesian Anthropometry



W. D. Lestari, N. Adyono, L. Z. Faiza, P. Bagas, and G. D. Widagda

## 1 Introduction

The challenges faced by amputees today are in carrying out daily activities and transportation. Prosthetics or orthotic devices have evolved to provide solutions to these problems in line with the needs of prosthetic users. An overview of currently developing prosthetic limbs can be found in various references (Ghaith 2012; Jimenez-Fabian et al. 2015; Kerkum et al. 2015; Corazza et al. 2014; Omasta et al. 2012; Rigney et al. 2015; Veneva et al. 2014). There are two types of ankle prosthesis that are currently being developed based on the type of movement, namely passive and active prostheses. Passive prostheses are more affordable for amputation rehabilitation, where active prostheses are growing rapidly but require power to generate energy. However, both types of ankle foot prosthetics have the same procedure, namely, how amputees can imitate normal walking functions. Passive devices may include springs to ensure storage and energy and dampers to suppress vibration. In the past, solid ankle-based cushioned heels were considered in designing ankle foot prosthetics (Casillas et al. 1995; Rao et al. 1998; Torburn et al. 1990). Several criteria that must be considered in designing passive prostheses are portability capacity in the form of size and level of lightness. Although active prostheses have several advantages, they require an actuator and a motor, so they are still limited in portability. The next criterion is how to keep the prosthesis simple and affordable.

Most of the research on ankle foot prosthetics that was developed previously and currently uses robots and exoskeletons. Although this device can be controlled, it is still quite complex and heavy, making it difficult for portability. Researchers are currently facing the challenge of creating lightweight prosthetic designs. This study developed the ankle foot design to be a lighter and more flexible structure. This study

---

W. D. Lestari (✉) · N. Adyono · L. Z. Faiza · P. Bagas · G. D. Widagda  
Department of Mechanical Engineering, Faculty of Engineering, University of Pembangunan Nasional “Veteran” Jawa Timur, Jawa Timur 60294, Indonesia  
e-mail: [wahyu.dwi.tm@upnjatim.ac.id](mailto:wahyu.dwi.tm@upnjatim.ac.id)

proposes an ankle foot design with a compliant mechanism (CM) model commonly known as a flexible mechanism. This mechanism is a special type of mechanism in mechanical engineering which has a friction-free system, no backlash and monolithic fabrication. Therefore, this compliant mechanism model has a lightweight. Several researchers have used this model to create various designs (Howell et al. 2013).

Compliant mechanisms can be found in a variety of applications such as aerospace, biomechanics and soft robotics (Dhote et al. 2015, 2018). The research group of (Dao and Huang 2015, 2017a) uses the compliant model mechanism to make design, modeling and optimization in several applications such as a one degree-of-freedom (DOF) mechanism (Dao 2016), a two DOF mechanism (Huang and Dao 2016a), a displacement sensor (Dao and Huang 2017b), a two DOF flexure-based mechanism (Huang and Dao 2016b). Most of the previous studies still have a complex structure. In particular, there are still shortcomings in creating an ankle joint that fits the natural human foot. In this study, we propose a new prosthetic ankle foot design to support smoother movement. So, this study develops a new ankle foot topology using a compliant mechanism model, chooses a material that is easy to manufacture and performs simulations to analyze the strength of the material.

Computational-based material strength simulation is one of the most effective steps taken to reduce trial error in manufacturing prosthetics from the design results. In addition, having a simulation beforehand will save costs, time and minimize the energy expended when the strength testing of the prosthetic model. Computational-based strength simulation is able to analyze a model to measure the value of deformation, stress, and strain that occurs in detail. This research is developing a biomechanical design and simulation for ankle foot prosthetics. The designs are made by mimicking actual human feet. The selected prosthetic materials are silicone for the skin and AISI 304 for the support core. Ankle foot prosthetic models are designed to be able to withstand the average human weight on the walking cycle mechanism. In addition, the model must also have a safe factor of safety before the manufacturing process is carried out. The results of this study are expected to improve the quality of life of people with disabilities, help people with disabilities in normal activities and can be produced on a mass scale.

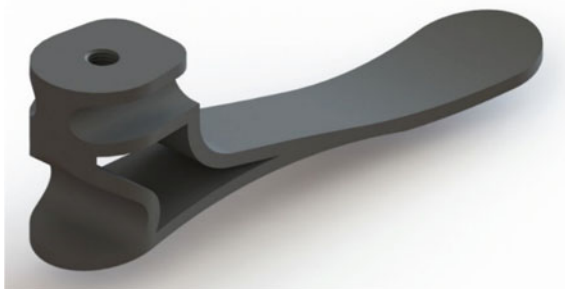
## 2 Material and Methods

### 2.1 Biomechanical Design

The initial stage in this research process is a literature study to look for similar research references and forms of prosthetic ankle foot models that have been studied. The next step is to determine the ankle foot design criteria to be made. The design criteria in this study can be seen in Table 1. Based on these criteria, the design process will be continued and the results will be analyzed. The model analysis aims to analyze how strong and feasible the design to produce and apply to patients with disabilities.

**Table 1** Design criteria

| Criteria                     | Description   |
|------------------------------|---|
| Strength (Chuan et al. 2010) | Able to withstand weight up to 100 kg                             |
| Light (Tayyari 2017)         | Has a lighter mass than the real leg which is less than 2.2686 kg |
| Ankle foot type              | Model compliant mechanism by imitating the human foot in general  |
| Convenience                  | Easy to use in walking position                                   |

**Fig. 1** Ankle foot design

If the analysis is not strong enough to withstand the load, then return to the model design stage.

Design and analysis were made by Solidworks software. In making the ankle foot design in this study, the lowest mass of Indonesian people was taken, which was 39.8 kg. The weight of the leg below the knee according to Tayyari (2017) is 5.7% of the human weight. So if the calculation is carried out, the weight of the prosthetic foot must be below 2.2686 kg so as not to burden the user. The ankle foot prosthetic designed using a compliant mechanism model and using AISI 304 material. The material was chosen because it has properties that has good formability or shaping power, making it easier to make the core support on the ankle foot design according to the desired shape. The mass of the designed artificial foot is 0,498,285 kg. The design results are shown in Fig. 1.

## 2.2 Simulation

The finite element method was used to analyze the ankle foot design in this study. The analysis was carried by Solidworks software to analyze the structural behavior of the model and determine the overall deformation, equivalent stress and strain energy. The characteristics of the AISI 304 material that are input into the simulation process are Young's modulus of 190,000 MPa and Poisson's ratio of 0.29. Testing based on ISO 10328 standard which applies angle and support to the ankle foot. Ankle foot

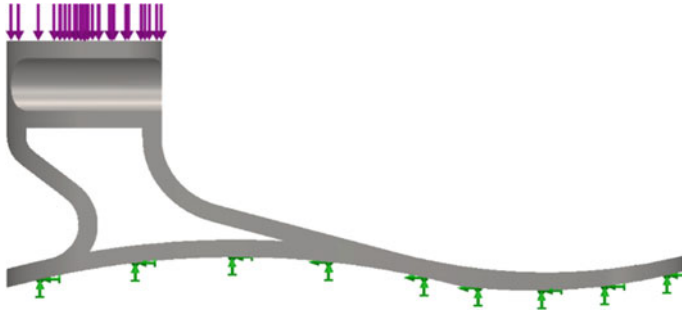


**Fig. 2** Simulation illustration of the midstance phase

prosthetic with a compliant mechanism model limits it to three kinds of fix support in the gait cycle. The three positions are the heel strike position, the midstance position and the toe-off position. In this study, the test was carried out on one of the conditions of the walking cycle, namely midstance. In this condition, the ankle foot has a fixed support located on the soles of the forefoot and back at an angle of  $0^\circ$ .

The magnitude of the load and the load direction given is based on gait analysis data from the percentage of body weight or vertical force and ankle angle in each phase of the gait cycle (Bovi et al. 2011). The body weight or the amount of load that is applied in accordance with the predetermined design criteria is 100 kg, so that the given load is 980 N. The illustration of the simulation carried out with the boundary condition of the midstance position of the human gait cycle is shown in Fig. 2.

### 3 Results and Discussion

The design testing of the prosthetic ankle foot was carried out in a walking condition in the midstance phase. In this condition, fixed geometry is placed on the entire base of the foot. The test is assumed that the support at the foot is fix. While the load is directed from the top to the bottom of the foot (Fig. 2). There are three types of data taken, namely in the form of Von Misses stress, displacement and strain.

#### 3.1 Stress Analysis Von Misses Stress

The Von Misses stress analysis parameter is used to determine the results of the stress that occurs in compliant ankle foot prosthetics during the walking mechanism in the midstance phase. The analysis results show that the maximum stress occurs in the midstance position of 91.18 MPa. In the midstance position, because it is supported by two supports at the front and rear, so that the stress distribution is more even. The area of maximum stress that occurs in the ankle foot design with the midstance

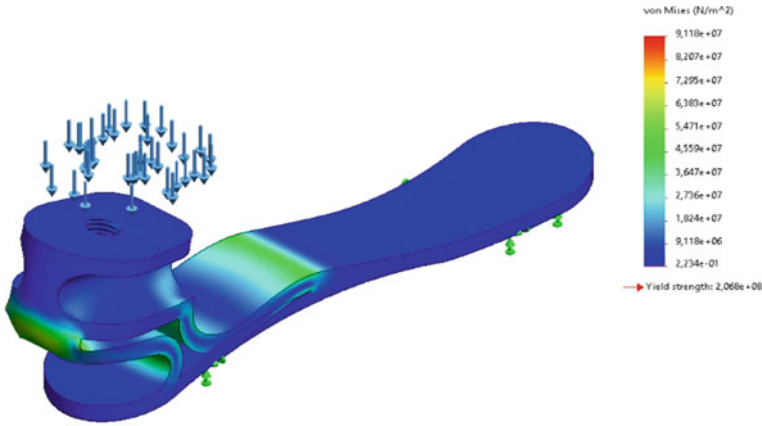


**Fig. 3** Von Mises stress ankle foot midstance phase

position is shown in Fig. 3. The safety factor of ankle foot prosthetics was evaluated using the following formula:

$$n = \frac{\sigma_{\text{yield}}}{\sigma_{\text{actual}}} \tag{1}$$

where  $n$  is the safety factor,  $\sigma_{\text{yield}}$  is the yield strength of the material,  $\sigma_{\text{actual}}$  and is the maximum stress that occurs. Based on these equations, the safety factor results of 2268. These results indicate that the stress that occurs is still below the yield strength limit of AISI 304 material with a safety factor above 1.5 which is quite safe. In other words, the ankle foot prosthetic design by adopting a compliant mechanism is still categorized as safe because it is still in the elastic area of the material.

### 3.2 Static Analysis Displacement

The total deformation is used as an analysis parameter to determine the changes in the shape of the model that occur when it is loaded. The result of the total deformation shows that the midstance position experiences a displacement of 004,887 mm. The shape of the deformation that occurs at that position is illustrated in Fig. 4. The material stiffness value in the ankle foot design in the midstance phase can be determined by using the formula  $K = F/d$ , where  $K$  is stiffness, (N/mm) is force and ( $N$ ) is displacement (mm). Based on these equations, it can be seen that the amount of stiffness that occurs in the midstance position is 20053,2024 N/mm.

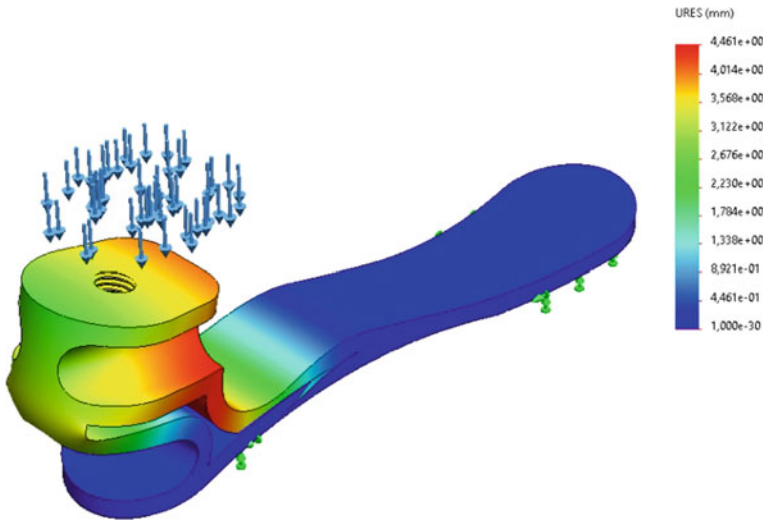


**Fig. 4** Total deformation results of the ankle foot design in midstance position

### 3.3 *Static Analysis Strain*

The next analysis parameter is to measure the stored strain energy. Based on the given load according to the magnitude of the gait cycle mechanism, the results show that at the midstance position, the maximum strain that occurs is 0.0003626. The area of maximum strain energy is located at the curvature between the toe and the sole of the foot with the maximum stress point as shown in Fig. 5.

## 4 Conclusion

Ankle foot prosthetics are mobility aids for people with disabilities to assist with daily activities. The purpose of the design and analysis of the compliant ankle foot prosthetic model is to determine the strength and feasibility before this model is fabricated. Based on the above discussion, it can be concluded that the ankle foot compliant prosthetic design is capable of performing motion with a gait cycle mechanism in the midstance phase with a load of 100 kg. This model has the advantage of being flexible because the elastic curve adopts the concept of a compliant mechanism and utilizes strain energy. In addition, the design made has a safety factor in accordance with the requirements. For further research, it is necessary to make artificial ankle foot according to the material used in the simulation so that their real capabilities are known.

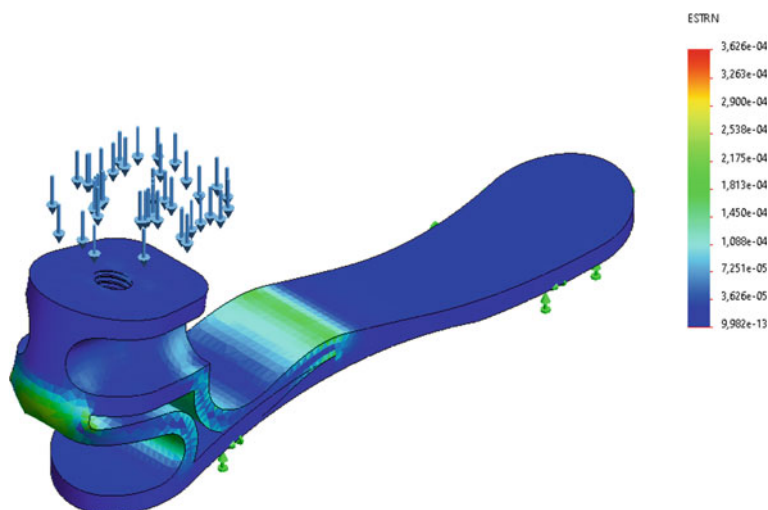


Fig. 5 Strain results of the ankle foot design in the midstance position

## References

- Bovi, G., Rabuffetti, M., Mazzoleni, P., Ferrarin, M.: A multiple-task gait analysis approach: kinematic, kinetic and EMG reference data for healthy young and adult subjects. *Gait Posture* **33**(1), 6–13 (2011). <https://doi.org/10.1016/j.gaitpost.2010.08.009>
- Casillas, J.M., Dulieu, V., Gras, P., Cohen, M., Marcer, I., Didier, J.P.: Bioenergetic comparison of a new energy-storing foot and sach foot in traumatic below-knee amputees or in vascular amputees. *Ann. Readapt. Med. Phys.* **38**(2), 57–63 (1995). [https://doi.org/10.1016/0168-6054\(96\)89302-0](https://doi.org/10.1016/0168-6054(96)89302-0)
- Chuan, T.K., Hartono, M., Kumar, N.: Anthropometry of the Singaporean and Indonesian populations. *Int. J. Ind. Ergon.* **40**(6), 757–766 (2010). <https://doi.org/10.1016/j.ergon.2010.05.001>
- Corazza, F., Parenti-Castelli, V., Stagni, R., Cappello, A., O'connor, J.J., Leardini, A.: Biomechanics of the intact and replaced human ankle joint. *J Mech Med Biol* **06**(01), 39–46 (2014). <https://doi.org/10.1142/s0219519406001819>
- Dao, T.P.: Multiresponse optimization of a compliant guiding mechanism using hybrid taguchi-grey based fuzzy logic approach. *Math. Problems Eng.*, **2016** (2016). <https://doi.org/10.1155/2016/5386893>
- Dao, T.P., Huang, S.C.: Design, fabrication, and predictive model of a 1-dof translational flexible bearing for high precision mechanism. *Trans. Can. Soc. Mech. Eng.* **39**(3), 419–429 (2015). <https://doi.org/10.1139/tcsme-2015-0031>
- Dao, T.P., Huang, S.C.: Compliant thin-walled joint based on zygoptera nonlinear geometry. *J. Mech. Sci. Technol.* **31**(3), 1293–1303 (2017a). <https://doi.org/10.1007/s12206-017-0228-8>
- Dao, T.P., Huang, S.C.: Design and analysis of a compliant micro-positioning platform with embedded strain gauges and viscoelastic damper. *Microsyst. Technol.* **23**(2), 441–456 (2017b). <https://doi.org/10.1007/s00542-016-3048-3>
- Dhote, S., Yang, Z., Zu, J.: Modeling and experimental parametric study of a tri-leg compliant orthoplanar spring based multi-mode piezoelectric energy harvester. *Mech. Syst. Signal Process.* **98**, 268–280 (2018). <https://doi.org/10.1016/j.ymssp.2017.04.031>



- Dhote, S., Zu, J., and Zhu, Y.: A nonlinear multi-mode wideband piezoelectric vibration-based energy harvester using compliant orthoplanar Spring, *Appl. Phys. Lett.*, **106**(16) (2015). <https://doi.org/10.1063/1.4919000>
- Ghaith, F.A.: Nonlinear finite element modeling of nano-indentation.: *Proc Int Conf Adv Robo Mech Eng Des*, pp. 1–4 (2012)
- Howell, L.L., Magleby, S.P., Olsen, B.M.: *Handbook of Compliant Mechanisms*. Wiley (2013)
- Huang, S.C., Dao, T.P.: Design and computational optimization of a flexure-based XY positioning platform using FEA-based response surface methodology. *Int. J. Precis. Eng. Manuf.* **17**(8), 1035–1048 (2016a). <https://doi.org/10.1007/s12541-016-0126-5>
- Huang, S.C., Dao, T.P.: Multi-objective optimal design of a 2-DOF flexure-based mechanism using hybrid approach of grey-taguchi coupled response surface methodology and entropy measurement. *Arab. J. Sci. Eng.* **41**(12), 5215–5231 (2016b). <https://doi.org/10.1007/s13369-016-2242-z>
- Jimenez-Fabian, R., Flynn, L., Geeroms, J., Vitiello, N., Vanderborght, B., Lefeber, D.: Sliding-bar MACCEPA for a powered ankle prosthesis. *J. Mech. Robot.* **7**(4), 1–11 (2015). <https://doi.org/10.1115/1.4029439>
- Kerkum, Y.L., Buizer, A.I., Van den Noort, J.C., Becher, J.G., Harlaar, J., Brehm, M.A.: The effects of varying ankle foot orthosis stiffness on gait in children with spastic cerebral palsy who walk with excessive knee flexion, *PLoS ONE*, **10**(11) (2015). <https://doi.org/10.1371/journal.pone.0142878>
- Omasta, M., Paloušek, D., Návrát, T., Rosický, J.: Finite element analysis for the evaluation of the structural behaviour, of a prosthesis for trans-tibial amputees. *Med. Eng. Phys.* **34**(1), 38–45 (2012). <https://doi.org/10.1016/j.medengphy.2011.06.014>
- Rao, S.S., Boyd, L.A., Mulroy, S.J., Bontrager, E.L., Gronley, J.K., Perry, J.: Segment velocities in normal and transtibial amputees: prosthetic design implications. *IEEE Trans. Rehabil. Eng.* **6**(2), 219–226 (1998). <https://doi.org/10.1109/86.681188>
- Rigney, S.M., Simmons, A., Kark, L.: Concurrent multibody and finite element analysis of the lower-limb during amputee running. *Proc Eng Med Biol Soc*, pp. 2434–2437 (2015)
- Tayyari, S.: Occupational ergonomics. *Occup. Ergon.* **3**, 6221 (2017). <https://doi.org/10.4324/9780203484913>
- Torburn, L., Perry, J., Ayyappa, E., Shanfield, S.L.: Below-knee amputee gait with dynamic elastic response prosthetic feet: a pilot study. *J. Rehabil. Res. Dev.* **27**(4), 369–384 (1990). <https://doi.org/10.1682/jrrd.1990.10.0369>
- Veneva, I., L., Vanderborght, B., Lefeber, D., Chelle, P.: Propulsion system with pneumatic artificial muscles for powering ankle-foot orthosis. *J. Theor. Appl. Mech.*, **43**(4), 3–16 (2014). <https://doi.org/10.2478/jtam-2013-0029>

# Automated Disinfection System for Polyethylene Terephthalate Bottles for Bacteria, Fungi, and Viruses Using UVC LED Camera



Gerson Orihuela , Esleiter Reyes , and Deyby Huamanchahua 

## 1 Introduction

Faced with the global crisis, which is being experienced due to SARS-CoV-2. Health problems are a topic to be addressed worldwide, such as infectious diseases caused by bacteria, viruses, parasites, and fungi, practically by pathogenic microorganisms, which are contagious and are transmitted by inhalation of particles indirectly or directly (Bloom and Cadarette 2019). Likewise, the risks of contracting the virus have been increasing exponentially due to new sources of contagion such as markets, supermarkets, and crowded places, with the most frequent transmission of the virus through microdroplets or droplets that come off the nose (May 2021). These can be deposited on the surfaces of nearby materials, which are mostly handled and discarded, likewise, they can survive a couple of hours or up to several days depending on the material or residue (Quitral Q 2020).

Faced with this, all materials must have optimal handling from their production, consumption, and final disposal, so there must be a control and hygiene treatment for the comfort of people working in the recycling sector, to guarantee their health and well-being (Soliz Torres et al. 2020). The spread of the virus occurs most often in enclosed and poorly ventilated places, such as recycled waste treatment plants where recycled materials, many of them contaminated, accumulate to be treated for reintegration (Huayanay 2020). Considering that the main transmission mechanism is by contact and inhalation (Li et al. 2020), category C (UVC) ultraviolet light offers an efficient alternative in cleaning air and surfaces, which by eliminating said microbial particles reduces the probability of human contagion by the virus that circulates in an environment or space where there is contaminated recycled material accumulated with viruses and bacteria (Cervino et al. 2021; Manuel et al. 2020).

---

G. Orihuela · E. Reyes (✉) · D. Huamanchahua  
Department of Mechatronics Engineering, Universidad Continental, Huancayo, Perú  
e-mail: [48267395@continental.edu.pe](mailto:48267395@continental.edu.pe)

According to studies and the ideal treatment with ultraviolet rays, it reduces the microbial load in contaminated material where UVC rays of the short wavelength of 200–280 nm are applied which generates a germicidal effect (Rattanakul and Oguma 2018; Kim et al. 2017; Hsu et al. 2021). UV rays possess a germicidal action that kills or neutralizes the action of viruses, bacteria, and other primitive microorganisms, so it is mainly used in the sterilization of surfaces and local medical, pharmaceutical, and food industry environments (Hsu et al. 2021; Raeiszadeh and Adeli 2020). The germicide lamp depends on the power and geometric shape considering the appropriate time of dose of UVC light emission, eliminating up to 99.9% of microorganisms (Nnadi et al. 2021; Dwivedi et al. 2021; Heilingloh et al. 2020).

UV irradiation has proven to be an effective physical means for the control of microorganisms, including viruses, with the UVC wavelength being most effective in practical application, followed by that of UVBs and finally that of UVA (Ou and Petersen 2008). The germicidal capacity against viruses lies in their ability to penetrate the viral structure, especially UVC and UVB (Nishisaka-Nonaka et al. 2018), which directly affect the genome preventing its replication and therefore leading to inactivation (Bono et al. 2021).

UVC treatment does not generate organoleptic variations, nor does it generate chemical residues and is effective in disinfecting the surfaces of products and materials (Raeiszadeh and Adeli 2020). Currently, UV light is used for the disinfection and sterilization of surgical products, cleaning of cell phones, purification of environments (Manuel et al. 2020; Rattanakul and Oguma 2018; Casini et al. 2019) process by which it performs to eliminate all forms of microbial life and bacteria (Kim et al. 2017; Dwivedi et al. 2021). It is also used in the disinfection of algae in ballast water based on a new treatment system with multiple ultraviolet waves in an approximate time interval of 20–30 s with a UV photocatalysis system (Lu et al. 2021).

Therefore, the objective of this article is to design a disinfection machine for recycled PET-type bottles using UVC radiation emitted by an LED camera, through an engineering development with the benefits of UV type C light, based on the mechatronic methodology of the Association of German Engineers (VDI 2206), composed of a mechanical, electrical-electronic and control system (Graessler and Hentze 2020), which makes it possible to sterilize recycled PET materials that accumulate in recycling plants for the process of insertion in society, since according to studies shows that 99.99% of viruses and bacteria are removed from the surface of materials and waste that are disposed of in urban areas and markets in general.

## 2 Methodology

The methodology used in the article is based on the VDI 2206 model. The methodology that represents the decomposition of the system is based on a V model for mechatronic systems that represents a logical sequence of activities composed of the left side the decomposition of the system and the right side the subsystems, which are constantly verified and validated (Graessler and Hentze 2020).

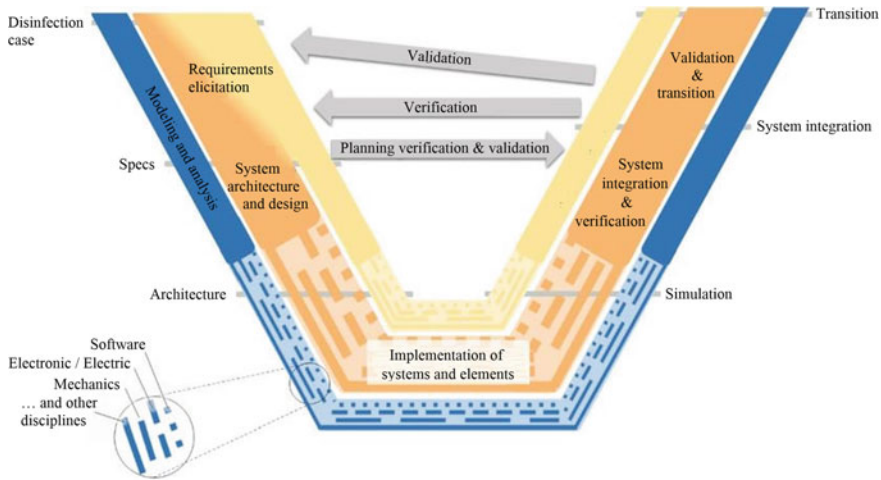


**Fig. 1** Activities to be carried out in the VDI2206 structure

In Fig. 1, the approach of combining activities is shown, and the guideline suggests three main phases followed by a fourth that accompanies the other three: First, the *System design* that has an idea of the result between the influence that specifies the essential particularities logical and physical design motive, second the *Domain Specific Design* which establishes the need for further illustration through more detailed interpretations and calculations separately for each technical system, and the third phase is the *System Integration* which consists of evaluating the overall performance of the system when individual domains are integrated and the fourth is a cross-sectional *Modeling and Simulation* phase that creates and examines the qualities of the system with the support of structural models, tools, and computer-aided simulation instruments. The cycles of this project are the design of the LED camera and the functional simulation prototype. The prototype process includes 3D CAD software, Ladder programming, and the Factory IO integration system.

### 3 Materials

*The mechanical system of the machine:* Composed of the main motor (0.75 HP) that drives the conveyor belt (Siegling Transilon MT black E8/2 U0/V5H with  $k1\% = 8 \text{ N/mm}$ ) generating the transfer of recycled PET bottles toward the LED disinfection chamber of approximately three-square meters of area, after that the exit conveyor will be activated.

*Electrical System–electronic machine:* Composed of the main sensor and three secondary sensors (Diffuse Sensors) (Gutiérrez and Iturralde 2017). The objective of the main sensor is to detect the recycled PET-type material when it is inside the

chamber, generating the stoppage of the conveyor belt and the start of the disinfection process. The ideal time to sanitize recycled bottles is 26 s (s) (Woo et al. 2019; Minamikawa 2008; Muramoto et al. 2008).

*Machine control system:* Employing a programmable logic controller (modular PLC) composed of programming lines in charge of giving instructions to the machine and storing them in its memory, represented by a control panel by pushbuttons, a liquid crystal display (LCD) for observing the count of disinfected materials, and light-emitting diodes (LEDs).

The prototype design of the UVC LED camera was developed in the Inventor program, to develop the virtual simulation of the Factory IO program with the use of PLC programming in the TIA Portal engineering system (Factory 2021; Download Inventor 2021; Software 2019). For the design, we must consider that when working with UV radiation with a range of 200–280 nm, the rays must be isolated, since produces a modification in DNA and this causes cancer (Muramoto et al. 2008; Buonanno et al. 2020). For this reason, strips of anti-ultraviolet ABS plastic sheet have been used to block the projection wave of the irradiation of ultraviolet rays at the beginning and the end of the disinfection chamber stroke (Rodríguez-Tobías et al. 2013).

Figure 2 shows the structural scheme of the prototype of the PET bottle disinfection system, whose structure is based on the process control system with the input and output signal. The vision system captures the input signal of the bottles to the conveyor belt with diffuse sensor inspection. The electronic system that turns on the feeding actuators of the PET bottles, the disinfection chamber that projects category C ultraviolet rays, and the removal of the disinfected material, generating a feedback signal or process concluded. The electromechanical system generates the mobilization of the conveyor belt, the illumination of the UVC LEDs, and the transport of the decontaminated PET bottles to their storage. The energy generates the impulse, the heat, the movement, the vibrations, and the light of the prototype.

## 4 Results

### 4.1 Disinfection Process Time

The maximum disinfection efficiency is 254 nm (nm), which depends on the time of 26 s (s) for the sterilization of the recycled PET bottles to be disinfected.

Figure 3 shows the disinfection chamber made up of four fundamental components; the first component is the chamber liner made of AISI 304 stainless steel from the American Iron and Steel Institute (Mundial 2021). The second component is the protection by strips of anti-ultraviolet ABS plastic sheet that blocks the projection wave of ultraviolet radiation (Rodríguez-Tobías et al. 2013). The third component is the LED type lights that project category C ultraviolet rays, and finally, the fourth component is the main stainless steel structure that ensures resistance, generates

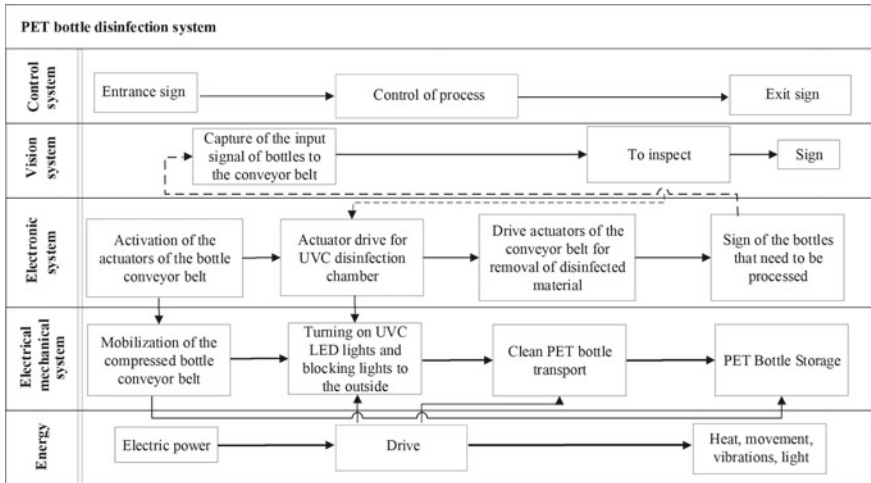


Fig. 2 Structural diagram of the disinfection system

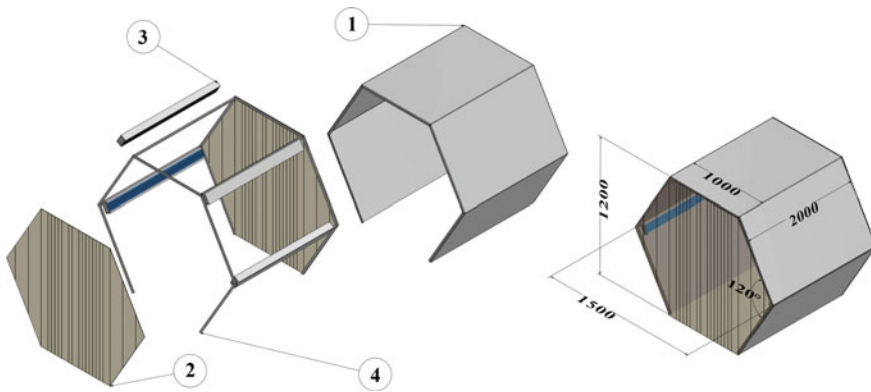


Fig. 3 LED camera that projects ultraviolet rays type C

the shape, and designs stability of the UVC LED camera, which has dimensions of 2000 cm long, 1200 cm high, and 1500 cm wide.

### 4.2 Conveyor Belt

It is based on the weight of the mass of 200 kg of PET bottles that will be transported approximately by the conveyor belt, and then the resistance of the conveyor belt to be used will be determined, consulting Eqs. 1 and 2. The maximum belt traction force ( $F_1$ ) is calculated, which is the result of multiplying the tangential force ( $F_u$ ) of 200

pounds equivalent to 1962 N by the smooth dry steel factor  $C_1$  of 1.5 at an angle of  $180^\circ$  (Siegling 2016).

$$F_1 = Fu(C_1) \quad (1)$$

With the result of 2943 N, maximum traction of the belt is divided with the width of the belt ( $b_0$ ) of one meter, it is compared with the maximum range factor of the type of tractor element of 2 that must have a conveyor belt multiplied by the tolerance  $k_1\%$  of 8 N millimeters (N/mm) so that it works properly with the values provided by the technical manual (Siegling 2016).

$$F_1/b_0 \leq 2(k_1\%) \quad (2)$$

Therefore, with the result obtained of 2943 N/mm less than and equal to 16 N/mm, it is stated that the conveyor belt will perfectly resist the force exerted by the motor since the value is within the adequate working range as shown in Fig. 4.

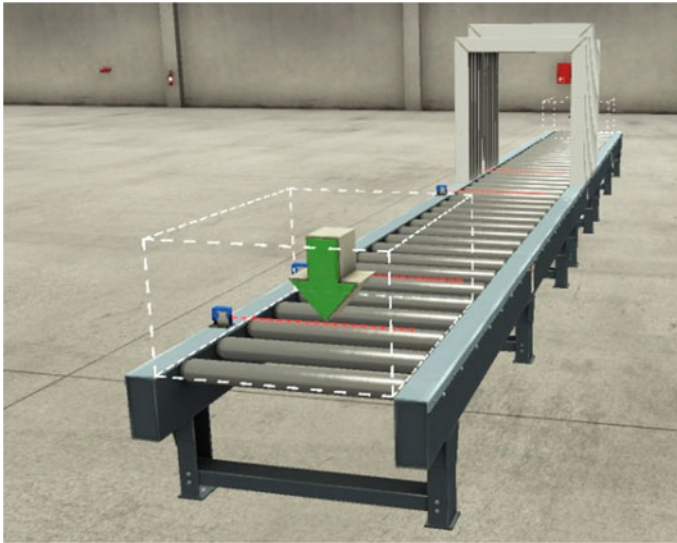


**Fig. 4** Automated machine conveyor belt

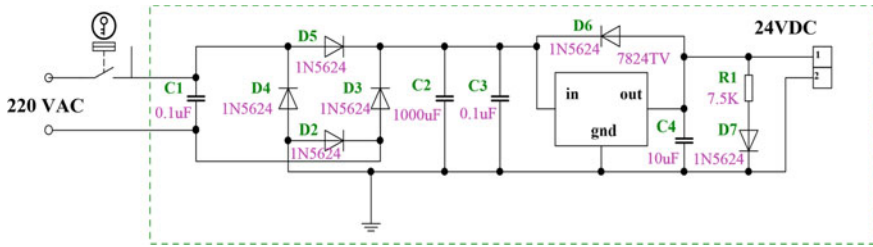


Fig. 5 Voltage regulation

### 4.3 Electronic Circuit and Programmable Logic Control Diagram

Figure 5 shows the electronic circuit that regulates the voltage from alternating current (VAC) of 220 V to a direct current voltage (VDC) of 24 V for the correct operation of the programmable logic controller.

Figure 6a shows the circuit diagram of the operation of the input and output PLC devices, and the outputs are seen as contactors KM1, KM2, and KM3, as well as the start and stop LEDs of the electronic receivers.

Figure 6b shows the power circuit, a part that generates the highest current consumption of the controller, this circuit oversees exciting the relays to activate the output devices, these work through semiconductor devices to control or modify the voltage or current of the machine.

Figure 6c shows the connection diagram of the input devices of the PLC that consists of a start, stop safety, emergency stop buttons, also inductive sensors, and control elements of the electronic diagram.

### 4.4 Ladder Programming Blocks

Figure 7a shows the segment with Ladder programming for the connection of Factory IO engineering programs with the TIA portal software.

Figure 7b shows the segment of the safety system and control drive of the automated machine.

Figure 8a shows the enumerator segment of the system, revealing the total amount of materials disinfected in a full working day.

Figure 8b shows the segment of the drive of the first conveyor belt that feeds the disinfection system, starting the count of material entering the C category UV LED chamber.

Figure 9a shows the segment of the drive of the ultraviolet led camera category C, with the estimated waiting time, while the material of the recycled PET bottles is



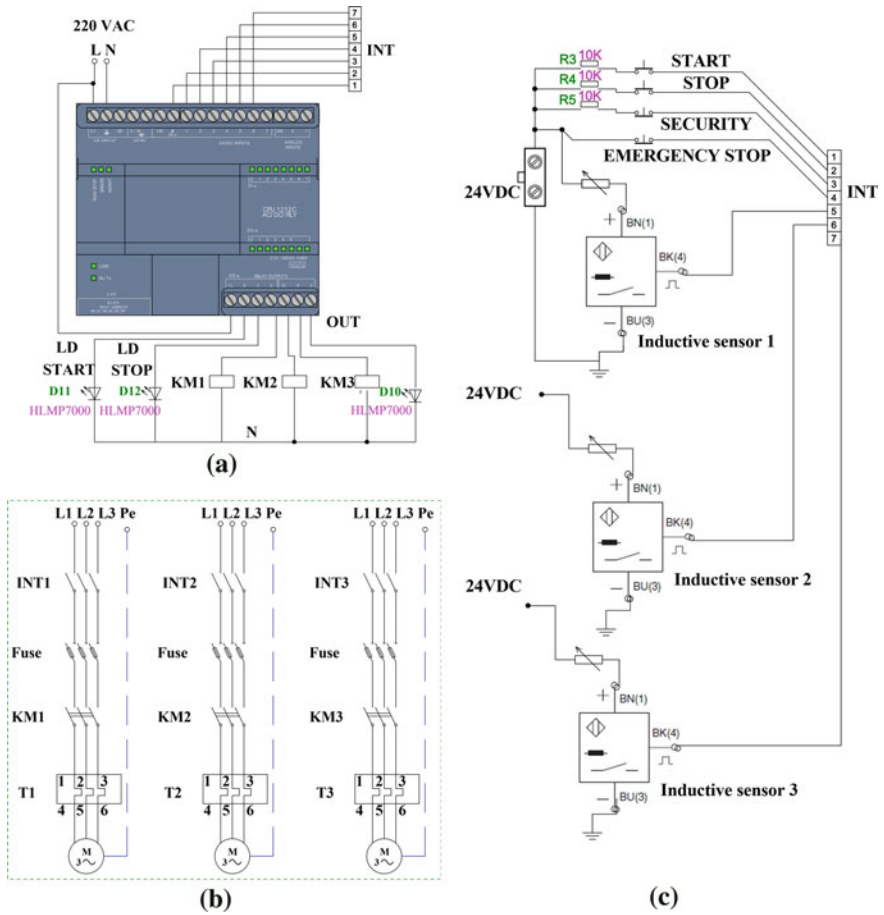


Fig. 6 a Programmable logic control, b power circuit and c PLC input connection diagram

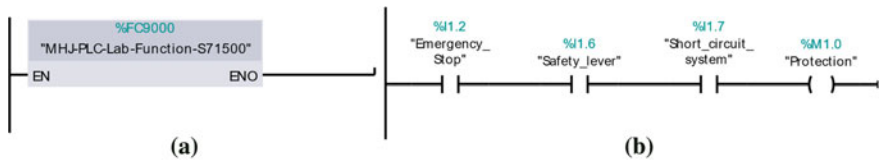


Fig. 7 a Connection factory IO-TIA portal and b security system

disinfected for 26 s, after which it generates the drive of the output conveyor belt for the warehouse of the recycling plant.

Figure 9b shows the segment of the outputs of the programmable logic controller that activates each drive component of the machine.

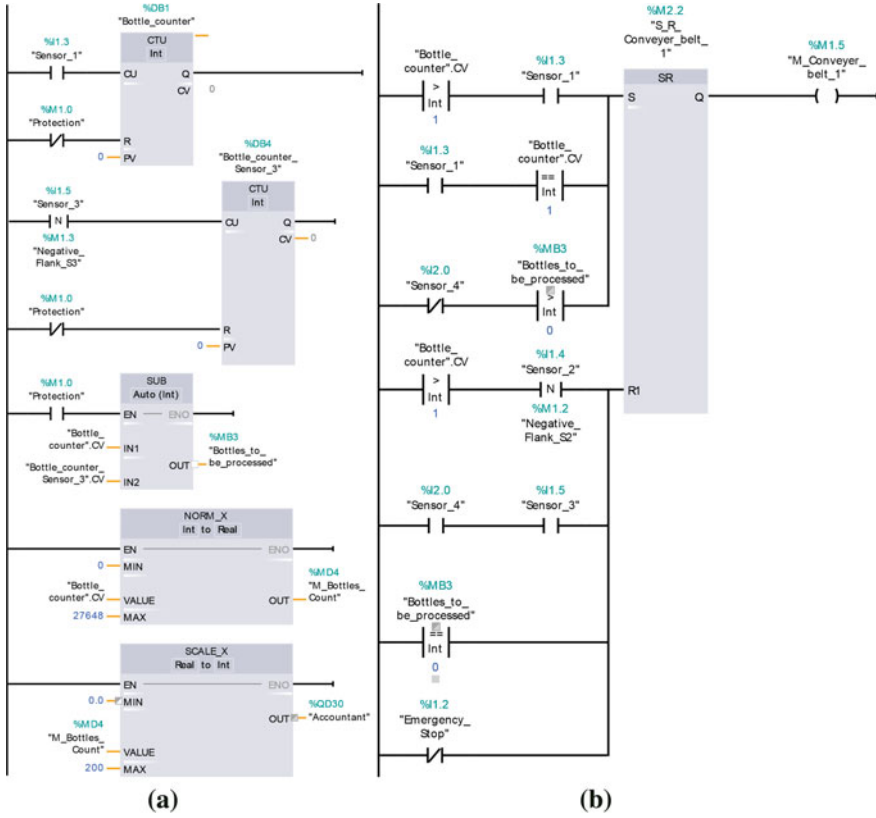


Fig. 8 a System counter and b drive of the conveyor belt and counter

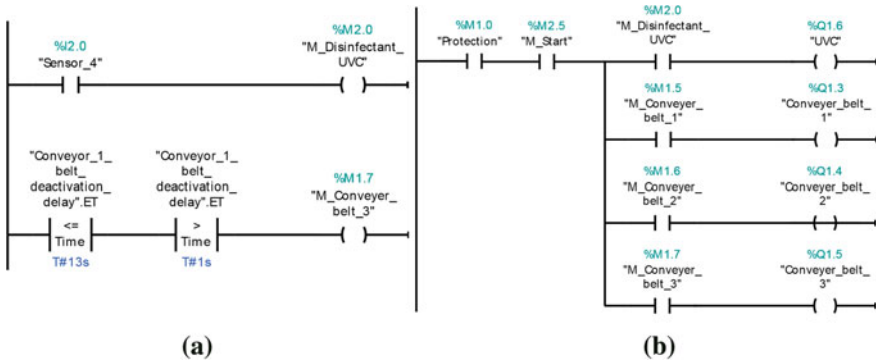


Fig. 9 a Disinfection and exit of the material and b component activation signal outputs



**Fig. 10** Automated disinfection in factory IO of polyethylene terephthalate bottles for bacteria, fungi, and viruses; by UVC LED camera

#### ***4.5 Automated PET Bottle Machine***

Figure 10 shows the final prototype of the automatic polyethylene terephthalate bottle disinfection machine that uses a 254 nm short-wave category C UV LED camera for the disinfection of bacteria, fungi, and viruses.

### **5 Discussion**

SARS-CoV-2 is a highly variant and contagious virus due to its rapid transmission through droplets that settle on the surfaces of surrounding materials or by materials handled and discarded. Therefore, the disinfection system focuses on PET bottle recycling treatment plants with poor ventilation and closed environments for waste storage processes. These droplets remain impregnated on the surface of any material and at the same time in the process of transferring or displacing the contaminated material to reinsert the recycled polyethylene terephthalate material into society, the risk of contagion increases since the virus can survive for hours or days depending on the material where it resides.

That is why automated disinfection is important and necessary, with an LED camera that projects type C ultraviolet rays, sterilizes PET bottles against the threat of SARS-CoV-2 and highly contagious variant particles, thus efficiently eliminating impregnated viruses, generating security for the population of the recycling sector that plays a very important role in the collection and transformation of recycled material.

In this process, the recycled PET bottles enter through the conveyor belt to the UVC LED camera which has a memory program that applies 26 s to sterilize 99.99% of fungi, bacteria, and viruses. With a short wavelength of 254 nm and an irradiation

dose of 220 (J/m<sup>2</sup>) Joule per square meter, the disinfected bottles are removed by the conveyor belt for their reinsertion process. This proposal is considered an emerging technology that agrees with the following studies (Rattanukul and Oguma 2018; Kim et al. 2017; Hsu et al. 2021; Raeiszadeh and Adeli 2020; Nnadi et al. 2021; Dwivedi et al. 2021) and (Heilingloh et al. 2020) which consists of control surfaces. The recycled PET bottles, at the illumination of the wave range of 200–280 nm, it is confirmed that there is greater sterilization with the emissions of 254 nm.

## 6 Conclusion

In conclusion, it is highlighted that the machine works with ideal automated treatment, with category C short-wave UV radiation, and this reduces the microbial load found on the surface of polyethylene terephthalate materials in the recycling plant. This UVC disinfection strategy is highly effective in eradicating up to 99.99% of microorganisms and viruses; this method being an alternative to help disinfect surfaces in the current pandemic, so this research shows how to safely disinfect the surface to be treated.

Implement the proposal both in different recycling and disinfection sectors, which will allow its effectiveness to be verified, and also to adapt and improve both the model and the proposed methodology and tools.

Finally, this research will serve for the development and improvement of similar machines; since its purpose is that viruses, fungi, and bacteria do not remain on the surfaces of the materials that are processed for their reintegration into our society.

## References

- Bloom, D.E., Cadarette, D.: Infectious Disease threats in the twenty-first century: strengthening the global response. *Front. Immunol.* **10**, 549 (2019). <https://doi.org/10.3389/fimmu.2019.00549>
- Bono, N., Ponti, F., Punta, C., Candiani, G.: Effect of UV irradiation and TiO<sub>2</sub>-photocatalysis on airborne bacteria and viruses: an overview. *Mater. (basel)* **14**(5), 1075 (2021)
- Buonanno, M., Welch, D., Shuryak, I., Brenner, D.J.: Far-UVC light efficiently and safely inactivate airborne human coronaviruses. *Res. Square* (2020)
- Casini, B., et al.: Evaluation of an ultraviolet C (UVC) light-emitting device for disinfection of high touch surfaces in hospital critical areas. *Int. J. Environ. Res. Public Health* **16**(19), 3572 (2019)
- Cervino, C.O., Almandoz, J.C., Mignone, M., Irusta, A., Leiton, G.: The use of UV-C radiation for disinfection in the face of the COVID-19 pandemic: new portable UV-C disinfection system, UNIMORON-Desinfector© (2021)
- Download Inventor 2022: *Autodesk.com*, [Online]. Available in: <https://latinoamerica.autodesk.com/products/inventor/free-trial>. Last accessed 06 Apr 2021
- Dwivedi, V. et al.: Rapid and efficient inactivation of SARS-CoV-2 from surfaces using UVC light-emitting diode device (2021)
- Factory I/O—Next-Gen PLC Training. *Factoryio.com*. [Online]. Available in: <https://factoryio.com/download-archive/>. Last accessed 15 Apr 2021

- Graessler, I., Hentze, J.: The new V-Model of VDI 2206 and its validation. *Autom.* **68**(5), 312–324 (2020)
- Gutiérrez, M., Iturralde, S.: Basic fundamentals of instrumentation and control, First Edition, Editorial EUPSE, Ecuador (2017)
- Heilingloh, C.S., et al.: Susceptibility of SARS-CoV-2 to UV irradiation. *Am. J. Infect. Control*, **48**(10), 1273–1275 (2020)
- Hsu, T.C., et al.: Perspectives on UVC LED: Its progress and application. *Photonics* **8**(6), 196 (2021)
- Huayanay, L.: Airborne transmission in closed spaces of SARS-Cov-2. *An. Fac. Med.* **81**(3), 342–347 (2020)
- Kim, D.K., Kim, S.J., Kang, D.H.: Bactericidal effect of 266 to 279 nm wavelength UVC-LEDs for inactivation of Gram-positive and Gram-negative foodborne pathogenic bacteria and yeasts. *Food Res. Int.* **97**, 280–287 (2017)
- Li, Q., et al.: Early transmission dynamics in Wuhan, China, of novel Coronavirus-infected pneumonia. *N. Engl. J. Med.* **382**(13), 1199–1207 (2020)
- Lu, Z., Wang, Y., Zhang, S., Zhang, K., Shi, Y., Meng, C.: Multi-wave UV-photocatalysis system (UVA+UVC+VUV/Cu-N-TiO<sub>2</sub>) for efficient inactivation of microorganisms in ballast water. *Mater. Express* **11**(9), 1608–1614 (2021)
- M. Manuel et al., “Development of a UV-C air sterilizer for the control of airborne transmission of COVID-19”, *Innovación y Desarrollo Tecnológico y Social*, vol. 2, num. 2, pp. 167–203, 2020.
- Material Mundial: AISI 304 Stainless Steel Technical Sheet, Properties, Density, Hardness. *Materialmundial.com*, [Online]. Available: <https://www.materialmundial.com/acero-inoxidable-ss-astm-sae-aisi-304-ficha-tecnica/>. Last accessed 15 Sept 2021
- May, U.: The risks—know them—avoid them. *Scpns.com*. [Online]. Available in: <http://www.scpns.com/wp-content/uploads/2020/06/The-Risks-Know-Them-Avoid-Them.pdf>. Last accessed 20 Oct 2021
- Minamikawa, T. et al.: Inactivation of SARS-CoV-2 by deep ultraviolet light-emitting diode: a review. *Jpn. J. Appl. Phys.*, **2008** (2021)
- Muramoto, Y., Kimura, M., Kondo, A.: Verification of inactivation effect of deep ultraviolet LEDs on bacteria and viruses, and consideration of effective irradiation methods. *Jpn. J. Appl. Phys.* **2008** (2021)
- Nishisaka-Nonaka, R., et al.: Irradiation by ultraviolet light-emitting diodes inactivate influenza a virus by inhibiting replication and transcription of viral RNA in host cells. *J. Photochem. Photobiol. B* **189**, 193–200 (2018)
- Nnadi, D.B.N., Araoye, T.O., Egoigwe, S.V., Vincent, D.A.: Application of robotics UV-light device in averting the spread of Coronavirus. *Res Square* (2021)
- Ou, Y., Petersen, P.M.: Application of ultraviolet light sources for in vivo disinfection. *Jpn. J. Appl. Phys.* (2008), **60**(10), 100501, (2021)
- Raeiszadeh, M., Adeli, B.: A critical review on ultraviolet disinfection systems against COVID-19 outbreak: applicability, validation, and safety considerations. *ACS Photonics* **7**(11), 2941–2951 (2020)
- Rattanakul, S., Oguma, K.: Inactivation kinetics and efficiencies of UV-LEDs against *Pseudomonas aeruginosa*, *Legionella pneumophila*, and surrogate microorganisms. *Water Res.* **130**, 31–37 (2018)
- Rodríguez-Tobías, H., Morales, G., Rodríguez-Fernández, O., Acuña, P.: Mechanical and UV-shielding properties of in situ synthesized poly(acrylonitrile-butadiene-styrene)/zinc oxide nanocomposites. *J. Appl. Polym. Sci.* **127**(6), 4708–4718 (2013)
- Siegling, F.: Conveyor belts, and processing, conveyor belt calculation. 2016. Retrieved from: <https://docplayer.es/11410149-Calculo-de-la-banda-transportadora.html>. Last accessed 20 Oct 2021
- “Software”: *Siemens.com*, [Online]. Available in: <https://new.siemens.com/mx/es/productos/automatizacion/industry-software/automation-software/tia-portal/software.html>. Last accessed 27 Aug 2019
- Soliz Torres, M.F., Durango Cordero, J.S., Yépez Fuentes, M.A., Solano Peláez, J.L.: The right to health in the recycling trade: community actions against COVID-19. Quito, EC: Universidad

- Andina Simón Bolívar, Ecuador Headquarters/VLIR-UOS/Zero Waste Campaign, Ecological Action/Global Alliance for Alternatives to Waste Incineration (2020)
- Woo, H., et al.: Efficacy of inactivation of human enteroviruses by dual-wavelength germicidal ultraviolet (UV-C) light-emitting diodes (LEDs). *Water (basel)* **11**(6), 1–1131 (2019)
- Quitral Q, Y.A.: Libraries in the face of the COVID-19 pandemic: fundamentals and actions in Latin America. *Bibl. Univ.*, (2020). <https://doi.org/10.22201/dgb.0187750xp.0.0.992>

# Design of the CNC Router Structure for Machining Wood Materials Using Reliability-Based Design Optimization Method



Huu Loc Nguyen and Van Thuy Tran

## 1 Introduction

The uncertainties of the structural system (i.e., loads, materials, dimensions, models, etc.) in deterministic design optimization are taken into account in an indirect and subjective method, based on partial safety factors determined in design ranges. Therefore, the level of reliability can be reduced when using deterministic optimal solutions (Beck and Santana Gomes 2012; Thuy and Nguyen 2018). The objective of a RBDO method is to optimize structures, and make sure that a minimum reliability level is upheld by the optimum structure.

The optimization algorithms of the RBDO method use the reliability methods to evaluate the probability constraints, and the objective functions are utilized to prescribe the reliability (Chiralaksanakul and Mahadevan 2005; Royset et al. 2001). In RBDO methods, the commonly used design parameters are the mean of random system parameters and solve a mathematical nonlinear programming problem to determine the optimized cost according to the prescribed probabilistic constraints. Therefore, the solution from RBDO supplies not only improves the design quality but also increases the reliability of the design, reduces the production cost and improves the model more beautiful (Youn and Choi 2004a; Tu et al. 2001).

There are two different methods used to evaluate the RBDO incorporating probabilistic constraints, the performance measure approach (PMA) and the reliability index approach (RIA) (Youn et al. 2003; Tu et al. 1999; Cheng et al. 2018). According

---

H. L. Nguyen (✉)

Faculty of Mechanical Engineering, Ho Chi Minh City University of Technology (HCMUT), 268 Ly Thuong Kiet Street, District 10, Ho Chi Minh City, Vietnam  
e-mail: [nhloc@hcmut.edu.vn](mailto:nhloc@hcmut.edu.vn)

Vietnam National University Ho Chi Minh City, Linh Trung Ward, Thu Duc City, Ho Chi Minh City, Vietnam

V. T. Tran

Faculty of Engineering - Technology, Pham Van Dong University, Quảng Ngãi, Vietnam

to the RIA method, the probability constraint is defined as reliability. Nevertheless, RIA does not converge for some problems or converges slowly. To avoid this shortcoming, PMA is recommended by solving an inverse problem for the first-order reliability method (FORM) (Youn and Choi 2004b; Enevoldsen and Sørensen 1994; Padmanabhan et al. 2006).

For reliability analysis, FORM has proven to be effective and widely used. Therefore, to evaluate the objective functions and the number of probabilistic constraints, the previous RBDO methods used FORM. Over the years, the structural and engineering disciplines have adopted. Several first-order RBDO methods have been shown to be more effective than previous RBDO methods (Loc et al. 2019).

## 2 Theoretical Background

RBDO problem in system parameter design is introduced as follows (Nguyen 2015; Wang and Ma 2017):

$$\text{Find } \mathbf{X} = \left\{ \begin{array}{c} X_1 \\ X_2 \\ \cdot \\ \cdot \\ \cdot \\ X_n \end{array} \right\} \quad (1)$$

To minimize  $f(\mathbf{X})$ ,

Subject to:

$$\begin{aligned} P(g_j(\mathbf{X}, \mathbf{p}) \geq 0) &\geq R_j^*; \quad j = 1, 2, \dots, n_g \\ h_k(\mathbf{X}, m_p) &\leq 0; \quad k = 1, 2, \dots, n_h \\ X_i^l &\leq X_i \leq X_i^u; \quad i = 1, 2, \dots, n. \end{aligned}$$

where  $X_i$  is the design variable (deterministic or random),  $\mathbf{X}$  is the design variable vectors (including deterministic and random),  $\mathbf{p}$  are random parameter vectors (mean value is  $m_p$ ),  $g_j(\mathbf{X}, \mathbf{p})$  is the limit state function,  $f(\mathbf{X})$  is the objective function,  $n$  are the numbers of design variables,  $n_g$  are the numbers of probability constraints,  $R_j^*$  are the desired reliability and  $X_i^l, X_i^u$  are the upper and upper limits of the design variable.

The inverse reliability analysis method is used to transform the RBDO problem into a deterministic optimization problem. To solve this problem, it is first necessary to determine the limit state function value  $g^F$  correspond with the desired reliability  $R_j^*$ . The steps are as follows (Fig. 2).

Find the value of limit state function  $g^F$  correspond with a failure probability  $F$ :



$$F = P(g(X) < g^F) \tag{2}$$

The new limit state function is obtained after estimation by an approximation method:

$$g'(X) = g(X) - g^F \tag{3}$$

Assume the most probable point (MPP) of a function  $P(g'(X) < 0) = P(g(X) < g^F)$  is  $u^*$ , according to the FORM, if the probability of failure  $F$  is known in advance, the index of reliability  $\beta$  is determined as follows:

$$\beta = |\Phi^{-1}(F)| \tag{4}$$

In Fig. 1, the most probable point  $u^*$  is the point of contact of a circle of radius  $g^F$  and the function  $g(X) - g^F = 0$ . In other words, it is the point of contact that determines the shortest distance from the limit state function surface  $g(X) - g^F = 0$  to the origin O in U space.

At the MPP  $u^*$ :

$$u^{*F} = -\|u^{*F}\|a^* = -\beta a^* \tag{5}$$

In the  $k$ th loop:

$$u^{k+1} = -\beta a^k \{u\} \tag{6}$$

where

$$a^k = \frac{\nabla g(u^k)}{\|\nabla g(u^k)\|} \tag{7}$$

**Fig. 1** Find MPP by inverse reliability analysis

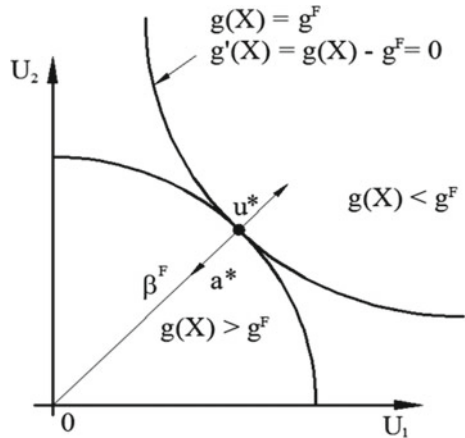
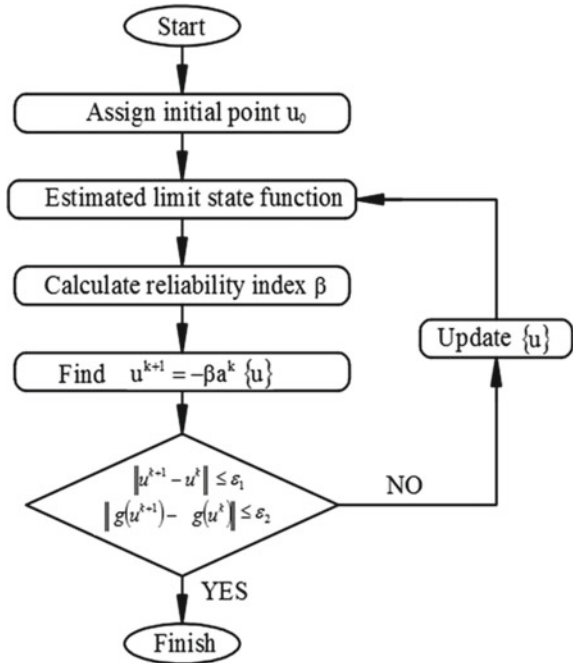


**Fig. 2** Algorithm to find MPP according to the inverse reliability analysis method



Convergence conditions are used to finish the loop:

$$\|u^{k+1} - u^k\| \leq \varepsilon_1 \text{ and } \|g(u^{k+1}) - g(u^k)\| \leq \varepsilon_2 \quad (8)$$

After determining the MPP  $u^*$ , the value of the function  $g^F$  is determined as follows:

$$g^F = g(u^*) \quad (9)$$

In summary, the algorithm to find the MPP according to the inverse reliability analysis method is presented as Fig. 2.

After determining  $g^F$ , the RBDO problem turns into a deterministic optimization problem and the first constraint of the RBDO problem (1) become  $g_j(\mathbf{X}, \mathbf{p}) \geq g^F$ .

### 3 Numerical Example

RBDO approach is used to optimize the design of the CNC router structure as shown in Fig. 3. Supposing that the CNC router structure is composed of four elements linked together such as the head (1), crossbeam (2), column (3) and the base (4). To simplify the calculations, it is accepted that the head, crossbeam and column are the

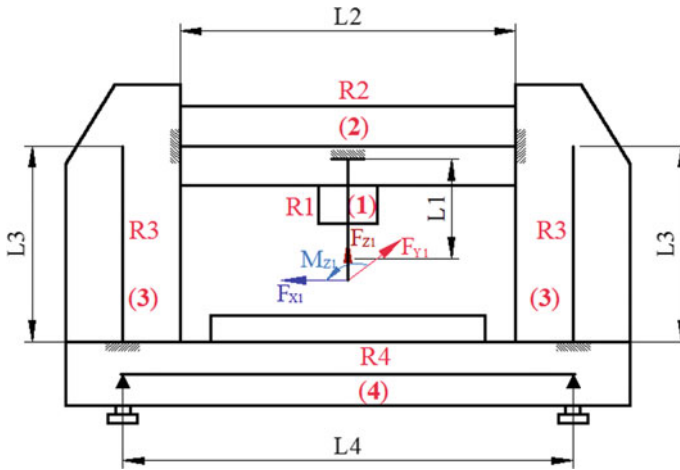


Fig. 3 Model of a CNC router structure

cantilever beam correspond with the length  $L_1, L_2, L_3$  and the base  $L_4$  which is fixed by 2 supports.

The applied forces  $F_{x1}, F_{y1}, F_{z1}$  and  $M_{z1}$  are put into the computational model. During machining, force components  $F_{x1}, F_{y1}, F_{z1}$  and torque  $M_{z1}$  from the cutting tool are applied to the spindle of the machine body structure (Nguyen and Tran 2022).

If we consider the planar problem, the element (1) is subjected to bending and compression. The compressive stress in the Z direction is usually small compared to the bending stress, so it can be ignored. The planar problem with element (1) is then only subjected to bending and torsion. Elements (2), (3) and (4) are similarly considered. Therefore, the structural design problem of the machine body is to solve the problems for elements (1), (2), (3) and (4), respectively, which are considered as bars and beams. Then, combining the solutions obtained together, we have the preliminary dimensions of the body. We separate elements (1), (2) and (3) from the model, convert the model to a simple form and set the force conditions (cutting force is constant) as shown in Fig. 4.

Preliminary selection of body structure geometry dimensions: The basis for preliminary selection of the geometric dimensions of the body structure is as follows: The CNC router on the market were analyzed, and it is found that the working area of the medium CNC router according to X is less than 1000 mm, Y less than 2000 mm and Z less than 100 mm. In addition, wood workpiece in sheet form is common, so the thickness in the Z direction is usually less than 100 mm. On that basis, the dimensions of the machine structure are preliminarily selected as follows:  $L_1 = 250$  mm,  $L_2 = 1000$  mm and  $L_3 = 350$  mm.

For the preliminary design of the CNC router body structure, the desired reliability  $R^* = 0.999$  is selected and the RBDO method is used. Two design variables that represent the height  $V_i$  and width  $H_i$  are determined and given in Table 1.

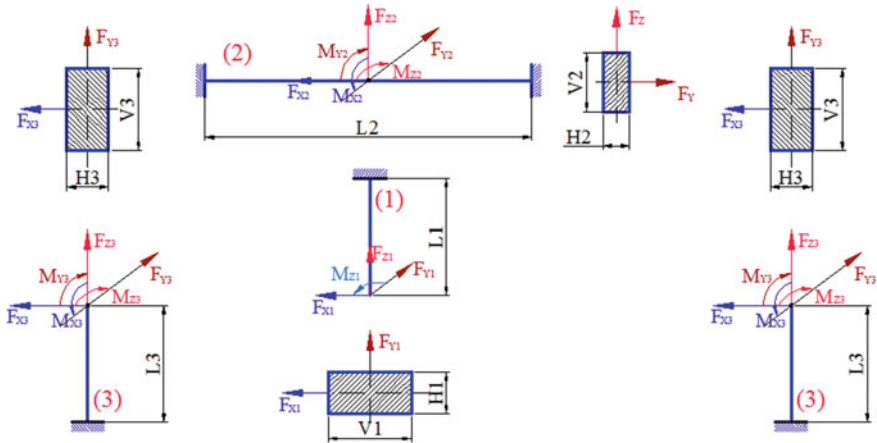


**Fig. 4** Simple model of elements (1), (2) and (3)

**Table 1** Dimensions of the upper and lower limits of the geometry parameters

| Elements    | Parameters | Basic values, mm | Lower limits<br>$V_{imin}, H_{imin}$ , mm | Upper limits<br>$V_{imax}, H_{imax}$ , mm |
|-------------|------------|------------------|---|---|
| Head 1      | $V_1$      | 200              | 150                                       | 250                                       |
|             | $H_1$      | 25               | 20  | 30  |
| Crossbeam 2 | $V_2$      | 275              | 225                                       | 325                                       |
|             | $H_2$      | 25               | 20  | 30  |
| Column 3    | $V_3$      | 350              | 300                                       | 400                                       |
|             | $H_3$      | 35               | 30  | 40  |

Material for all elements is steel C45, yield strength  $\sigma_y = 360$  MPa and standard deviation  $S_y = 6$  MPa. Coefficient of variation of forces and moment is 0.1. Mechanical properties of steel materials C45 are in Table 2.

The processing material is Golden oak wood, whose scientific name is *Homalium Caryophyllaceum Benth* with the density of  $1000 \text{ kg/m}^3$ , durability at 70 MPa, hardness at 7.7 HB and humidity of 15%. The components of the applied force are defined rely on a cutting force in a woodworking process. Components of the applied force are presented in Table 3 (Wang and Ma 2017).

According to the strength criteria, the limit state function is written as follows:

**Table 2** Mechanical properties of steel material C45

| C        | Si        | Mn        | S            | P            | Cr      |
|----------|-----------|-----------|--------------|--------------|---------|
| 0.42–0.5 | 0.15–0.35 | 0.50–0.80 | $\leq 0.025$ | $\leq 0.025$ | 0.2–0.4 |

**Table 3** Applied forces

| Elements    | Force $F_{Zi}$ , N | Force $F_{Xi}$ , N | Force $F_{Yi}$ , N | Moment $M_{Xi}$ , Nmm | Moment $M_{Yi}$ , Nmm | Torque $M_{Zi}$ , Nmm | Length $L_i$ , mm |
|-------------|--------------------|--------------------|--------------------|-----------------------|-----------------------|-----------------------|-------------------|
| Head 1      | 215                | 390                | 390                | 0                     | 0                     | 1170                  | 250               |
| Crossbeam 2 | 215                | 390                | 390                | 97,500                | 97,500                | 1170                  | 1000              |
| Column 3    | 185                | 120                | 196                | 533                   | 48,843                | 16,607                | 350               |

$$g(\sigma_{iy}, \sigma_{ieq}) = \sigma_y - \sqrt{\left(\frac{F_{Zi}}{H_i V_i} + 6F_{Xi} L_i \left(\frac{1}{H_i V_i^2} + \frac{1}{V_i H_i^2}\right)\right)^2 + 4\left(\frac{M_{Zi}}{3.07 V_i H_i^2}\right)^2} \tag{10}$$

According to the stiffness criteria, the limit state function is written as follows:

$$g(u_{i \text{ lim}}, u_{i \text{ max}}) = u_{i \text{ lim}} - u_{i \text{ max}} = u_{i \text{ lim}} - \sqrt{\left(\frac{F_{Xi} L_i^3}{3EI_{Yi}}\right)^2 + \left(\frac{F_{Yi} L_i^3}{3EI_{Xi}}\right)^2} \tag{11}$$

The RDBO problem for the elements is presented as follows:

Design variable:  $V_i, H_i$ .

Objective function:  $m_i = \rho L_i V_i H_i \rightarrow \min$ .

Subject to:

$$\left\{ \begin{array}{l} V_{i \text{ min}} \leq V_i \leq V_{i \text{ max}} \\ H_{i \text{ min}} \leq H_i \leq H_{i \text{ max}} \\ P(g(\sigma_{iy}, \sigma_{ieq}) > 0) = P((\sigma_{iy} - \sigma_{ieq}) > 0) \geq R_i^* \\ P(g(u_{i \text{ lim}}, u_{i \text{ max}}) > 0) = P((u_{i \text{ lim}} - u_{i \text{ max}}) > 0) \geq R_i^* \end{array} \right. \tag{12}$$

where limit displacement  $u_{i \text{ lim}} = 0.035$  mm and desired reliability  $R_i^* = 0.999$ .

The inverse reliability analysis method is utilized to shift the RDBO problem into the deterministic optimization problem. After four loops, the function  $g^F$  at the MPP has the following value in Table 4.

Thus, the RDBO problem is transformed into the deterministic optimization problem as follows:

Design variable:  $V_i, H_i$ .

**Table 4** Calculation results

| The limit state function $g_i^F$   | Head 1                 | Crossbeam 2            | Column 3               |
|------------------------------------|------------------------|------------------------|------------------------|
| $g_{i\sigma}^F = g_{i\sigma}(u^*)$ | 0.0327                 | 0.0362                 | 0.0298                 |
| $g_{iS}^F = g_{iS}(u^*)$           | $-7.65 \times 10^{-4}$ | $-8.21 \times 10^{-4}$ | $-6.82 \times 10^{-4}$ |

Objective function:  $m_i = \rho L_i V_i H_i \rightarrow \min.$

Subject to:

$$\left\{ \begin{array}{l} V_{i \min} \leq V_i \leq V_{i \max} \\ H_{i \min} \leq H_i \leq H_{i \max} \\ g(\sigma_{iy}, \sigma_{ieq}) = \sigma_{iy} - \sigma_{ieq} \geq g_{i\sigma}^F \\ g(u_{i \lim}, u_{i \max}) = u_{i \lim} - u_{i \max} \geq g_{iS}^F \end{array} \right. \quad (13)$$

The genetic algorithm method in Tool Optimization of MATLAB is utilized to solve the design optimization problem. The results achieved after optimizing of the machine head, horizontal beam and vertical column of the CNC router are presented in Table 5.

Equivalent stresses  $\sigma_{eq1}$ ,  $\sigma_{eq2}$ ,  $\sigma_{eq3}$  and displacement  $u_{1max}$ ,  $u_{1max}$ ,  $u_{1max}$ , respectively, of machine head, crossbeam and vertical column of CNC router are all smaller than the limit strength value  $\sigma_y$  and displacement  $u_{lim}$ .

The MCS method is used to analyze the reliability of the machine structure after optimal design. The reliability analysis results according to the MCS method are compared with the desired reliability of the body structure. Simulation results with sample number  $N = 5.10^6$  are presented in Figs. 5 and 6.

**Table 5** Optimal design results

| Elements    | Mass $m_i$ , kg | Height $H_i$ , mm | Width $V_i$ , mm | Stress $\sigma_{eqi}$ , MPa | Maximum displacement $u_{imax}$ , mm |
|-------------|-----------------|-------------------|------------------|-----------------------------|--------------------------------------|
| Head 1      | 13.326          | 29                | 230              | 3.56                        | 0.0199                               |
| Crossbeam 2 | 34.67           | 28                | 300              | 4.22                        | 0.0184                               |
| Column 3    | 33.66           | 35                | 353              | 1.40                        | 0.0195                               |

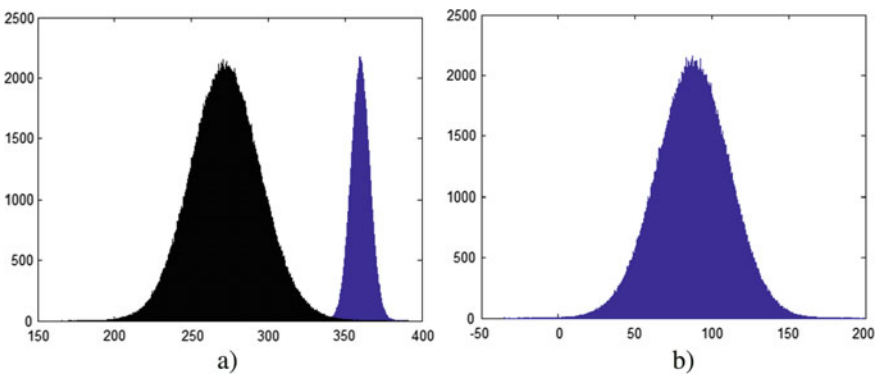


**Fig. 5** Monte Carlo simulation according to the strength criteria: **a** yield strength  $\sigma_y$  and stress  $\sigma_{max}$  and **b** limit state function  $g(X)$

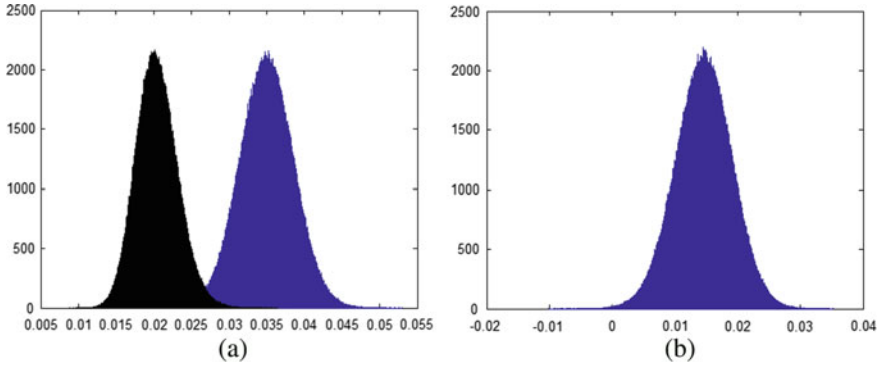


**Fig. 6** Monte Carlo simulation according to the stiffness criteria: **a** displacement  $u_{max}$ ,  $u_{lim}$  and **b** limit state function  $g(\mathbf{X})$

The results of the reliability analysis of the MCS method: according to the strength criteria  $R_{MCS\sigma} = 0.99977$  and stiffness criteria  $R_{MCSu} = 0.99973$ . Because  $R_{MCS\sigma}$  and  $R_{MCSu}$  are more than  $R^* = 0.999$ , the body structure after optimizing the design according to RBDO method is satisfactory.

After the complete design, CAD model has the form as shown in Fig. 7a, an analysis and a test are conducted according to strength and stiffness on the CAE system as shown in Fig. 7b, c. The results of the test in accordance with the stiffness and strength criteria is satisfactory.

After the complete design, CAD model has the form as shown in Fig. 7a, an analysis and a test are conducted in accordance with the stiffness and strength on the CAE system as shown in Fig. 7b, c. The results of the test in accordance with the stiffness and strength criteria are satisfactory.

## 4 Conclusions

This paper applies the RBDO approach to analyze and design CNC router structure. With desired reliability  $R^*$ , the inverse reliability analysis method is utilized to transform the RBDO problem into a deterministic optimization problem.

Genetic Algorithm method in Tool Optimization of MATLAB is utilized to solve the design optimization problem. The results obtained after design optimization include equivalent stresses  $\sigma_{eq1}$ ,  $\sigma_{eq2}$ ,  $\sigma_{eq3}$  and displacement  $u_{1max}$ ,  $u_{1max}$ ,  $u_{1max}$ , respectively, of machine head, crossbeam and vertical column of CNC router are all smaller than limit strength value  $\sigma_y$  and displacement  $u_{lim}$ .

MCS is used to analyze the machine structure reliability after an optimal design according to strength and stiffness criteria. The reliability analysis results according to the MCS method are compared with the desired reliability  $R^*$  of the body structure.

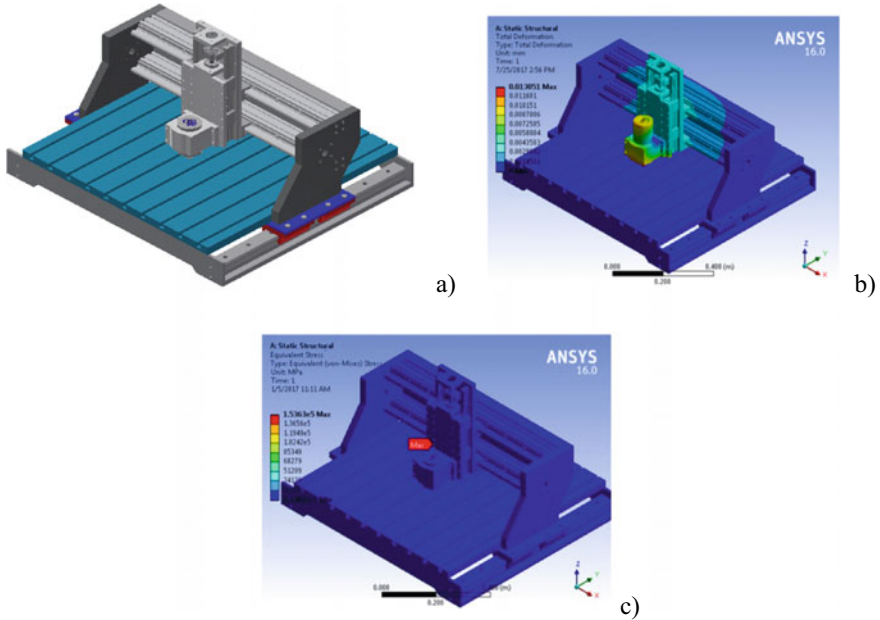


**Fig. 7** CAD and CAE model

The obtained findings highlighted that body structure after optimizing the design according to the RDBO method is satisfactory.

**Acknowledgements** We acknowledge Ho Chi Minh City University of Technology (HCMUT), VNU-HCM for supporting this study.

## References

- Beck, A.T., de Santana Gomes, W.J.: A comparison of deterministic, reliability-based and risk-based structural optimization under uncertainty. *Probabilistic Eng. Mech.* **28**, 18–29 (2012)
- Van Thuy, T., Nguyen, H.L.: Investigation on influence of cutting parameters on spindle vibration of CNC wood milling machine. *MATEC Web Conf.* **213**, 01007 (2018)
- Chiralaksanakul, A., Mahadevan, S.: First-order approximation methods in reliability-based design optimization (2005)
- Roysset, J., Kiureghian, A.D., Polak, E.: Reliability-based optimal design of series structural systems. *J. Eng. Mech.* **127**, 607–614 (2001)
- Youn, B.D., Choi, K.K.: An investigation of nonlinearity of reliability-based design optimization approaches. *J. Mech. Des.* **126**, 403–411 (2004a)
- Tu, J., Choi, K.K., Park, Y.H.: Design potential method for robust system parameter design. *AIAA J.* **39**, 667–677 (2001)
- Youn, B.D., Choi, K.K., Park, Y.H.: Hybrid analysis method for reliability-based design optimization. *J. Mech. Des.* **125**, 221–232 (2003)



- Tu, J., Choi, K.K., Park, Y.H.: A new study on reliability-based design optimization (1999)
- Cheng, Q., Zhao, H., Zhao, Y., Sun, B., Gu, P.: Machining accuracy reliability analysis of multi-axis machine tool based on Monte Carlo simulation. *J. Intell. Manuf.* **29**, 191–209 (2018)
- Youn, B.D., Choi, K.K.: A new response surface methodology for reliability-based design optimization. *Comput. Struct.* **82**, 241–256 (2004b)
- Enevoldsen, I., Sørensen, J.D.: Reliability-based optimization in structural engineering. *Struct. Saf.* **15**, 169–196 (1994)
- Padmanabhan, D., Agarwal, H., Renaud, J.E., Batill, S.M.: A study using Monte Carlo simulation for failure probability calculation in reliability-based optimization. *Optim. Eng.* **7**, 297–316 (2006)
- Loc, N.H., Van Thuy, T., Trung, P.Q.: Reliability-based analysis of machine structures using second-order reliability method. *J. Adv. Mech. Des. Syst. Manuf.*, **13**, JAMDSM0063-JAMDSM0063 (2019)
- Nguyen, H.L.: *Reliability based Design and Analysis of Mechanical Systems*, National University publisher HCMC, Viet Nam (2015)
- Wang, G., Ma, Z.: Hybrid particle swarm optimization for first-order reliability method. *Comput. Geotech.* **81**, 49–58 (2017)
- Nguyen, H.L., Tran, V.T.: Applying FCCCD response surface method in studying the cutting power of wood materials. *Solid State Phenom.* **329**, 25–31 (2022)

# Development of Intelligent Drone for Cassava Farming



Orapadee Joochim, Kridtat Satharanond, and Wirachat Kumkun

## 1 Introduction

At present, cassava is cultivated in Thailand as it is the main economic crop of the country. The industrial sector needs the quality cassava to be processed into various products. Therefore, it is necessary to maintain the cassava to meet the quality requirements. However, the quality control is difficult because most of the cassava plantation areas are large. Moreover, at the moment, farmers are still facing the problem of Cassava Mosaic Disease (CMD), which is spreading in large numbers. It can spread out in the immediate vicinity quickly. When there is a problem or damage, the caregiver is unable to figure out the problem and the amount of severity it caused. Therefore, the actual production quantity is not known whether it is sufficient for production or not. This paper thus proposes an idea to develop a drone to detect anomalies by creating a system to detect, find and analyse the abnormalities in cassava fields and collecting credentials to show the location of the disease on a large diagram. Presently, the number of cassava plantation business is increasing. To meet both domestic and international markets, which are more than 9,000,000 rai (1 rai is equal to 1600 km<sup>2</sup>) at present. In the past, they have faced the crisis of CMD. As a result, cassava is damaged at a level of 80–100%, wasting both time and productivity. Hence, the desired profit proportion is not obtained. The problem arises from the use of diseased cassava cuttings for further planting. Additionally, the whitefly pests are vector, causing widespread outbreaks quickly. Walking to survey the farmer's plot is slow and not thorough. It takes a lot of walking time to explore. However, there are no studies related to artificial intelligence (AI) for pest inspection of cassava plants with drone.

---

O. Joochim (✉) · K. Satharanond · W. Kumkun  
Institute of Field Robotics, King Mongkut's University of Technology Thonburi, Bangkok,  
Thailand  
e-mail: [orapadee.joo@kmutt.ac.th](mailto:orapadee.joo@kmutt.ac.th)

This study aims to help cassava farmers for detecting the abnormalities in plots by using the developed drone for survey and preliminary analysis of the abnormalities so that people walk in to check what the malfunction is. The main emphasis is on the speed of the survey. This will be useful for farmers and general users to access the location of the abnormal area to shorten the time spent exploring. In this research, the structure of the drone is designed, developed and equipped with a camera to be used for surveying. The intelligent detection system to find the abnormal cassava leaves is studied and implemented using machine learning models.

## 2 Developed Drone Structure

The drone used for cassava farm surveying is developed in this research. The survey drone has to bear the burden while surveying the multispectral camera weighing 500 g and flying for a minimum of 15 min. The 6-bladed multi-rotor drone is designed in Hex-V format to provide the stability during the flight. There is a system to determine the coordinates with GPS, and two positions for accuracy in indicating the coordinates are sent back to the base by Telemetry. The structure is designed to be lightweight with composite materials. Figure 1 shows the structure of developed drone. The drone is tested by lifting a load of 5 kg, and it is found that the structure is able to withstand the forces that occurred without damage. Safety factor is 1.6 (see Fig. 2).

## 3 Cassava Abnormality Detection

The detection of cassava abnormalities uses artificial intelligence techniques combined with colour image analysis and enhancement through image processing where the human vision is important. It is also one of the complex image acquisition mechanisms. It provides information needed for simple tasks such as object recognition, and for complex tasks such as planning, decision making and researching. The interest of vision or visual information is image processing which is the process of dealing with the digital image data with the aim of improving and developing the visual information in order to be able to interpret to better describe the image. Image processing process can be divided into three steps. The initial process is image data acquisition and image enhancement, namely image sharpness correction, image conversion and image signal recovery. The intermediate process is the isolation of the elements of an image and the extraction of important features or identities and the advanced process is the interpretation and image recognition (Chowalit 2016).

For artificial intelligence (AI) techniques, the detection of abnormalities of cassava leaves from drone photographs using deep learning techniques is applied, which is an adaptation of the original models with advanced object detection capabilities. In this

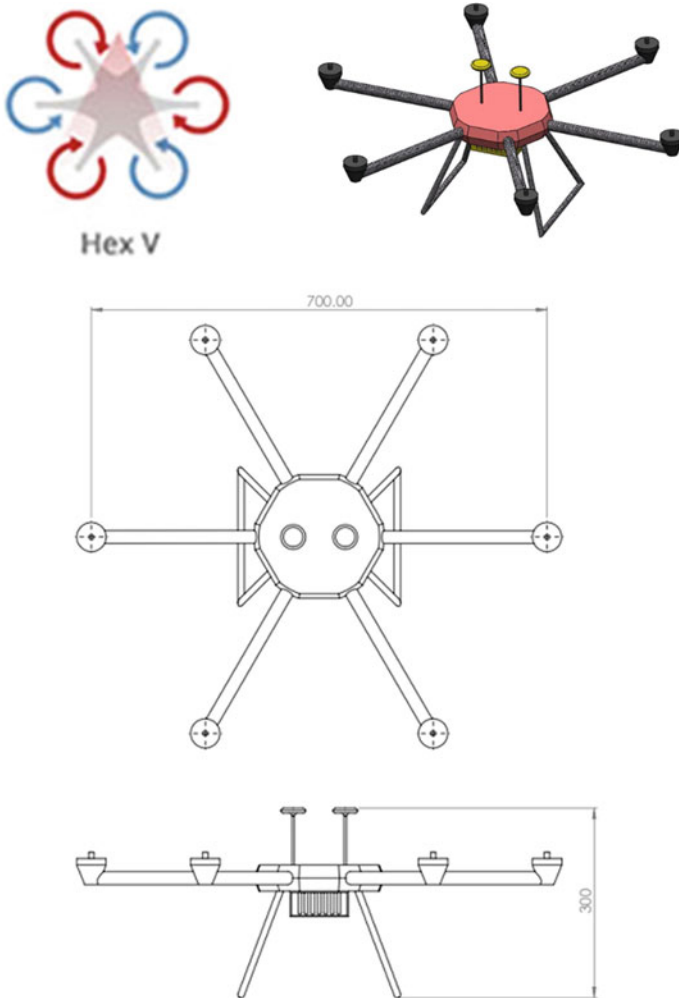


**Fig. 1** Structure of developed drone

study, teaching AI to learn is divided into two steps: preparing the data for creating AI to detect cassava plants and creating AI to detect the location of abnormal cassava plants.

### ***3.1 Data Set Preparation***

Data sets play a key role in teaching AI to learn the unusual locations of cassava plants. However, because the drone photos are too large and the details of the cassava

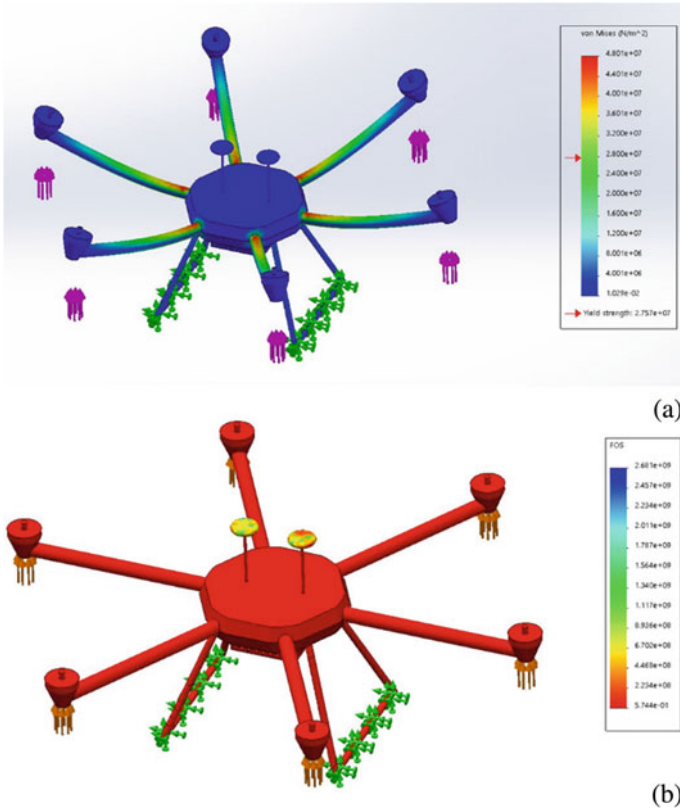


**Fig. 2** Simulation of drone: **a** simulation of drone while carrying the weight and **b** load simulation to determine safety factor

plants are not clearly visible. Therefore, it is necessary to cut the image into 36 sub-images before creating a data set. The split images have a filename that represents the order of the segments from the original image. The format of the file name is “DJI\_XXXX\_YY”, where XXXX refers to the numbered sequence of the image taken by the drone, while YY refers to the part number from the original image (see Fig. 3). The cropped image is  $912 \times 608$  pixels.

### 3.2 Image Identification and Amount of Data

To pinpoint for teaching AI to learn what unusual cassava leaves are. Visual Geometry Group Image Annotator (VIA) is utilized, which is a web platform for generating the location data within the image data for AI. The programme can create a location file from the bounding box for using as the sample data for developing AI object

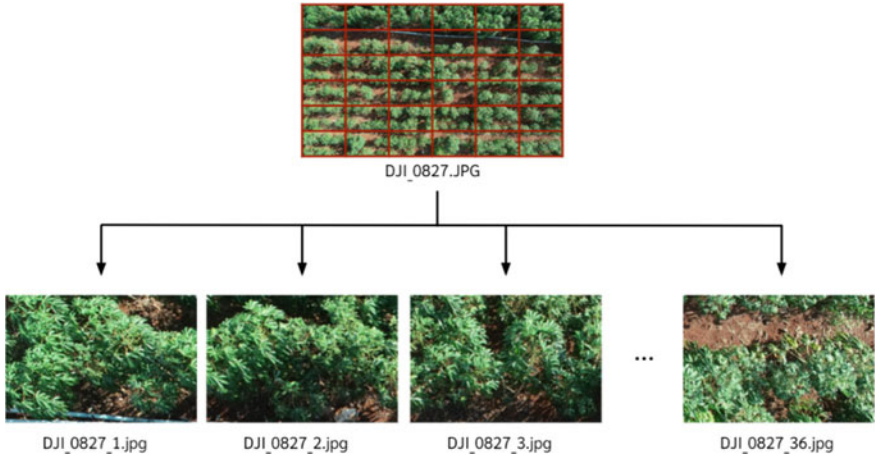


Fig. 3 Example of segmenting an image into 36 sub-images

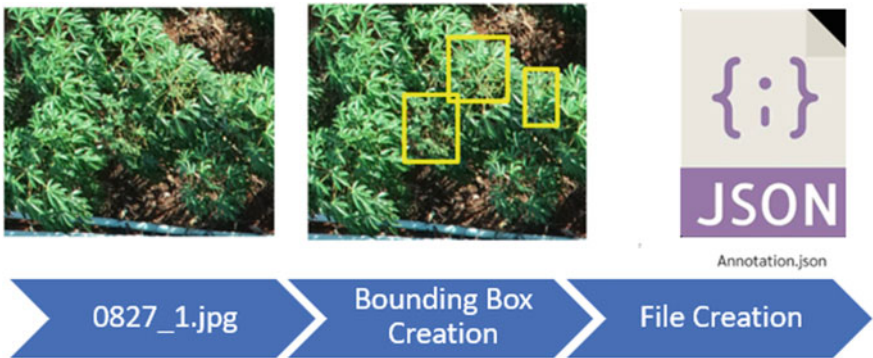


Fig. 4 Example of creating the dataset

detection. The amount of data used to teach AI will be adjusted for each version of the data to study the trend of AI’s ability to detect abnormal locations of cassava. As a result, the total of 4 versions of the data set is implemented. They are used to teach AI. Agronomists who specialize in CMD assist in validation of the data set (see Fig. 4). Cassava abnormality data set is selected (2500 images).

### 3.3 Creating AI to Detect Cassava (Object Detection)

To create an AI to detect cassava plants, the research project selected 4 AI algorithm techniques, i.e. Mask R-CNN, EfficientDet, RetinaNet and YOLOv5, for the object



detection and localization of cassava plants. There are advantages in common. The developers of each technique have taught AI to learn the basic of the object detection from Big Data; therefore, it can take specific data that would like to detect. Figure 5 shows the example of prediction results of AI algorithm techniques. Figures 6, 7, 8 and 9 illustrate the structures of AI algorithm techniques.

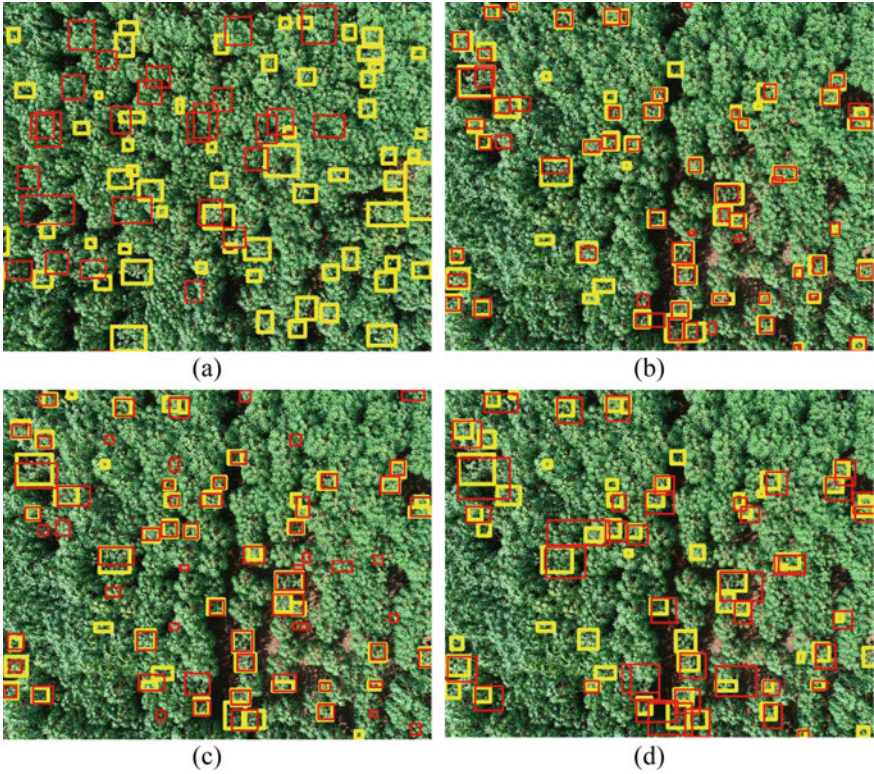


Fig. 5 Example of prediction results: a Mask R-CNN, b RetinaNet and c EfficientDet, d YOLOv5

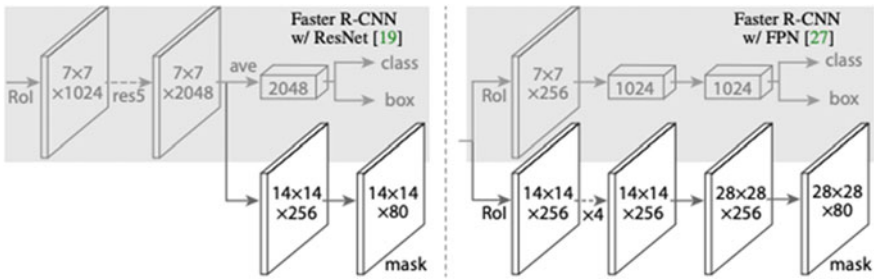


Fig. 6 Sample of Mask R-CNN structure (Kaiming et al. 2017)

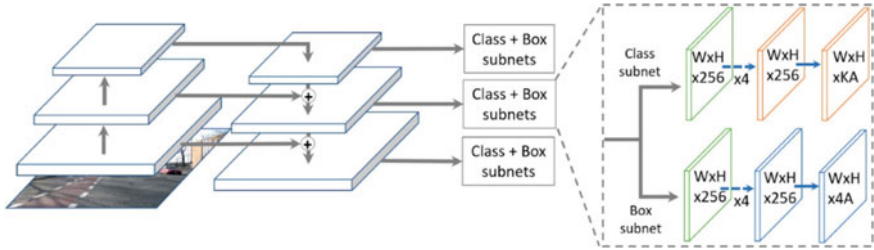


Fig. 7 Sample of RetinaNet structure (Toan et al. 2019)

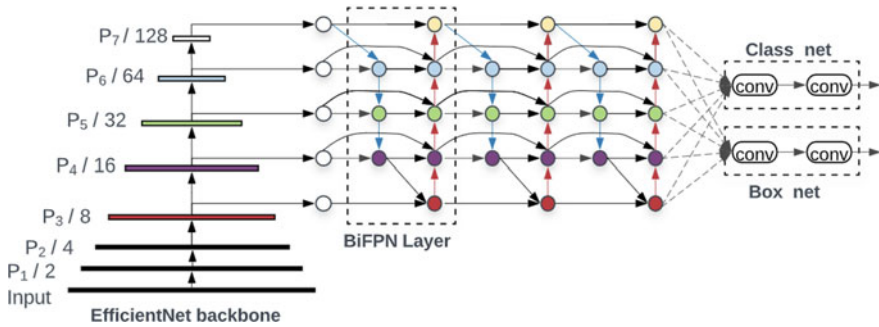


Fig. 8 Sample of EfficientDet structure (Mingxing and Adams 2020)

Mask R-CNN is an instance segmentation model that helps us locate pixels smarter. “Instance Segmentation” means grouping individual objects within a scene regardless of whether they are of the same type. In addition to specify the class and bounding box location, it also can display coloured pixels in the corresponding region (Kaiming et al. 2017).

RetinaNet is able to deal with unequal class problems. For example, there are two classes, Disease A and Disease B. The labelled figures of Disease A are more than of Disease B. RetinaNet can solve this problem well and able to use all the information in learning effectively. Although the amount of data used to learn is small, it still has good performance (Tsong-Y et al. 2018).

EfficientDet is different from other models. Other models are normally developed based on the idea that the model has the depth because it allows the model to remember information well, but EfficientDet is the model developed by the idea that the model has both depth to remember information well and the ability to extract features of the data as much as possible, making EfficientDet more efficient than other models. It also uses less computational resources compared to other models (Mingxing and Quoc 2019).

YOLOv5 is developed with a focus on real-time object detection regardless of the version. The higher version is more accurate, making YOLO popular for applications



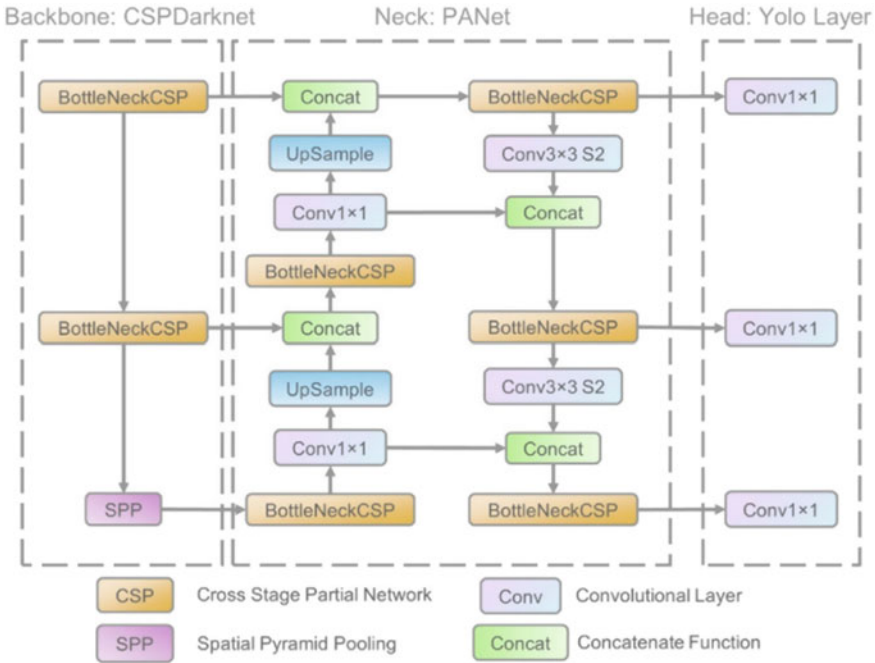


Fig. 9 Sample of YOLOv5 structure (Renjie et al. 2021)

that require real-time object detection, such as detecting objects from a video camera and detecting fast moving objects (Raphaël et al. 2021).

By comparing the best results of all models, RetinaNet-50 is the most efficient model with 0.675 mAP, the highest, and precision and recall at 0.75 and 0.77, respectively. This means that the model can detect irregular cassava leaves with the high accuracy and can cover a large number of labelled spots. Compared to Mask R-CNN, which is a benchmark model to compare its performance. The research project increased the mAP from 0.034 to 0.675, an increase of 0.641 from the original, so it is chosen as the model to be put into practise.

## 4 Conclusion

This research develops the drone to help cassava farmers for detecting the area in plots that may be caused by CMD. The drone used for the cassava farm surveying is developed. The 6-bladed multi-rotor drone is designed in Hex-V format for providing the stability during the flight. It can be concluded that the developed drone can be used to inspect and find the abnormal area that may be caused by CMD. The intelligent detection system for finding the abnormal cassava leaves is investigated

and implemented using machine learning models. The results show that RetinaNet-50 is the best performance with 0.675 mAP, 0.75 precision, 0.774 recall and takes around 0.06 s to process per image. Comparing with Mask R-CNN benchmark, mAP is improved up to 0.641 with RetinaNet-50 trained on round 4 data set. The images are collected, which are 2500 labelled training images successfully.

**Acknowledgements** This work would not have been possible without the financial support of National Science and Technology Development Agency (NSTDA), Thailand.

## References

- Chowalit, K.: Thailand. Plant Leaf Disease Diagnosis System From Color Imagery Using Co-Occurrence Matrix and Artificial Intelligence Approach. (Master Thesis, Suranaree University of Technology, Thailand (2016))
- Kaiming, H., Georgia, G., Piotr, D., Ross, B.G.: Mask R-CNN, IEEE International Conference on Computer Vision (ICCV) (2017)
- Mingxing, T., Adams, Y.: EfficientDet: Towards Scalable and Efficient Object Detection (Google Research) (2020)
- Mingxing, T., Quoc, V.L.: EfficientNet: Rethinking Model Scaling for Convolutional Neural Networks. In *Proceedings of the 36th International Conference on Machine Learning*, Long Beach, California, PMLR 97 (2019)
- Raphaël, C., Hassan, N.N., Ola, S., Abderrahmane, S.: A Deep Learning Object Detection Method for an Efficient Clusters Initialization (2021). <https://arxiv.org/pdf/2104.13634.pdf>
- Renjie, X., Haifeng, L., Kangjie, L., Lin, C., Yunfei, L.: A Forest Fire Detection System Based on Ensemble Learning (MDPI Forest) (2021)
- Toan, M.H., Phong, H.N., Noi, Q.T., Young, W.L., Kang, R.P.: Deep RetinaNet-Based Detection and Classification of Road Markings by Visible Light Camera Sensors. MDPI Special Issue “Deep Learning-Based Image Sensors” (2019)
- Tsung-Y, L., Priya, G., Ross, G., Kaiming, H., Piotr, D.: Focal Loss for Dense Object Detection. Facebook AI Research (FAIR). <https://arxiv.org/pdf/1708.02002.pdf> (2018)

# Calculation and Optimization of the Two Stage Worm-Gear Reducers Speed Ratio



Le Thuy Anh and Nguyen Huu Loc

## 1 Introduction

Worm gear drives are used in transmission systems because of their ability to achieve high reduction ratio with compact size (Rai and Barman 2019). Currently, there have been a number of studies in the world on worm gear optimization (Mogal and Wakchaure 2013; Padmanabhan et al. 2013; Godwin Raja et al. 2017; Alexandru 2010). The growing demand for compact, efficient, and reliable reducers forces the designer to use the optimal design approach.

Rai and Barman (2019) presented the power loss reduction of worm gear drive (objective function) using simulated annealing (SA), together with design variables (gear tooth number  $z_2$ , helix angle  $\gamma$ , and coefficient of friction) and constraints on bending stress, deflection of worm and linear pressure. The obtained results showed that the performance of SA is better than that of other approaches used previously to minimize power loss. The reduction percentage in power loss using SA ranged from 78.02 to 22.98%. Mogal and Wakchaure (2013) used genetic algorithm (GA) to optimize the worm using design variables, including gear ratio, face width, and pitch circle diameters. The obtained results were 17.91% reduction in volume of worm and worm wheel, 20.34% reduction in center distance between worm and worm wheel, and 51.05% reduction in deflection of worm. Padmanabhan et al. (Padmanabhan et al. 2013) built an optimization model for worm gear drives in terms of design variables  $m$ ,  $z_2$ , and  $p$  and design constraints on stress, using ant colony optimization (ACO) method and objective functions on capacity, mass, efficiency, and shaft distance, obtaining problem values with modulus between 4 and 8 mm. Godwin Raja

---

L. T. Anh · N. H. Loc (✉)

Faculty of Mechanical Engineering, Ho Chi Minh City University of Technology (HCMUT), 268 Ly Thuong Kiet Street, District 10, Ho Chi Minh City, Vietnam  
e-mail: [nhloc@hcmut.edu.vn](mailto:nhloc@hcmut.edu.vn)

Vietnam National University Ho Chi Minh City, Linh Trung Ward, Thu Duc City, Ho Chi Minh City, Vietnam

Ebenezer et al. (2017) used optimization algorithms including SA, FA, CS, and GA by MATLAB solver with design variables as gear ratio, face width, and pitch circle diameters. The result was a 42.06% reduction in worm drive mass. The design parameter values reduced by 13.04% in gear ratio, 35.53% in face width, and increased by 32.97% in pitch circle diameter of worm.

Some other studies also gave similar results on optimizing geometric parameter values (Alexandru 2010; Dudas 2005; Park et al. 2013; Su and Peng 2008; Chong et al. 2002), increasing efficiency values (Padmanabhan et al. 2013; Krol and Sokolov 2021), reducing power loss (Rai and Barman 2019; Patil et al. 2019), volume reduction (Mogal and Wakchaure 2013; Godwin Raja Ebenezer et al. 2017; Patil et al. 2019; Golabi et al. 2014), low noise (Chul Kim et al. 2020), yet with old and incomplete formulas. Optimizing the design of a worm drive is complex and time consuming because of the variety of objectives, design variables, constraints, empirical formulas, various graphs, and tables (Padmanabhan et al. 2013; Chandrasekaran et al. 2015; Elkholy and Falah 2015; Marjanovic et al. 2012).

At present, the speed ratio distribution in the two stage worm-gear reducer is mainly done according to the graph (Miltenović et al. 2017). Based on the pre-selected parameters and the total speed ratio  $u_h$  of the reducers, researchers look up the speed ratio  $u_1$  of the fast drive in the graph, then calculate the speed ratio  $u_2$  of the low drive according to the formula  $u_h = u_1 u_2$ .

This method not only has low accuracy due to the need to look up information in the graph but is also inconvenient because of the necessity to carry lookup documents, and it is very difficult to program automatic calculations. In addition, studies only focus on the worm type in the below position, while the worm in the above position and two stage worm-gear reducers with bevel gear have not had enough research.

In this paper, the speed ratio distribution in a two stage worm-gear reducer with the worm in the above position, spur gears (straight and helical) and bevel gears is presented. The calculation is based on the constant condition of the torque on the worm shaft and the uniform contact strength condition of the drives in the reducer, satisfying the oil-immersed lubrication conditions and the minimum volume.

## 2 Fundamental of Gear and Worm Drives Calculations

For well-lubricated gear and worm drives, design calculations are required according to contact strength. To save manufacturing materials, when designing, engineers must ensure equal contact strength of worm drive and gear pairs. The problem of distribution of gear speed ratios of two stage worm-gear reducers to ensure that uniform contact strength and lubrication conditions with minimization volume is considered as an optimization problem and is stated as follows

$$X = \begin{Bmatrix} u_{12} \\ u_{34} \\ \dots \\ u_{n-1,n} \end{Bmatrix} \tag{1}$$

Along with constraints:

- Equal contact strength between the drives

$$\sigma_{H12} \approx \sigma_{H34} \approx \dots \approx \sigma_{H(n-1),n} \tag{2}$$

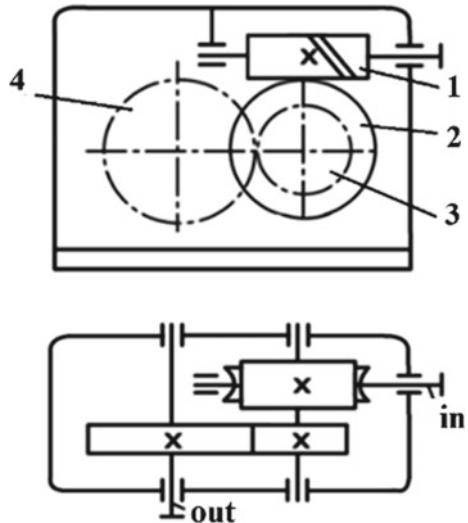
- Gear oil immersion lubrication conditions  $1 \geq \frac{d_2}{d_4} \geq \frac{2}{3}$ .
- The parameters have standard values: gear ratio, gear width, gear width factor, and diameter factor...
- Constraint volume: minimum volume  $d_2 = d_4$ .

In addition, depending on the goal of the problem, there may be many different constraints.

### 2.1 Speed Ratio Distribution in Two Stage Worm-Spur Gear Reducer

The scheme of the two stage worm-spur gear reducer is shown in Fig. 1: 1–2 is worm drive, and 3–4 is spur gear pair.

**Fig. 1** Kinematic scheme of two stage worm-spur gear reducer



**For Worm Drive 1–2.** According to Nguyen (2020), the center distance of the worm drive is determined by the formula

$$a_w = \left(1 + \frac{q}{z_2}\right) \sqrt[3]{\left(\frac{5400}{[\sigma_H]}\right)^2 \frac{T_2 K_H}{(q/z_2)}} \quad (3)$$

where  $q$  is the diameter factor;  $z_2$  is the number of worm gear teeth;  $a_w$  is the center distance of worm drive;  $T_2$  is the torque on the worm gear shaft [Nm];  $K_H$  is the contact calculated factor;  $[\sigma_H]$  is the allowable contact stress of the worm gear wheel.

From (3), it is possible to determine the allowable torque on the worm gear shaft

$$[T_2] = \frac{1}{5400^2} \left(\frac{a_{12}}{1 + q/z_2}\right)^3 \cdot \frac{(q/z_2)[\sigma_{H2}]^2}{K_{H2}} \quad (4)$$

Substituting  $a_{12} = \frac{1}{2}d_2(1 + q/z_2)$  into formula (4), we have

$$[T_2] = \frac{d_2^3}{8 \cdot 5400^2 \cdot u_{12} \cdot \tan \gamma} \frac{[\sigma_{H2}]^2}{K_{H2}} \quad (5)$$

where  $d_2 = mz_2$  is the pitch circle diameter and the worm wheel;  $u_{12}$  is the speed ratio of worm drive, and  $\gamma$  is lead angle

$$\tan \gamma = \frac{z_1}{q} = \frac{z_2}{u_{12} \cdot q} \quad \text{or} \quad \frac{q}{z_2} = \frac{1}{u_{12} \cdot \tan \gamma} \quad (6)$$

**For Second Stage of Spur Gear Pair 3–4.** For well-lubricated gear pairs, we calculate by contact strength (Nguyen 2020; ISO 6336-2:2006), and we have

$$\sigma_{H3} = Z_M Z_H Z_\varepsilon \sqrt{\frac{2T_3 \cdot 10^3 \cdot K_H (u_{34} \pm 1)}{u_{34} b_{\omega 34} d_1^2}} \leq [\sigma_{H3}] \quad (7)$$

where  $Z_M$  is the elasticity factor that takes into account gear material properties (modulus of elasticity and Poisson's ratio);  $Z_H$  is the factor taking into account the shape of the contact surface;  $Z_\varepsilon$  is the factor taking into account the effect of total contact length (contact ratio factor);  $T_3$  is the torque on the driving shaft;  $b_{\omega 34}$  is the width of driving gear 3;  $d_3$  is the pitch diameter of the driving gear 3; and  $u_{34}$  is the speed ratio of worm drive.

From (7), the allowable torque on the driving gear can be determined by

$$[T_3] = \frac{u_{34} b_{\omega 34} d_3^2 [\sigma_{H3}]}{2 \times 10^3 \cdot (Z_M Z_H Z_\varepsilon)^2 K_{H3} (u_{34} \pm 1)} \quad (8)$$

where  $b_{w34} = \psi_{bd34} d_3$  is width of spur gear;  $\psi_{bd34}$ ,  $\psi_{ba34}$  is a width ratio; and  $\psi_{ba34}$  is taken from the sequence of standard numbers: 0.1, 0.125, 0.16, 0.2, 0.25,

0.315, 0.4, 0.5, and 0.63 depending on the wheel position relative to the bearings  $\psi_{bd34} = \frac{1}{2}\psi_{ba34}(u_{34} \pm 1)$ .

From (8) and replacing  $d_4 = u_{34} \cdot d_3$ , we have

$$[T_3] = \frac{\psi_{ba34}d_4^3[\sigma_{H3}]^2}{2K_d^3K_{H3}u_{34}^2} \quad (9)$$

where  $K_d = \sqrt[3]{2 \times 10^3 \cdot (Z_M Z_H Z_\varepsilon)^2}$ , since the gear material is steel, then calculated value  $K_d = 756$  for straight and  $K_d = 680$  for helical spur gears.

To ensure the conditions of equal contact stress, from (5), (9), with  $u_{12} = \frac{u_h}{u_{34}}$ ,  $u_h$  is the speed ratio of the two stage worm-gear reducer, we infer

$$u_{34}^3 = 4 \cdot 5400^2 \cdot \tan \gamma \frac{d_4^3}{d_2^3} \frac{\psi_{ba34}}{K_d^3} \frac{[\sigma_{H3}]^2}{[\sigma_{H2}]^2} \frac{K_{H2}}{K_{H3}} \cdot u_h \quad (10)$$

The obtained formula depends on the following conditions:

1. Worm gear—gear material;
2. The width ratio of the gear drive, type of the spur gear: straight or helical;
3. The relationship between  $d_2$  and  $d_4$ :  $d_2 = d_4$  or  $1 \geq \frac{d_2}{d_4} \geq \frac{2}{3}$

To ensure oil-immersed lubrication conditions, we have the formula

$$1 \leq u_{34}^3 = 4 \cdot 5400^2 \cdot \tan \gamma \frac{d_4^3}{d_2^3} \frac{\psi_{ba34}}{K_d^3} \frac{[\sigma_{H3}]^2}{[\sigma_{H2}]^2} \frac{K_{H2}}{K_{H3}} \cdot u_h \leq \left(\frac{3}{2}\right)^3 \quad (11)$$

## 2.2 Speed Ratio Distribution in Two Stage Worm-Bevel Gear Reducer

The scheme of the two stage worm-bevel gear reducer is shown in Fig. 2 (1–2 is worm drive, and 3–4 is bevel gear drive). The contact stress for bevel gears is determined

$$\sigma_{H3} = 2 \cdot Z_M Z_H Z_\varepsilon \sqrt{\frac{T_3 \cdot 10^3 \cdot K_{H\beta 3} \cdot u_{34}^2}{0.85 \cdot (1 - 0.5 \cdot \psi_{be})^2 \cdot \psi_{be} \cdot d_4^3}} \leq [\sigma_{H3}] \quad (12)$$

From here, we deduce the formula to determine the allowable torque value

$$[T_3] = \frac{d_4^3}{(2 \cdot Z_M Z_H Z_\varepsilon)^2 \cdot 10^3} \frac{0.85 \cdot (1 - 0.5 \psi_{be})^2 \cdot \psi_{be} \cdot [\sigma_{H3}]^2}{K_{H\beta 3} \cdot u_{34}^2} \quad (13)$$

Or shorten to

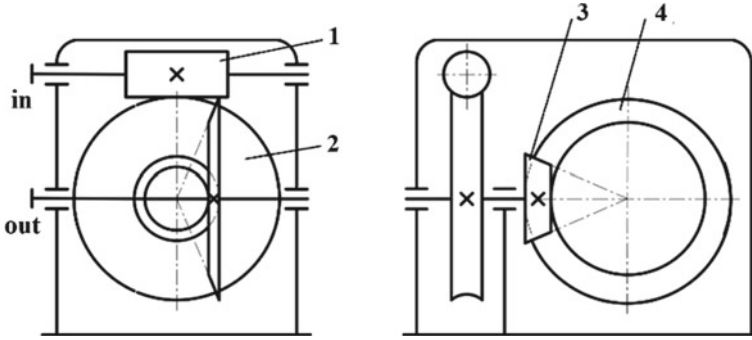


Fig. 2 Scheme of two stage worm-bevel gear reduce

$$[T_3] = \frac{d_4^3}{2 \cdot K_d^3} \cdot \frac{0.85 \cdot (1 - 0.5\psi_{be})^2 \cdot \psi_{be} \cdot [\sigma_{H3}]^2}{K_{H\beta 3} \cdot u_{34}^2} \quad (14)$$

with  $K_d = \sqrt[3]{2 \cdot 10^3 \cdot (Z_M Z_H Z_\varepsilon)^2}$ .

The conditions of equal contact stress  $[T_3] = [T_2]$ ; from (5) and (14), we deduce

$$\frac{d_4^3}{2 \cdot K_d^3} \cdot \frac{0.85 \cdot (1 - 0.5 \cdot \psi_{be})^2 \cdot \psi_{be} \cdot [\sigma_{H3}]^2}{K_{H\beta 3} \cdot u_{34}^2} = \frac{d_2^3}{8 \cdot 5400^2 \cdot u_{12} \cdot \tan \gamma} \cdot \frac{[\sigma_{H2}]^2}{K_{H2}} \quad (15)$$

Replacing  $u_{12} = \frac{u_h}{u_{34}}$  and after simplifying, we get

$$u_{34}^3 = \left( \frac{d_4}{d_2 \cdot K_d} \right)^3 \cdot 4 \cdot 5400^2 \cdot \tan \gamma \cdot 0.85 (1 - 0.5 \cdot \psi_{be})^2 \psi_{be} \frac{K_{H2}}{K_{H\beta 3}} \frac{[\sigma_{H3}]^2}{[\sigma_{H2}]^2} u_h \quad (16)$$

To ensure oil-immersed lubrication conditions, we choose  $1 \geq \frac{d_2}{d_4} \geq \frac{2}{3}$ , and from there deduce the formula

$$1 \leq u_{34}^3 = \left( \frac{d_4}{d_2} \right)^3 \cdot 4 \cdot 5400^2 \cdot \tan \gamma \cdot 0.85 \cdot \frac{K_{H2}}{K_{H\beta 3}} \frac{(1 - 0.5\psi_{be})^2 \cdot \psi_{be} \cdot [\sigma_{H3}]^2}{K_d^3 \cdot [\sigma_{H2}]^2} u_h \leq \left( \frac{3}{2} \right)^3 \quad (17)$$

To ensure the minimum volume,  $d_2 = d_4$ , we should choose the smallest value  $u_{34}$  in the range of the above gear ratio values.



### 3 Calculation Results and Applications

#### 3.1 Speed Ratio Distribution in Two Stage Worm-Spur Gear Reducer

For worm drive, we choose the lead angle  $\gamma = 10^\circ (< 30^\circ)$  and the material for making worm gear: tinless bronze and brass are used with intermediate slip velocities ( $< 5$  m/s). This bronze has high mechanical strength, but low score resistance, so it is used together with quenched ( $> 45$  HRC) ground and polished worms (Grote and Antonsson 2009).

$$[\sigma_{H2}] = (276 \div 300) - 25v_s \approx 200 \text{ MPa}$$

Calculated factors  $K_{H2} = K_v \cdot K_\beta = 1.1$  (Nguyen 2020), where  $K_v$  is internal gearing dynamics caused by manufacturing errors (accuracy grade 7, slip velocities  $v_s = 3 - 7.5$  m/s), and  $K_\beta \approx 1$  is the factor that takes into account the unevenness of the load distribution in the contact area due to distortion of the worm and wheel shaft.

For spur gear pairs, material selection for gear train with driving gear being made of C45 steel, normalization or refining with the hardness of 300HB,  $\sigma_{0H \text{ lim}} = 2 \cdot HB + 70 = 670$  MPa, we select  $[\sigma_{H3}] = 603$  MPa.

For design, we select  $K_{H3} = K_{H\beta} = 1.01$  depending on factor  $\psi_{bd}$  and hardness (Grote and Antonsson 2009). The width ratio taken from the sequence of standard numbers depending on the wheel position relative to the bearings: for symmetrical arrangement, we select  $\psi_{ba34} = 0.315$ ;  $\psi_{ba34} = 0.4$ ; and  $\psi_{ba34} = 0.5$ .

The calculation results and the combination of selecting the gear ratio  $u_{34}$  of the second stage are according to 2 standard ranges (series 1 is the priority series in bold), and the smallest value should be selected to ensure the smallest volume and weight as shown in Table 1.

Analysis of the results on Minitab software obtained the dependence of the minimum gear ratio of the gear pair  $u_{34}$  and the gear pair ratio of the two speed reducer  $u_h$  in the form of the quadratic regression equations with testing for lack of fit (R-square = 99.7%) presented in Table 2.

We draw a graph showing the relationship between speed ratio  $u_h$  of two stage worm-spur gear reducer and speed ratio  $u_{34}$  of the second stage to ensure equal strength, lubrication and minimum volume with respective width ratio in Fig. 3.

**Table 1** Calculation results of the distribution of minimum gear speed ratio  $u_{34}$

| uh   | Spur gear             |         |                     |         |                     |         | Bevel gear |
|------|-----------------------|---------|---------------------|---------|---------------------|---------|------------|
|      | $\psi_{ba34} = 0.315$ |         | $\psi_{ba34} = 0.4$ |         | $\psi_{ba34} = 0.5$ |         |            |
|      | Straight              | Helical | Straight            | Helical | Straight            | Helical |            |
| 22.4 | 1.49                  | 1.66    | 1.62                | 1.80    | 1.74                | 1.94    | 1.23       |
| 25   | 1.55                  | 1.72    | 1.68                | 1.86    | 1.81                | 2.01    | 1.28       |
| 28   | 1.61                  | 1.79    | 1.74                | 1.94    | 1.88                | 2.09    | 1.33       |
| 31.5 | 1.67                  | 1.86    | 1.81                | 2.01    | 1.95                | 2.17    | 1.38       |
| 35.5 | 1.74                  | 1.93    | 1.88                | 2.10    | 2.03                | 2.26    | 1.44       |
| 40   | 1.81                  | 2.01    | 1.96                | 2.18    | 2.11                | 2.35    | 1.50       |
| 45   | 1.88                  | 2.09    | 2.04                | 2.27    | 2.20                | 2.44    | 1.56       |
| 50   | 1.95                  | 2.17    | 2.11                | 2.35    | 2.28                | 2.53    | 1.61       |
| 56   | 2.03                  | 2.25    | 2.19                | 2.44    | 2.36                | 2.63    | 1.68       |
| 63   | 2.11                  | 2.34    | 2.28                | 2.54    | 2.46                | 2.73    | 1.74       |
| 71   | 2.19                  | 2.44    | 2.37                | 2.64    | 2.56                | 2.84    | 1.81       |
| 80   | 2.28                  | 2.54    | 2.47                | 2.75    | 2.66                | 2.96    | 1.89       |
| 90   | 2.37                  | 2.64    | 2.57                | 2.86    | 2.77                | 3.08    | 1.96       |
| 100  | 2.46                  | 2.73    | 2.66                | 2.96    | 2.87                | 3.19    | 2.03       |
| 110  | 2.54                  | 2.82    | 2.75                | 3.05    | 2.96                | 3.29    | 2.10       |
| 125  | 2.65                  | 2.94    | 2.87                | 3.19    | 3.09                | 3.43    | 2.19       |
| 140  | 2.75                  | 3.06    | 2.98                | 3.31    | 3.21                | 3.57    | 2.27       |
| 160  | 2.87                  | 3.20    | 3.11                | 3.46    | 3.35                | 3.73    | 2.38       |
| 180  | 2.99                  | 3.32    | 3.24                | 3.60    | 3.49                | 3.88    | 2.47       |
| 200  | 3.10                  | 3.44    | 3.35                | 3.73    | 3.61                | 4.02    | 2.56       |

**Table 2** Regression equations determines the minimum gear ratio

| Two stage reducer       | Factor $\psi_{ba}$ | Regression equations                       | R-square (%) |
|-------------------------|--------------------|--|--------------|
| Worm-straight spur gear | 0.315              | $u_{34} = 1.205 + 0.01598u - 0.000034u^2$  | 99.7         |
|                         | 0.4                | $u_{34} = 1.304 + 0.01731u - 0.000036u^2$  | 99.7         |
|                         | 0.5                | $u_{34} = 1.406 + 0.01866u - 0.000039u^2$  | 99.7         |
| Worm-helical spur gear  | 0.315              | $u_{34} = 1.337 + 0.01781u - 0.000038u^2$  | 99.7         |
|                         | 0.4                | $u_{34} = 1.452 + 0.01923u - 0.000040u^2$  | 99.7         |
|                         | 0.5                | $u_{34} = 1.567 + 0.02062u - 0.000043u^2$  | 99.7         |
| Worm-bevel gear         | 0.285              | $u_{34} = 0.9954 + 0.01323u - 0.000028u^2$ | 99.7         |

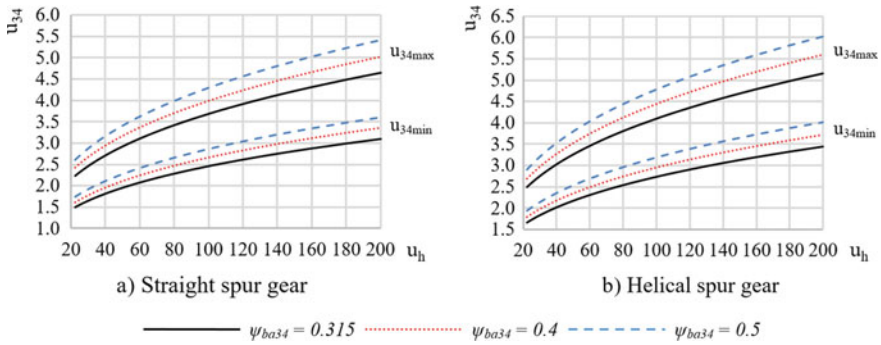


Fig. 3 Speed ratio distribution of two stage worm-spur gear reducer

### 3.2 Speed Ratio Distribution in Two Stage Worm-Bevel Gear Reducer

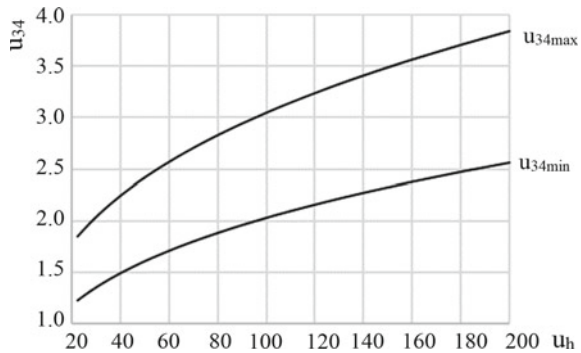
We select worm drive the same as two stage worm-spur gear reducer. For bevel gear, material selection for gear train with driving gear being made of C45 steel, normalization or refining with the hardness of 300 HB:  $\sigma_{0H\lim} = 2HB + 70 = 670$  MPa, we select  $[\sigma_{H3}] = 603$  MPa. Preliminary selection of factor  $K_{H3} = K_{H\beta} = 1.07$ .

The calculation results and the combination of selecting the bevel gear ratio  $u_{34}$  of the second stage are according to standard ranges (series 1 is the priority series), and the smallest value should be selected to ensure the minimum volume and weight as shown in the last column of Table 1.

The results of the quadratic regression equations showing the dependence of minimum gear ratio  $u_{34}$  on  $u_h$  are presented in Table 2.

We construct a graph showing the relationship between speed ratio  $u_h$  of two stage worm-bevel gear reducer and speed gear ratio  $u_{34}$  of the second stage to ensure equal strength, lubrication and minimum volume in Fig. 4

Fig. 4 Speed ratio distribution of two stage worm-bevel gear reducer



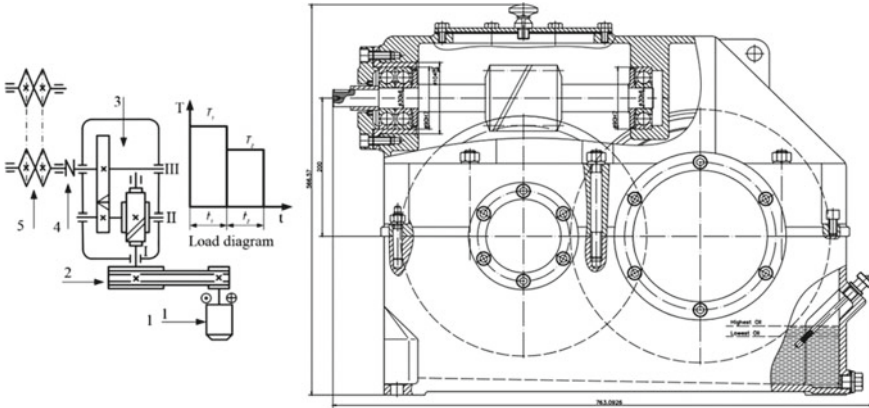


**Fig. 5** Kinematic scheme and front view drawing of two stage worm-spur gear

In this section, the above research results are applied to select the gear ratio and to design the transmission systems for loads chain system with the kinematic scheme shown in Fig. 5.

The loads chain system includes: 1—motor; 2—V belt drive; 3—double stage worm-helical gear reducer; 4—coupling; 5—loads chain sprocket; and 6—loads chain. Input data for design: force on chain  $F = 23,000$  [N]; chain velocity  $v = 0.2$  [m/s]; pith diameter of loads chain sprocket  $d = 315$  [mm].

According to the power 4.825 [kW], with the common speed ratio of the two stage reducer  $u_r = 50$ , we choose the gear ratio of the gear pair according to the priority set of value  $u_{34} = 2.5$ . To optimize the product volume of the reducer, we should choose  $d_2 \approx d_4$ , illustrated in drawing Fig. 5.

## 4 Conclusion

This paper has established an analytical formula for the distribution of speed ratios in a two stage worm-gear reducer with either spur gear or bevel gear. The research addresses the combination of three goals, which are to ensure the conditions of equal contact stress and conditions of oil-immersed lubrication as well as the minimum volume. Formulas in Table 2 not only allow quick and accurate determination of speed ratios  $u_{12}, u_{34}$  according to the total speed ratio  $u_h$ , but also facilitate programming to design automatically. The paper has constructed a series of speed ratios and graphs in the two stage worm-gear reducer (Figs. 3 and 4) to look up the gear ratios corresponding to each gear width ratio value. In addition, we can also extend this calculation method to apply to another scheme of two stage and triple stage worm-gear reducers.

This paper results can be used to design and calculate the distribution of speed ratios in two stage worm-gear reducers, as a scientific basis for the distribution of speed ratios for other types of reducers and used as reference when researching, as well as teaching and learning.

**Acknowledgements** We acknowledge Ho Chi Minh City University of Technology (HCMUT), VNU-HCM for supporting this study.

## References

- Alexandru, A.T.: Worm gears with optimized main geometrical parameters and their efficiency. *Mechanika*, Nr.1.81 (2010)
- Chandrasekaran, M., Padmanabhan, S., Srinivasa Raman, V.: Swarm intelligence optimization of worm and worm wheel design. *ARPN J. Eng. Appl. Sci.* **10**(13) (2015). ISSN 1819-6608
- Chong, T.H., Bae, I., Park, G.-J.: A new and generalized methodology to design multi-stage gear drives by integrating the dimensional and the configuration design process. *Mech. Mach. Theory* **37**(3), 295–310 (2002)
- Chul Kim, S., Gon Moon, S., Hyeon Sohn, J., Jun Park, Y., Ho Choi, C., Ho Lee, G.: Macro geometry optimization of a helical gear pair for mass efficiency and transmission error. *Mech. Mach. Theory* **144** (2020)
- Dudas, I.: *The Theory and Practice of Worm Gear Drives*. British Library Cataloguing in Publication Data (2005)
- Elkholy, A.H., Falah, A.H.: Worm gearing design improvement by considering varying mesh stiffness. *Int. J. Mech. Mechatron. Eng.* **9**(9)
- Godwin Raja Ebenezer, N., Saravanan, R., Ramabalan, S., Navaneethasanthakumar, S.: Worm gear drive optimization considering industry constraints based on nature inspired algorithms. *World Sci. News (WSN)* **87**, 205–221 (2017). EISSN 2392-2192
- Golabi, S.I., Fesharaki, J.J., Yazdipoor, M.: Gear train optimization based on minimum volume/weight design. *Mech. Mach. Theory* **73**, 197–217 (2014)
- Grote, K.-H., Antonsson, E.: *Springer Handbook of Mechanical Engineering* (2009)
- ISO 6336-2:2006: Calculation of load capacity of spur and helical gears—Part 2: Calculation of surface durability (pitting) (2006)
- Krol, O., Sokolov, V.: Selection of worm gearing optimal structure for machine rotary table. *Diagnostyka* **22**(1) (2021)
- Marjanovic, N., Isailovic, B., Marjanovic, V., Milojevic, Z., Blagojevic, M., Bojic, M.: A practical approach to the optimization of gear trains with spur gears. *Mech. Mach. Theory* **53**, 1–16 (2012)
- Miltenović, A., Banić, M., Miltenović, D.: Load capacity of worm gear transmission from aspect of maximal use of available resources. *MATEC Web Conf.* **121** (2017)
- Mogal, Y.K., Wakchaure, V.D.: A multiobjective optimization approach for design of worm and worm wheel based on genetic algorithm. *Bonfring Int. J. Man Mach. Interface* **3**(1) (2013)
- Nguyen, H.L.: *Fundamentals of Machine Design*, 1st edn. Publishing House, Vietnam National University of Ho Chi Minh City (2020)
- Padmanabhan, S., Chandrasekaran, M., Srinivasa Raman, V.: Design optimization of worm gear drive. *Int. J. Min. Metall. Mech. Eng. (IJMMME)* **1**(1) (2013). ISSN 2320-4060
- Park, N., Sohn, J., Baek, G., Oh, C.: Optimal design of worm gear system using in CVVL for automobiles. In: *Proceedings of ASME 2013 International Mechanical Engineering Congress & Exposition (IMECE 2013)*, November 15–21, San Diego, CA, USA (2013)
- Patil, M.B., Ramkumar, P., Shankar, K.: Multi-objective optimization of two-stage helical gearbox with tribological constraints. *Mech. Mach. Theory* **138**, 38–57 (2019)

- Rai, P., Barman, A.G.: Design optimization of worm gear drive with reduced power loss. IOP Conf. Ser. Mater. Sci. Eng. **635** (2019)
- Su, D., Peng, W.: Optimum design of worm gears with multiple computer aided techniques. Proc. ICCES **08**, 575–658 (2008)

# Project-Based Learning in Product Design Engineering: A Case Study of External Gear Pump Design



Muhammad Izzuddin Sabaruddin,  
Mohammad Habib Fadillah Mohammad Mazni Latiff,  
Nur Saidah Awang Abdullah, Wahyu Caesarendra, and Juliana Zaini

## 1 Introduction

A gear pump is a pump that uses the meshing of two gears to seal an amount of liquid and transmit it when the gears are moving. There are two types of gear pumps, namely the external gear pump and the internal gear pump. However, the scope of this project is to focus on the external gear pump. As part of the Product Design Engineering (PDE) module.

This project requires research and a survey of the types of gear pump characteristics and functions, such as size, type of gear, etc., that are desirable from a customer standpoint. From there, the design problem can be understood, and multiple concept designs and alternative concept designs were generated. Concepts were weighted using a Pugh matrix, with evaluation criteria such as manufacturability and durability being one of the important ones. A parametric design for the gear pump was performed using an Excel spreadsheet to determine an optimal spur gear configuration. A risk assessment was performed on the pump to reduce the overall potential risk of the pump.

External gear pumps effectively manage solids-free and lubricating fluids and perform well in sectors such as fuel and food industry as lubricant oil pumps and high viscosity fluid pumps, respectively. A gear pump has three cycles: filling, transfer and delivery as presented in Carletti et al. (2016). In the filling stage, the unmeshed gears expand the pump's inlet volume, creating a vacuum that allows the fluid to be pushed in by external pressure. In the transfer stage, the trapped fluid between the gear teeth and the cavity of the wall casing is transferred from the pump inlet to the outlet as the gears rotate. Fluid is forced out under pressure in the delivery stage as the

---

M. I. Sabaruddin · M. H. F. Mohammad Mazni Latiff · N. S. Awang Abdullah ·  
W. Caesarendra (✉) · J. Zaini

Manufacturing Systems Engineering, Faculty of Integrated Technologies, Universiti Brunei  
Darussalam, Jalan Tungku Link, Gadong 1410, Brunei  
e-mail: [wahyu.caesarendra@ubd.edu.bn](mailto:wahyu.caesarendra@ubd.edu.bn)

**Table 1** Component types with their functions

| No | Components   | Type                  | Function   |
|----|--------------|-----------------------|--|
| 1  | Seal         | Standard parts        | To prevent water leak                                      |
| 2  | Cover        | Special purpose parts | To prevent damage to the internal components               |
| 3  | Drive Shaft  | Special purpose parts | To drive and turn the idler gear                           |
| 4  | Driving Gear | Special purpose parts | To alter the speed and/or direction generated by the motor |
| 5  | Inlet        | –                     | For fluid intake   |
| 6  | Driven Gear  | Special purpose parts | To transfer motion from the driving gear                   |
| 7  | Bushing      | Standard parts        | To reduce vibration and friction between moving parts      |
| 8  | Casing       | Special purpose parts | To prevent damage to the internal components               |

gears interlock on the outlet side. A helical, spur and herringbone gear is used in an external gear pump. Spur gears can handle high differential pressures, whereas helical gears are silent and reduce trapped fluid. Herringbone gears combine the benefits of helical and spur gears but are more expensive to manufacture and more prone to fluid trapping. According to Carletti et al. (2016), the components of external gear pumps are classified into three categories: standard components, standard assemblies and special-purpose components. The function of each component is presented in Table 1.

## 2 Methodology

### 2.1 Design Problem Formulation

An Engineering Design Specification (EDS) was used to define the design requirements of the external gear pump, that is, the requirements of the customer and the team. In order to know the customer requirements, a survey was created and distributed to know if the available external gear pump on the market meets the customer needs and expectations. According to the survey, most of the respondents are students, engineers and practitioners, general assistants and self-employed, and their preferred external gear pumps are the following: medium size, lightweight, medium water displacement, complex build, low noise and low vibration. These functions are quantified in Table 2 and are directly related to the team method to meet these requirements using the House of Quality (HoQ) in Fig. 1. The HoQ shows that the type of gear plays the most crucial factor in achieving the customer's requirements, followed by the cost of production, lifespan and casing thickness.

In this study, five alternative design concepts were proposed in Table 3. These alternative design concepts were then evaluated based on a few criteria such as



**Table 2** Product function and engineering characteristic of the external gear pump

| Function                  | Engineering characteristics     | Units                 | Limits   |
|---------------------------|---------------------------------|-----------------------|--|
| Medium size               | Dimension of overall components | Cubic centimetres     | The total height, width and depth is at least 9 cm by 13 cm by 24 cm |
| Lightweight               | Weight of all components        | Gram                  | 100–300 g  |
| Medium water displacement | Displacement                    | Cubic centimetres/rev | 20 cc/rev  |
| Complex assembly          | Components' design              |                       |  |
| Regular services          | Casing's design                 |                       |  |
| Low noise                 | Number of teeth                 |                       | Have more than 9 teeth   |

manufacturability, durability, rigidity, functionality, efficiency, lightweight and low cost. A weight is given to quantitatively measure the alternative design concepts as presented in Table 4. The weight is based on the customer survey results and potential user surveys. The alternative design concept with the highest weight is selected as the final concept design.

### 3 Results and Discussion

#### 3.1 Gear Parametric Design

After the design concept is made, the gear design needs to be considered for the performance. The team decided on the design using a gear calculator in Excel to calculate the gear parameters such as the number of teeth, pitch diameter and gear face width. After careful deliberation, the pitch diameter was set to 5.5 cm, the pressure angle was set to 20° to reduce the undercut, and the number of teeth was set to 18 to pair with the pressure angle. The gear parameters set were set into an Excel file where it calculated the theoretical displacement value of 17.12 cm<sup>3</sup>/rev.

The gear parameter value was tested with different slip coefficient values and different pressure values which in turn affect the volumetric efficiency, actual flow and the time it takes to fill a 5-L tank. From the simulated values, with increasing pressure and a higher value of slip flow coefficient, the lower the flow value, and thus the time spent to fill a 5-L tank increases.

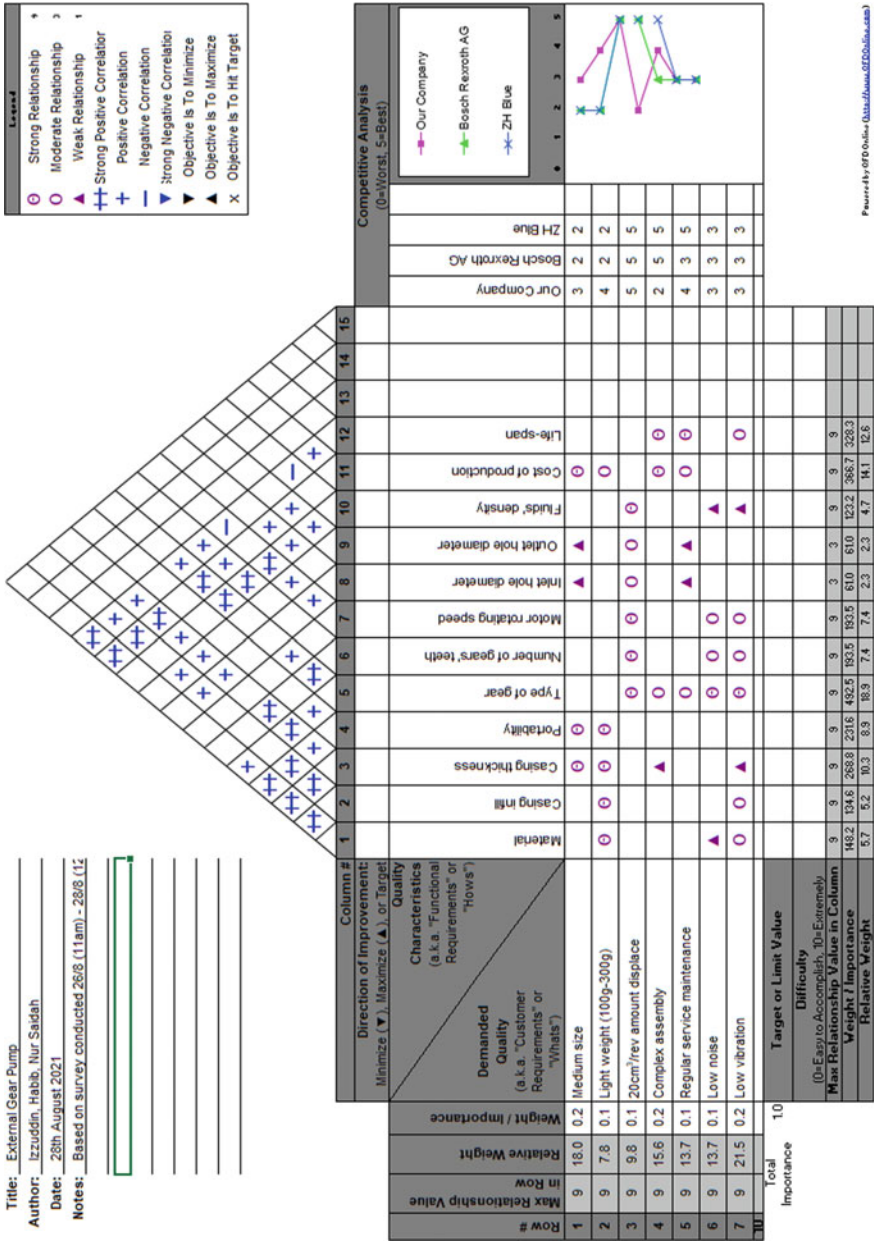


Fig. 1 HoQ for the team's external gear pump

**Table 3** Alternative design concepts

| Design | Standard                                   | Concepts  |
|--------|--|---|
| 1      | Physical principle<br>Material<br>Geometry | Spur gear<br>PLA<br>Box shaped with rounded edges             |
| 2      | Physical principle<br>Material<br>Geometry | Spur gear<br>PETG<br>Box shaped                               |
| 3      | Physical principle<br>Material<br>Geometry | Spur gear<br>PLA with transparent acrylic cover<br>Box shaped |
| 4      | Physical principle<br>Material<br>Geometry | Herringbone gear<br>PLA<br>Box shaped                         |
| 5      | Physical principle<br>Material<br>Geometry | Herringbone gear<br>PETG<br>Pill shaped                       |

### 3.2 Final Concept Design

Figure 2 illustrates the final concept design based on the evaluation of Concept #3 and the parametric design selected. The design was created using SOLIDWORKS 2020 and Gear DXF.

### 3.3 Failure Mode Analysis

Failure cannot be permanently eliminated in the manufacturing industry. However, it can be reduced using an analysis called failure mode and effects analysis, FMEA, by calculating the Risk Priority Number (RPN). This RPN is based on three factors: severity ( $S$ ), occurrence ( $O$ ), and detection ( $D$ ) (Bhattacharjee et al. 2020). Each factor has a rating of 10, 1 is the least and 10 is the maximum. Equation (1) is the formula to find the RPN value. Hence, the range value for the RPN value is between 1 and 1000.

$$\text{RPN} = S \times O \times D. \quad (1)$$

A thorough discussion was conducted among the team members to identify the possibility of failure modes that can happen to the external gear pump. The RPN rating of the external gear pump is presented in Table 5. A descriptive of the RPN rating for the following failure mode: (1) External gear pump leaked, (2) External gear pump severe pressure fluctuation and (3) External gear pump power loss.

To reduce the failure mode, the following is the recommended action for each failure mode:

**Table 4** Final evaluation of alternative design concepts

| Evaluation criteria | Importance Weight (%) | Concepts   |                 |            |                 |            |                 |            |                 |            |                 |   |      |
|---------------------|-----------------------|------------|-----------------|------------|-----------------|------------|-----------------|------------|-----------------|------------|-----------------|---|------|
|                     |                       | Concept #1 |                 | Concept #2 |                 | Concept #3 |                 | Concept #4 |                 | Concept #5 |                 |   |      |
|                     |                       | Rating     | Weighted rating | Rating     | Weighted rating | Rating     | Weighted rating | Rating     | Weighted rating | Rating     | Weighted rating |   |      |
| Manufacturability   | 15                    | 3          | 0.45            | 3          | 0.45            | 2          | 0.3             | 2          | 0.3             | 2          | 0.3             | 3 | 0.3  |
| Durability          | 10                    | 2          | 0.2             | 3          | 0.3             | 3          | 0.3             | 2          | 0.2             | 3          | 0.3             | 3 | 0.3  |
| Rigidity            | 15                    | 2          | 0.3             | 3          | 0.45            | 4          | 0.6             | 2          | 0.3             | 3          | 0.45            | 3 | 0.45 |
| Functionality       | 15                    | 3          | 0.45            | 3          | 0.45            | 3          | 0.45            | 3          | 0.45            | 3          | 0.45            | 3 | 0.45 |
| Efficiency          | 20                    | 3          | 0.6             | 3          | 0.6             | 4          | 0.8             | 4          | 0.8             | 4          | 0.8             | 4 | 0.8  |
| Lightweight         | 10                    | 4          | 0.4             | 2          | 0.2             | 2          | 0.2             | 3          | 0.3             | 2          | 0.2             | 2 | 0.2  |
| Low cost            | 15                    | 3          | 0.45            | 2          | 0.3             | 2          | 0.3             | 2          | 0.3             | 2          | 0.3             | 2 | 0.3  |
| Total percentage    | 100                   |            | 2.85            |            | 2.75            |            | 2.95            |            | 2.65            |            | 2.8             |   | 2.8  |

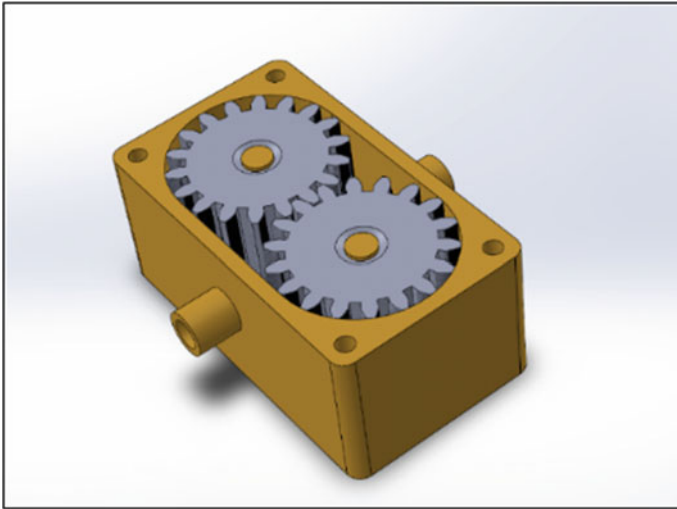


**Fig. 2** Final concept design

**Table 5** RPN rating

| Failure mode                                   | Severity (S)                       |          | Occurrence (O)                              |          | Detection (D) |          | RPN |
|--|------------------------------------|----------|---|----------|---------------|----------|-----|
|  | Effects                            | S rating | Causes                                      | O rating | Control tests | D rating |     |
| External gear pump leaked                      | Improper fluid transfer and spills | 3        | Improper seal inside the external gear pump | 6        | Very easy     | 1        | 18  |
|  |                                    |          | Cracks                                      |          |               |          |     |
| External gear pump severe pressure fluctuation | Fluid transfers fluctuate          | 5        | Cavitation                                  | 7        | Likely        | 4        | 140 |
| External gear pump power loss                  | Improper shaft RPM                 | 3        | Motor speed fluctuation                     | 1        | None          | 5        | 15  |

1. External gear pump leaked
  - a. Proper installation of the gasket
2. External gear pump severe pressure fluctuation
  - a. Install pressure gauge
3. External gear pump loss of power
  - a. Automatic tapping gearbox
  - b. RPM meter on the shaft.

## 4 Conclusions

To conclude the project, proper and strategical planning from the lab practical helps team members solve the problems encountered during planning and studying, especially with assistance from the instructor. From the class lecture, combined with the multiple labs practical, the team member was able to identify the possible problem that can occur in the manufacturing process. The team also developed another skill, creating the possible survey question using Google Forms services elicited from developing an external gear pump. With the second wave of the pandemic affecting Brunei, various limitations arise, one of which is that the campus is not accessible to students, making the fabrication of the project difficult. Moreover, the limited supply of material, such as PLA puts a constraint on team members.

**Acknowledgements** The first, second and third Authors would like to thank to Dr. Wahyu Caesarendra as a lecturer for Product Design Engineering (PDE) module and Dr. Juliana Zaini as a lecturer for Computer Aided Design (CAD) module.

## References

- Bhattacharjee, P., Dey, V., Mandal, U.K.: *Saf. Sci.* **132**, 104967 (2020)
- Carletti, E., Miccoli, G., Pedrielli, F., Parise, G.: *Arch. Acoust.* **41**, 285 (2016)
- Information on <https://www.michael-smith-engineers.co.uk/resources/useful-info/external-gear-pumps>. Accessed on 9 Jan 2022
- Information on <https://dienerprecisionpumps.com/external-gear-pumps/>. Accessed on 8 March 2022
- Information on [https://www.engineersedge.com/pumps/helix\\_spur\\_gear\\_pump.htm](https://www.engineersedge.com/pumps/helix_spur_gear_pump.htm). Accessed on 8 March 2022

# **Machining and Manufacturing**

# Tool Wear Analysis on Time-Domain and Frequency-Domain Data of Machining S45C Using Signal Processing Technique



P. Jirapipattanaporn, A. Chanpariyavatevong, W. Lawanont,  
and W. Boongsood

## 1 Introduction

Nowadays, the machining process is important in many industries and engineering applications. Because the machining process is the first for preparing materials for the next steps. Milling is one machining process is widely used in industrial (Al-Zubaidi et al. 2011). Due to high material removal rate, it ensures accurate cuts. And milling is perfect for producing individual pieces in small or large batches (Liu et al. 2019). However, the milling process is necessary to use a cutting tool to cut material. Simultaneously, tool wear is usually occurs in the machining process. And tool wear is one of the main reasons leading to quality of the workpiece, machine power consumption, and production cost (Siddhpura and Paurobally 2013). Commonly, tool wear investigation can be classified into two categories. The direct method is observation by optical microscope or scanning electron microscope (Čerče et al. 2015). The advantage of the direct method is that it can record geometric changes or degrees of cutting tool. However, the equipment for this method is expensive and fragile. Moreover, to track the process, it is also necessary to stop the machine, in which result in delays (Snr 2000). And on the word of Ambhore et al. (Ambhore et al. 2015) “Direct

---

P. Jirapipattanaporn (✉) · A. Chanpariyavatevong · W. Lawanont (✉) · W. Boongsood  
School of Manufacturing Engineering, Suranaree University of Technology, Nakhon Ratchasima,  
Thailand  
e-mail: [m6201111@g.sut.ac.th](mailto:m6201111@g.sut.ac.th)

W. Lawanont  
e-mail: [worawat.law@sut.ac.th](mailto:worawat.law@sut.ac.th)

A. Chanpariyavatevong  
e-mail: [d6400392@g.sut.ac.th](mailto:d6400392@g.sut.ac.th)

W. Boongsood  
e-mail: [wanwanut@sut.ac.th](mailto:wanwanut@sut.ac.th)



methods are rather less beneficial on largely cutting tools because the visual inspection equipment has limitations in area of inspection.” Indirect method observes a relation between related parameters, such as cutting force during machining process by a load cell, vibration measured by dynamometers, and machine power consumption. García-Ordás et al. (García-Ordás et al. 2017) comment on direct method methods is constrained to use expensive equipment or high-performance computer to analyze.

However, the methods mentioned above are complex and difficult, complicated, and expensive equipment. For example, the measuring tool is difficult in real situations by taking pictures. This is difficult because setup systems are time-consuming. In the world of work, a professional technician can able to identify changes in tools during machining (Chen et al. 2009).

Therefore, the sound signal is one of alternative methods to investigate the deformation degree of tool wear during the machining process. Weller et al. (Li et al. 2019) observed changing of cutting tool in machining the 6061 aluminum. It was found that a degree of tool wear is related to time–frequency-domain data. The study mentioned that different frequency ranges are affected by the degree of tool wear. Moreover, they investigated degree of tool wear in machining AISI 1045 steel by using sonic signals (Weller and Schrier 1969). After the 2000s, there are many studies published online that are related to sound and signal processing in the machining process (Vaseghi 2008). Most of the studies used a microphone connected to a computer or data acquisition device to receive audio signals and proceed with data analysis. In Kothuru et al. (2018), the study investigated the sound of end mill during machining 6061 aluminum. The study used a microphone, which was connected to computer, and converted the sound signal to frequency spectrums of pre-processed data samples. Likewise, Salgado and Alonso (Salgado and Alonso 2007) observed the sound of cutting AISI 1040 steel. They carried out the study by using a microphone to record sound and used singular a spectrum process for the analysis. Juan Emilio Noriega-Linares (Noriega-Linares and Navarro Ruiz 2016) developed a prototype for a low-cost acoustic sensor based on the Raspberry Pi platform to analyze and monitor environmental sound. Another use case of Raspberry Pi was from Mitrović et al. (2017) that proposes a solution for water flow sound classification with the Raspberry Pi platform. From the aforementioned studies, Raspberry Pi met our requirements in many aspects whether to its ease of use to programming with Python and its ability to control the sampling rate and time of the recording sound to be the same in each experiment.

In this study, we proposed a milling process monitoring method using acoustic signal during machining S45C steel plate due to widely used in many industries (İpekoğlu et al. 2019) related to mechanical parts with high-speed steel end mills under no cooling. We adopted signal processing (Rioul and Vetterli 1991) technique to analyze milling sound. Sound of the milling process was recorded using a microphone array which was controlled by Raspberry Pi. The organization of this study starts with the introduction, methodology, experiment and results, and conclusion and discussion, respectively.

## 2 Methodology

Overall. This study conducted an experiment on several scenarios. The purpose of the experiment was for the data collection process. This section discussed the material used in the experiment as well as the experiment parameters. Later in the section, data collection devices and data visualization techniques are explained.

**Tool and Materials.** This study performed the experiment by using the three-axis computer numerical control (CNC) in face milling process. The cutting tool was an uncoating high-speed steel end mills. The details of the cutting tool are shown in Table 1. The experiment was conducted with fixed cutting parameters under no cooling. Table 2 shows the parameters used in the experiment. S45C steel plate with a thickness of 15 mm and the dimension of 70 (W) × 300 (H) mm was used in the experiment. After that, we observed the tool wear for flank wear following ISO 8688-2:1989 using a light microscope with ×5 magnification and a scanning electron microscope.

**Data Collection.** This section discussed instruments and methods for collecting data of milling sound. The experiment was performed according to cutting parameters shown in Table 2. Face milling processing was carried out by varying the process time starting from 1 to 6 min, respectively. During this experiment, new end mill was replaced in every experiment. This resulted in a total six experiments with each of them differing in process time.

For the sound recording device, a Re-speaker 2-Mics Pi Hat microphone array was used to record the milling process sound produced from the CNC machine. The microphone array was programmed to control the recording time and sampling rate of the recorded sound. In every experiment, the sound was recorded at the sampling of 22,050 Hz. The microphone array was set up 40 cm away from the front of the workpiece while maintaining the same level of the workpiece as shown in Fig. 1. The device starts recording the ambient sound for 10 s. Then, the CNC machine’s spindle starts, during this period, it takes about 15 s before the tool start milling the workpiece. During the milling process, the microphone continues to record the sound until the milling process is finished, which will take about 1 min. After that, the device stops the recording 10 s after the milling process is completed. When the

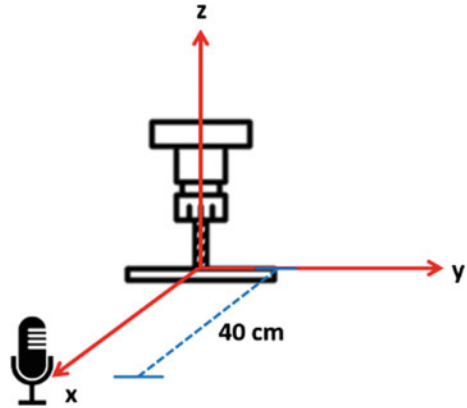
**Table 1** Details of HSS end mill

|              |                  |
|--------------|------------------|
| Material     | high-speed steel |
| Dimeter      | 10 mm            |
| Cutting edge | 2 Flute          |
| Cut length   | 25 mm            |

**Table 2** Cutting parameter

|                     |                    |                   |
|---------------------|--------------------|-------------------|
| Cutting speed (rpm) | Feed rate (mm/min) | Depth of cut (mm) |
| 800                 | 90                 | 0.5               |

**Fig. 1** Work area and setting of a data collection device



recording is done sound data will be stored in WAV file type, and this file was used later for the data visualization.

**Data Visualization.** In this study, Python programming was implemented to generate the graphs for the data visualization. Graph that we considered in this work is time-domain and frequency-domain (Stein and Shakarchi 2011) graph. The main library that we are using to import sound data and generate the digital signal is Librosa (McFee et al. 2015). First, we generated the time-domain graph of every milling process sound we recorded to see what the sound wave looks like in each condition of welding. This can be considered as the raw data of the recorded sound. To emphasize, time-domain data can be misleading as this type of data only shows the magnitude of the recorded data and not the whole frequency distribution of the data.

To extract more data from the time-domain data, a frequency-domain graph was generated to see the difference between the range of frequency that occurred in each milling condition. To generate the frequency domain, the imported sound data need to be passed through Fourier transform (Vaseghi 2008) algorithm. This was processed locally on the data collection device with The Python programming technique. Fourier transform (Vaseghi 2008) is the method to convert data from the time-domain function to the frequency-domain function.

### 3 Result and Discussion

From the experiment, milling S45C with no cooling, the study found that the end mill showed signs of wear in flank wear as shown in Fig. 2a. This relates to the assumption that heat generated and hard particle in S45C steel is the main effect of rapid tool wear and shortened the tool life span (Kataoka and Shamoto 2019). Figure 2b shows that the cutting tool used in the experiment causes tool wear over time, when the machining time increased tool wear increased.

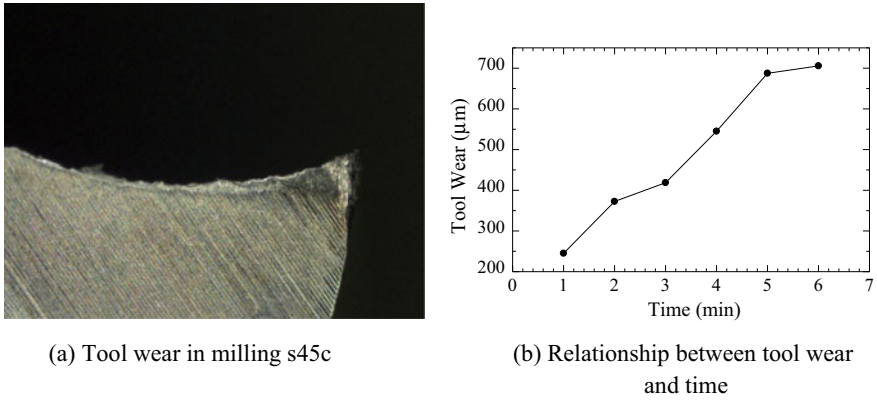


**Fig. 2** **a** Tool wear in milling s45c and **b** relationship between tool wear and time

After visualizing all the milling process sound data with the time-domain graph, we found that each time-domain graph in every experiment had the same pattern as shown in Fig. 3. The time-domain graph can indicate the occurred milling process procedure in each period based on the magnitude of the graph. However, based on the same Fig. 3, it was not possible to identify the relation between the waveform and the tool wear in the experiment because there is too many data points in the time-domain graph.

To identify the relationship between the sound of the milling process and tool wear. We further investigate the sound in the milling period that has occurred by generating the frequency-domain graph using the original time-domain data. After generating the frequency-domain graph, it was found that the tool wear is related to some frequency range shown in Fig. 4, which is the frequency domain of one of

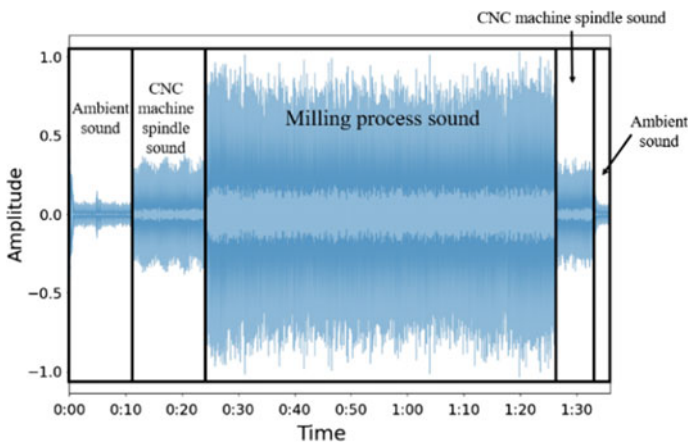


**Fig. 3** Time-domain graph of the milling process

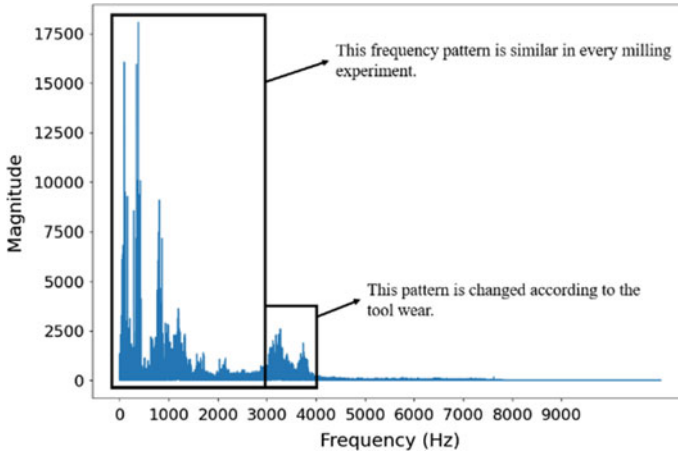


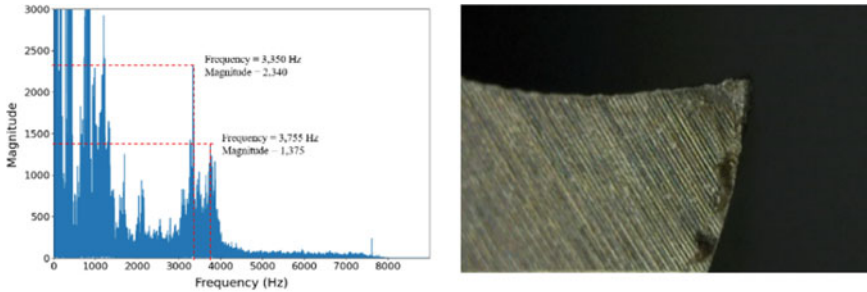
**Fig. 4** Frequency domain of the milling process

our experiments. Every frequency-domain graph shows the same pattern in every experiment. As seen in Fig. 4, we found that the frequency in the range between 0 and 3000 Hz has a similar magnitude and pattern occurred.

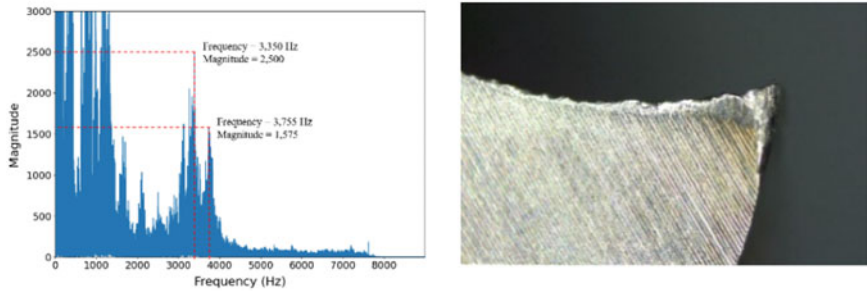
However, after investigating all the frequency-domain graphs, there are some frequency ranges that the magnitude was changed according to the tool wear. To emphasize that results, we further analyzed the frequency range between 3000 and 4000 Hz by enlarging the graph. As a result, Fig. 5 shows the frequency domain of one of our experiments that had a significant difference between the frequency magnitude that occurred in each tool wear condition. The experiment that we selected to show is sound after milling with the cutting tool for 1 min, 4 min, and 6 min as shows in Fig. 5a–c, respectively. Each figure shows the image of tool wear compared with the frequency domain in a focused frequency range. After comparing all the frequency-domain graphs, it was found that there are two frequency bands that its magnitude changed significantly according to the tool wear. These two frequency bands are 3350 and 3755 Hz. The magnitude of these two frequency bands increased after the tool went through the milling process for a prolonged period. And the magnitude increased significantly compared to the tool wear change.

## 4 Conclusion

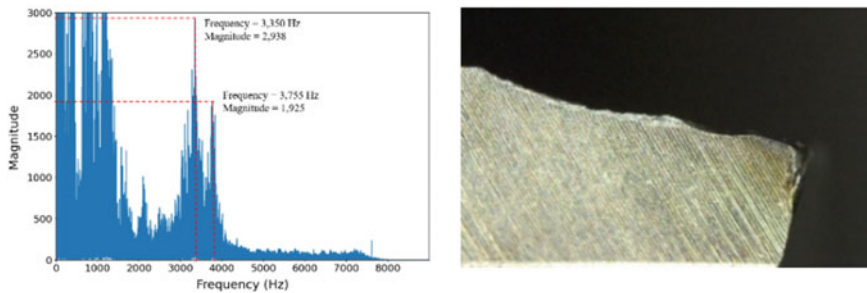
In this study, signal processing techniques have been applied for the milling process to monitor the wear of a cutting tool by milling sound. All milling sounds are recorded with a microphone array, and the data was visualized using signal processing technique to transform the time-domain data into frequency-domain data. It was found in this study that each frequency band can indicate tool wear increased and used



(a) after 1 minutes of milling



(b) after 4 minutes of milling



(c) after 6 minutes of milling

**Fig. 5** Frequency-domain graph and tool wear

for monitoring the milling process. The frequency band from 0 to 3000 Hz of every milling condition has a similar magnitude and pattern on the graph. Therefore, we can conclude that these frequency bands are the normal frequency band of the milling process. Furthermore, two frequency bands have a relationship with the tool wear over time. From the graph, the magnitude of the frequency band 3350 and 3755 Hz increased as the tool wear level increased. Thus, this can be summarized that we can track 3350 and 3755 Hz frequencies to monitor the wear of the cutting tool.

Finally, by identifying the frequency band relate to the tool wear level, the results can be further used as a foundation to develop a smarter monitoring system with the implementation of machine learning or artificial intelligence technology. Implementing such technologies on monitoring the milling process in this suggested frequency band for tool wear level would greatly reduce delays in manufacturing, resulting in cost reduction of the process.

## References

- Al-Zubaidi, S., Ghani, J.A., Che Haron, C.H.: Application of ANN in milling process: a review. *Model. Simul. Eng.* **2011** (2011)
- Ambhore, N., et al.: Tool condition monitoring system: a review. *Mater. Today: Proc.* **2**(4–5), 3419–3428 (2015)
- Čerče, L., Pušavec, F., Kopač, J.: A new approach to spatial tool wear analysis and monitoring. *Strojniški Vestnik-J. Mech. Eng.* **61**(9), 9 (2015)
- Chen, T.-H., et al.: Study of sound signal for tool wear monitoring system in micro-milling processes. In: *International Manufacturing Science and Engineering Conference* (2009)
- García-Ordás, M.T., et al.: A computer vision approach to analyze and classify tool wear level in milling processes using shape descriptors and machine learning techniques. *Int. J. Adv. Manuf. Technol.* **90**(5), 1947–1961 (2017)
- ĀpekoĀlu, G., et al.: Investigation of microstructure and mechanical properties of friction stir welded dissimilar St37/St52 joints. *Mater. Res. Express* **6**, 046537 (2019)
- Kataoka, R., Shamoto, E.: Influence of vibration in cutting on tool flank wear: fundamental study by conducting a cutting experiment with forced vibration in the depth-of-cut direction. *Precis. Eng.* **55**, 322–329 (2019). LNCS Homepage, <http://www.springer.com/lncs>. Last accessed 21 Nov 2016
- Kothuru, A., Nooka, S.P., Liu, R.: Application of audible sound signals for tool wear monitoring using machine learning techniques in end milling. *Int. J. Adv. Manuf. Technol.* **95**(9), 3797–3808 (2018)
- Li, Z., Liu, R., Wu, D.: Data-driven smart manufacturing: tool wear monitoring with audio signals and machine learning. *J. Manuf. Process.* **48**, 66–76 (2019)
- Liu, M.-K., Tseng, Y.-H., Tran, M.-Q.: Tool wear monitoring and prediction based on sound signal. *Int. J. Adv. Manuf. Technol.* **103** (2019)
- McFee, B., et al.: Librosa: audio and music signal analysis in python. In: *Proceedings of the 14th Python in Science Conference* (2015)
- Mitrović, A., Djukanović, S., Radonjić, M.: Implementation of signal classification using frequency spectrum features on the raspberry Pi platform. In: *2017 25th Telecommunication Forum (TELFOR)*. IEEE (2017)
- Noriega-Linares, J.E., Navarro Ruiz, J.M.: On the application of the raspberry Pi as an advanced acoustic sensor network for noise monitoring. *Electronics* **5**(4), 74 (2016)
- Rioul, O., Vetterli, M.: Wavelets and signal processing. *IEEE Signal Process. Mag.* **8**(4), 14–38 (1991)
- Salgado, D., Alonso, F.: An approach based on current and sound signals for in-process tool wear monitoring. *Int. J. Mach. Tools Manuf.* **47**(14), 2140–2152 (2007)
- Siddhpura, A., Paurobally, R.: A review of flank wear prediction methods for tool condition monitoring in a turning process. *Int. J. Adv. Manuf. Technol.* **65**(1–4), 371–393 (2013)
- Snr, D.E.D.: Sensor signals for tool-wear monitoring in metal cutting operations—a review of methods. *Int. J. Mach. Tools Manuf.* **40**(8), 1073–1098 (2000)

Stein, E.M., Shakarchi, R.: Fourier Analysis: An Introduction, vol. 1. Princeton University Press (2011)

Vaseghi, S.V.: Advanced Digital Signal Processing and Noise Reduction. Wiley (2008)

Weller, E., Schrier, H.M., Weichbrodt, B.: What sound can be expected from a worn tool?



# Optimization of the Weight and Size Characteristics of the Power Bracket for Additive Manufacturing Based on Topological Optimization Algorithms



A. V. Zhdanov, S. A. Baranov, and L. V. Belyaev

## 1 Introduction

Currently, one of the intensively developing technological methods of manufacturing products is the method of selective laser melting. This method has a number of technological advantages over traditional methods of material processing, allowing you to obtain products of almost any geometric complexity from a large range of materials (Sadeghilaridjani 2021; King et al. 2015). However, it is not economically feasible to manufacture products whose geometry is not adapted to the peculiarities of additive manufacturing (Bajaj et al. 2020).

One of the methods of such adaptation is the use of topology optimization. Topology optimization is a mathematical tool that allows you to optimize the distribution of material in a part at the design stage. There are various topology optimization algorithms developed over the past three decades. For instance, set level approach, homogenization method, SIMP method and density approach are among the main topology optimization techniques (Rozvany 2009; Sigmund and Maute 2013).

The purpose of this article is to investigate the possibility of optimizing the weight and size characteristics for additive manufacturing based on the selected algorithm of topological optimization.

## 2 Materials and Methods

The object of the study was a bracket used as a swivel mount and experiencing heavy loads, with overall dimensions of  $176 \times 170 \times 95$  mm (Fig. 1), made of EN-AW 2024 material and weighing 1.75 kgf. EN-AW 2024 alloy is a typical 2xxx

---

A. V. Zhdanov (✉) · S. A. Baranov · L. V. Belyaev  
Vladimir State University, 87 Gorky Street, Vladimir 600000, Russia  
e-mail: [Zhdanov@vlsu.ru](mailto:Zhdanov@vlsu.ru)

series (Al–Cu–Mg) wrought Al alloy, and it has the advantages of low density, high specific strength, excellent fatigue resistance and good machinability (Chen et al. 2019; Zhang et al. 2019; Bonfils-Lahovary et al. 2024). The EN-AW 2024 is resilient material with increased strength values, which is mainly used in the aerospace and automotive industries. The properties of the EN-AW 2024 material and its chemical composition are provided in Tables 1 and 2.

The use of aluminum is justified by the fact that the design of the bracket should be lightweight and at the same time withstand the loads applied to it. At the same time,

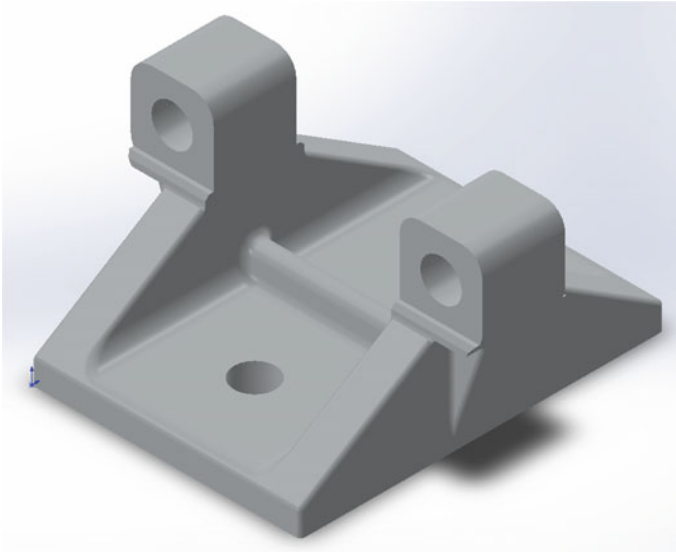


**Fig. 1** 3D-model of power bracket

**Table 1** Physical and mechanical properties of the material EN-AW 2024

| Parameter                  | Value  |
|----------------------------|--------|
| Modulus of elasticity, MPa | 70,000 |
| Poisson's ratio            | 0.3897 |
| Shear modulus, MPa         | 27,000 |
| Density, kg/m <sup>3</sup> | 2780   |
| Tensile strength, MPa      | 440    |
| Yield strength, MPa        | 290    |

**Table 2** Chemical composition of the material EN-AW 2024 [% weight]

| Si   | Fe   | Cu      | Mn      | Mg      | Cr   | Zn    | Ti    | Other | Al        |
|------|------|---------|---------|---------|------|-------|-------|-------|-----------|
| ≤0.5 | ≤0.5 | 3.8–4.9 | 0.3–0.9 | 1.2–1.8 | ≤0.1 | ≤0.25 | ≤0.15 | ≤0.15 | 90.7–94.7 |

the use of this material imposes a number of significant restrictions on the physical characteristics of the product. These include lack of load capacity, high probability of fatigue failure and temperature resistance. Nevertheless, it is worth pointing out that in the process of optimization, fine-tuning of the design is possible, taking into account all complicating factors.

The original design of the bracket is an integral structure of complex geometric shape, consisting of several holes and stiffeners. Fixing the bracket to the surface of the fit is carried out through the lower plane and the corresponding hole in it. The fastening of the mating part of the moving structure is carried out through holes having a cylindrical shape.

The mechanical and physical properties of the material used are listed below.

Topological optimization was carried out in the SOLID WORKS 2020 software product (Dassault Systems, France). This software product uses the SIMP method for topology optimization (SOLID WORKS 2020).

The optimization conditions were as follows:

- the optimized geometry must fit within the original part envelope; minimum material feature size (wall thickness or central rib): 18.4 mm;
- the part was fixed through holes in the base;
- the load was 10 kN and applied at an angle of  $90^\circ$  to the base plane (horizontal plane);
- the aim of the study is to reduce the weight by 60%.

To determine the effectiveness of the topological optimization process, the stress–strain state of the initial and obtained geometries was evaluated under the same loading conditions.

### 3 Results and Discussion

As a result of the topological optimization of the initial geometry of the product based on the finite element method, a new geometry of the bracket in question was obtained (Fig. 2).

In the process of topology optimization, the product was transformed and geometrically underwent some complications. Thus, the resulting geometry had a less monolithic base, but an increased number of support points. Geometric cutouts were formed at the base of the product to reduce the weight of the entire structure. The stiffeners were also changed in the direction of complicating the geometry, but reducing the total mass and area.

The analysis of the stress–strain state of the part allowed us to obtain pictures of the von Mises stress distribution, deformations and the safety factor, which are shown in Figs. 3 and 4.

Stress fields have shown that the greatest load falls on the central stiffener of the product at the base. Nevertheless, these stresses are moderate values that are not critical for the applied loads and the material used.

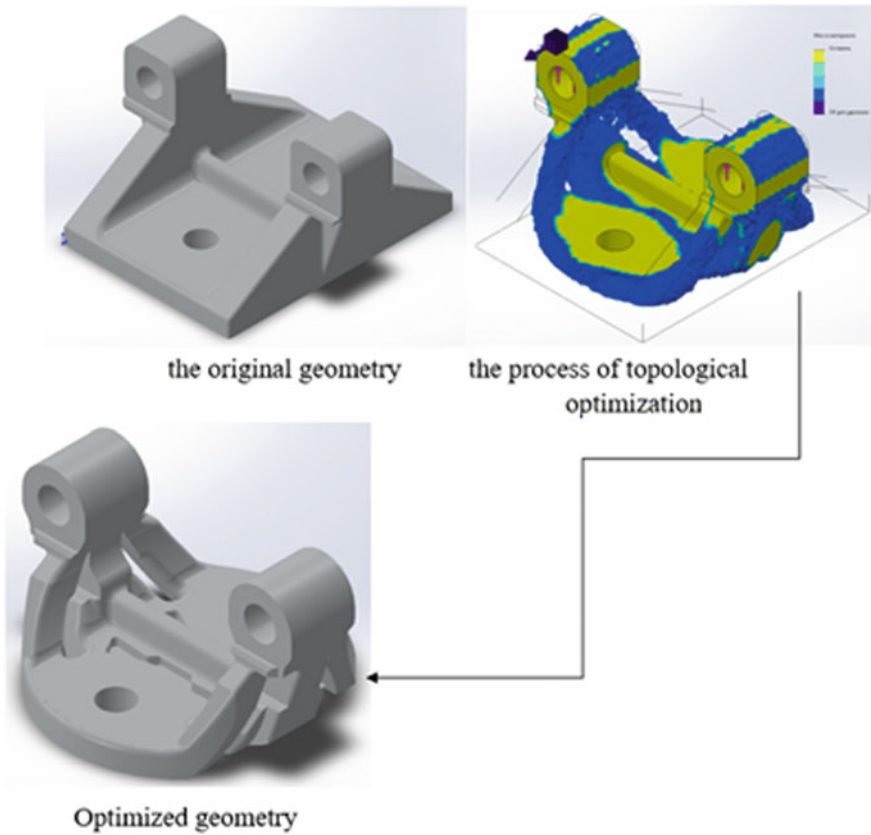


**Fig. 2** Topological transformation of geometry

The von Mises stresses values were reduced and now they are about 133 MPa on average, over the entire length of the edge. The graph of rib loading along the length shows a sharp decrease in stresses in the area from 50 to 80 mm. This is due to the distribution of the load over the newly formed geometry, which allows us to delegate the load along the entire length of the edge. In addition, the graph shows that the average values of the emerging stresses do not exceed 140 MPa. This is a significant improvement.

The maximum values of these parameters are given in Tables 3 and 4.

A comparison of the results obtained from the tables above shows the possibility of reducing the mass of the part without losing its mechanical properties.

The reduction of weight saves huge amount of material and processing energy thus huge amount of money. It also shows that the capability of topology optimization can be fully utilized with additive manufacturing techniques, as the manufacturing constraints in the conventional methods are no longer available. As a result of the work, the weight of the product decreased by 31.5%, and the average values of stresses

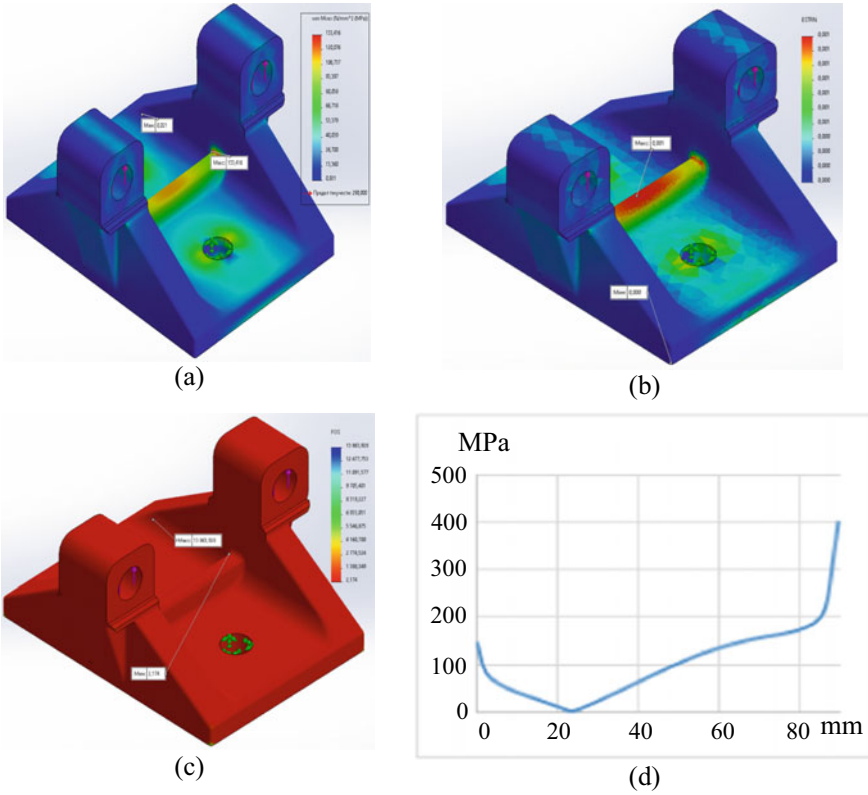


**Fig. 3** Diagrams of stresses (a), deformations (b), safety factor (c), and stress distribution graph along the edge length (d) for the initial geometry of the product

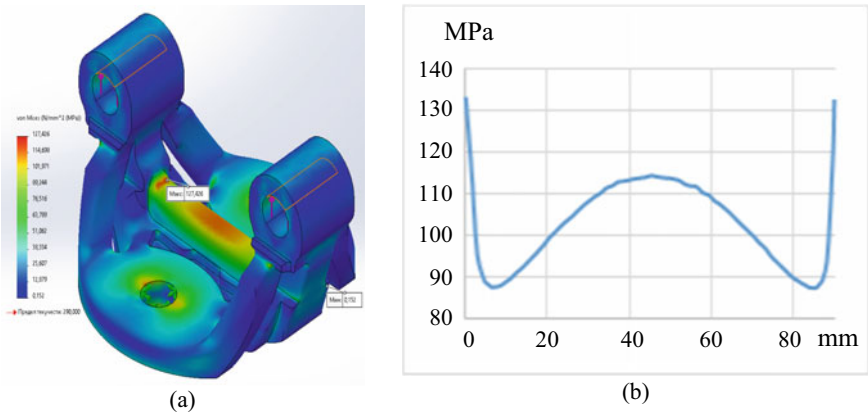


**Fig. 4** Stress plots (a) and stress distribution graph along the edge length (b)

**Table 3** Results of static analysis of the model without topological changes

| Parameter               | Value   |
|-------------------------|---------|
| Von Mises stresses, MPa | 117.858 |
| Deformation, ESTRN      | 0.002   |
| Safety margin           | 2.461   |
| Weight, kgf             | 1.180   |

**Table 4** Results of static analysis of the model with topological changes

| Von Mises stress, MPa | Deformation, ESTRN | Safety margin |
|-----------------------|--------------------|---------------|
| 113.416               | 0.001              | 2.174         |

arising during the load decreased by almost a half. The results require practical confirmation in working conditions, which is the next stage of the study.

## 4 Conclusion

From the case study, it can be concluded that topology optimization is a powerful design concept to reduce the weight of structural products. The reduction of weight saves huge amount of material and processing energy thus huge amount of money. It also shows that the capability of topology optimization can be fully utilized with additive manufacturing techniques, as the manufacturing constraints in the conventional methods are no longer available. From the case study result, which is 31.5% weight and 11.5 von Mises stress reduction, respectively, it can also be concluded that topology optimized design for additive manufacturing can reduce huge portion of the mass thus result in lightweight design.

**Acknowledgements** This work was supported by the Russian Foundation for Basic Research (Grant 20-08-00310) and was carried out using the equipment of the interregional multispecialty and interdisciplinary center for the collective usage of promising and competitive technologies in the areas of development and application in industry/mechanical engineering of domestic achievements in the field of nanotechnology (CCP VISU).

## References

- Bajaj, P., Hariharan, A., Kini, A., Kürnsteiner, P., Raabe, D., Jägle, E.A.: Steels in additive manufacturing: a review of their microstructure and properties. *Mater. Sci. Eng., A* **772**, 138633 (2020)
- Chen, G., Liu, J., Shu, X., Gu, H., Zhang, B., Feng, J.: Beam scanning effect on properties optimization of thick-plate 2A12 aluminum alloy electron-beam welding joints *Mater. Sci. Eng. A* **744**, 583–592 (2019)

- de Bonfils-Lahovary, M., Josse, C., Laffont, L., Blanc, C.: Influence of hydrogen on the propagation of intergranular corrosion defects in 2024 aluminium alloy. *Corrosion Sci.* **148**:198–205
- King, W., Anderson, A., Ferencz, R., Hodge, N., Kamath, C., Khairallah, S., Rubenchik, A.: Laser powder bed fusion additive manufacturing of metals; physics, computational, and materials challenges. *Appl. Phys. Rev.* **2**, 041304 (2015)
- Rozvany, G.: *Struct. Multidiscipl. Optim.* **37**(3), 217–237 (2009)
- Sadeghilaridjani, M.: Review of powder bed fusion additive manufacturing for metals. *Metals* **11**, 1391 (2021)
- Sigmund, O., Maute, K.: *Struct. Multidiscipl. Optim.* **48**(6), 1031–1055 (2013)
- SOLID WORKS 2020. [https://help.solidworks.com/2019/English/SolidWorks/cworks/c\\_simp\\_method\\_topology.htm](https://help.solidworks.com/2019/English/SolidWorks/cworks/c_simp_method_topology.htm). Last accessed 21 Nov 2021
- Zhang, S., Zhang, T., He, Y., Liu, D., Wang, J., Du, X., Ma, B.: Long-term atmospheric corrosion of aluminum alloy 2024–T4 in coastal environment: surface and sectional corrosion behaviour. *J. Alloys Compd.* **789**, 460–471 (2019)

# Identification and Active Control of the Chatter Phenomenon in the Milling Process Using a Pneumatic Actuator



Peyman Enteshari Najafabadi, Reza Nosouhi, Milad Soleimani, and Mahmood Mirkhanzadeh

## 1 Introduction

Given the advances in metal cutting in recent years, the issue of metal machining with milling and turning machines is still in the spotlight, and these machines are progressing every day. In today's advanced industries, especially the aerospace, military and medical industries, components of high dimension precision and roughness, are needed. Reduction of production time is also one of the most important issues of concern to the industry. However, one of the problems making these demands fail is the chatter vibration phenomenon. This vibration causes poor surface quality, reduced dimensional accuracy, increased production time and damage to the machines and tools. Many studies have been conducted on this subject, and they all try to suppress or reduce the negative effects of this vibration using different methods.

Generally speaking, any phenomenon that alters the cutting forces in machining process periodically, can be candidate of the chatter source. There are two main different types of chatter vibrations. The first type is caused by the cutting process phenomena including: friction between the tool and the workpiece, effects of the elevated temperature on the cutting tool and the workpiece which increase the tool length and consequently, alters the tool length contact length with the workpiece, and the mode coupling effect; which occurs when relative vibration between the tool and the workpiece is present in at least two directions on the cutting plane. The second type, on the other hand, is due to the successive waves created on the surface

---

P. E. Najafabadi · R. Nosouhi (✉)  
Modern Manufacturing Technologies Research Center, Najafabad Branch, Islamic Azad University, Najafabad, Iran  
e-mail: [rezanosuhi@pmc.iaun.ac.ir](mailto:rezanosuhi@pmc.iaun.ac.ir)

Department of Mechanical Engineering, Najafabad Branch, Islamic Azad University, Najafabad, Iran

M. Soleimani · M. Mirkhanzadeh  
R&D Department, Naein Abzar Co. Ltd, Isfahan, Iran



of the workpiece which alternatively changes the cutting forces. The latter is called regenerative chatter and is the main cause of the chatter phenomenon.

In the literature, several methods have been employed to address the chatter phenomenon. Some researchers have worked on determination of the machining parameters (i.e., mainly the spindle speed and depth of cut) so that the chatter would not occur. In these strategies (Tyler et al. 2015; Dai et al. 2018; Grossi et al. 2017), the main objective is the stability lobes diagram, by which the stable chatter-free zones in machining are distinguished from the unstable zones. These methods, however, do not alter the dynamic behavior and the stable zones of the machine tool; it enables the machine tool user to carry out the machining process with the highest achievable material removal rate while avoiding the destructive chatter phenomenon.

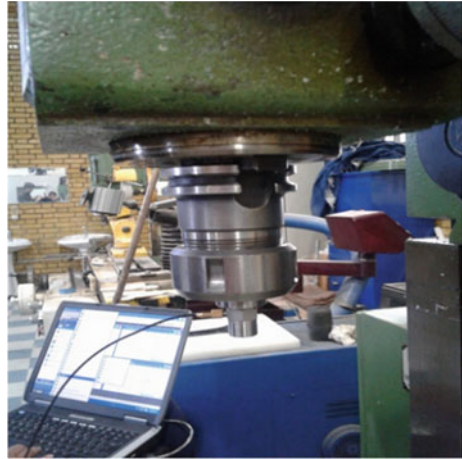
Some other researchers have approached differently toward the chatter problem. They have devised methods by which the dynamic behavior of the machine could be altered. These methods are divided into two main categories: namely active and passive methods. The distinction criteria between these two methods are that in the active chatter control methods (Shi et al. 2018; Fallah et al. 2019), the vibration parameters of the machine are detected and measured precisely, and an excitation in accordance with the vibration parameters is applied to the machine system. While in the passive methods (Wang et al. 2019; Fujimaki et al. 2020), there is no feedback from the machine, the dynamic behavior of the machine is altered via some methods that are known to be helpful in all machining chatter conditions. Some examples of these methods are the redesign of the dynamically weak components of the machine, and the variable helix and pitch angles end mills.

The advantage of the active method is that in this case, the dynamic state of the machine is controlled at any moment and when the system malfunctions, the controller acts and changes the system to a more stable state. Such systems typically use a controller that is specifically designed for the vibration characteristics of the system, an accelerometer or strain gage as the vibration sensor, and an actuator, usually for damping the vibrations (Quintana and Ciurana 2011).

The study of the machine dynamic behavior would eventually lead to a diagram which is called stability lobes diagram (SLD). The horizontal axis of the diagram is the spindle speed, while the vertical axis is the depth of cut. The lobes of the machine tool stability are depicted in this diagram, below which the machining is stable or chatter-free, and over which the machining is unstable and chatter phenomenon occurs. The calculations of the SLD are, in fact, based on the dynamics of the machine and the tool giving the operator a graph for each particular material. This chart shows how much depth of cut at each selected spindle speed is accessible before occurring the chatter and reaching unstable state.

According to Fig. 1, it can be said that if, by any means, the diagram could be shifted upward, higher cutting depths can be selected for the cutting operation, which results in higher material removal rates and lower production time, which is economically more advantageous. Furthermore, due to the periodic nature of the diagram, shifting the diagram into right or left directions might, in some cases, stabilize an unstable point. The shifting of the SLD upward primarily, and to the

**Fig. 1** Milling machine used with accelerometer



right and left directions secondarily, is the main objective of the research works in chatter suppression/control literature.

Recent research efforts rely on the use of active and passive methods of chatter phenomenon control. Active methods are based on the measurement of the vibration parameters which enable the controller to detect the chatter occurrence and its parameters, and then excitation of the machine in accordance to the chatter parameters using an actuator. The most commonly used actuators include piezoelectric stacks and magnetostrictive actuators. Passive methods are designed based on changes in system structure and by changing the system natural frequencies by adding and deducting masses, changing machining parameters or redesigning machine tool accessories (Munoa et al. 2016).

Ahrens et al. (2016) used an electromagnetic actuator, tried to suppress the chatter in the grinding process using the active method. The idea of an active chatter damper is to estimate the shape of the waves on the tool and create a force against the forces on the workpiece that is the cause of the surface waves. Bort et al. (2016) attempted to control the chatter using a model-predictive-control (MPC). By using an MPC, the process time and roughness improved by 46% and 22%, respectively. Burtscher and Fleischer (2017) presented an adaptive tuned mass damper (ATMD) that its design and results are based on the genetic algorithm. When the machine's frequency values change through the working position, the ATMD reduces the chance of the chatter occurring by adjusting and dominating these frequency values. When the damper was activated, the vibrations were reduced by 36%.

As a conclusion of the review of previous studies, it is clear that none of the abovementioned studies, has used pneumatic actuators to control the chatter. These actuators, in addition to their many capabilities, are inexpensive and affordable and, as far as their operating frequency allows, can be used as a chatter control actuator. The compressed air for the actuator is available in almost all machining workshops, which enables the machine shop owners to use this system with minimum cost.

## 2 Materials and Methods

We need to obtain SLD for the milling machine to know chatter frequency occurs at what speed range. To obtain SLD, the basis for predicting chatter in theory, the machine's natural frequencies are required. For this purpose, an experimental modal analysis is carried out in order to obtain the dynamic behavior parameters of the machine.

### 2.1 Experimental Modal Analysis

Modal analysis is the process of determining the dynamic properties of a system in terms of natural frequencies, damping coefficients and mode shapes (He and Fu 2001). We apply them to create a mathematical model for the system dynamic behavior. The basis of this technique is based on the relationship between vibrational response at one point of the structure with the excitation at the same point or another. The equipment used in the experiments is an impact hammer (Bruel & Kjaer brand), which analyzes the input data using PULSE LabShop software Version 6.1. The accelerometer is made in DJB Instruments with part number of A/120/V, and the hammer used was type of RION PH-51. The milling machine is a DECKEL FP4M type, made in Tabriz Machinery Manufacturing Company. Since the structural chatter phenomenon occurs in collet and collet holder when the tool is involved with the workpiece, the accelerometer is directly installed beneath the collet holder. The hammer impact point is on the collet holder nut. The vibration bandwidth in structural chatter is between 0 and 200 Hz (Quintana and Ciurana 2011). Figure 1 shows the milling machine with the accelerometer attached to it.

At the beginning of the modal experiments, the force range applied by the operator to the object with the hammer is measured. The coherence diagram illustrates the relationship between the final response and the input impulse to stimulate the system. If the vertical value of the diagram is less than 0.8, the response obtained is considered as a noise signal. This indicates that the stimulus generated in the system has been caused by an external factor. The way to obtain natural frequencies from the obtained graphs is by simultaneously examining the coherence graph and the frequency response graph. When the number shown on the Y-axis of coherence graph is between 0.8 and 1. The corresponding peak in the frequency response diagram is the natural frequency. Finally, for the first and second modes, the values of 16 and 48 Hz were obtained.

In order to obtain the SLD, the cutting force coefficient is also needed. The force coefficients are mostly influenced by the workpiece material and the cutting tool parameters (i.e., geometry, size and material). The materials used in this study are Inconel 617 superalloy and austenitic stainless steel 316. The cutting forces are measured using a Kistler 9443B dynamometer. The end mill is a WC tool with

the diameter of 12 mm manufactured in YG-1 company under the code number G9453912.

After measurement of the machining forces, the cutting coefficients are derived from the following Eqs. 1 and 2:

$$K_{tc} = \frac{4\bar{F}_{yc}}{ac} \quad (1)$$

$$K_{rc} = \frac{-4\bar{F}_{xc}}{ac} \quad (2)$$

where  $\bar{F}$  is the average of the force measured,  $a$  is the depth of cut and  $c$  is the feedrate per tooth.

Finally, the stability lobes are calculated as follows:

Selection of a chatter frequency from transfer functions around a dominant mode. Solution of the eigenvalue, by use of transfer function gotten in modal test, from

$$a_0\Lambda^2 + a_1\Lambda + 1 = 0 \quad (3)$$

Calculation of the critical depth of cut from

$$a_{lim} = -\frac{2\pi\Lambda_R}{NK_t}(1 + \kappa^2) \quad (4)$$

where  $\Lambda_R$  is the real part of the eigenvalue real part,  $\kappa$  is obtained by dividing the real and imaginary part of eigenvalue and  $N$  is the tool tooth flute. Calculation of the spindle speed from for each stability lobe  $k = 0, 1, 2, \dots$ , from

$$n = \frac{60}{NT} \quad (5)$$

where  $T$  is tooth-passing period. Repeat the procedure by scanning the chatter frequencies around all dominant modes of the structure evident on the transfer functions.

### Pneumatic Actuator

To damp the vibration of the machine actively, an actuator is required for excitation of the system in accordance to the chatter parameters.

In this study, after investigations, it was decided to use a pneumatic actuator. One advantage of this actuator is its cost-effectiveness compared to other actuators for its use in the first modes of the system. The compact cylinder, has force of 1000 N, made by SNS Company in model of SDA 63X40-S.

An air solenoid valve is required to command the cylinder to generate the signal sent to the valve. The VUVG-L14-M52-MT-G18-1P3 model solenoid valve made by FESTO Company is used for this purpose. The valve is able to withstand pressure

up to 800 kPa and has an operating frequency of 16.5 Hz. To produce desired signal an AFG-2125, GW INSTEK arbitrary function generator is employed.

## 2.2 Equipment

Since the purpose of this study is to control the vibrations and motion of the machine tool, a sensor is required to measure the vibration amplitude during machining. In this research, a MicroSense 5810 non-contact capacitance displacement sensor precision made by MicroSense Inc. is used. This sensor, which is shown in Fig. 2, measures the spindle vibration amplitude by voltage variation and has the ability to measure vibrations in frequencies up to 100 kHz.

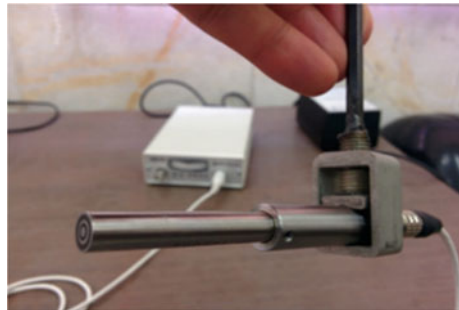
Due to the fact that this sensor shows the values in an analog way, it is necessary to connect it to a data acquisition card (DAC). The 12-bit POS-760 data card made by Advantech Company is used for this purpose.

The active controller constantly receives and processes the input signals online. Therefore, a host computer is needed to establish a connection between the input and output data. LabView 2018 software is employed to design the controller. Finally, the control cycle is depicted in Fig. 3. The spindle vibration is measured during machining using the displacement sensor. Whenever the chatter phenomenon occurs, the controller detects the chatter as the vibration amplitude increases, and it excites the pneumatic actuator in the chatter frequency.

## 3 Results and Discussion

The capacitance displacement sensor and the DAC are used to detect the chatter by checking the displacement versus time diagram of the device in the LabView software. The experiments are carried out in different spindle speeds with and without the controller to study the advantage of the active control. When the chatter occurs, the displacement vs. time diagram shows a peak, as it can be seen in Fig. 4.

**Fig. 2** Capacitance displacement sensor



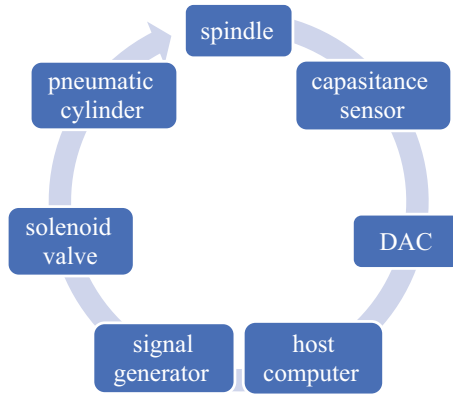


Fig. 3 Active control cycle

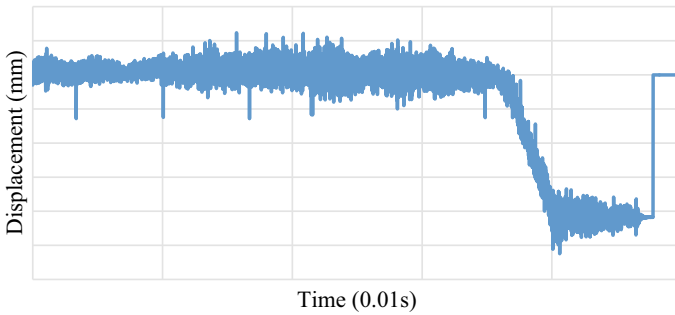


Fig. 4 Displacement versus time diagram

This is the method of detecting the chatter by a displacement–time diagram. The horizontal axis of the graph represents the time with a resolution of 0.01 s, and the vertical axis represents the spindle housing displacement by monitoring this diagram online during the machining, operator can stop the operation when the chatter phenomenon is started.

According to the experiments performed when the controller was switched off, the average voltage range was 0.3 V. As a result, this value was defined as a condition for the controller to send a signal via the signal generator to the solenoid valve if the amount of change has been exceeded during operation. The signal sent through the generator to the solenoid valve was 16 Hz square wave, with 75% duty cycle and a voltage of 5. The force applied to the spindle by the actuator was 154 N. Figure 5 illustrates the displacement sensor and cylinder installed on machine tool.

Workpieces require machining on each to determine the depth of cut at different speeds. For this purpose, the workpieces are designed with an inclined surface. Thus, depth of cut will be increasing during the machining. Since the feedrate did not affect the chatter, it was considered constant in all experiments with value of 12 mm/min.

**Fig. 5** Installed capacitance sensor and cylinder



The results of the experiments on the austenitic stainless steel 316.

The machining experiments are carried out without the controller at the spindle speeds of 315, 400, 500, 1250, 1600 and 2000 rpm with a feedrate of 12 mm/min to reach critical depth of cut before occurring chatter. The above-mentioned experiments are performed once again with the presence of the controller.

Figure 6 is the final workpieces obtained from tests. It can be seen that when the actuator is exciting the system at the spindle speeds in the first mode in the SLD, the critical depth of cut increases. At the covering speeds of second mode, excitation of the machine in the first mode frequency has a negative effect and decreases the critical depth of cut.

Table 1 contains the final values obtained for the critical depth of cut at different speeds. The last column shows the percentage increase or decrease of the cutting depth in the presence of the operator, with a positive and a negative sign, respectively. At spindle speeds 315, 400 and 500 rpm, which lie in the first mode of the machine in the SLD, the amount of the critical of depth, in the presence of the actuator is increased up to 47%. The higher spindle speeds, which lie in the second mode of the machine, show a sharp decrease in critical depth of cut. The reason for such a decrease is that the excitation with the frequencies far from the mode frequency

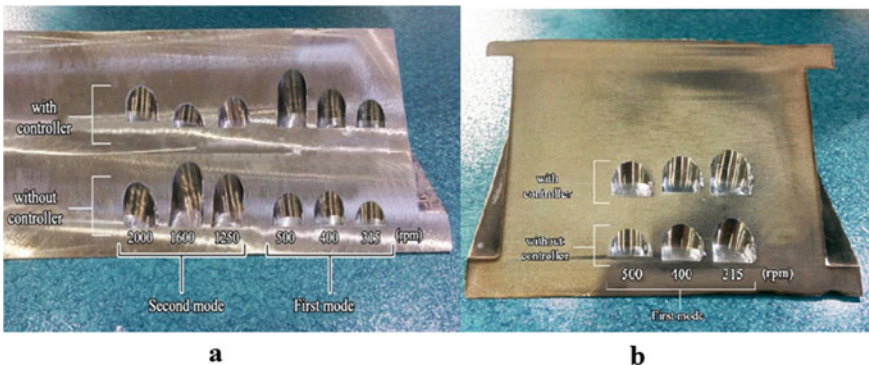


**Fig. 6** a Final austenitic stainless steel 316 and b Inconel 617 workpieces

**Table 1** Obtained values for austenitic stainless steel 316

| Spindle speed (rpm) | Depth of cut (mm) without controller | Depth of cut (mm) with controller | Increase or decrease depth-of-cut percentage |
|---------------------|--------------------------------------|-----------------------------------|--|
| 315                 | 4.85                                 | 6.15                              | + 21   |
| 400                 | 6.9                                  | 8.45                              | + 18   |
| 500                 | 6.65                                 | 12.7                              | + 47   |
| 1250                | 10.25                                | 6.6                               | - 55   |
| 1600                | 12.75                                | 4.45                              | - 186  |
| 2000                | 8.95                                 | 6.8                               | - 31   |

would only add extra energy to the system, which eventually makes the system more prone to the chatter.

### 3.1 *The Results of the Experiments on the Inconel 617 Super Alloy*

Inconel 617 tests conducted at speeds of 315, 400 and 500 rpm with and without the presence of the controller. When the actuator is on, at the covering speeds of the first mode in the SLD, the critical depth of cut is increased.

In Table 2, the final values obtained for the Inconel 617 super alloy are shown when the controller is on and off. The three tests for Inconel were all in the first mode. In the first mode, critical depth of cut increases.

Note that the chatter phenomenon is mainly occurring in the roughing operations, where the depth-of-cut values are high enough. The roughing operations, specifically, in hard-to-cut materials such as austenitic stainless steels and super alloys, are usually carried out in low cutting speeds. Therefore, although the pneumatic actuator is unable to suppress the chatter phenomenon in higher spindle speeds due to the limitation of the actuator bandwidth, the excitation of the machine in the first mode is adequate, and the excitation of the machine in the second mode sounds redundant.

**Table 2** Obtained values for Inconel 617 super alloy

| Spindle speed (rpm) | Depth of cut (mm) without controller | Depth of cut (mm) with controller | Increase or decrease depth-of-cut percentage |
|---------------------|--------------------------------------|-----------------------------------|--|
| 315                 | 6.95                                 | 7.5                               | + 7  |
| 400                 | 5.65                                 | 6.3                               | + 10   |
| 500                 | 4.75                                 | 5.3                               | + 10   |



## 4 Conclusions

The main purpose of this study was to identify the chatter phenomenon and control it using the active method. As explained in previous chapters, an active control system requires data online to identify the chatter. An actuator is also used to actively control the vibrations. So, it can receive the signal and apply it to the desired area using the host computer and the controller defined for it.

After reviewing the final results, it is found that the pneumatic actuator is capable of increasing the critical depth of cut and mitigating the chatter in the first mode. But at speeds related to the second mode, the presence of the actuator reduces the cutting depth compared to the absence of it. The reason for this is due to the operating frequency of the solenoid valve. The frequency of the solenoid valve is 16 Hz, which corresponds to the frequency of the device first mode (16 Hz). The frequency value of the device second mode is 48 Hz. As a result, at the speeds of the second mode, the presence of the actuator stimulates the vibration more and helps the chatter to occur faster. Using this actuator in the first mode of the device increases the average cutting depth for austenitic stainless steel 316 and Inconel 617 super alloy by 28 and 10 percent, respectively. Therefore, due to the low price of this type of actuator, it can be said that the pneumatic actuator can be more economical than other actuators in order to damp the first modes of the device.

The employed pneumatic actuator bandwidth is limited to the first mode frequency due to the limitation in operating frequency of the valve. Although this is one of the disadvantages of the pneumatic system, since the chatter occurs mostly in roughing operations, and the roughing operations of the hard-to-cut materials are mainly carried out in the low cutting speeds, the first mode speeds are high enough in economic machining of these materials.

## References

- Ahrens, M., Dagen, M., Denkena, B., et al.: An active damping method for chatter vibration in plunge grinding using electromagnetic actuators. *Procedia CIRP* **46**, 197–200 (2016)
- Bort, C.M., Leonesio, M., Bosetti, P.: A model-based adaptive controller for chatter mitigation and productivity enhancement in CNC milling machines. *Rob. Comput. Integr. Manuf.* **40**, 34–43 (2016)
- Burtscher, J., Fleischer, J.: Adaptive tuned mass damper with variable mass for chatter avoidance. *CIRP Ann* **66**(1), 397–400 (2017)
- Dai, Y., Li, H., Xing, X., et al.: Prediction of chatter stability for milling process using precise integration method. *Precis. Eng.* **52**, 152–157 (2018)
- Fallah, M., Moetakef-Imani, B., Hosseini, A., et al.: Boring Bar chatter control using feedback filtered-x normalized least mean square algorithm. *IFAC-Papers OnLine*; **52**(10), 358–363 (2019)
- Fujimaki, S., Shibayama, T., Hayasaka, T., et al.: Proposal of “curved-profile wiper turning” for efficient, stable, and smooth finishing. *Precis. Eng.* **61**, 152–159 (2020)
- Grossi, N., Sallese, L., Scippa, A., et al.: Improved experimental-analytical approach to compute speed-varying tool-tip FRF. *Precis. Eng.* **48**, 114–122 (2017)
- He, J., Fu, Z.F.: *Modal Analysis*. Butterworth-Heinemann Publications (2001)

- Munoa, J., Beudaert, X., Dombovari, Z., et al.: Chatter suppression techniques in metal cutting. *CIRP Ann.* **65**(2), 785–808 (2016)
- Quintana, G., Ciurana, J.: Chatter in machining processes: a review. *Int. J. Mach. Tools Manuf.* **51**(5), 363–376 (2011)
- Shi, F., Cao, H., Li, D., Chen, X., et al.: Active chatter control in high speed milling processes based on  $H_\infty$  almost disturbance decoupling problem. *Procedia CIRP* **78**, 37–42 (2018)
- Tyler, C.T., Troutman, J., Schmitz, T.L.: Radial depth of cut stability lobe diagrams with process damping effects. *Precis. Eng.* **40**, 318–324 (2015)
- Wang, C., Zhang, X., Yan, R., et al.: Multi-harmonic spindle speed variation for milling chatter suppression and parameters optimization. *Precis. Eng.* **55**, 268–274 (2019)

# SHS Extrusion of a Composite Material Based on Aluminum-Magnesium Spinel



Andrey Chizhikov, Alexander Konstantinov, Pavel Bazhin,  
and Mikhail Antipov

## 1 Introduction

An urgent task for the modern scientific and technical complex is the development of new promising materials and products based on them. These materials include composites based on oxide ceramics. Oxide ceramic materials are widely used in various industries as cutting ceramics (Guo et al. 2018; Pronin et al. 2019; Stolin et al. 2018), refractory materials (Ren et al. 2021), protective coatings (Tang et al. 2021; Kozerzhets et al. 2021), as materials for fuel cells (Wang et al. 2022), etc. Among a wide range of oxide ceramic materials, materials based on magnesium aluminum spinel  $MgAl_2O_4$  can be singled out. These materials have a high melting point (2135 °C), high hardness, high chemical and corrosion resistance to acids and molten metals (Ganesh 2013; Shi et al. 2020). The described properties make materials based on aluminum-magnesium spinel promising for use in the chemical and metallurgical industries for the manufacture of protective covers for thermocouples, various crucibles and molds, and refractory linings (Meng et al. 2018; Ma et al. 2016).

The synthesis of materials based on  $MgAl_2O_4$  is complicated due to the fact that the formation of this compound occurs as a result of an endothermic reaction of magnesium and aluminum oxides and requires the use of high temperatures. There are also low-temperature methods for the synthesis of spinels, such as the sol–gel method (Wu et al. 2022) and hydrothermal synthesis (Panasyuk et al. 2019). However, these methods are complicated by the need to process acids, solutions, gels and the complexity of the equipment. The high melting point of  $MgAl_2O_4$  makes it difficult to obtain finished products from this material.

---

A. Chizhikov (✉) · A. Konstantinov · P. Bazhin · M. Antipov  
Merzhanov Institute of Structural Macrokinetics and Materials Science, Russian Academy of Sciences, Chernogolovka, Moscow, Russia  
e-mail: [chij@ism.ac.ru](mailto:chij@ism.ac.ru)

A promising approach to obtaining products from composite materials based on aluminum-magnesium spinel is a combination of self-propagating high-temperature synthesis (SHS) and shear plastic deformation (Bazhin et al. 2019). This combination is implemented in the SHS-extrusion method (Bazhin et al. 2015). The flow of SHS occurs due to the release of internal heat of the system during the chemical reaction between the components and is characterized by high process temperatures ( $> 1800$  °C). This makes it possible to carry out the synthesis of refractory compounds without the use of external heating sources. At the same time, since the synthesis products are in a heated state, this makes it possible to form finished products by shear plastic deformation.

The purpose of this work was the SHS extrusion of a ceramic composite material based on aluminum-magnesium spinel reinforced with titanium diboride particles, as well as the study of the effect of deformation rate on the structure of the resulting products.

## 2 Materials and Methods

Powders of boron oxide ( $\geq 99\%$ ,  $< 1 \mu\text{m}$ ), aluminum ( $\geq 99.5\%$ ,  $< 5 \mu\text{m}$ ), magnesium ( $\geq 99\%$ ,  $250\text{--}450 \mu\text{m}$ ) and titanium (98%,  $280 \mu\text{m}$ ) were used as initial reagents in this work. These powders were pre-dried at a temperature of  $50$  °C for 12 h, after which they were mixed in a ratio of  $2\text{B}_2\text{O}_3\text{:f-}2\text{Al-}3\text{Mg-}2\text{Ti}$  in a drum mill for 12 h. Next, cylindrical blanks weighing 25 g and a relative density of 0.65 were prepared from the obtained powder mixture by cold uniaxial pressing. The synthesis of materials was carried out in the SHS mode (Vidyuk et al. 2021; Shaikh et al. 2019; Bazhin et al. 2021). The SHS process occurred due to the reduction of boron oxide with aluminum and magnesium with the formation of the corresponding metal oxides. The reduced boron reacted with titanium to form titanium diboride. Since the formation of spinel occurs with the absorption of heat, the reactions listed above, which have a high thermal effect, create favorable conditions for the synthesis of spinel. To obtain products based on the synthesized material, the SHS-extrusion method was used, which combines the SHS process and high-temperature shear deformation.

Thermodynamic calculations were carried out using the ISMAN-Thermo software package developed to estimate the probable phase composition of the reaction products, their phase state, and the adiabatic combustion temperature of the system. An experimental study of the combustion temperature was carried out using tungsten-rhenium thermocouples in a setup that simulates the real conditions of SHS extrusion.

The phase composition was studied by X-ray phase analysis (XRD) on a DRON-3M diffractometer. The microstructure of the obtained materials was studied by scanning electron microscopy (SEM) using a Carl Zeiss LEO 1450 VP electron microscope. The results of energy dispersive analysis are given in mass percent.

### 3 Results and Discussion

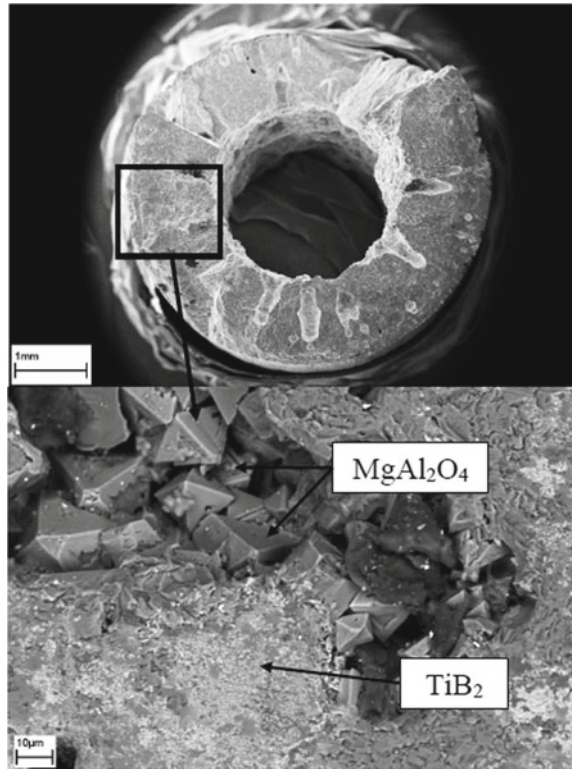
According to the results of thermodynamic calculations, the adiabatic combustion temperature of the system under study was 2827 °C. According to the results of an experimental study of the combustion characteristics of the system under study, the actual combustion temperature was 2027 °C. The strong discrepancy between the calculated and experimental results of determining the combustion temperature is explained by the high heat removal that occurs between the sample and the walls of the metal tooling despite the presence of asbestos insulation on the sample.

Since the combustion of the material during SHS occurs in a non-equilibrium mode, and also due to the error of the thermocouple measurement method, it can be assumed that the actual combustion temperature of the material exceeded the melting temperature of aluminum oxide (2072 °C). Also, the combustion temperature significantly exceeded the melting point of the initial components (the most refractory of them is titanium—1668 °C). Thus, in the course of synthesis, a liquid phase appears in the material, as a result of which a suspension is formed from liquid initial components, partially liquid synthesis products and solid particles of synthesis products. The formation of a suspension leads to the fact that the material acquires viscoelastic properties and the ability to plastically deform (Chizhikov et al. 2019). Due to the ability to high-temperature plastic deformation, this object of study is promising for the production of products by the SHS-extrusion method. To control the process of SHS extrusion, there are a number of technological parameters: delay time before applying pressure, strain rate, pressing pressure as well as design parameters of the forming matrix.

In the course of establishing the influence of technological and structural parameters on the SHS-extrusion process, ceramic hollow rods based on aluminum-magnesium spinel and titanium diboride up to 100 mm long and with an outer diameter of 5, 6 and 7 mm were obtained. Figure 1 shows a general view of the fracture of the obtained hollow rods.

One of the most important parameters affecting the SHS-extrusion process is the delay time. At low values of this parameter, chemical transformations and structure formation processes are not completed in the material, there is an excess amount of the liquid phase, since in this case, the synthesis proceeds with the formation of a sufficiently large amount of the liquid phase. At high values of this parameter, the material undergoes a complete crystallization process, as a result of which the material loses its ability to plastic deformation and extrusion. Thus, there is an optimal delay time interval in which the material has the ability to plastically deform, and also has a sufficient level of viscoelastic properties necessary for the formation of hollow rods. For this material, the optimal delay time was 4–5.5 s. Another key technological parameter affecting the SHS extrusion of ceramic refractory hollow rods is the strain rate. The “jet swelling” effect (Barus effect) (Lombardi and Tammaro 2021; Wang et al. 2018), which is the basis for the formation of ceramic hollow rods in this work, manifests itself at sufficiently high extrusion rates. In the course of the work, it was found that there is a threshold value of the strain rate, below which the formation

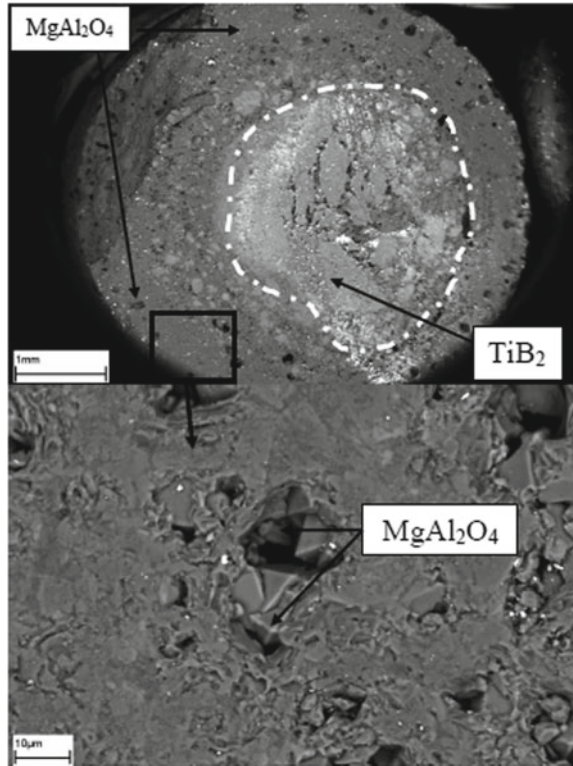
**Fig. 1** SEM results of the fracture of the resulting hollow rod



of ceramic hollow rods does not occur. Although the extrusion still occurs. For the studied model composition, such a threshold value was 65 mm/s. At a lower value of the strain rate, there is no accumulation of a sufficient amount of elastic deformation necessary for the occurrence of normal stresses at the exit from the forming hole, which stretch the material jet. In this case, extrusion occurs in a stationary mode. As a result, based on the studied composition, rods were obtained, which are a compact core, mainly consisting of titanium diboride, which is covered with a shell of aluminum-magnesium spinel with a thickness of less than 1 mm, Fig. 2.

In this case, there is also a limiting value of the rate of deformation of the press, above which extrusion does not occur. For the studied model composition, this value was 90 mm/s. Above this value, the viscosity of the material, which depends on the strain rate, increases so much that it completely prevents extrusion. Another important technical parameter is the molding pressure. It was found in the work that high molding pressure is not required to obtain ceramic hollow rods. There is a threshold value above which increasing the molding pressure has no effect on the length and quality of the resulting products. For the studied model composition, this value was 30 MPa. This is due to the fact that the viscosity of the studied materials depends more on the extrusion rate than on pressure. Structural parameters also have

**Fig. 2** SEM results of the section of the rod obtained at a strain rate below 65 mm/s



a great influence on the process of SHS extrusion. So, with a decrease in the angle of the conical part of the matrix, the contact area of the synthesized material with the matrix increases, while the magnitude of heat removal increases. As a result, the near-matrix regions rapidly lose their ability to undergo plastic deformation, and blockage of the exit hole of the matrix occurs. The optimal value of the angle of the conical part for the studied model composition is  $160^\circ$ .

It was shown that by changing the diameter of the exit section of the matrix, it is possible to obtain hollow rods with different inner diameters. In this case, the outlet of the matrix must necessarily be less than the diameter of the quartz caliber into which the extrusion is carried out. An important parameter is also the length of the forming channel of the matrix. With insufficient length during extrusion, there is no sufficient accumulation of elastic deformation, as a result of which tensile normal stresses do not arise, and hollow rods do not form. When the optimal value of the length of the forming belt is exceeded, the elastic deformation is relaxed directly in the forming channel, which also prevents the formation of ceramic hollow rods. It has been established that an increase in the outer diameter of the obtained ceramic hollow rods due to an increase in the diameter of the quartz caliber, the speed of the press plunger and the mass of the workpiece leads to a decrease in the size of

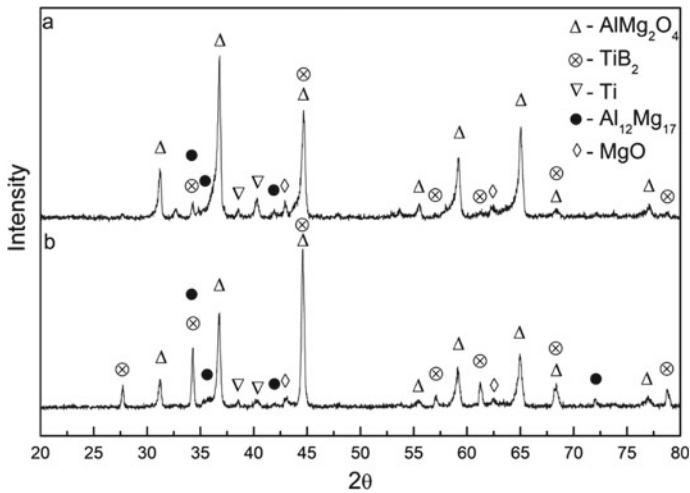


**Fig. 3** XRD results: **a** hollow rod and **b** rod obtained at a strain rate below 65 mm/s

the structural components. This is facilitated by an increase in heat removal that occurs when the material contacts the walls of the quartz caliber. According to the XRD results, the obtained ceramic hollow rods had a uniform distribution of the phase composition along the entire length. It is also shown that under the conditions of SHS and shear deformation of the studied model composition, the formation of aluminum and magnesium intermetallic compounds occurs, as well as the deformation of the crystal lattice of the aluminum-magnesium spinel. Thus, by adjusting the parameters of SHS extrusion, it is possible to influence the phase composition of the resulting products.

According to the SEM results, the resulting hollow rods had a composite structure. The basis of the rods was octahedral grains characteristic of spinel, 10–40  $\mu\text{m}$  in size. Cubic grains of titanium diboride were distributed over the entire volume of the obtained hollow rods and had a size of less than 1  $\mu\text{m}$ . The XRD results showed that the resulting rods mainly consist of two phases:  $\text{MgAl}_2\text{O}_4$  and  $\text{TiB}_2$ . At the same time, the products also contain traces of unreacted titanium, magnesium oxide, which did not react with  $\text{Al}_2\text{O}_3$ , and  $\text{Al}_{12}\text{Mg}_{17}$  intermetallic compound. The XRD results also showed that the resulting hollow, Fig. 3a, and compact rods, Fig. 3b, had a similar phase composition. At the same time, the intensity of the  $\text{TiB}_2$  peaks in the compact rod is higher due to its larger amount.

## 4 Summary

Ceramic rods based on the  $\text{MgAl}_2\text{O}_4$ - $\text{TiB}_2$  composite material with a length of more than 100 mm and an outer diameter of 5–7 mm were obtained by SHS extrusion.



Thermodynamic calculations of the adiabatic combustion temperature of the specified material were carried out, which amounted to 2827 °C. As a result of an experimental study of the combustion characteristics of this material, it was shown that the actual process temperature due to heat removal conditions is much lower than the adiabatic one and is 2027 °C. The influence of technological and design parameters on the extrusion process has been studied. It is shown that the strain rate has a significant effect on the process of extrusion of the specified material. This parameter has a threshold value, for the studied material it was 65 mm/s, above which hollow rods are formed during extrusion. When extruding at a speed below 65 mm/s, a compact rod is formed, which is a core based on TiB<sub>2</sub> in a shell of MgAl<sub>2</sub>O<sub>4</sub>.

**Acknowledgements** This work was supported by the Russian Science Foundation, project no. 20-73-00235.

## References

- Bazhin, P.M., Stolin, A.M., Alymov, M.I., Chizhikov, A.P.: *Inorg. Mater. Appl. Res.* **6**, 187 (2015)
- Bazhin, P.M., Kostitsyna, E.V., Stolin, A.M., Chizhikov, A.M., Bychkova, MYa., Pazniak, A.: *Ceram. Int.* **45**, 9297 (2019)
- Bazhin, P.M., Kostitsyna, E.V., Chizhikov, A.P., Konstantinov, A.S., Neganov, L.E., Stolin, A.M.: *J. Alloys Compd.* **856**, 157576 (2021)
- Chizhikov, A.P., Bazhin, P.M., Stolin, A.M., Alymov, M.I.: *Dokl. Chem.* **484**, 79 (2019)
- Ganesh, I.: *Int. Mater. Rev.* **58**, 63 (2013)
- Guo, X.L., Zhu, Z.L., Ekevad, M., Bao, X., Cao, P.X.: *Adv. Appl. Ceram.* **117**, 16 (2018)
- Kozerozhets, I.V., Panasyuk, G.P., Azarova, L.A., Belan, V.N., Semenov, E.A., Voroshilov, I.L., Danchevskaya, M.N.: *Theor. Found. Chem. Eng.* **55**, 1126 (2021)
- Lombardi, L., Tammaro, D.: *Phys. Fluids* **33**, 033104 (2021)
- Ma, B., Yin, Y., Zhu, Q., Zhai, Y., Li, Y., Li, G., Yu, J.: *Refract. Ind. Ceram.* **56**, 494 (2016)
- Meng, J.X., Chen, W.Q., Zhao, J.Z., Liu, L.: *High Temp. Mater. Process* **37**, 581 (2018)
- Panasyuk, G.P., Kozerozhets, I.V., Danchevskaya, M.N., Ivakin, Y.D., Murav'eva, G.P., Izotov, A.D.: *Dokl. Chem.* **487**, 218 (2019)
- Pronin, A.I., Myl'nikov, V.V., Rybalkin, A.A.: *Glass Ceram.* **76**, 99 (2019)
- Ren, X.M., Ma, B.Y., Wang, L.L., Liu, G.Q., Yu, J.K.: *Ceram. Int.* **47**, 31130 (2021)
- Shaikh, N., Patel, K., Pandian, S., Shah, M., Sircar, A.: *Arab. J. Geosci.* **12**, 11 (2019)
- Shi, Z.Q., Zhao, Q.L., Guo, B., Ji, T.Y., Wang, H.: *Mater. Des.* **193**, 108858 (2020)
- Stolin, A.M., Bazhin, P.M., Konstantinov, A.S., Chizhikov, A.P., Kostitsyna, E.V., Bychkova, M.Y.: *Ceram. Int.* **44**, 13815 (2018)
- Tang, S.W., Liu, P.F., Su, Z., Lei, Y., Liu, Q., Liu, D.S.: *High Temp. Mater. Process* **40**, 77 (2021)
- Vidyuk, T.M., Korchagin, M.A., Dudina, D.V., Bokhonov, B.B.: *Combust. Explos. Shock Waves* **57**, 385 (2021)
- Wang, J.N., Wang, T., Xu, J., Yu, J.C., Zhang, Y.M., Wang, H.P.: *J. Appl. Polym. Sci.* **135**, 8 (2018)
- Wang, H., Lei, Z., Zhang, H., Li, Y., Jing, J., Jin, Y., Yang, Z., Peng, S.: *J. Electrochem. Energy Convers. Storage* **19**, 011007 (2022)
- Wu, Q., Feng, G., Jiang, F., Miao, L., Jiang, W., Liang, J., Liu, J., Tan, J., Zhang, X., Lao, X.: *Ceram. Int.* **48**, 3351 (2022)

# **Fluid Mechanical Engineering and Engineering Thermodynamics**

# Visual Observation of the Vortex Flow from the Same Diameter Circular Cylinders Which Sandwiched a Partition Disk



Yoshifumi Yokoi 

## 1 Introduction

In the experiment of the flow from two dimensional bluff cylinders, such as a circular cylinder, it is carried out by providing an end plate in order to maintain two dimensional conditions at the cylinder edge. In the end plate, in a leading edge, the flow is divided and the separated flow is unified in a trailing edge. It is imagined that the unified flow becomes complicated flow structure. Nevertheless, influence condition of the structure of the complicated flow is not made into the object of interest. So, there is no consideration about the size and shape of the end plate. The knowledge about the influence of the size of the end plate to the size of the bluff cylinder is hardly found. Although the size of the end plate is enough enlarged compared with the projection width of the bluff cylinder, the concrete reason is not shown. Szepessy and Bearman (1992) and Norberg (1994) have reported influence of as opposed to the flow and the vortex shedding in the space and the end plate itself which the end plate makes. The study on the influence of the size of the end plate is seen by a Hara and Suzuki (1989, 1991), Yamada (1992). Those study investigates about the influence of the size of the end plate exerted on the cylinder base pressure and vortex shedding in the test section inserted into the end plate. Even if it provides an end plate and prepares the flow of the inspection section, it does not have the meaning of rectification, if the turbulence element which generated interference by the wake is fed back. It is required to solve the mechanism which the turbulence element feeds back, and an aspect in engineering. Yokoi (2019) divided into the circular cylinder span central part, prepared the plate, varied the size (the length of a partition plate) of the partition section, and investigated influence on the aspect of a flow by visualization experiment. And the following results are reported. The Karman vortex street from which a phase differs on the front side and the back side of the partition plate

---

Y. Yokoi (✉)

National Defense Academy of Japan, 1-10-20 Hashirimizu, Yokosuka, Kanagawa, Japan  
e-mail: [yokoi@nda.ac.jp](mailto:yokoi@nda.ac.jp)

may be formed. Two flows which pass over the partition plate and join are forming a complicated flow field. Transfer of the information on the turbulence is dependent on the size of the partition plate. In order to verify the universality of the obtained matter, it is important to carry out by changing experiment environment (e.g., an apparatus, a method, and an observation viewpoint). Therefore, in this study, the size of a partition disk was varied and visualization observation was carried out for the flow around a circular cylinder with a partition disk using the closed circuit water channel apparatus.

## 2 Experimental Apparatus and Method

### 2.1 Outline of Experimental Apparatus

Experimental apparatus consists of the closed circuit water channel apparatus, a circular cylinder with partition disk, a visualization apparatus, and a video recording apparatus. The overall experimental apparatus is shown in Fig. 1. The experiment situation in the test section of the closed circuit water channel apparatus is shown in Fig. 2. The closed circuit water channel apparatus is a small closed circuit water channel with a water volume of  $0.4 \text{ m}^3$ , a test section is a product made from transparent acrylics, the cross-sectional size is  $0.3 \text{ m} \times 0.3 \text{ m}$ , and the length is 1.2 m. The upper part of the test section is opened wide, and the plate for circular cylinder attachment is prepared in the part. The mirror leaned under the test section bottom is prepared, a camera is placed by the side, and the aspect of the flow seen from the circular cylinder axis is photographed. The range of the flow velocity in the test section is 0.07–0.98 m/s, and adjustment of the flow velocity is carried out by operating an operation controller (digital operator). The water level of the test section at the time of the experiment was adjusted to 0.2 m.

The circular cylinder with a partition disk consists of two circular cylinders of the same diameter, and one disk. The circular cylinder is metal, and three kinds of diameters of 10, 16, and 20 mm were prepared. The circular cylinder with a diameter of 10 mm is a product made from brass, and the circular cylinder with a diameter of 16 mm and a diameter of 20 mm is a product made from aluminum. The thickness of the disk is a product made from transparent acrylics in 2 mm. The disk does not have cutting off the corners, and the attachment hole ( $\varphi 4 \text{ mm}$ ) is provided in the center of the disk. Twelve disks with which diameters differ are prepared. As for the structure of the circular cylinder with a partition disk, the disk with a thickness of 2 mm is put between the circular cylinder with a length of 199 mm and the circular cylinder with a length of 99 mm so that full length may be set to 300 mm. The circular cylinder with a partition disk is set in the plate for circular cylinder attachment prepared in the test section upper part of the small closed circuit water channel. When it does so, the partition disk will be located in a place with a depth of 100 mm at the time of the test.

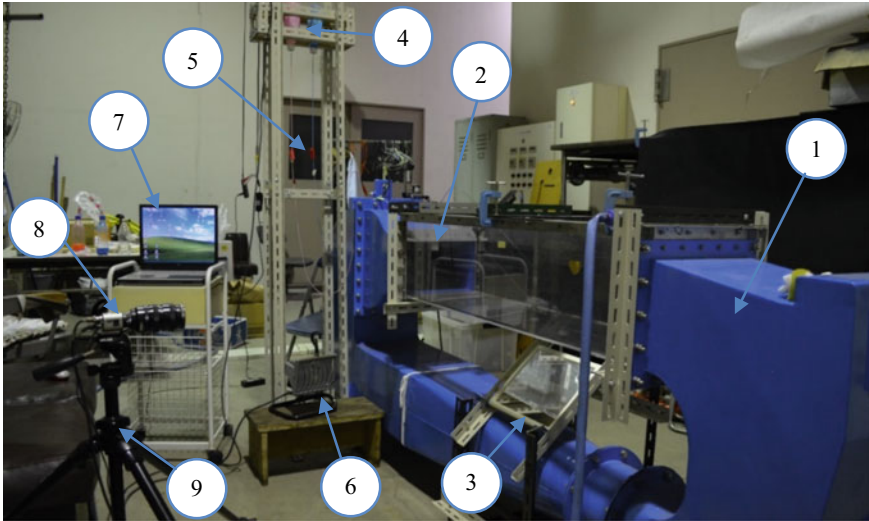


**Fig. 1** Photograph of the overall experimental apparatus: **1** closed circuit water channel apparatus, **2** test section, **3** mirrors, **4** tracer tank, **5** the amount adjustment clamp of tracers, **6** halogen lamp, **7** personal computer, **8** CCD video camera, and **9** tripod mounts

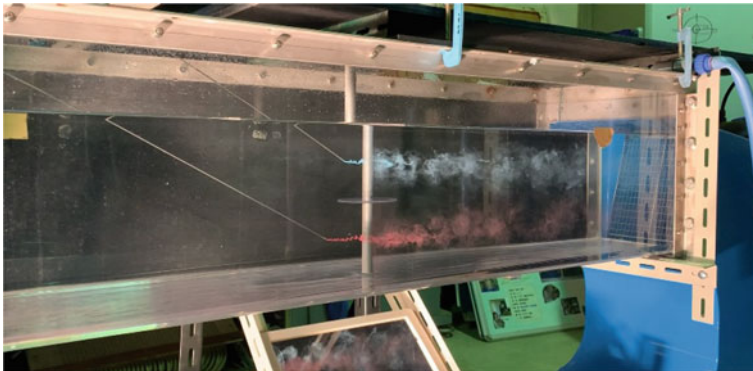


**Fig. 2** Experiment situation in the test section: the flow is flowing into the right from the left. Two tracer introduction small tubes are aslant inserted from the upstream side at the flow

The visualization apparatus consists of a tracer ink introduction apparatus and the halogen light (one piece) of 500 W. As the tracer ink, the poster color (the product made by TURNER; red, blue) by which specific gravity adjustment was carried out was used. Introduction to the flow field of tracer ink was carried out for the purpose of the circular cylinder upstream side stagnation point using the stainless steel tube of 1.5 mm of outer diameters. The introductory depth of water of the tracer was made into the position (the depth of water of 150 mm and position of 50 mm) distant about

50 mm, respectively, from the partition plate. The video recording apparatus is a digital camcorder (WAT-250D2, product made by Watec), and a personal computer (LaVie PC-LL990FD by NEC Corp.). The digital camcorder (it is hereafter called a video camera) is equipped with the zoom lens. Between the video camera and the personal computer, the signal converter (USB conversion unit AX-200, made in Carrots Systems) is prepared, and the picture signal from a video camera can be taken now into a direct personal computer. Here, since photography of an aspect that it saw from the circular cylinder axis through the mirror set in the lower part of the test section is carried out, in this side, with the image, the bottom and depths side becomes the water surface side. The video camera is being fixed with the tripod mount so that the photography position may not change for every photography time.

## 2.2 *Experimental Procedure*

Water is filled so that it may become a closed circuit water channel with the depth of water of 0.2 m in predetermined amount of water and a predetermined test section. Preparation operation is carried out at this time and fine-tuning of depth of water is also carried out. Secondly, the diameter of the circular cylinder and the size of the partition disk are selected, and the circular cylinder with a partition disk is assembled. The circular cylinder with a partition disk is set in the attachment plate. In the section of the circular cylinder which sandwiched the partition disk, the tracer ink introduction small tube is set in the upstream side of the stagnation point of the circular cylinder. The test flow velocity operates and sets up the inverter for the flow velocity setup. Two kinds of tracer ink in which colors differ is poured in into the flow after adjustment of the test flow velocity, and flow visualization is carried out. The aspect of the visualized flow takes a photograph with the video camera and takes the image into the personal computer. If the photography is completed, the aspect of the flow will be similarly observed about another partition disk and another flow velocity. And also in order to make it legible in the case of observation, it illuminated using the halogen light.

## 2.3 *Experimental Parameters*

The main experiment parameters are the circular cylinder diameter  $d$  (10, 16, and 20 mm), the diameter  $D$  of the partition disk, and the main flow velocity  $U$ . The diameters of the partition disk are 24, 32, 40, 48, 56, 64, 72, 80, 88, 96, 160, and 240 mm. If diameter ratio  $D/d$  formed into the-less dimension for the cylinder diameter is used, the applicability of diameter ratio  $D/d$  will be set to 1.5–240. Moreover, in order to compare, the state where the partition disk was not used was also carried out. In this case, diameter ratio  $D/d$  is set to 1.0. The main flow velocity wrote the inverter input frequency of the digital operator for operation with 2, 3, and 4 Hz, and

became 0.065, 0.098, and 0.131 m/s. The range of Reynolds number  $Re (= Ud/\nu, \nu$  is the kinematic viscosity of water) corresponding to each flow velocity was  $Re = 660$  to  $Re = 2630$ .

### 3 Experimental Results and Discussion

The experiment was performed from confirming the repeatability of the experimental result described by previous report (Yokoi 2019). Figure 3 shows the aspect of the flow carried out in the state without the partition disk (Fig. 3a), and the state using the partition disk (diameter of 240 mm) of the maximum size (Fig. 3b), respectively. The main flow velocity at this time was 0.098 m/s. It is shown by Fig. 3a that the red tracer streak line and the blue tracer streak line have overlapped. Roll up of those vortices can be seen synchronize. On the other hand, in Fig. 3b, the tracer streak line of two colors can be recognized clearly. There, it is shown that the timing of the vortex shedding from the circular cylinder set to each section differs. It seems that the 90-degree phase gap has occurred in the vortex shedding. There is nothing that is interrupted over the spanwise of the circular cylinder, when there is no partition. Therefore, the information on roll up of the vortex and the information on the timing of separation propagate to the spanwise. As a result, the vortex shedding constitutes the same phase. If the partition is provided, the information transmitted to the spanwise will be interrupted there. Therefore, the vortex is discharged independently in each section. If it thinks such, it will be easy to understand that a phase gap occurs. Figure 4 shows the aspect of the flow in each section when changing the main flow velocity. Here, the diameter of a partition disk is 240 mm and the largest disk is used. The main flow velocity is  $U = 0.065$  m/s in Fig. 4a and is  $U = 0.131$  m/s in Fig. 4b. It is shown that 90-degree phase difference has occurred in both of the figures in the vortex shedding which sandwiched the partition disk. The phase gap is because the communication of information of the spanwise is intercepted physically, and it was shown that it is not dependent on the flow velocity.

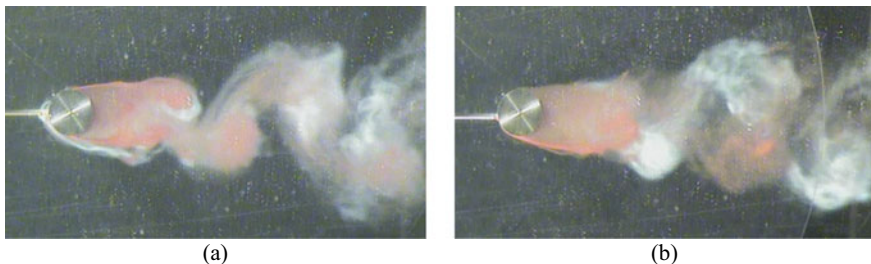


**Fig. 3** Comparison of the flow pattern by the existence of a partition disk,  $U = 0.098$  m/s, **a** without disk, **b** with disk,  $D/d = 15$

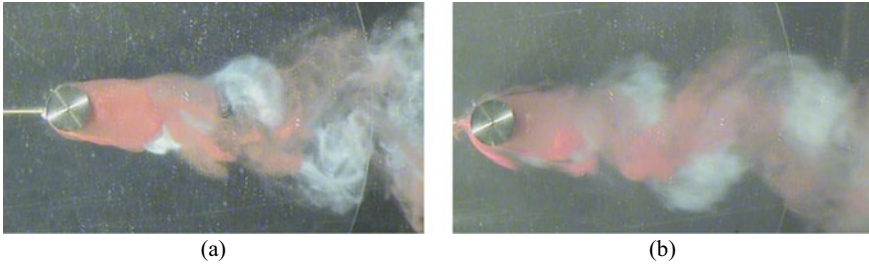


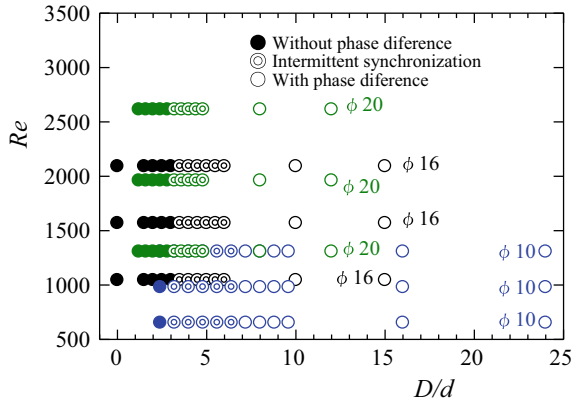
**Fig. 4** Comparison of the flow pattern according to the variation of main flow velocity at the diameter ratio  $D/d = 15$ , **a**  $U = 0.065$  m/s, **b**  $U = 0.131$  m/s

It is one of the most interesting matters of this study to investigate the influence which the size of the partition disk has on roll up of the vortex or the phase difference at the time of the vortex shedding. Figure 5 shows the result of having observed the existence of the phase difference in the both sides when varying the size of the partition disk. An abscissa is diameter ratio  $D/d$  and an ordinate is Reynolds number ( $Re = Ud/\nu$ ). Here, the diameter ratio  $D/d$  is defined by the ratio of the partition disk diameter and the circular cylinder diameter. In the figure, when ● mark does not have phase difference and ⊙ mark has phase difference, ⊙ mark shows the state where these two states were changed intermittently. And  $\varphi_{10}$ ,  $\varphi_{16}$ , and  $\varphi_{20}$  which are written in the figure are the circular cylinder diameter, and they show the result when varying the flow velocity (Reynolds number). In the figure, when diameter ratio  $D/d$  is 7 or more, phase difference occurs, and when diameter ratio  $D/d$  is three or less, it is shown that there is no phase difference. And it can grasp that the existence of phase difference is the same distribution, without being dependent on Reynolds number. Thus, it is found that depend for the partition effect by the disk on the size, and it is not dependent on the flow velocity. Yokoi and Kamemoto (1993) have described that the characterization of the vortex formation is carried out when have been rolled by the separating shear layer, and turbulence is supplied by the recirculating flow near the separation position. When the outer end of a partition disk is in the upstream side rather than the position rolled by the first vortex, relation of the spanwise of the recirculating flow cannot be intercepted. Since the information on the turbulence is transmitted near the separation position, the vortex shedding in the both sides of the partition disk is considered to become the same phase.

It is important to grasp the position in which the separating shear layer rolls around and the vortex is formed at the beginning. Taneda (1972) has described that the maximal domain of the twins vortex formation produced behind the circular cylinder is about  $3d$  from behind the circular cylinder in the case where the circular cylinder leaves suddenly, and is about  $2.5d$  from behind the circular cylinder in the case where the circular cylinder carries out uniform acceleration. If they are converted into diameter ratio  $D/d$  used by this study,  $3d$  behind circular cylinder will be diameter ratio  $D/d = 7$ , and  $2.5d$  behind circular cylinder will be diameter ratio  $D/d = 6$ . Nishioka (1992) described that the position where the isolated vortex which



**Fig. 5** Distribution of phase difference generating



constitutes the vortex street is produced is  $3d$  in position from the circular cylinder center. It is  $D/d = 6$  when expressed with the diameter ratio. In the visualization experiment which Yokoi and Hirao (2008) performed, the observation points of vortex shedding frequency were the position of  $2.5d$  circular cylinder behind, and the position of  $5.5d$  circular cylinder behind. They are  $D/d = 6$  and  $D/d = 12$  when those positions are expressed with the diameter ratio. It became clear that are the vortex shedding without phase difference from the result in these references and the experimental result at the time of the diameter ratio  $D/d < 3$ , and the partition disk is not working.

When the diameter ratio  $D/d$  exceeds 3, probably because the partition disk affects the exchange of the information on turbulence, phase difference occurs intermittently in roll up of the vortex. When the circular cylinder is seen from an axis, each Karman vortex seen in two sections divided with the partition disk will overlap or shift. Figure 6 shows the intermittent existence of the phase difference as an example. Here, the diameter ratio is  $D/d = 4.5$  and Reynolds number is  $Re = 1570$ . Figure 6a shows the case of the same phase. Red tracer ink overlaps with blue tracer ink, and seems to be one Karman vortex. On the other hand, Fig. 6b shows the case where there is phase difference. Red tracer ink and blue tracer ink show each Karman vortex. Probably, it will be difficult to recognize it as the Karman vortex, if a color exception is not carried out. Although it is very interesting to get to know the characteristic of both phase difference, it is very difficult to carry out in the visualization experiment. So, it is expected that details will be clarified by carrying out comparison examination of the waveform obtained by the point measurement using a hot wire anemometer, for example with wind tunnel equipment. When there is a position where the first vortex is formed inside the partition disk, the exchange of each other information is intercepted on the both sides of the partition disk. Therefore, vortex street formation which became independent each other will be carried out. However, since the flow which passed over the partition disk joining and inducing turbulence not a little is foreseen, the size in which the partition disk had a margin is needed. In this study, since the size is not clarified, the elucidation is expected from future study. It seems

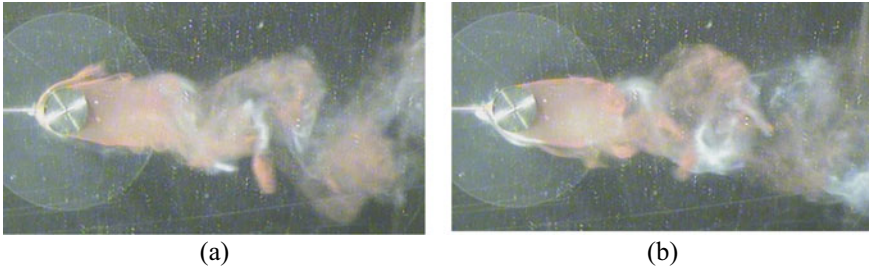


**Fig. 6** Appearance of intermittent phase difference,  $U = 0.098$  m/s,  $D/d = 4.5$ , **a** same phase, **b** different phase

that it is hard to receive the influence of unification of the flow produced after passing the partition disk when the partition disk is large enough. Therefore, the Karman vortex from which the phase differs on the both sides of the partition disk as shown in Fig. 1b will be formed. Thus, in order not to receive the mutual interference but to obtain the independent Karman vortex, 7 or more diameter ratio  $D/d$  is needed.

## 4 Conclusions

In the closed circuit water channel experiment, the visualization experiment which provides the partition disk and controls transfer of turbulence of the circular cylinder spanwise was performed. The following conclusions were obtained.

- (1) It was confirmed also with another apparatus that the Karman vortex street from which the phase differs on the both sides of the partition disk may be formed.
- (2) When the diameter ratio  $D/d$  is 3 or less, there is no effect as the partition disk.
- (3) As for the size of a partition disk, it is desirable that it is larger than the position in which the first vortex is formed, and it needs more than diameter ratio  $D/d = 7$  to obtain the Karman vortex which did not receive the mutual interference but became independent.
- (4) The matters of the conclusion (2) and (3) were able to be seen not depend on Reynolds number in this experiment range.

## References

- Hara, S., Suzuki, T.: Effects of end-plate dimensions on hydrodynamic forces on circular cylinders oscillating sinusoidally in water. *Trans. Jpn. Soc. Mech. Eng.* **55**(513), 1368–1371 (1989)
- Hara, S., Suzuki, T.: Effects of end-plate dimensions on hydrodynamic forces on square cylinder oscillating sinusoidally in water. *Trans. Jpn. Soc. Mech. Eng.* **57**(533), 14–17 (1991)

- Nishioka, M.: On the formation process of Karman vortex street. In: Special Publication of National Aerospace Laboratory, SP vol. 18, pp. 41–45 (1992)
- Norberg, C.: An experimental investigation of the flow around a circular cylinder: influence of aspect ratio. *J. Fluid Mech.* **258**, 287–316 (1994)
- Szepessy, S., Bearman, P.W.: Aspect ratio and end plate effects on vortex shedding from a circular cylinder. *J. Fluid Mech.* **234**, 191–217 (1992)
- Taneda, S.: Observation on unsteady separated vortices. *Trans. Jpn. Soc. Aeronaut. Space Sci.* **20**(226), 600–610 (1972)
- Yamada, H.: Effect of end plates on spanwise characteristics of flow around a circular cylinder. *Trans. Jpn. Soc. Mech. Eng.* **58**(552), 2368–2373 (1992)
- Yokoi, Y.: Visual observation of the vortex flow structure from a circular cylinder with a partition plate. Fedconf19, Prepr. of Jpn. Soc. Mech. Eng., pp. OS3–03–1–OS3–03–4. Toyohashi (2019)
- Yokoi, Y., Hirao, K.: Vortex flow around an in-line forced oscillating circular cylinder. *Trans. Jpn. Soc. Mech. Eng.* **74**(746), 2099–2108 (2008)
- Yokoi, Y., Kamemoto, K.: Initial stage of a three-dimensional vortex structure existing in a two-dimensional boundary layer separation flow (visual observation of laminar boundary layer separation over a circular cylinder from the side of a separated region). *JSME Int. J., Ser. B* **36**(2), 201–206 (1993)

# Experimental Study of the Porous Emitter Installed in a Gas Porous Burner



Panuwat Chanmak, Wapee Sripunya, and Bundit Krittacom

## Nomenclature

|               |   |
|---------------|---|
| $d_{PA}$      | Diameter of the porous absorber, cm                 |
| $d_{PE}$      | Diameter of the porous emitter, cm                  |
| HE            | Heat exchanger                                      |
| $H_{PE}$      | Thickness of porous emitter, cm                     |
| LPG           | Liquefied petroleum gas                             |
| PA            | Porous absorber                                     |
| PE            | Porous emitter                                      |
| $Q_w$         | Water flow rate fed into heat exchanger, L/min      |
| $T$           | Temperature profile of porous burner, °C            |
| $V_{mix}$     | Volumetric premixed-gas velocity, m <sup>3</sup> /h |
| $X$           | Burner length, cm                                   |
| $\varepsilon$ | Effectiveness of the heat exchanger                 |
| $\phi$        | Porosity  |
| $\Phi$        | Equivalent ratio                                    |

---

P. Chanmak · W. Sripunya · B. Krittacom (✉)

Development in Technology of Porous Materials Research Laboratory (DiTo-Lab), Department of Mechanical Engineering, Faculty of Engineering and Architecture, Rajamangala University of Technology Isan, Nakhonratchasima, Thailand  
e-mail: [bundit.kr@rmuti.ac.th](mailto:bundit.kr@rmuti.ac.th)

P. Chanmak

Department of Mechanical Engineering, Faculty of Industrial Education, Rajamangala University of Technology Suvarnabhumi, Nonthaburi, Thailand

## 1 Introduction

The benefit of the porous emitters (PE) is to absorb energy and generate higher heat radiation. This is the reason why many engineers and researchers have been encouraged to conduct numerical studies and experimental investigations of porous emitters (PE) for the development of thermal efficiency (Vafai 2000; Jugjai et al. 2002; Jugjai and Polmart 2003; Thongtem and Jugjai 2008; Chuenchit and Jugjai 2012; Lekpradit and Krittacom 2013; Krittacom et al. 2011; Pranpanya and Krittacom 2016; Kaewchart and Krittacom 2017). If the two porous materials are separated from each other (see in Fig. 1) (Krittacom 2009), higher heat radiation between the porous absorber (PA) and the porous emitter (PE) is obtained. From the advantages of the porous emitter (PE), many applications of heating work are widely used (Jugjai et al. 2003; Jugjai and Phothiya 2006, 2007; Krittacom and Amatachaya 2011).

According to where the flame was located, the gas porous burner was often divided into two categories (Krittacom and Kamiuto 2009). The first type was the stabilized flame inside the porous matrix or embedded flame with high porosity ( $\phi$ ) of 0.5–0.99. The second one was the surface flame (spread flame) where the porosity ( $\phi$ ) of porous burner became below 0.5. In the last five years, the application of a low porosity case of the porous burner played a role as PA without PE was experimentally studied by our previous works (Sripunya et al. 2016; Amatachaya and Krittacom 2017). The heat exchanger of staggered tube banks was installed below the porous burners (PB) or the porous absorber (PA). Water was used as the working fluid and liquefied petroleum gas (LPG) was adopted as fuel. The porous media packed as a porous matrix was made of an alumina-cordierite ball (Al-Co). Noticeably, the results of our experiment confirmed that the temperature ( $T$ ) at the exhaust gas outlet zone was existed high (over 420 °C). From this behavior, the high temperature at the exit zone should be not ignored. Thus, to improve the combustion mechanism and thermal efficiency of the heat exchanger, heat recirculation from such temperature was needed. The PE was one of the choices to solve this point.

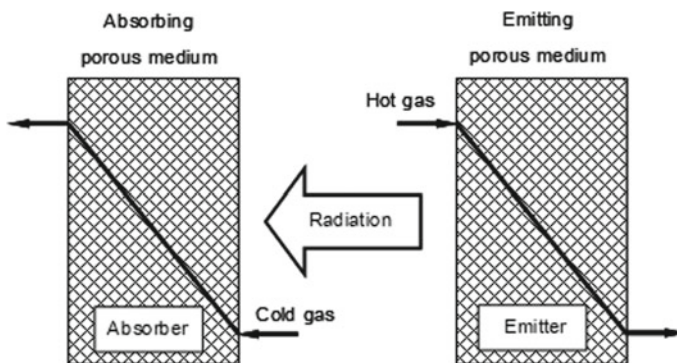


**Fig. 1** Property of porous absorber (PA) and porous emitter (PE) (Krittacom 2009)

From the advantage of the porous emitter (PE) on the gas porous burner, the PE was incorporated with the PA in the present work. The PE was installed at the outlet zone of exhaust gas below the tube-bank heat exchanger. Similar to earlier experiments (Sripunya et al. 2016; Amatachaya and Krittacom 2017), the operating fluid in cold-line and fuel continued to be water and liquefied petroleum gas (LPG). To propose the performance of the present application and the combustion mechanism from the influence of PE, the temperature distribution along the porous burner ( $T$ ) and the heat exchanger-effectiveness ( $\varepsilon$ ) were explained.

## 2 Experimental Apparatus

Figure 2 presents the schematic diagram of the porous emitter installed in a gas porous burner. The experimental equipment consisted of eight sections, i.e., the LPG and air mixture, the injection chamber, the porous absorber (PA), the combustion zone and the heat exchanger of staggered tube-bank (HE), the porous emitter (PE), the exhaust gas outlet, the working-fluid system, and the measurement equipment. The premixed gas (air and LPG) was a mixture and flow into the injection chamber. The porous absorber (PA) and the porous emitter (PE) were made of an alumina-cordierite ball (Al-Co) with a mean diameter of 0.5 cm and a porosity ( $\phi$ ) of 0.413. The 19 mm outside diameter and 1 mm thickness of the SUS 304-stainless tube were modified to form 15 tubes for a staggered tube-bank heat exchanger. Pitch measurements for the transverse (ST), longitudinal (SL), and diagonal (SD) directions were 35 mm, 35 mm, and 39 mm, respectively. The working fluid of the heat exchanger was water at a continual temperature of  $29 \pm 1$  °C. The PE was installed at the outlet zone of exhaust gas. In the present study, alumina-cordierite (Al-Co) was also employed as the examined PE with three different thicknesses ( $H_{PE}$ ): 2.5, 5, and 10 cm.

To understand the present work, the experimental procedure was described as follows in this paragraph. In the beginning, the premixed-gas mixture (air and LPG) was supplied into the injection chamber. The mixture flowed through the porous absorber as a preheating process and, then, burned at the exit of the porous surface. The absorption of energy from high temperatures occurred in the PA and the PE. The heat transfer process between the working fluid (water) and the high temperature of flame was obtained at the combustion zone and HE. Twenty N-type thermocouples were attached along the length of the testing apparatus (PA, HE, and PE) to monitor the profile of temperature ( $T$ ). The inlet and outlet temperatures of the water ( $T_{c, in}$  and  $T_{c, out}$ ) were also monitored by the N-type thermocouples.

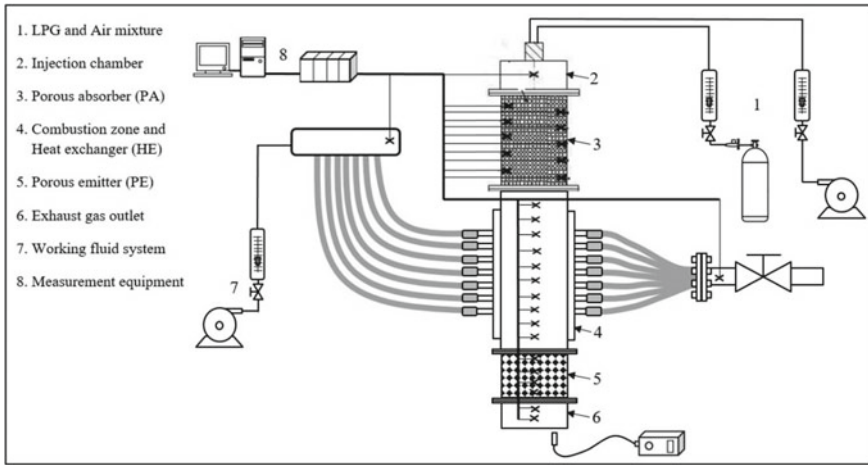


Fig. 2 Schematic diagram of the porous emitter installed in a gas porous burner

### 3 Results and Discussion

#### 3.1 Influence of Thickness of Porous Emitter ( $H_{PE}$ )

The influence of the thickness of porous emitter ( $H_{PE}$ ) on temperature distribution ( $T$ ) in the length of the experimental burner is presented in Fig. 3. The testing conditions included a volumetric premixed-gas velocity ( $V_{mix}$ ) of  $30 \text{ m}^3/\text{h}$ , a diameter of the porous emitter ( $d_{PE}$ ) of  $0.5 \text{ cm}$  having appeared porosity ( $\phi$ ) of  $0.413$ , an equivalent ratio ( $\Phi$ ) of  $0.8$ , and a water flow rate fed into the HE ( $Q_w$ ) of  $30 \text{ L}/\text{min}$ . As the  $H_{PE}$  rose, it was discovered that the status of  $T$  increased because a higher thickness of porous emitter can raise the energy absorption (Krittacom and Amatachaya 2011; Krittacom and Kamiuto 2009; Peamsuwan and Krittacom 2014; Krittacom and Tongbai 2018).

Figure 4 demonstrates the influence of PE thickness ( $H_{PE}$ ) on the effectiveness ( $\varepsilon$ ) with the same experimental conditions as shown in Fig. 3. According to the findings, which can be seen in Fig. 4, the value of  $\varepsilon$  marginally rose as greater  $H_{PE}$  was attained as a result of the little ability in energy absorption between the working fluid (water) of a heat exchanger and the high temperature of the flame (Krittacom and Kamiuto 2009).

#### 3.2 Influence of Volumetric Premixed-Gas Flow Rate ( $V_{mix}$ )

Figure 5 depicts the impact of the volumetric premixed-gas velocity ( $V_{mix}$ ) on the temperature profile ( $T$ ) along the experimental length. The experiment was conducted

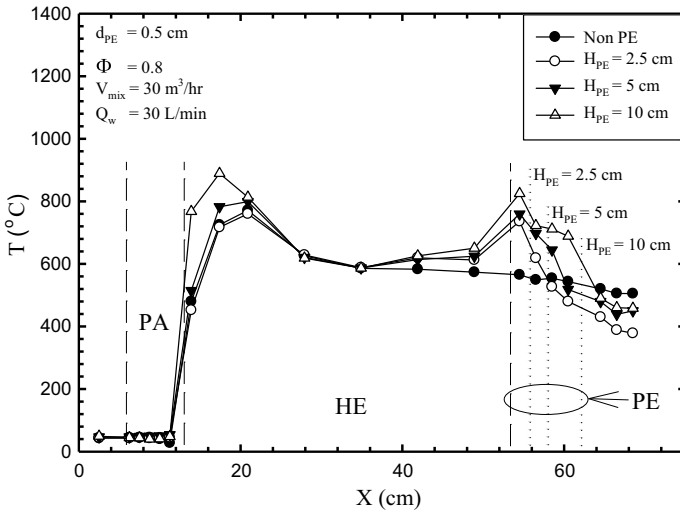


Fig. 3 Influence of  $H_{PE}$  on  $T$

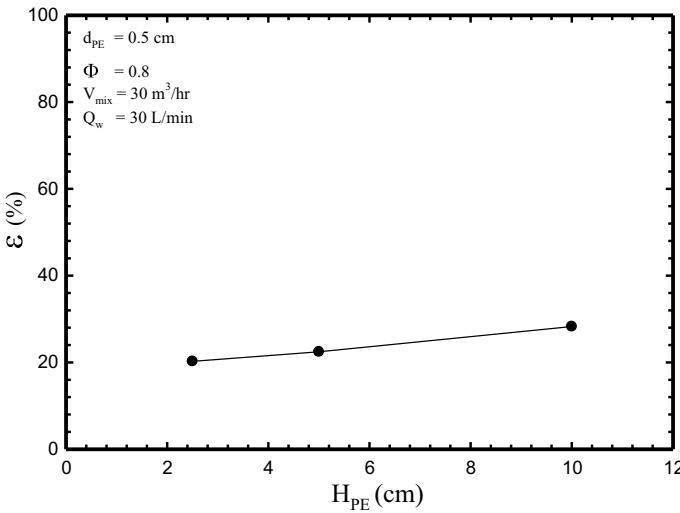


Fig. 4 Influence of  $H_{PE}$  on  $\epsilon$

in this situation: a PE thickness ( $H_{PE}$ ) of 10 cm, a diameter of the porous emitter ( $d_{PE}$ ) of 0.5 cm having appeared porosity ( $\phi$ ) of 0.413, an equivalent ratio ( $\Phi$ ) of 0.8, and a water flow rate fed into the HE ( $Q_w$ ) of 30 L/min. The results showed that the trend of  $T$  was explicitly enhanced with increasing  $V_{mix}$ , as shown in Fig. 5. When the fuel was initially introduced to the system, more potent combustion should have emerged, followed by an increase in  $T$  (Glassman 1996).



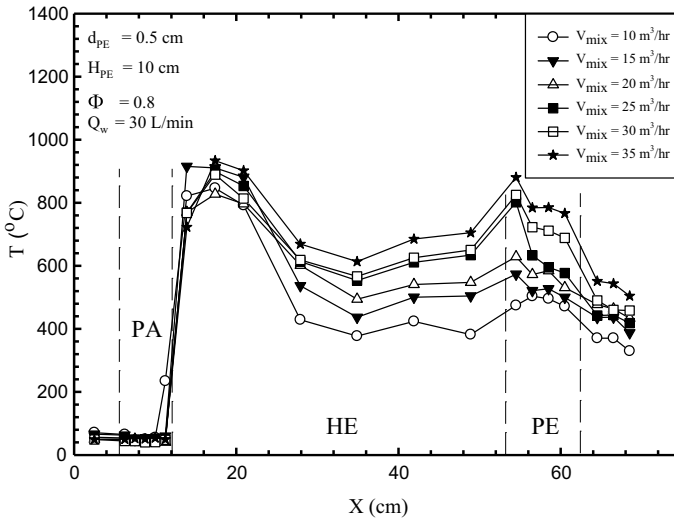


Fig. 5 Influence of  $V_{\text{mix}}$  on  $T$

In relation to Figs. 5, 6 illustrates how volumetric premixed-gas velocity ( $V_{\text{mix}}$ ) affects the effectiveness ( $\varepsilon$ ). The experiment's setting was comparable to Fig. 5. The experiment revealed the following: the value of  $\varepsilon$  was decreased as increasing  $V_{\text{mix}}$  because the system had an increased amount of hot gas. This was further explained by an effectiveness equation of the difference on the staggered tube-bank heat exchanger (Sripunya and Krittacom 2021). Moreover, the value of  $\varepsilon$  explicitly increased with installed the PE as compared in Fig. 6. This finding was the fact phenomena resulted from the benefit of PE (Jugjai et al. 2002; Lekpradit and Krittacom 2013; Jugjai and Phothisya 2007; Krittacom and Amatachaya 2011).

## 4 Conclusion

The research investigation of the porous emitter (PE) installed in a gas porous burner with LPG as fuel and the heat exchanger of staggered tube-bank with the water as working fluid was performed. The combustion phenomena, i.e., the profile of temperature on a burner length ( $T$ ) and the HE effectiveness ( $\varepsilon$ ) were investigated. In the present study, alumina-cordierite (Al-Co) was employed as the examined porous emitter with different thicknesses ( $H_{\text{PE}}$ ). The  $T$  tended to increase with the  $H_{\text{PE}}$  and the  $V_{\text{mix}}$ . The quantity of  $\varepsilon$  was decreased as increasing  $V_{\text{mix}}$  but increased slightly as increasing  $H_{\text{PE}}$ . Moreover, the value of  $\varepsilon$  explicitly increased with the installation of the PE.

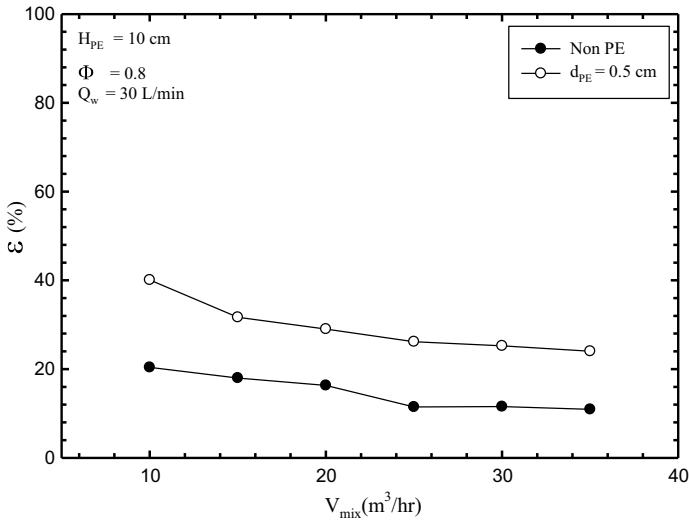


Fig. 6 Influence of  $V_{mix}$  on  $\epsilon$

## References

Amatachaya, P., Krittacom, B.: Combustion mechanism of gas porous burner installed an in-line tube-bank heat exchanger. *Energy Procedia* **138**, 50–55 (2017)

Chuenchit, C., Jugjai, S.: Effect of tube length on combustion characteristics of a self-aspirating radiant tube burner (SRTB). *J. Res. Appl. Mech. Eng.* **1**(2), 19–23 (2012)

Glassman, I.: *Combustion*, 3rd edn. Academic Press (1996)

Jugjai, S., Polmart, N.: Enhancement of evaporation and combustion of liquid fuels through porous media. *Exp. Thermal Fluid Sci.* **27**(8), 901–909 (2003)

Jugjai, S., Wongpanit, N., Laoketkan, T., Nokkaew, S.: The combustion of liquid fuels using a porous medium. *Exp. Thermal Fluid Sci.* **26**(1), 15–23 (2002)

Jugjai, S., Phothiya, C.: Cyclic flow reversal combustion (CFRC) of liquid fuel within porous medium. In: *The 20th Conference of the Mechanical Engineering Network Thailand (18–20 October 2006)* (in Thai)

Jugjai, S., Phothiya, C.: Liquid fuels-fire porous combustor-heater. *Fuel* **86**(7–8), 1062–1068 (2007)

Jugjai, S., Chuwisit, K., Chalermponchai, K., Iampai, N.: Potential for porous-medium combustion technology as applied to liquid fuel without spray atomization. In: *The 17th Conference of the Mechanical Engineering Network Thailand (15–17 October 2003)* (in Thai)

Kaewchart, K., Krittacom, B.: Comparison of combustion behavior between solid porous burners installed the porous emitter and non-porous emitter. *Energy Procedia* **138**, 2–7 (2017)

Krittacom, B.: *Studies on thermal characteristics of open-cellular porous burners*. Doctor Engineering Dissertation, Oita University (2009)

Krittacom, B., Kamiuto, K.: Radiation emission characteristics of an open-cellular porous burner. *J. Therm. Sci. Technol.* **4**(1), 13–24 (2009)

Krittacom, B., Tongbai, P.: The effective thermal conductivity (ETC) of spherical packed-bed porous media for modification of the color surface as black color. *Mater. Sci. Forum* **911**, 100–104 (2018)

Krittacom, B., Amatachaya, P., Srimuang, W., Inla, K.: The pack-bed sphere liquid porous burner. *Int. J. Mech. Mech. Eng.* **5**(9), 1917–1921 (2011)

- Krittacom, B., Amatachaya, P.: The effect of porous emitter on the combustion of diesel oil porous burner. In: Proceeding of the 2nd TSME International Conference on Mechanical Engineering, pp. 19–20. TSME-ICOME (19–21 October 2011)
- Lekpradit, T., Krittacom, B.: Enhancement of combustion of liquid fuel on porous burner using porous emitter. *Eng. J. Res. Dev.* **24**(2), 36–44 (2013). (in Thai)
- Peamsuwan, R., Krittacom, B.: Estimating correlation of effective thermal conductivity on the spherical packed bed porous media. *Appl. Mech. Mater.* **575**, 282–286 (2014)
- Pranpanya, S., Krittacom, B.: Effect of porous-emitter porosity on the combustion behavior of a bi-layer liquid porous burner. In: The 30th Conference of the Mechanical Engineering Network Thailand (5–8 July 2016) (in Thai)
- Sripunya, W., Krittacom, B.: Improvement of thermal effectiveness of the tube-bank heat exchanger in a porous burner with installed the porous emitter. In: The 3rd International Conference on Energy and Power (18–20 November 2021).
- Sripunya, W., Amatachaya, P., Krittacom, B.: The effect of factors on effectiveness of the tube-bank heat exchanger installed in a porous burner using LPG as fuel. In: 30th Conference of the Mechanical Engineering Network Thailand (5–8 July 2016) (in Thai)
- Thongtem, P., Jugjai, S.: Nonpremixed porous burners for gaseous fuels. In: The 22nd Conference of the Mechanical Engineering Network Thailand (15–17 October 2008) (in Thai)
- Vafai, K.: *Hand Book of Porous Media*. CRC Press, New York, USA (2000)

# Experimental and Numerical Investigations of Effects of Wall Friction and Vibrational Amplitude on Convection Phenomena in Granular Materials Under Vertical Vibrations



Tanapon Yachai, Itthichai Preechawuttipong ,  
and Pawarut Jongchansitto 

## 1 Introductions

In the engineering context, granular materials can be defined as a cluster of solid particles, whose macroscopic behaviors are controlled by the interaction forces between particles, for example, rock, soil, sand, plastic pellets, pharmaceuticals, etc. Indeed, particle mixing and segregation often occur in many industrial processes involved the transportation and handling of granular mixtures under vibrated or shaken systems. Convection is one of key driving mechanism for such phenomena (Windows-Yule et al. 2013, 2014; Windows-Yule 2016). The strength of the granular convection depends on many parameters such as number of particles (Windows-Yule et al. 2013, 2014; Windows-Yule 2016), aspect ratio of container dimensions (Windows-Yule and Parker 2014; Hsiau et al. 2011), material properties (Windows-Yule et al. 2013, 2014), dimensionless vibrational acceleration ( $\Gamma$ ) (Zhang et al. 2014), and wall friction (Song and Zhang 2020). Among these parameters, the wall friction dominates compared to the others (Windows-Yule and Parker 2014; Then et al. 2020). Only, a few previous studies considered the strength of convection due to the friction coefficient between particle and wall container. Grossman (Grossman 1997) numerically examined the effects of boundary conditions on convection in vibrated granular systems. The results showed that the net shear force exerted by the walls on the particles determines the strength and direction of the convection rolls. Hsiau et al. (2002) and Zeilstra et al. (2008) performed experiments and simulations to investigate the effect of sidewalls roughness on the convection under vertically vibrated granular bed. The results showed that the strength of the convection increases with the sidewalls roughness. Nevertheless, the effect of the particle–wall friction on convection

---

T. Yachai (✉) · I. Preechawuttipong · P. Jongchansitto  
Department of Mechanical Engineering, Faculty of Engineering, Chiang Mai University, 239  
Huay Kaew Rd., Muang 50200, Chiang Mai, Thailand  
e-mail: [tanapon\\_ya@cmu.ac.th](mailto:tanapon_ya@cmu.ac.th)

phenomena has been still unclear. Therefore, the present study is aimed to investigate the influence of wall friction and vibrational amplitude on convection phenomena in a vertically vibrated granular system by means of experiments and reproduced numerical simulations.

## 2 Methodology

The experiment and simulation setup as well as the analysis of convection through the dimensionless angular velocity is presented in this section.

### 2.1 Experimental Setup

Figure 1A shows a preparation of our experiments. A particle was made from the polymethyl methacrylate (PMMA). The particle has a mean diameter ( $D_m$ ) of 10 mm and a thickness of 5 mm. The particle density obtained from the supplier datasheet is  $1190 \text{ kg/m}^3$ . Each particle was then randomly placed inside the container covering the front and back sides by a clear PMMA sheet, as shown in Fig. 1b. The aspect ratio between bed height and bed width was equal to 1. A granular sample consisted of 4000 particles with a uniform distribution of five different diameter sizes  $D \in [9.0, 9.5, 10.0, 10.5, 11.0] \text{ mm}$ . A fluorescent sticker with the diameter of 5 mm was also attached to each particle. This sticker is glowed in the dark under UV light, as presented in Fig. 1c. Note that the center of the sticker was coincident to the centroid of the particle. This is very novel and useful technique for extracting the location of the particles from an image processing. To vary the coefficient of friction between particle and wall container, seven types of materials consisting of a polytetrafluoroethylene (PTFE) tape, a polyethylene (PE) tape, a masking tape, a sandpaper No. 10, 000, a sandpaper No. 5000, and a polyurethane (PU) tape were attached to the sidewalls of the container. These materials provide the coefficient of the particle–wall friction  $\mu_w \in [0.15, 0.26, 0.36, 0.46, 0.61, 0.81, 0.95]$ , respectively. The coefficient of interparticle friction ( $\mu_p$ ) is equal to 0.5. Note that  $\mu_w$  and  $\mu_p$  were obtained from the measurement based on the ASTM D4918-97 standard (ASTMD4918-97 2007).

The granular sample under a gravity was subjected to a vertical vibration with a sinusoidal wave. The vertical vibration was provided by a vertical testing machine through a scotch-yoke mechanism, as shown in Fig. 1a. The level of vibration was controlled by dimensionless acceleration ( $\Gamma$ ). The dimensionless acceleration can be defined as  $\Gamma = A\omega^2/g$ , where  $g$  is the gravity,  $A$  is the vibrational amplitude, and  $\omega = 2\pi f$  is the vibrational frequency. In this study, the dimensionless acceleration was fixed at 5 for a chaotic state of granular system (Chen 2020), while the vibrational frequency was adjusted suitable for the vibrational amplitude of  $0.5D_m$  and  $1.0D_m$ , respectively. During the experiments, the center of each particle was recorded by a high-speed camera with 240 fps. Each considered frame of the video was used to

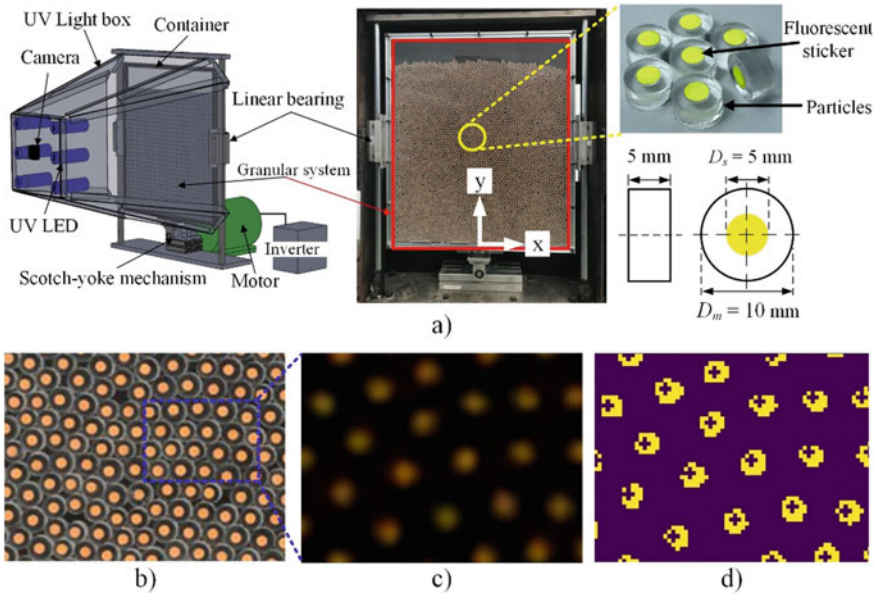


**Fig. 1** **a** Experimental preparation and sample of tested particles. **b** A snapshot of granular sample under visible light. **c** A snapshot of granular sample under UV light. **d** Result obtained from image processing. Note that the plus sign represents the center of the particle

extract the location of the particle center by an image processing technique. Figure 1d presents the obtained image after performing the image processing.

## 2.2 Numerical Setup

The simulations were carried out by means of the non-smooth contact dynamics (NSCD) method, which was originally developed by Moreau and Jean (Jean 1999). This method is suitable for simulating large assemblies of rigid massive particles. In this method, the equations of motion (i.e., Newton’s second laws) are integrated over a small-time step and combined with the kinematic constraints resulting from contact interactions. An open-source software named “LMGC90” (<http://mimetics-engineering.fr/index.php/en/lmgc90-2/>), which was developed in Montpellier, was used for the simulations in this study. The 2D simulations were compared with the experiments under the same conditions. The experiments and simulations were performed up to 300 s. The time step of simulation used for updating the particle position was set to  $1/2^7$  fs. For a comparison between experiments and simulations, an average velocity field was plotted to reveal the convection. The average velocity field can represent the motion of each particle corresponding to the flow behavior of granular media. To determine the average velocity field, the center locations of

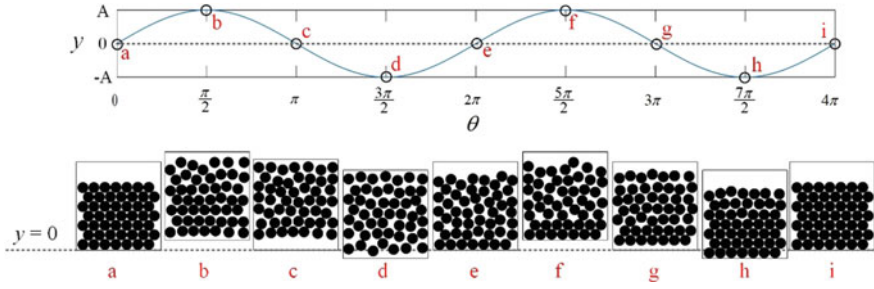


**Fig. 2** Schematic of a phase of vibration corresponding to the sinusoidal wave. Note that the dotted line is the reference line of the container movement

each particle at each phase of  $4\pi$  were exported every 4 s. It is clearly seen that the selected phase of  $4\pi$  is the highest compaction after a rearrangement of the particles, as illustrated in Fig. 2. These locations were then employed to compute the velocity of each particle for every 4 s. Eventually, the average velocity field was determined by averaging all the velocity data for 300 s.

### 2.3 Dimensionless Angular Velocity ( $W$ )

In the previous studies, the granular temperature ( $T$ ) (Windows-Yule and Parker 2014) and the dimensionless convection flow rate ( $J$ ) (Windows-Yule 2016) are commonly applied as the indicators to describe the quantity of convection. The granular temperature is used to quantify the kinetic energy of the flow, while the dimensionless convection flow rate is used to quantify the mass flow rates at the horizontal plane crossing the center of convection. However, the major disadvantage of both indicators is that they cannot explain the direction of convection and the convection at low velocity. Therefore, the dimensionless angular velocity ( $W$ ) was introduced in the present study to describe the quantity of the strength convection. The dimensionless angular velocity is defined as the ratio of the angular velocity of the convection to the angular frequency of the sinusoidal wave of vibration, which can be expressed as:

$$W = \frac{W_L + W_R}{2\omega} \quad (1)$$

where  $W_L$  and  $W_R$  are the average angular velocity of the left and right convection rolls, respectively. The center of rotation for each convection roll can be obtained under the concept that a point having the highest number of velocity vectors rotating around that point, as represented by the blue circle in Fig. 3a. The  $W_L$  and  $W_R$  can be determined by:

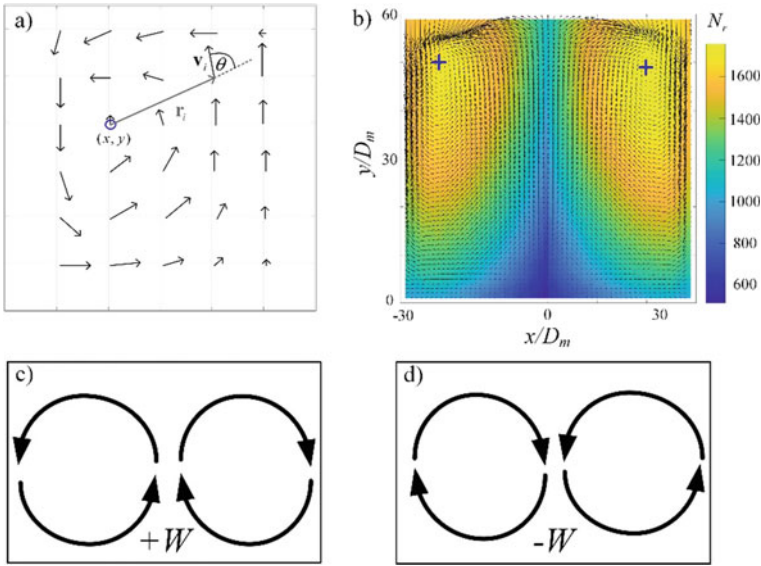


**Fig. 3** a An illustration of a velocity field for determination of the center of the convection. b The number of vectors rotating around point ( $N_r$ ). c An illustration of the normal convection. d An illustration of the reverse convection

$$W_L = \frac{\sum_{i=1}^{N_L} \left( \frac{|v_i| \sin \theta}{|r_i|} \right)}{N_L} \text{ and } W_R = \frac{\sum_{i=1}^{N_R} \left( \frac{|v_i| \sin \theta}{|r_i|} \right)}{N_R} \quad (2)$$

where  $N_L$  and  $N_R$  are number of vectors on left and right convection roll, respectively.  $\theta$  is the smallest angle between the magnitude of a radial vector  $|r_i|$  the magnitude of a velocity vector  $|v_i|$  of  $i$ th vector. The term of  $\sin \theta$  is positive when  $v_i$  rotates counterclockwise about the considered point. On the other hand,  $\sin \theta$  is negative when  $v_i$  rotates clockwise about the considered point. Figure 3b shows a surface plot of the number of vectors rotating about each considered point. Two blue crosses represent the center of the convection having the highest number of rotating vectors. Hence,  $W$  varies from  $-1$  to  $1$ . The dimensionless angular velocity is equal to  $1$ , corresponding to the largest strength of the normal convection, as shown in Fig. 3c. On the contrary, the largest strength of the reverse convection (see in Fig. 3c) exhibits when  $W = -1$ . When the dimensionless angular velocity is close to  $0$ , it means that the convection does not occur.

### 3 Results

In this section, experimental and simulation results of the convection due to the effects of the wall friction and the vibrational amplitude are discussed.



### 3.1 Effect of the Wall Friction

Figure 4A shows the evolution of the dimensionless angular velocity ( $W$ ) as function of the particle–wall friction obtained from the experiment and simulation results for both the vibrational amplitude of  $0.5D_m$  and  $1.0D_m$ . The trend of both experiment and simulation results is well correlated. It can be said that the dimensionless angular velocity starts to increase and then stabilizes at a constant value after  $\mu_w > 0.6$ . Figure 4b presents the average velocity fields of points a, b, and c at different levels of  $\mu_w$ . For  $\mu_w < 0.26$ , it was observed that the convection does not appear, i.e.,  $W \approx 0$ . The strength of the convection then tends to increase with  $\mu_w$  until reached its maximum value. Finally, the strength of the convection is steady after  $\mu_w > 0.6$ . It was also found that the magnitude of the dimensionless angular velocity for the experiments is slightly greater than that for the simulations. This can be explained by the front and rear covers of the container used in the experiments affect to the flow behavior in granular system, which is consistent to the previous study (Fortini and Huang 2015).

Let us consider the strength of the convection when  $\mu_w > \mu_p$ , it is clearly seen that only the effect of the particle–wall friction cannot cause an enhancement of the dimensionless angular velocity. Therefore, the particle at the container wall is required the interparticle friction from an adjacent particle to migrate downward into

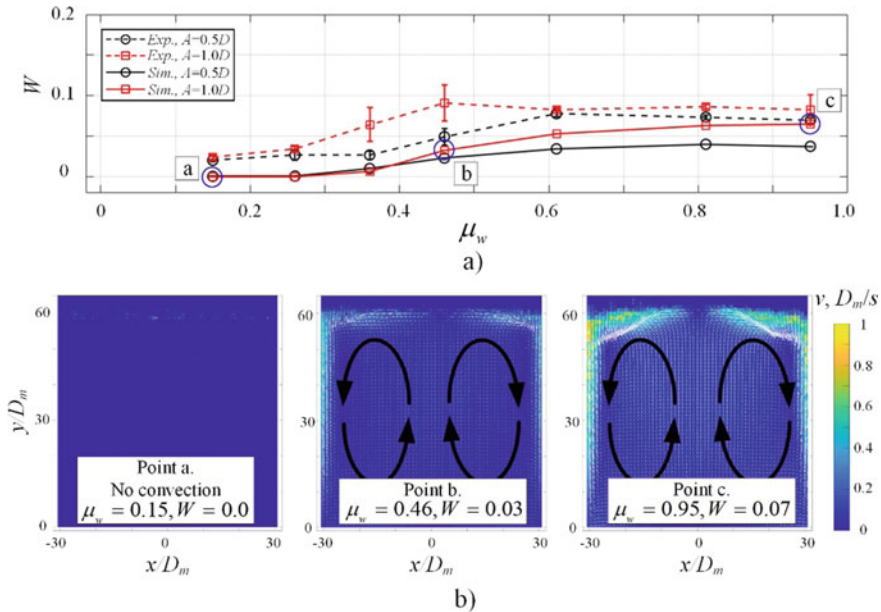
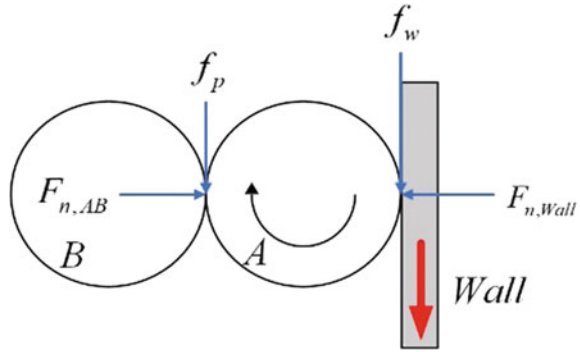


**Fig. 4** a Dimensionless angular velocity as a function of the particle–wall friction obtained from experiments and simulations for the vibrational amplitude of  $0.5D_m$  and  $1.0D_m$ . b Examples of the average velocity field of points a–c corresponding to Fig. 4a

**Fig. 5** Free-body diagram of particles at the container wall while the container is moving down



the bottom of the container (Song and Zhang 2020). This can be explained by a free-body diagram, as illustrated in Fig. 5, where  $F_{n, wall}$  is the normal force acting by the container wall,  $f_w$  is the particle–wall friction force,  $F_{n, AB}$  is the normal force between particle A and particle B, and  $f_p$  is the friction force between particle A and particle B.

### 3.2 Effect of the Vibrational Amplitude

It was observed that when the vibrational amplitude was increased, the strength of the convection is increased for any  $\mu_w$ . This is due to the fact that larger vibrational amplitude provides the larger displacement of the container, thus leading to more spaces between the particles for the movement (Zhang et al. 2014; ASTM D4918-97 2007). Time for the particle movement is also increased when the vibrational amplitude was increased, thus causing the higher velocity. Comparison with the simulations, the strength of the convection due to the vibrational amplitude obtained from the experiment’s overestimates for any  $\mu_w$ .

## 4 Conclusion

This work pointed out the first step for a better understanding of the effect of the wall friction and the vibrational amplitude on convection phenomena in 2D granular system under vertical vibration. The appearance and the strength of convection mechanisms were characterized by the dimensionless angular velocity ( $W$ ). All cases of an occurrence of the convection were normal. The convection started to occur when the wall friction  $\mu_w > 0.26$  and then reached to the maximum for  $\mu_w$  close to  $\mu_p$ . The strength of convection was no longer increased for  $\mu_w > \mu_p$  because the particles rotated about itself. In addition, the convection was much clearer when the vibrational amplitude was increased. It must be noted that the experimental and numerical

results are correlated, but an underestimation of the results by the simulation was observed. The contribution of this work can be considered as the basic data for the segregation and mixing of the binary materials.

**Acknowledgements** This work was supported by TA/RA Scholarships from Graduate School, Chiang Mai University and Graduate Research Assistant Scholarships from Faculty of Engineering, Chiang Mai University.

## References

- ASTMD4918-97 (2007)
- Chen B.: Powder Technol. **363**, 575–583 (2020)
- Fortini, A., Huang, K.: Phys. Rev. E **91**, 032206 (2015)
- Grossman, E.: Phys. Rev. E **56**, 3290 (1997)
- Hsiau, S., Wang, P., Tai, C.: AICHE J. **48**, 1430–1438 (2002)
- Hsiau, S., Liao, C., Sheng, P., Tai, S.: Exp. Fluids **51**, 795–800 (2011)
- Jean, M.: Comput. Method. Appl. M **177**, 235–257 (1999)
- LMGC90 Homepage. <http://mimetics-engineering.fr/index.php/en/lmgc90-2/>
- Song, X., Zhang, G.: Powder Technol. **372**, 40–47 (2020)
- Then, H., Sekiguchi, T., Okumura, K.: Soft Matter **16**, 8612–8617 (2020)
- Windows-Yule, C.: New. J. Phys. **18**, 033005 (2016)
- Windows-Yule, C., Parker, D.: Powder Technol. **261**, 133–142 (2014)
- Windows-Yule, C., Rivas, N., Parker, D.: Phys. Rev. Lett. **111**, 038001 (2013)
- Windows-Yule, C., Weinhart, T., Parker, D., Thornton, A.: Phys. Rev. E **89**, 022202 (2014)
- Zeilstra, C., et al.: Powder Technol. **184**, 166–176 (2008)
- Zhang, F., Wang, L., Liu, C., Wu, P., Zhan, S.: Phys. Lett. A **378**, 1303–1308 (2014)

# Comparative Study of Radiative Flux from Mushroom BLEVE Model



Anas Mbarki, Aziz Ettahir, and Abderraouf Guelzim

## Nomenclature

|              |   |
|--------------|---|
| $V_{FB}$     | The total volume of the fireball ( $m^3$ )  |
| $V_S$        | Spherical volume ( $m^3$ )  |
| $V_C$        | Cylindrical volume ( $m^3$ )  |
| FL           | Filing level of the vessel  |
| $t_d$        | The fireball duration (s)   |
| $t_{lo}$     | The fireball Liftoff Time (s)   |
| $D_{max}$    | Maximum fireball diameter (m)   |
| $D_{FB}$     | The fireball diameter (m)   |
| $r_{FB}$     | The fireball radius (m)   |
| $H_{FB}$     | The height of the center of the fireball (m)  |
| $r_S$        | The radius of the spherical part of the mushroom (m)                                      |
| $r_C$        | The radius of the disk of the cylindrical part of the mushroom (m)                        |
| $h_C$        | The height of the cylindrical part of the mushroom (m)                                    |
| $m_{t_{lo}}$ | The mass of fuel involved on the liftoff time (kg)  |
| $\rho$       | The density ( $kg/m^3$ )  |
| $\alpha$     | The coefficient of proportionality or the volume ratio                                    |
| $L_*$        | The linear scale length   |
| $U_*$        | The linear scale velocity (the characteristic velocity owing to the buoyancy force) (m/s) |
| $t_*$        | The linear scale time   |
| $V_*$        | Characteristic volume   |

---

A. Mbarki (✉) · A. Ettahir  
Materials, Energy and Acoustics Team (MEAT), Mohammed V University in Rabat—EST Salé,  
Rabat, Morocco  
e-mail: [anas\\_mbarki@um5.ac.ma](mailto:anas_mbarki@um5.ac.ma)

A. Guelzim  
Forensic Institute of the Royal Gendarmerie, Rabat, Morocco

|              |   |
|--------------|---|
| $\Delta H_c$ | Heat of combustion (kJ/kg)  |
| $M_0$        | Mass of fuel involved (kg)  |
| $\rho_a$     | The density of ambient air density (kg/ m <sup>3</sup> )              |
| $c_{p,a}$    | The specific heat capacity of air (kJ/kg)                             |
| $T_a$        | The temperature of ambient air (K)                                    |
| $a$          | Constant  |
| Fr           | The Froude number   |
| $U_0$        | The release velocity (m/s)  |
| $g$          | Acceleration due to gravity (m/s)                                     |
| $X$          | The distance (m)  |
| $F_{FB}$     | The max geometric view factor for a spherical emitter (–)             |
| $C_{max}$    | The max geometric view factor for a cylindrical emitter (–)           |
| $C_V$        | The vertical view factor for a cylindrical emitter (–)                |
| $C_h$        | The horizontal view factor for a cylindrical emitter (–)              |
| $q$          | The radiative flux (kW/m <sup>2</sup> )                               |
| $E_s$        | The emissive power of fire per unit surface area (W/m <sup>2</sup> )  |
| $f_h$        | The radiative fraction of the heat of combustion (–)                  |
| $M$          | The initial mass of fuel in the fireball (mass) (kg)                  |
| $\tau_{a,n}$ | The atmospheric transmissivity (–)                                    |
| $R$          | The fractional relative humidity                                      |
| $P_v$        | The saturated vapor pressure of water at the ambient temperature (Pa) |

## 1 Introduction

The prevention of risks associated with major industrial accidents is a necessity for those responsible for site safety management. Since the slightest error in estimating its dangers may have disastrous consequences on both people and structures, hence the need to set up efficient and valid analytical models for estimating the effects of these phenomena. This study is an attempt to model the thermal effects of a Bleve, taking into consideration the numerous hazards that can influence this phenomenon, namely the time and the distance from the source of the radiation, and finally the behavior of the flaming gas cloud facing the upward entrainment of ambient air. The mushroom Bleve model can be an alternative, making it possible to take into account all its hazards by containing them in a single model, which varies throughout the combustion duration.

## 2 Methods

During failure or total rupture of a storage tank for flammable chemicals or hydrocarbons, the increased difference in the pressure of the products contained and the

ambient pressure favors the evaporation the liquid almost instantaneously; the spread evaporated liquid forms a cloud which gradually grows following the entrainment of the ambient air toward the interior of the cloud. The operation accentuated by the phenomena of turbulence and ascending velocity, as observed in different experiments, gives a shape resembling mushroom to the fireball in the phase of volume growth. These phenomena are not taken into account by the dynamic model which claims that the shape of the cloud is almost spherical and that only its size varies with time.

In this work, we calculate the radiative flux from a proposed mathematical model, and then compare it with that obtained by using the dynamic forecasting model, which assumes the fireball to have a spherical geometry. This proposed mathematical model is applied to a reservoir with a total volume of 10,796 m<sup>3</sup>, with a filling level of 40%, under a pressure of 15 bars, and then compared to Martinsen and Marx’s dynamic model (Martinsen et al. 1999; INERIS 2017; Johnson and Pritchard 1990; <https://www.aiche.org/resources/publications/books/guidelines-consequence-analysis-chemical-releases>).

### 3 Discussion of Results

#### 3.1 The Real Fireball Geometry: “Mushroom Shape”

The model of fireball’s mushroom shape behavior is similar to the one described by the following figure (Fig. 1); the total volume  $V_{FB}$  is composed of a spherical volume and a cylindrical volume denoted, respectively  $V_S$  and  $V_C$ .

So, we have:

$$V_{FB} = V_S + V_C \tag{1}$$



Fig. 1 Mushroom Bleve volume

The volumes of the geometric shapes (spherical and cylindrical) obtained are proportional to the volume of the initial fireball, considering that:

$$V_C = \alpha \cdot V_{FB}. \quad (2)$$

$$V_S = (1 - \alpha) \cdot V_{FB} \quad (3)$$

where  $\alpha$ : is a dimensionless constant between 0 and 1, it is introduced to express the proportionality between the volume of the sphere of the Martinsen and Marx model (Martinsen et al. 1999) and the volume of the spherical part of the considered mushroom geometry.

### 3.2 Modeling of the Mushroom Shape Approach

As observed in several accidents and confirmed in various recent experiments (British Gas experiments), the mushroom shape model illustrates a more realistic representation of the true behavior of fireballs. By employing adequate equations that take into account the fireball growth, the lift-off, the changing radiation characteristics, the visible cloud expansion velocity, the fuel properties (boiling temperature, heat of evaporation), the uplift velocity time scale of the fireball (Makhvilade et al. 1996, 1997, 1999a, 1999b, 2000; Makhviladze and Yakush 2005; Gostintsev 2022), the air entrainment as well as the turbulence associated to the ascendant air flux.

During the first third of Bleve's life, the analysis of the behavior associated with phenomenon's study is similar to that used in a dynamic model. The fireball has a spherical shape.

Thereafter, during the beginning of the second third of the burning time, the fireball stretches to take a new shape similar to that of a mushroom, formed by the superposition of two geometric shapes, a spherical part above the cylindrical part. The radius of this spherical part is less than that of the initial sphere; however, it always remains proportional to it.

### 3.3 Determination of the Volume's Characteristics Forming the Mushroom and of the Volume Ratio A

The radius, the height of the cylindrical part of the mushroom, and its radius are given by the following equations:

$$r_C = \frac{2}{3} \cdot \sqrt{\frac{\alpha}{t - \sqrt[3]{1 - \alpha/3}}} \cdot r_{FB} \quad (4)$$

$$h_C = H_{FB} - r_S \quad (5)$$

$$r_S = \sqrt[3]{1 - \alpha} \cdot r_{FB} \quad (6)$$

**Determination of Alpha** According to Makhviladze et al. (<https://www.aiche.org/resources/publications/books/guidelines-consequence-analysis-chemical-releases>; Makhvilade et al. 1996, 1997, 1999a), the characteristic volume  $V_*$  of the fireball is determined by equating the total combustion energy of the fuel  $\Delta H_C M_0$  to the thermal energy of the cloud  $\rho_b c_p (T_b - T_a) V_*$ , where the subscript b corresponds to the combustion products.

And using the dimensionless analysis, for the linear scale length and the characteristic velocity owing to the buoyancy forces, we find:

$$V_* = \Delta H_C M_0 / \rho_a c_{p,a} T_a \quad (7)$$

$$L_* = v_*^{1/3} \quad (8)$$

$$U_* = (L_* g)^{1/2} \quad (9)$$

Reducing the initial Eqs. (7–9), the Froude number which describes the buoyancy of the phenomenon can thus be expressed by:

$$Fr = \left( \frac{U_0}{U_*} \right)^2 = \frac{U_0^2}{g} \left( \frac{\rho_a c_{p,a} T}{\Delta H_C M_a} \right)^{1/3} \quad (10)$$

After using the empirical relation which gives the maximum diameter of the fireball as the mass's function of the fuel entrained by ambient air:

$$D_{\max} = a \cdot M_0^{1/3} \quad (11)$$

Then, the explicit form of the dimensionless constant  $\alpha$  is as follows:

$$\alpha = 1 - \left[ \frac{1}{M_0} \cdot (U_0^2 / a \cdot g Fr)^3 \right] \quad (12)$$

where  $\alpha$  is the constant of the ratio between the maximum diameter of the fireball and the mass to the power 1/3.



### 3.4 Radiative Flux Measurement

The numerical values are calculated from the input data proposed in Sect. 2 methodology; the equations constituting the dynamic model are illustrated in (Eqs. 1–3).

**First Step:**  $0 < t < t_d/3$  We calculated the heat flux  $q$  at a certain distance from the fire experienced by the receiver per  $m^2$ , utilizing:

$$q = E_s \cdot F_{FB} \cdot \tau_a \quad (13)$$

$$E_s(t) = 0.0133 \cdot f_h \cdot H_c \cdot M^{12} \quad (14)$$

$$E_s(t) = 359.347, \text{ for } \rightarrow 0 \leq t \leq 2.127$$

$$F_{FB}(X, t) = D_{FB}(t)^2 / 4 \cdot [H_{FB}(t)^2 + X^2] \quad (15)$$

$$F_{FB}(X, t) = \frac{\left(8.664 \cdot M^{1/4} t^{1/3}\right)^2}{4 \cdot \left[\left(4.332 \cdot M^{1/4} t^{1/3}\right)^2 + X^2\right]}$$

$$F_{FB}(X, t) = 3772.905 \cdot t^{2/3} / 4 \cdot \left(943.226 \cdot t^{2/3} + X^2\right)$$

$$\tau_a(x, t) = 2.02 \cdot \left\{ \text{RPV} \left[ \sqrt{H_{FB}(t)^2 + x^2} - \frac{D(t)}{2} \right] \right\}^{-0.09} \quad (16)$$

$$\tau_a(x, t) = 1.03 \cdot \left[ \sqrt{943.226 \cdot t^{2/3} + X^2} - 30.712 \cdot t^{1/3} \right]^{-0.09}$$

**Second Step:**  $t_d/3 < t < t_d$  The radiative flux  $q$  at a certain distance from the fire experienced by the receiver, using:

$$q = q_{\text{spherical}} + q_{\text{cylindrical}} \quad (17)$$

$$q = E_s \cdot (F_{\text{spherical}} + F_{\text{cylindrical}}) \cdot \tau_a \quad (18)$$

$$E_s(t) = E_{\text{max}} \cdot \frac{3}{2} \left(1 - \frac{t}{t_d}\right), \text{ for } \rightarrow \frac{1}{3}t_d < t \leq t_d \quad (19)$$

$$E_s(t) = 539 - 84.48 \cdot t, \text{ for } \rightarrow 2.127 < t \leq 6.381$$

$$\alpha = 1 - \left[ \frac{1}{M_0} \cdot (U_0^2/a \cdot gFr)^3 \right] \quad (20)$$

$$\alpha = 34.25\% \approx 34\%$$

- $r_C = 0.381 \cdot \sqrt{\frac{1}{t-0.29}} \cdot r_{FB}$

$$r_C = 15.353 / \sqrt{t - 0.29}$$

- $h_C = H_{FB} - r_S = 18.570 \cdot t - 34.388$

- $r_S = 0.871 \cdot r_{FB} = 34.388 \text{ m}$

$$F_{\text{Mushroom}_{\max}} = F_{\text{spherical}} + F_{\text{cylindrical}} \quad (21)$$

$$F_{\text{spherical}} = D_S(t)^2 / 4 \cdot [H_{FB}(t)^2 + X^2] \quad (22)$$

$$F_{\text{spherical}} = 4730.103 / 4 \cdot (344.852 \cdot t^2 + X^2)$$

$$F_{\text{cylindrical}} = \sqrt{C_H^2 + C_V^2} \quad (23)$$

$$C_H = \frac{1}{\pi} \cdot \left[ \tan^{-1} \left( \frac{X + r_C}{X - r_C} \right)^{1/2} - \frac{X^2 - r_C^2 + h_C^2}{\sqrt{A \cdot B}} \cdot \tan^{-1} \left( \frac{(X - r_C) \cdot A}{(X + r_C) \cdot B} \right)^{1/2} \right] \quad (24)$$

$$C_V = \frac{1}{\pi} \cdot \left[ \frac{r_C}{X} \tan^{-1} \left( \frac{h_C^2}{X^2 - r_C^2} \right)^{1/2} + \frac{h_C \cdot (A - 2X \cdot r_C)}{X \cdot \sqrt{A \cdot B}} \right. \\ \left. \tan^{-1} \left( \frac{(X - r_C) \cdot A}{(X + r_C) \cdot B} \right)^{1/2} - \frac{h_C}{X} \tan^{-1} \left( \frac{X - r_C}{X + r_C} \right)^{1/2} \right] \quad (25)$$

With:

$$A = (X + r_C)^2 + h_C^2 \quad (26)$$

$$B = (X - r_C)^2 + h_C^2 \tag{27}$$

$$\tau_a(X, t) = 2.02 \cdot \left\{ \text{RP}_V \left[ \sqrt{H_{\text{FB}}(t)^2 + X^2} - \frac{D_S(t)}{2} \right] \right\}^{-0.09} \tag{28}$$

$$\tau_a(X, t) = 1.03 \cdot \left[ \sqrt{344.852 \cdot t^2 + X^2} - 17.194 * 2 \right]^{-0.09}$$

### 3.5 Graphic Comparison Between the Two Models

Figures 2, 3, 4, 5, and 6 are plots of the same data calculated by the mushroom approach compared to the measurements taken during British Gas test no. 4 and Martinsen and Marx model, at several distance. These plots give us an overview on the validity of the analytical predictions. who have been calculated from the mushroom Bleve model, compared to the analytical prediction of Martinsen and Marx model and to the measurements recorded during test no. 4 of the BG experience and this at several times during the combustion time, depending on the distance of the target from the tank. At the same time, it illustrates the variation of the incident thermal radiation received as a function of distance and as a function of time. The variation of the thermal radiation incident represented in Figs. 2, 3, 4, 5, and 6 shows a strong similarity to the trend and a strong positive correlation almost perfect to the results collected on the BG experiment no. 4.

The analysis of Fig. 7 gives us the following information:

The thermal dose of the spherical part during the last two thirds of the combustion time of the Bleve is equal to the area  $s$  (104.112). While the thermal dose of the cylindrical part during the same period of combustion of the Bleve is equal to the area  $t$  (45.76).

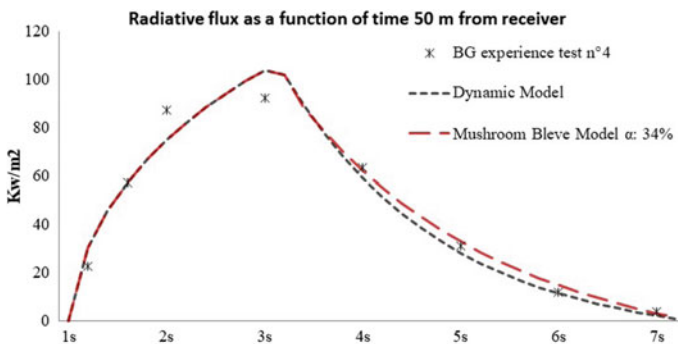


Fig. 2 Radiative flux as a function of time calculated at 50 m from receiver

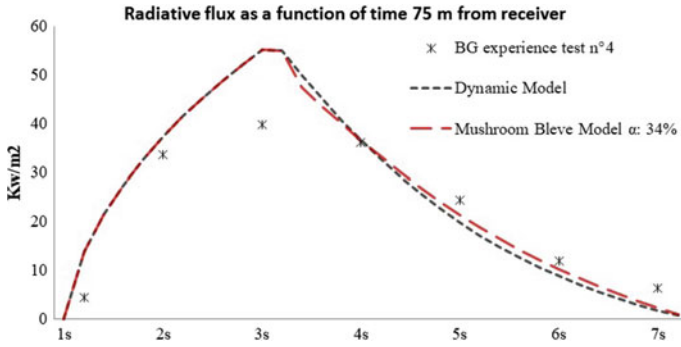


Fig. 3 Radiative flux as a function of time calculated at 75 m from receiver

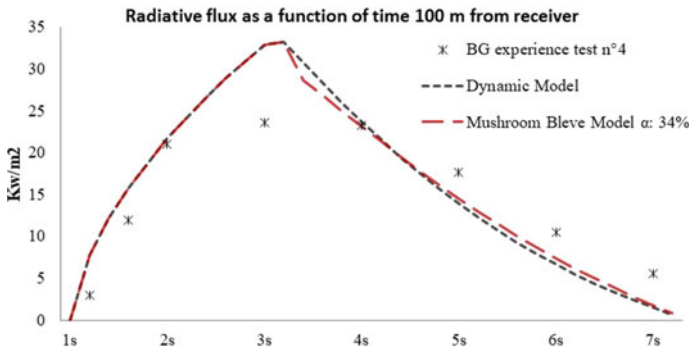


Fig. 4 Radiative flux as a function of time calculated at 100 m from receiver

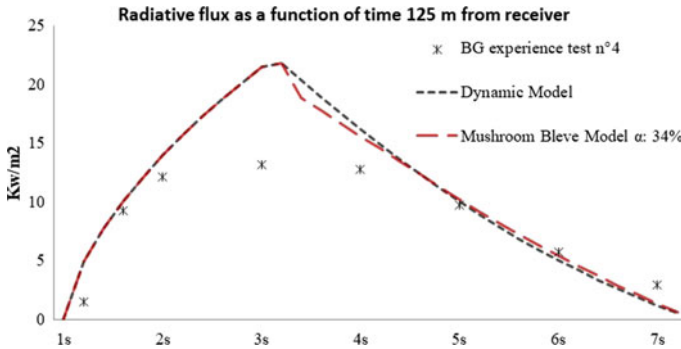


Fig. 5 Radiative flux as a function of time calculated at 125 m from receiver

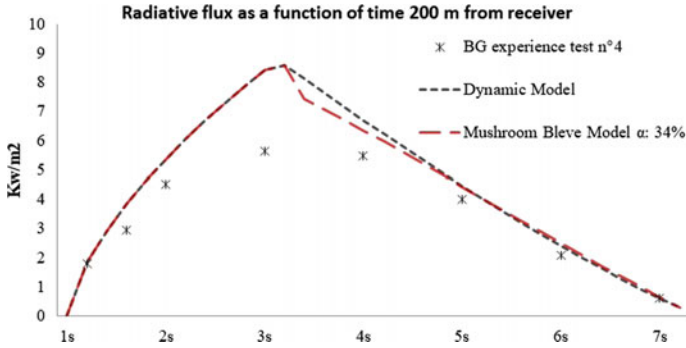


Fig. 6 Radiative flux as a function of time calculated at 200 m from receiver

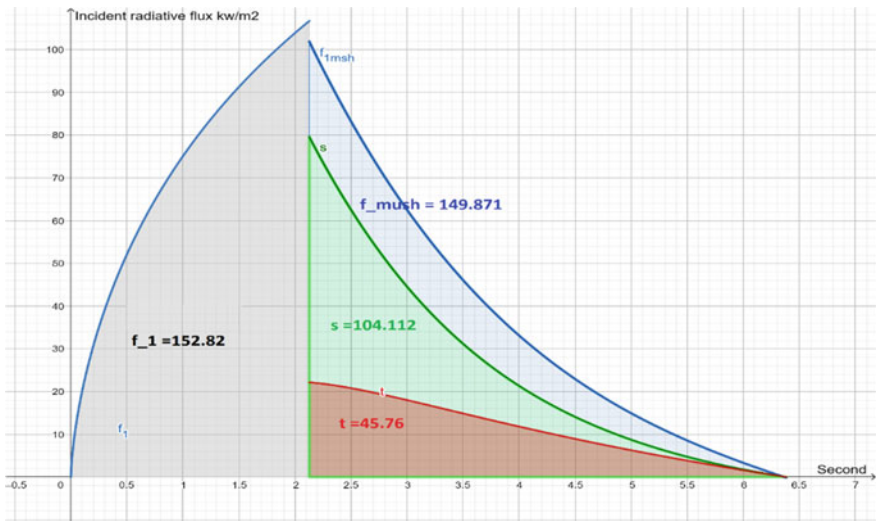


Fig. 7 Contribution of the cylindrical part of the Bleve mushroom in the calculation of the incident radiative flux at 50 m—measured during the simulation of BG test 4

The contribution of the cylindrical part is almost 30% of the thermal dose received by a target moving away from 50 m from the center of the phenomenon and this during the last two thirds of the combustion time of the Bleve, and more than 15% of the total thermal dose received by a target exposed to the incident radiative flux throughout the duration of the Bleve.

### 3.6 Discussion

The mushroom Bleve model has a great similarity with the dynamic model of Martinsen. It can be seen that, the radiative fluxes are calculated as a function of time and can be split into two parts:

- The first part at any instant  $t$  of the first third of the Bleve duration:

The two models give the same values of the radiative flux.

- The second part at any instant  $t$  is greater than the first third:

At the start of the second third, the radiative flux calculated by the dynamic model is greater than that calculated by the mushroom Bleve model, by few milliseconds for receivers located at a short or medium distance that does not exceed 100 m from the center of the geometric mushroom shape. In addition, the difference between the radiative fluxes calculated by the two models does not exceed  $2.6 \text{ kw/m}^2$ ; this translates in a negative variance which does not exceed 6% for the radiative flux calculated by our approach. While this duration is extended to more than one second for receivers placed at a greater distance, and the difference between the radiative fluxes calculated by the two models does not exceed  $1.6 \text{ kw/m}^2$ , this is transcribed into a negative variance which does not exceed order of 7% for the radiative flux calculated by our approach.

The ratio is quickly reversed, and the radiative flux calculated by the mushroom Bleve model takes values higher than that calculated by the dynamic model and this throughout the remaining existence time.

For receivers located at a short or medium distance, which does not exceed 100 m from the center of the geometric mushroom shape, the difference between the radiative fluxes calculated by the two models does not exceed  $5 \text{ kw/m}^2$ ; this translates into a positive variance which does not exceed 24% for the radiative flux calculated by our approach. While this variance does not exceed  $1 \text{ kw/m}^2$ , i.e., an increase of less than 5% of the radiative flux calculated by our approach. The magnitude of the calculation difference margin between the two models dissipates as the receiver moves away from the radiation source.

## 4 Conclusion

A In this study, two models relating to the effects of radiative transfers of a fireball generated by a Bleve were compared:

- Martinson and Marx's dynamic model, whose fireball geometry is considered to be spherical;
- Andour proposed model, whose fireball's geometry is considered to have a mushroom shape.

The comparison of the two models was made based to the experimental data for medium-scale fireball tests realized by Johnson and Pritchard (1990) as part of the experiments conducted by British Gaz and cited by INERIS (INERIS 2017).

The mushroom Bleve model is an attempt in which we made sure to take into account the real behavior of the fireball through the combustion duration following the analysis of the media library of the tests carried out, in order to define its temporal behavior.

This attempt will allow us to minimize the margin of error relating to the calculation of the thermal dose received by an individual relative to its distance from the radiation source. Thus, the effective distances and the impact on structure and people are expected to be more severe.

Although the difference is not appreciable in terms of safety, it takes into account the geometric reality of the Bleve phenomenon throughout its lifetime.

## References

- Gostintsev: Theory of the Aerodynamics, Autoignition. Google Scholar. [https://scholar.google.com/scholar\\_lookup?title=Theory%20of%20the%20aerodynamics%2C%20self%20ignition%2C%20and%20burnup%20of%20turbulent%20thermals%2C%20vortex%20rings%2C%20and%20jets%20in%20a%20free%20atmosphere&journal=Khim.%20Fiz.&volume=9&pages=1279-1290&publication\\_year=1982&author=Gostintsev%2CYu.%20A.&author=Solodovnik%2CA.%20F.&author=Lazarev%2CV.%20V](https://scholar.google.com/scholar_lookup?title=Theory%20of%20the%20aerodynamics%2C%20self%20ignition%2C%20and%20burnup%20of%20turbulent%20thermals%2C%20vortex%20rings%2C%20and%20jets%20in%20a%20free%20atmosphere&journal=Khim.%20Fiz.&volume=9&pages=1279-1290&publication_year=1982&author=Gostintsev%2CYu.%20A.&author=Solodovnik%2CA.%20F.&author=Lazarev%2CV.%20V). Last accessed 2022 Feb 25
- Guidelines for Consequence Analysis of Chemical Releases. <https://www.aiche.org/resources/publications/books/guidelines-consequence-analysis-chemical-releases>. Last accessed 2022 Feb 25
- INERIS: OMEGA5 Le BLEVE, phénoménologie et modélisation des effets. INERIS, Verneuil-en-Halatte (2017)
- Johnson, D., Pritchard, M.: Large scale experimental study of boiling liquid expanding vapour explosions (BLEVES) (1990)
- Makhvilade, G.M., Roberts, J.P., Yakush, S.E.: Burning regimes for the finite-duration releases of fuel gases. In: Symposium (International) on Combustion, vol. 1, pp. 1549–1555 (1996). [https://doi.org/10.1016/S0082-0784\(96\)80377-8](https://doi.org/10.1016/S0082-0784(96)80377-8)
- Makhviladze, G.M., Yakush, S.E.: Modelling of formation and combustion of accidentally released fuel clouds. *Process Saf. Environ. Prot.* **83**, 171–177 (2005). <https://doi.org/10.1205/psep.04242>
- Makhviladze, G.M., Roberts, J.P., Yakush, S.E.: Modelling the fireballs from methane releases. *Fire Saf. Sci.* **5**, 213–224 (1997)
- Makhviladze, G.M., Roberts, J.P., Yakush, S.E.: Fireball during combustion of hydrocarbon fuel releases II thermal radiation. *Combust Explos Shock Waves* **35**, 359–369 (1999b). <https://doi.org/10.1007/BF02674465>
- Makhviladze, G., Roberts, J., Yakush, S.: Modelling and scaling of fireballs from single -and two-phase hydrocarbon releases. *Fire Saf. Sci.* **6**, 1125–1136 (2000). <https://doi.org/10.3801/IAFSS.FSS.6-1125>
- Makhviladze, G.M., Roberts, J.P., Yakush, S.E.: Fireball during combustion of hydrocarbon fuel releases. I. Structure and lift dynamics. *Combust. Explos. Shock Waves* **35**, 219–229 (1999a). <https://doi.org/10.1007/BF02674442>
- Martinsen, W.E., Marx, J.D., By, P.: An improved model for the prediction of radiant heat from fireballs quest an improved model for the prediction of radiant heat from fireballs (1999)

# **Applied Mechanics and Engineering Mechanics**



# Belt Layer Effects on Non-pneumatic Tire Performance by Finite Element Analysis



Juthanee Phromjan and Chakrit Suvanjumrat

## 1 Introduction

The non-pneumatic tires (NPTs) are recently developed to overcome the disadvantages of conventional pneumatic tires such as flat tires, tire pressure maintenance, even though the uncomfortable ride of solid tires (Phromjan and Suvanjumrat 2018a). The basic concept of NPT design is a combination of composite shear band and spoke structure (Rhyen and Cron 2006). The shear band is developed to have similar primary functions as the belt plies of a pneumatic tire which provide strength and stability to the tire tread. Consequently, a good deal of previous research attempted to develop the shear band of NPT. Ju et al. (2010) designed the shear band with different cellular geometries instead of the belt layers. They studied the contact pressure profile of the developed shear bands from the finite element analysis (FEA). There was found that a higher negative cell angle provided a lower contact pressure. Veeramurthy et al. (2014) found that the shear band thickness was a greater effect on rolling resistance than the spoke thickness. It was an important parameter for design NPT with low rolling resistance. Ju et al. (2013) studied a porous composite shear band of NPT by finite element method (FEM). The simulation results indicated that the decrease of elastomer volume reduced the hysteretic energy dissipation. The research, as previously mentioned, simplified the NPT model with a smooth and continuous tread for the investigation. The authentic NPT, TWEEL by Michelin, inserted belt layers for the increase of stiffness in its circumference. The homogenization approach was proposed to model the shear band of TWEEL. It precisely accomplished the deformation of the TWEEL model when compared against the experiment (Phromjan and

---

J. Phromjan · C. Suvanjumrat (✉)

Department of Mechanical Engineering, Faculty of Engineering, Mahidol University, Nakhon Pathom, Thailand

e-mail: [chakrit.suv@mahidol.ac.th](mailto:chakrit.suv@mahidol.ac.th)

Department of Mechanical Engineering, Faculty of Engineering, Laboratory of Computer Mechanics for Design (LCMD), Mahidol University, Nakhon Pathom, Thailand

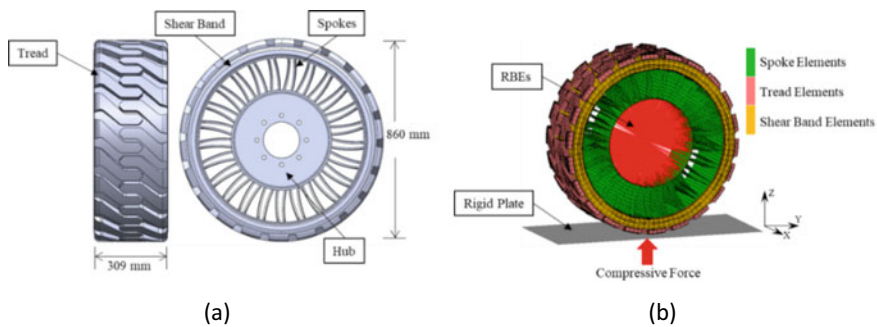
Suvanjumrat 2020). The full-scale NPT model has also carried out the dynamic analysis (Rugsaj and Suvanjumrat 2021). However, the previous studies did not focus to evaluate the belt layer effects on NPT performances. Therefore, it is piquancy to clarify the effects of belt layers. This research aimed to model the full-scale TWEEL with belt layers inside the shear band. The numbers and positions of the belt layer in the shear band that was the composite material were varied. The hyperelastic models which were carried out by testing the material property of each TWEEL component were used to model material of finite element (FE) model. The vertical stiffness, contact area, contact pressure, and safety factor of NPT were carried out to study the belt layer effects. These performances were mainly discussed for the NPT (Phromjan and Suvanjumrat 2021). The results from this interesting will be useful for the extension of the agricultural tires. In general, the agricultural machines which were driven by pneumatic tires were the cause of soil compaction (Hamza and Anderson 2005). Therefore, these useful simulation results will be a guidance tool for solving that problem.

## 2 Finite Element Method

In the first stage, the computer-aided design (CAD) was performed to create the three-dimensional (3D) model of the TWEEL NPT which was developed by Michelin in 2015. It consists of 4 main components which are the rubber tread, composite shear band, polyurethane (PU) spokes, and steel hub as shown in Fig. 1a.

### 2.1 Finite Element Model

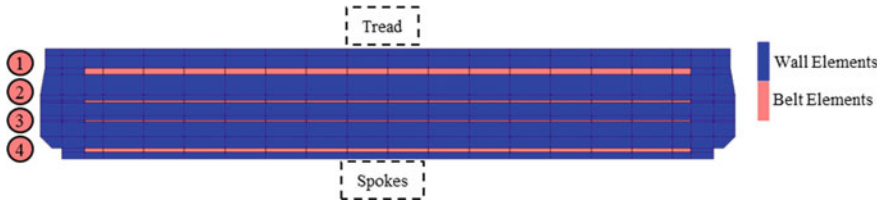
To analyze the NPT structure by FEM, the FE model of TWEEL was created according to the CAD model. The hexagonal elements were used to create the tread



**Fig. 1** NPT model of **a** CAD model and **b** FE model

**Table 1** Details of finite element model of each NPT component

| Component  | Element type   | Number of element | Average element length (mm) |
|------------|----------------|-------------------|-----------------------------|
| Tread      | Solid, 8 nodes | 18,304            | 11.48                       |
| Shear band | Solid, 8 nodes | 24,576            | 13.38                       |
| Spoke      | Shell, 4 nodes | 11,550            | 11.67                       |

**Fig. 2** Cross-section of shear band

and shear band, while spokes were constructed by thick shell elements. The rigid bar elements (RBEs) act as the steel hub of NPT are gathered at the center of TWEEL as shown in Fig. 1b. The composite shear band was prepared following the homogenized model which was already developed and validated by Phromjan and Suvanjumrat (2020). The details of the FE model of each TWEEL component are presented in Table 1. The center of the TWEEL model was fixed, while it was compressed by the rigid flat plate for static performance analysis. The compression force was 4650 N from the weight of the small tractor was applied by moving the rigid plate. In the beginning, the shear band is inserted by 4 belt layers according to TWEEL as shown in Fig. 2. Each layer was defined by the number from 1 to 4 where layer 1 was located next to the tread and layer 4 was located next to the spoke structure. The thicknesses were 3, 1, 1, and 2 mm for layers no. 1, 2, 3, and 4, respectively. After that, the various NPT models with different numbers and positions of belt layer were prepared. The descriptions of NPT models are presented in Table 2.

## 2.2 Finite Element Analysis

To prevent the volumetric locking, the hybrid displacement/pressure formulation was established to analyze the incompressible analysis of the NPT model. It is a good effective formulation for the analysis of rubberlike material which has a large strain. The governing equation can be written by the following equation (Bathe 1997).

$$d_0^t \bar{W} = {}_0^t \bar{S} d_0^t \varepsilon_{ij} \quad (1)$$

where  $d_0^t \bar{W}$  is the incremental potential energy,  ${}_0^t \bar{S}$  is Piola–Kirchhoff stress which is computed only from the displacement field, and  $d_0^t \varepsilon_{ij}$  is the incremental strain.

**Table 2** Description of belt layers for NPT models

| NPT model                                | Belt layers inserting sequence from tread to spoke |
|--|--|
| <i>Group 1 (4 belt layers, original)</i> |  |
| M1-1                                     | 1 2 3 4  |
| <i>Group 2 (3 belt layers)</i>           |  |
| M2-1                                     | 2 3 4  |
| M2-2                                     | 1 3 4  |
| M2-3                                     | 1 2 4  |
| M2-4                                     | 1 2 3  |
| <i>Group 3 (2 belt layers)</i>           |  |
| M3-1                                     | 1 2  |
| M3-2                                     | 1 3  |
| M3-3                                     | 2 3  |
| M3-4                                     | 3 4  |
| M3-5                                     | 2 4  |
| M3-6                                     | 1 4  |
| <i>Group 4 (1 belt layer)</i>            |  |
| M4-1                                     | 1  |
| M4-2                                     | 2  |
| M4-3                                     | 3  |
| M4-4                                     | 4  |
| <i>Group (No belt layer insertion)</i>   |  |
| M5-1                                     | –  |

The hyperelastic material model, Mooney–Rilvin model (Phromjan and Suvanjumrat 2018b), was defined to describe the mechanical properties of the NPT model. This model is written following Eq. 2, which is a popular constitutive model. The spoke model was the most resilient part; therefore, the generalized Maxwell's viscoelastic model was also used to gain more precision of results. These models are written as follows:

$${}^t_0\bar{W} = C_1({}^t_0J_1 - 3) + C_2({}^t_0J_2 - 3) + \frac{1}{2}K({}^t_0J_3 - 1)^2 \quad (2)$$

where  $C_i$  is hyperelastic material constants,  $J_i$  is the reduced invariants, and  $K$  is the bulk modulus.

$$G(t) = G_0 - \sum_{i=1}^n G_i(1 - e^{-t/\tau_i}) \quad (3)$$

$$\tau_i = \eta_i/E_i \quad (4)$$

**Table 3** Constants of material property of the NPT model

| Component  | Mooney–Rivlin’s constant |        |           | Young’s modulus (GPa) | Poisson’s ratio |
|------------|--------------------------|--------|-----------|-----------------------|-----------------|
|            | $C_1$                    | $C_2$  | $K$ (MPa) |                       |                 |
| Tread      | 1.19085                  | 0      | 9670.24   | –                     | –               |
| Wall       | 1.19085                  | 0      | 11,908.5  | –                     | –               |
| Steel belt | –                        | –      | –         | 200                   | 0.3             |
| Spoke      | 0.5063                   | 4.2552 | 42,449    | –                     | –               |

**Table 4** Constants of generalized Maxwell’s viscoelastic model of spoke model (Phromjan and Suvanjumrat 2020)

| $i$ th term | $\tau_i$ | $G_i$ |
|-------------|----------|-------|
| 1           | 0.2      | 0.125 |
| 2           | 0.02     | 0.125 |
| 3           | 0.002    | 0.125 |

where  $G(t)$  is the shear relaxation modulus,  $G_0$  is the initial shear modulus,  $G_i$  is  $i$ th terms of the shear modulus,  $t$  is time,  $\tau_i$  is  $i$ th terms of the relaxation time,  $\eta_i$  is the viscoelasticity, and  $E_i$  is the modulus of elasticity.

The constants of material property and constants of generalized Maxwell’s viscoelastic model of each NPT component are presented in Tables 3 and 4, respectively.

### 3 Results and Discussion

The various NPT models with different numbers and positions of belt layer were compressed by the compression force of 4,650 N in the vertical direction. When the shear band is inserted by 4 belt layers (M1-1), the NPT model is deformed by the vertical load as shown in Fig. 3a. Spokes in the contact region were buckled because of supporting the vehicle’s load from a center of NPT. On the other hand, spokes in the support region were stretched to compensate for the deformation of the shear band. These phenomena happened only when the spoke structures work properly in their role as resilient parts. If the shear band was removed all the belt layers out, it would be a role as the resilient part instead. Figure 3b presents that the NPT model is distorted when no belt layers were inserted inside the shear band. It is noted that the belt layer’s existence is an important effect on the NPT performance. The NPT performances by varying numbers and positions of belt layers are presented in Table 5.

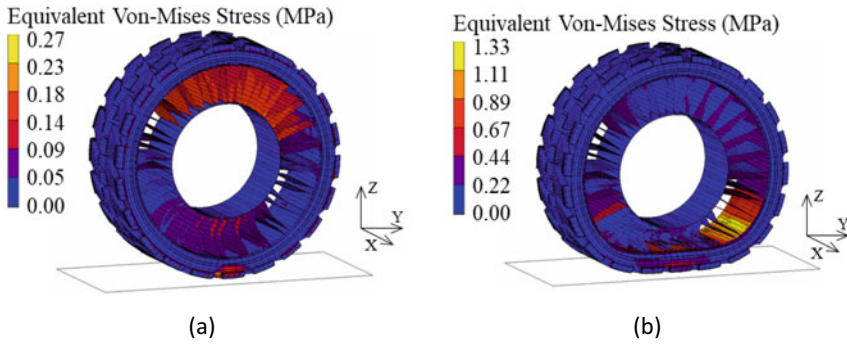


**Fig. 3** Simulation results of **a** M1-1 and **b** M5-1 NPT models

**Table 5** Simulation results of NPT models with various numbers and positions of belt layers

| NPT model      | Vertical stiffness (N/mm) | Safety factor of NPT's spoke | Contact area (cm <sup>2</sup> ) | Contact pressure (MPa) |
|----------------|---------------------------|------------------------------|---------------------------------|------------------------|
| <i>Group 1</i> |                           |                              |                                 |                        |
| M1-1           | 683.82                    | 22.22                        | 144.83                          | 1.064                  |
| <i>Group 2</i> |                           |                              |                                 |                        |
| M2-1           | 512.40                    | 16.52                        | 161.09                          | 1.144                  |
| M2-2           | 578.80                    | 16.75                        | 151.79                          | 1.177                  |
| M2-3           | 579.19                    | 16.75                        | 151.79                          | 1.177                  |
| M2-4           | 551.36                    | 16.38                        | 151.79                          | 1.187                  |
| <i>Group 3</i> |                           |                              |                                 |                        |
| M3-1           | 523.61                    | 16.20                        | 153.56                          | 1.195                  |
| M3-2           | 529.02                    | 16.24                        | 151.13                          | 1.192                  |
| M3-3           | 438.25                    | 13.96                        | 159.03                          | 1.153                  |
| M3-4           | 475.53                    | 15.48                        | 162.95                          | 1.128                  |
| M3-5           | 487.96                    | 15.68                        | 155.94                          | 1.145                  |
| M3-6           | 561.80                    | 16.57                        | 151.79                          | 1.181                  |
| <i>Group 4</i> |                           |                              |                                 |                        |
| M4-1           | 483.61                    | 15.14                        | 150.23                          | 1.203                  |
| M4-2           | 370.96                    | 12.31                        | 159.95                          | 1.149                  |
| M4-3           | 368.11                    | 12.32                        | 158.97                          | 1.122                  |
| M4-4           | 428.76                    | 13.85                        | 163.83                          | 1.108                  |
| <i>Group</i>   |                           |                              |                                 |                        |
| M5-1           | 104.87                    | 4.50                         | 260.32                          | 1.938                  |

### ***3.1 Effects on the Vertical Stiffness***

The existence of the belt layer affected severely on the NPT deformation which is involved in the vertical stiffness. The load capacity of NPT could be dramatically increased by inserting proper belt layers. The simulation results indicated that the existence of layer 1 resulted in the high vertical stiffness observed in every simulation group. If this belt layer was eliminated from the shear band, the vertical stiffness would be extremely reduced. It should be noted that not only the layer 1 has the highest thickness, but it is also located next to the tread which is the first part to be deformed by the ground. Furthermore, the existence of layers 2 or 3 insignificantly affected the vertical stiffness of NPTs. Particularly, the average vertical stiffness was decreased by reducing the number of belt layers.

### ***3.2 Effects on the Safety Factor***

The yield stress of TWEEL's spokes was 6 MPa (Rugsaj and Suvanjumrat 2020). The safety factor was observed by the stress occurrence at spokes. It was quite varied the vertical stiffness of NPT. There was resulted in an increase of vertical stiffness following the increase of safety factors. When all the belt layers were removed from the shear band of NPT, the safety factor was dramatically reduced.

### ***3.3 Effects on the Contact Area***

The contact area happening under the NPT model is investigated by using a red color contour as shown in Fig. 4. It was found that no belt layer (M5-1) appeared the contact area higher than the original one (M1-1) about 79.74%. It should be noted that the existence of belt layers extremely affected the contact area between NPT and road. It was also observed that the contact area was high on the NPT model without layer 1. This is because the first layer which was located next to the tread had an important role to prevent excessive deformation of the shear band. The contact area would increase when the belt layers were inserted far from the NPT's tread. However, the existence of layer 4 resulted in a higher contact area although the vertical stiffness was still maintained because it was thicker than a layer no. 2 and 3. The existence of a layer no. 2 and 3 was the insignificant difference in the contact area changing.

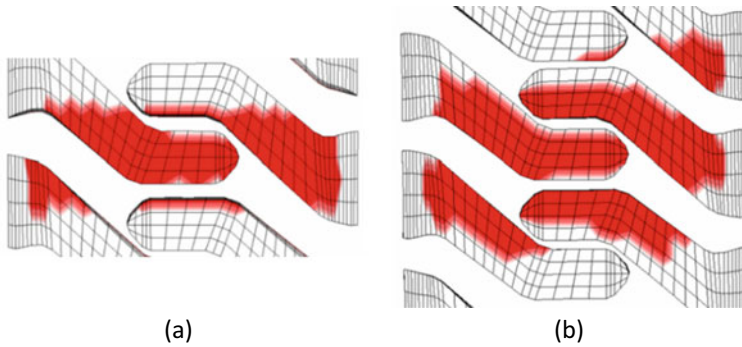


**Fig. 4** Footprint of **a** M1-1 and **b** M5-1 NPT models

### 3.4 *Effects on the Contact Pressure*

The contact pressure is defined by the ratio of the vertical load to the true contact area. FEA results represented the contact pressure as the normal contact stress on NPT tread (Phromjan and Suvanjumrat 2021). The simulated results, therefore, indicated that the NPT which had the higher contact area almost had the lower contact pressure. It should be noted that the existence of layer 1 made a higher contact pressure. However, all the belt layers which were removed from the shear band caused the higher contact area but caused not the lower contact pressure. It is because the more contact force happening that the contact pressure remains a higher value. There was observed that the maximum contact stress happened on the tread of NPT.

## 4 Conclusions

To study the effects of the belt layer in the shear band on the NPT performances, the compression test of NPT models with different numbers and positions of belt layers was simulated by FEM. The different numbers of belt layers inserting in the shear band resulted in the difference in vertical stiffness. Therefore, it can be concluded that belt layer 1 is the most important layer for the NPT performances. The existence of layer 1 always brings the high vertical stiffness and safety factor. However, the contact pressure was not increased as much, while the contact area was low. In contrast, layers 2 and 3 were insignificant effects on the NPT performances. It was investigated the thickness of the belt layer also affected the NPT performances. The belt layer which has a higher thickness can increase the strength of NPTs. Moreover, the positioning of belt layers in the shear band was found to be a severe effect on the contact area of the NPT model. These FEA results will be a useful tool for the design and development of NPT in many applications shortly.



**Acknowledgements** This work was financially supported by the Thailand Science Research and Innovation (TSRI) and National Research Council of Thailand (NRCT) through the Royal Golden Jubilee Ph. D. Program (Grant No. PHD/0049/2561).

## References

- Bathe, K.J.: Finite element procedures. Prentice Hall, London (1997)
- Hamza, M., Anderson, W.: Soil compaction in cropping systems a review of the nature, causes and possible solutions. *Soil Tillage Res.* **82**, 121–145 (2005)
- Ju, J., Ananthasayanam, B., Summers, J.D., Joseph, P.: Design of cellular shear bands of a non-pneumatic tire-investigation of contact pressure. *SAE Int. J. Passenger Cars-Mech. Syst.* **3**(1), 598–606 (2010)
- Ju, J., Veeramurthy, M., Summers, J.D., Thompson, L.: Rolling resistance of a non-pneumatic tire having a porous elastomer composite shear band. *Tire Sci. Technol.* **41**(3), 1–26 (2013)
- Phromjan, J., Suvanjumrat, C.: The modification of steel belt layer of airless tire for finite element analysis. *IOP Conf. Ser.: Mater. Sci. Eng.* **773**(012047) (2020)
- Phromjan, J., Suvanjumrat, C.: Vibration effect of two different tires on baggage towing tractors. *J. Mech. Sci. Technol.* **32**(4), 1539–1548 (2018a)
- Phromjan, J., Suvanjumrat, C.: Material properties of natural rubber solid tires for finite element analysis. *Key Eng. Mater.* **775**, 560–564 (2018b)
- Phromjan, J., Suvanjumrat, C.: Development of solid tire model for finite element analysis of compressive loading. *Songklanakarin J. Sci. Technol.* **43**(1), 229–236 (2021)
- Rhyen, T.B., Cron, S.M.: Development of a non-pneumatic wheel. *Tire Sci. Technol.* **34**(3), 150–169 (2006)
- Rugsaj, R., Suvanjumrat, C.: Study of geometric effects on nonpneumatic tire spoke structure using finite element method. *Mech. Based Des. Struct. Mach.* **50**(7), 2379–2399 (2022). <https://doi.org/10.1080/15397734.2020.1777875>
- Rugsaj, R., Suvanjumrat, C.: Dynamic finite element analysis of rolling non-pneumatic tire. *Int. J. Automot. Technol.* **22**(4), 1011–1022 (2021)
- Veeramurthy, M., Ju, J., Thompson, L.L., Summers, J.D.: Optimisation of geometry and material properties of a non-pneumatic tyre for reducing rolling resistance. *Int. J. Veh. Des.* **66**(2), 193–216 (2014)

# Analysis of Hybrid Viscoelastic Sheets Adhered to the Hull of a GFRP Vessel to Reduce Impact Damage



Patrick Townsend , Juan C. Suárez Bermejo ,  
and Alvaro Rodríguez-Ortíz

## 1 Introduction

Since the world set out to protect the environment, multiple ways to do so have developed. The maintenance of ships built in glass fiber reinforced plastic (GFRP) generates pollution which requires high investments so that they do not harm the surrounding environment. In the Galapagos Islands, there is a significant fleet of GFRP planing hull vessels. As these boats sail at high speeds, they must be light and cover long distances between islands to comply with tourist programs; this causes severe damage to the laminates of the hull in the bow due to the impact with the waves. Sailing at high speeds increases a phenomenon known as slamming (Kapfenberg and Veer 2002). This is a fatigue event on the material of the hull of the boat, which considerably reduces its useful life, making more frequent maintenance required within the nature reserve.

Vessels built with composite materials (with different combinations of reinforcing fibers and polymeric matrix) are more and more numerous, due to the good mechanical properties of these materials. Manufacturing with composite materials involves the placement of successive layers of reinforcing fibers (glass, carbon, polyaramid, etc.) that are impregnated with a resin that acts as a matrix, providing adhesion between the fibers, between the layers stacked in thickness and provides continuity to the laminated assembly. This means in practice that the hulls are built (together with other parts of the boat) by placing several layers, one on top of the other, until the total thickness of the laminate is obtained according to their structural stresses. The number of layers is associated with the structural resistance (Qin and Batra 2009; Baucoma and Zikryb 2005) or with the other parts of the boat (decks, bulkheads,

---

P. Townsend (✉)

Escuela Superior Politécnica del Litoral, ESPOL, Guayaquil, Ecuador  
e-mail: [ptownsen@espol.edu.ec](mailto:ptownsen@espol.edu.ec)

J. C. Suárez Bermejo · A. Rodríguez-Ortíz  
Universidad Politécnica de Madrid, UPM, Madrid, Spain

etc.). A boat made of composite materials will weigh less than a boat made of steel or aluminum. The use of GFRP partially sacrifices some aspects of its structural strength. The capacity to respond to impacts, fatigue events, and internal stresses is diminished, which is directly reflected in the extension of its useful life, in service (Belingardini and Bador 2002).

On the other hand, because they are multilayer materials, it is possible to introduce some type of energy dissipation mechanism into the lamination sequence. In such a way that a viscoelastic sheet that goes inside the laminate has been proven to protect it from low energy impacts. It does not apply in cases of ballistic impacts, which imply very high deformation rates in the material.

Slamming is a phenomenon that occurs during navigation, usually above 20 km/h. The boat begins to rise or support itself on the surface of the water, and when the weight of the ship and the pressure of the water become unbalanced, it causes the ship to sink back to the initial position producing an impact on the surface of the hull. This impact supposes a sudden contribution of energy, which can be increased by the waves. This energy must be absorbed by the hull material, which after the impact returns part of the energy (compliance restoration) (Blake and Shenoi 2002).

The insertion of viscoelastic sheets inside GFRP panels has been studied extensively in a numerical way, and according to our own research on specimens tested in the laboratory, the modification proposal gives results and is ready to go to ships (Townsend and Suárez 2016, 2018). Even its adherence is applicable to the theory of hybrid bonds in the case of these materials, in which the stresses generated at the ends of the adhesive bond influence the adjacent layer of the bond (Dominguez and Carral 2020).

This time, it is proposed to analyze by means of fatigue tests, the behavior of the viscoelastic layer superimposed on the laminate to obtain the energy data that the viscoelastic absorbs and the protection it offers. The solution to the premature aging of the planing hull vessels and the way they are used in boats already built would represent a great option for the tourism fleet in the Galapagos Islands and the world.

## **2 Viscoelastic Layers as Energy Dissipators in the Construction of GFRP Laminates**

In the Galapagos Islands, there is an important fleet of planing hull vessels between 12 and 15 m in length. They sail 4 h between Puerto Ayora and Puerto Baquerizo Moreno at 22 knots in some cases. They carry tourists seated on the main deck on cushions. In this area of the Pacific Ocean, the wind level and wave height have a Beaufort scale of degree 4 half the year, and the other half with the arrival of the cold current from Antarctica, there are several months of degree 5. The captains must be attentive to the waves during the entire navigation because at that speed and in these sea conditions, the impacts with the bottom of the hull are very strong. The noise of the impact even becomes a nuisance to the human ear when reaching levels of 90 dB.

**Table 1** Characteristics of the ship at maximum load condition

| Characteristic     | Value       |
|--------------------|-------------|
| Material           | GFRP        |
| L (length)         | 13,500 [mm] |
| Δ (displacement)   | 9100 [kg]   |
| B (breadth)        | 4300 [mm]   |
| T (deadrise angle) | 4.5 [°]     |
| V (maximum speed)  | 22 [Kn]     |

The slamming phenomenon has the following specific characteristics: its nonlinear character in which the domain of time and not frequency predominates, and that it is completely random. The slamming pressures for the type of vessel considered, according to the classification societies of ships, especially the American Bureau of Shipping (ABS), consider that they range between the order of  $2.25 \times 10^3$  [kN/m<sup>2</sup>] to  $1.10 \times 10^3$  [kN/m<sup>2</sup>] depending on its longitudinal position at the bottom of the ship and by the curvature of the hull. Table 1 shows the characteristic data of the ship selected for experimentation.

The hull of these vessels corresponds to laminates by impregnation of type  $[0^{MI}/(0^M/0^{WR})_4^O/0^{MO}]$  with mat-type isophthalic fabrics, at Ortoftalic, Woveng Robing Ortoftalica. In the nomenclature, the number on the right is described as the first layer of the laminate on the outside of the hull. Due to the type of manual construction, there is a high percentage of porosity of up to (7%), which is reflected in the beginning of damage due to slamming impacts during navigation. The micropores line up forming microcracks, to later appear as fractures inside the ship. In most cases, it produces water leaks. In Fig. 1, the interior connection of the hull with the fore bulkhead of the selected ship is observed. In it, you can clearly see the breaking line that is propagating because of the tensile stresses that occur inside due to the deformation.

Previous research considered including viscoelastic sheets within the laminate, that is to say, placed under the second layer of rowing fabric protecting the rest of the layers. They are not used in the entire hull of the boat, but more critical where the phenomenon of slamming has the greatest incidence. The impact area occurs both to port and starboard, which directly affects the laminate of the hull, producing microcracks that change the flexural stiffness of the structure. To achieve this behavior, the protection layers are manufactured in very thin thicknesses with the viscoelastic polymer, encapsulating it in cells of another much more rigid polymer, constraining the deformation capacity of the viscoelastic polymer in its two main directions, in the plane of the sheet. In this way, the property of the viscoelastic material of having a Poisson’s ratio close to 0.50 is taken advantage of, that is, the relationship between the deformations that the material experiences when it is compressed in the thickness direction with the deformations in the two perpendicular directions in the plane of the sheet. A material with a Poisson’s ratio of 0.5 essentially keeps the volume constant when it is deformed in one direction.

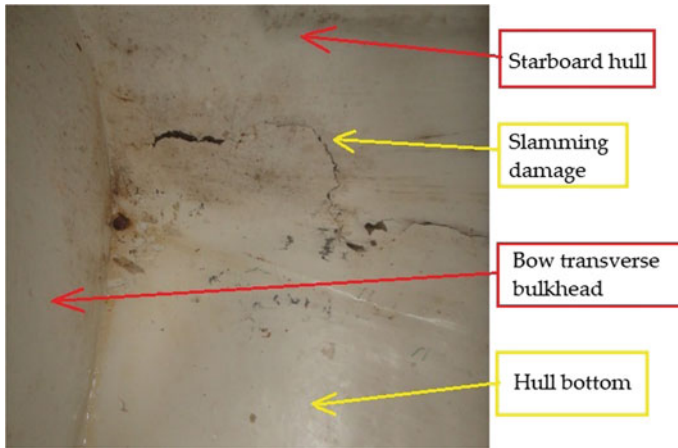


**Fig. 1** Slamming damage observed inside the vessel

When a viscoelastic is deformed by an impact without restricting its directions, it is compressed until it can no longer absorb any more energy and then expands dissipating all the elastic energy stored. On the contrary, if its deformation (expansion) is constricted in its two main directions in the plane of the viscoelastic layer, encapsulating the viscoelastic material in closed cells formed by a more rigid polymer, the material is given a great storage capacity of energy. The more the pressures due to impact increase, the stiffer the viscoelastic material becomes, and consequently, the more energy it absorbs. Through this viscoelastic cell design, when the protection layer is placed within the composite material laminate, the stiffness of the material grows exponentially as the impact energy attempts to deform the ship's hull. The response is nonlinear and instantaneous, with a large amount of energy being stored in the viscoelastic layer, which, however, does not transfer it to the rest of the laminate, but rather slowly dissipates it. In this way, it is possible to reduce the damage generated in the laminate by the impact of slamming, slowing down its progression, and, consequently, making it possible to extend the useful life of the boat.

The present work proposes the placement of the viscoelastic sheet on the surface of a boat hull already built and in use. Through laboratory tests with GFRP specimens, observe the energy behavior of the impact and if the laminate is effectively protected. This would allow the use of viscoelastic sheets to be extended and spread more widely to improve the useful life of vessels. Figure 2 shows the difference in a section of a ship's hull. In (a) the viscoelastic sheet is inserted into the laminate which corresponds to its initial conception. In (b) the proposal to adhere it to the laminate so that it does not affect the hydrodynamics of the boat and protects from damage by slamming.

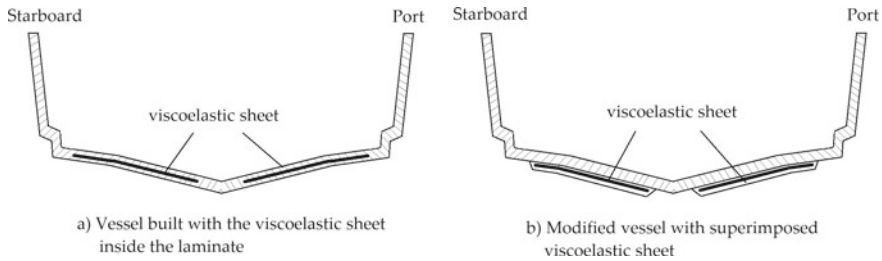


**Fig. 2** Cross-section of the planing hull vessel with a viscoelastic sheet **a** built new **b** modified not new

### 3 Experimental Observation of the Protection of the Superimposed Viscoelastic Layer

For the experimental observation of the behavior of the viscoelastic sheet superimposed on the hull of a ship, 3 panels were manufactured with the same characteristics of the selected boat, and the superimposed viscoelastic layer was added. The panels to be tested for fatigue, reproducing the slamming impact, were mounted on a base of a shaker-type vibrating equipment to deform them. This equipment, its base, the panel and the superimposed viscoelastic sheet, can be seen in Fig. 3.

Using a load cell on the top of the vibrator to compress with the panel, the force that deforms the panel is measured. As the vibrating equipment tries to maintain a deformation speed, it regulates the acceleration, and therefore, the load cell fulfills the function of registering the changes in force versus cycle. The equipment records the accelerations and the deformation velocity at the center of the impact. Strain gauges were also used to control the deformation of the panel at 4 [cm] of impact



**Fig. 3** Impact vibrator with the test panel placed on the top

**Table 2** Experimental values of the tests carried out

| # Panel | Frequency range [Hz] | Applied cycles [n] | Average strength [kJ] | Amplitude [G] |
|---------|----------------------|--------------------|-----------------------|---------------|
| A       | 5–10                 | $5 \times 10^4$    | 50                    | 1             |
| B       | 5–10                 | $5 \times 10^4$    | 40                    | 1             |
| C       | 5–10                 | $5 \times 10^4$    | 30                    | 1             |

for control. In Table 2, the experimental values of the developed experiments are presented. The fatigue phenomenon was reduced on three panels at different force conditions, equal amplitude, and acceleration.

To evaluate the energy that the panel returns as mechanical work, the principle that a force  $F$  travels a distance  $x$  is applied. Laboratory reproductions were made for different frequencies  $\omega$  over the angle between the force vector and the displacement vector  $Y$ , for each acceleration  $G$  at time  $t$  obtain the Eq. 1 which corresponds to the energy returned by the panel over the shaker.

$$E = Y.\omega \int G(t).dt \tag{1}$$

When carrying out the tests, results were obtained such as those shown in Fig. 4. In (a) it is observed that the acceleration imposed by the vibrating equipment on panel A is rectified to maintain a regular profile curve. The peaks of highs and lows correspond to microdamage produced during deformation due to the laminate opposing bending. The acceleration curve corresponds to a test time of 60 [ms]. With this imposed acceleration, it is observed in (a) that the panel impacted at  $7 \times 10^3$  cycles presents microcracks around the areas of the viscoelastic in a minimal amount. In (b) at  $5 \times 10^4$  cycles of impacts made on average at 50 [KJ], microcracks have increased without detachment of the viscoelastic layer in the matrix.

Data were taken on the force exerted by the vibrator equipment in the impact versus cycles, and this is observed in Fig. 5. For panels A and C, there is a tendency to decrease, being greater that of panel A. On the other hand, the panel B showed a very complex dispersion to evaluate a trend. The results of panel B are not conclusive.

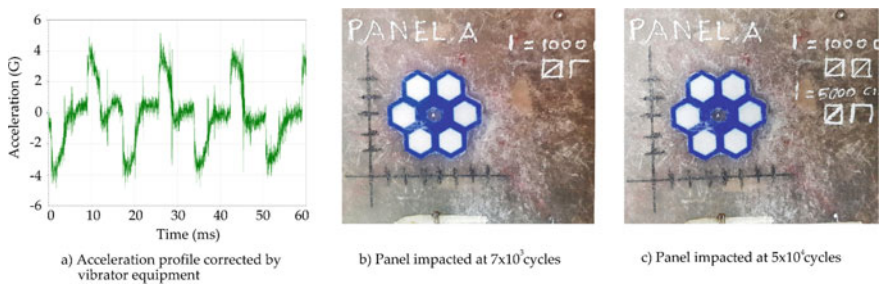


**Fig. 4** Results of the tests carried out on panel A

**Fig. 5** Sampling of the applied force in the panels versus impact cycles

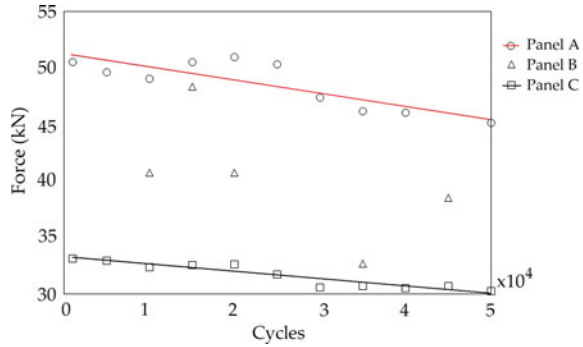
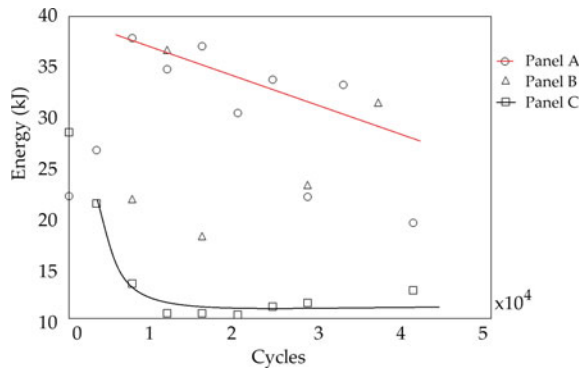


**Fig. 6** Energy returned by the panels versus impact cycles



During the tests, it was found that the force tends to regulate with the acceleration since the vibrating equipment stabilizes in the acceleration to deform in constant values over time. Force values are sampled because the type of load cell used does not allow a permanent record to be kept.

When these force values are transformed to returned energy, they draw the trend curves shown in Fig. 6. Panel A permanently loses its ability to return energy since the measured force that is regulated in the vibrator is still at damage levels. Panel B, product of force dispersion, does not show a trend curve. Panel C draws a trend curve that tends to stabilize, meaning that flexural stiffness has increased due to the level of damage reaching the threshold.

## 4 Conclusions

By superimposing the viscoelastic layer on the GFRP panels, the impact damage can be effectively mitigated. Figure 6 shows that the increase in flexural stiffness in a panel works in conjunction with the viscoelastic sheet stabilizing the damage. This trend curve, as it stabilizes, is the increase in useful life that we wanted to



demonstrate. The generation and propagation of damage is controlled by improving the dissipation of the energy that remains in the form of damage in the GFRP. This approach opens up new perspectives in the design of the planing hull ship since the superposition of the viscoelastic layers changes the way in which the stresses due to the phenomenon of slamming within the laminate are to be distributed and concentrated.

## References

- Baucoma, J., Zikryb, M.: Low-velocity impact damage progression in woven E-glass composite systems. *Compos. Part A. Appl. Sci. Manuf.* **36**, pp. 658–664 (2005), Section 5
- Belingardini G, Bador V (2002) Low velocity impact tests of laminate glass-fiber-epoxy matrix composite material plates *International Journal of Impact Engineering*, Vol 27, section 2, pp. 213–219
- Blake, J., Sheno, R.: Strength modelling in stiffened FRP structures with viscoelastic inserts for ocean structures. *University of Southampton, UK Ocean Engineering* **29**, 849–869 (2002)
- Dominguez, F., Carral, L.: The hybrid joints between an FRP panel and a steel panel through tubular reinforcements: a methodology for interlaminar stress calculations. *Appl. Phys.* **10**(11), 3962 (2020). <https://doi.org/10.3390/app10113962>
- Kapfenberg, G., Veer, A.: Whipping loads due to aft body slamming. In: 24th Symposium on Naval Hydrodynamics, Japan, pp. 336–337 (2002)
- Qin, Z., Batra, R.: Local slamming impact of sandwich composite hulls. *Int. J. Solids Struct.* **46**, 2011–2035 (2009)
- Townsend, P., Suárez, J.C.: The effect of slamming impact on out-of-autoclave cured prepregs of GFRP composite panels for hulls. *Procedia Eng.* **167**, 252–326 (2016)
- Townsend, P., Suárez, J.C.: Reduction of slamming damage in the hull of high-speed crafts manufactured from composite materials using viscoelastic layers. *Ocean Eng.* **159**, 253–267 (2018)

# On the Contact Between Viscoelastic Tube with Inner Nonuniform Coating and Several Rigid Inserts



Kirill E. Kazakov  and Svetlana P. Kurdina 

## 1 Introduction

In industry, mechanical engineering, construction, pipes made of several layers are often used. This is due to the fact that structures made of pipes can be exposed to a variety of aggressive environments, must meet safety requirements, meet additional requirements, etc. Some layers of such pipes may be inhomogeneous due, for example, to the peculiarities of the manufacturing process (Parshin and Manzhairov 2018; Parshin 2021). Ring-shaped rigid inserts can be used to connect various pipe sections, as well as for reinforcing long sections. The presence of inserts leads to a change in the stress–strain state of the pipe. The article is devoted to the formulation and construction of an analytical solution to the problem of the interaction of several annular inserts and a viscoelastic aging pipe with an internal inhomogeneous coating. The solution of such a problem is reduced to the solution of a system of integral equation with integral operators of two types (Arutyunyan and Manzhairov 1999).

The construction of a solution for such a system is carried out using a special approach and is similar to what was done in articles (Kazakov 2018; Kazakov and Parshin 2019; Kazakov and Kurdina 2019).

---

K. E. Kazakov (✉)

Ishlinsky Institute for Problems in Mechanics of the Russian Academy of Sciences, pr. Vernadskogo 101-1, Moscow, Russia  
e-mail: [kazakov@ipmnet.ru](mailto:kazakov@ipmnet.ru)

S. P. Kurdina

Bauman Moscow State Technical University, ul. 2 Baumanskaya 5-1, Moscow, Russia  
e-mail: [kurdinasp@bmstu.ru](mailto:kurdinasp@bmstu.ru)

## 2 Mathematical Model of the Problem

Let the pipe consists of two layers: an outer viscoelastic aging layer with a thickness of  $H$  and an inner elastic layer with a thickness of  $h$ . If  $r_{in}$  is the inner radius of the outer layer, and  $r_{out}$  is its outer radius, then thickness  $H = r_{out} - r_{in}$ . We will assume that inner layer thickness  $h$  is much less than the pipe inner radius  $r_{in}$  and the outer layer thickness  $H$ . There is a smooth contact between layers. It is believed that the stiffness of the inner layer is less than the stiffness of the outer layer. Inner layer has longitudinal inhomogeneity, i.e., its properties (Young’s modulus  $E_{in}(z)$  and Poisson’s ratio  $\nu_{in}(z)$ ) depend on longitudinal coordinate  $z$ . The construction of a solution for such a system is carried out using a special approach and is similar to what was done in articles (Kazakov 2018; Kazakov and Parshin 2019; Kazakov and Kurdina 2019).

At time  $\tau_{start}$ , several cylindrical inserts are placed inside such a tube with tension. There is a smooth contact between the inner layer and the inserts. All of them can have different external radii and widths significantly exceeding the thickness of the inner layer of the pipe. Inserts external radii are not less than the inner radius of the inner layer. The contact areas do not change over time and coincide with the widths of the inserts.

The interaction scheme is shown in Fig. 1.

Generalization of the results presented in papers (Arutyunyan and Manzhurov 1999; Manzhurov and Chernysh 1990) allows us to establish that the mathematical model of the problem is the following system of  $n$  mixed integral equations ( $n$  is account of inserts):

$$E_{in}^{-1}(z)h[1 - \nu_{in}^2(z)]p_i(z, t) + 2\pi^{-1}(1 - \nu_{out}^2) \sum_{j=1}^n \left[ E_{out}^{-1}(t - t_{out}) \int_{a_j}^{b_j} C_c(r_{in}^{-1}(z - \zeta))p_j(\zeta, t)d\zeta \right]$$

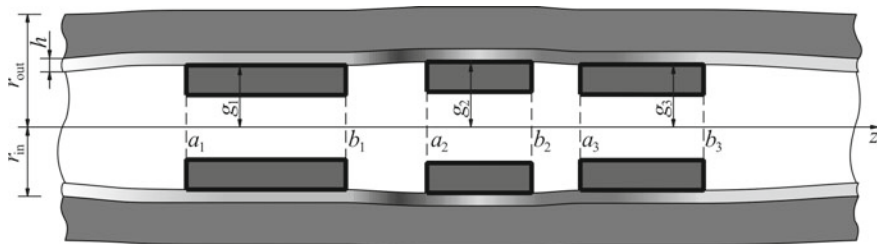


Fig. 1 Interaction of tube with coating and three rigid inserts

$$\left. - \int_{\tau_{\text{start}}}^t E_{\text{out}}^{-1}(\tau - \tau_{\text{out}}) V_{\text{out}}(t - t_{\text{out}}, \tau - t_{\text{out}}) \int_{a_j}^{b_j} F_c(r_{\text{in}}^{-1}(z - \zeta)) p_j(\zeta, \tau) d\zeta d\tau \right]$$

$$= g_i - (r_{\text{in}} - h), \quad a_i \leq z \leq b_i, \quad t \geq \tau_{\text{start}}, \quad i = 1, 2, \dots, n. \tag{1}$$

The following designations are introduced here:  $p_i(x, t)$  is distribution of contact pressures in the region of interaction between the  $i$ th insert and the pipe;  $\nu_{\text{out}}$  and  $E_{\text{out}}(t)$  are Poisson's ratio and Young's modulus of outer viscoelastic aging layer;  $t_{\text{out}}$  is the moment of manufacture of the outer layer;  $V_{\text{out}}(t, \tau)$  is creep kernel of outer layer (Arutyunyan and Manzhairov 1999; Arutyunyan 1927); it can be presented, for example, as

$$V_{\text{out}}(t, \tau) = \partial [C_{\text{out}}(t, \tau) + E_{\text{out}}^{-1}(\tau)] / \partial \tau E_{\text{out}}(\tau),$$

where  $C_{\text{out}}(t, \tau)$  is the tensile creep function,  $F_c(y)$  is known kernel of the contact problem for cylindrical tube with inner loading (Arutyunyan and Manzhairov 1999; Manzhairov and Chernysh 1990):

$$F_c(y) = \int_0^\infty \cos(yu) u^{-1} L(u) du,$$

in which following notations are introduced ( $I_0(u), I_1(u), K_0(u), K_1(u)$  are modified Bessel functions of first and second kind)

$$\begin{aligned}
 L(u) &= S^{-1}(u) u [k_r^{-1} + s(k_r, u) D_1^2(u) - u^2 k_r C_1^2(u)], \\
 s(r, u) &= 2r^{-1} (1 - \nu_{\text{out}}) + r u^2, \quad k_r = r_{\text{in}}^{-1} r_{\text{out}}, \\
 S(u) &= s(k_r, u) + k_r^{-1} s(1, u) - s(k_r, u) B_1^2(u) u^2 + k_r A_1^2(u) u^4 \\
 &\quad + s(1, u) s(k_r, u) D_1^2(u) - k_r u^2 s(1, u) C_1^2(u), \\
 A_1(u) &= -I_0(uk_r) K_0(u) + I_0(u) K_0(uk_r), \quad B_1(u) = I_1(uk_r) K_0(u) + I_0(u) K_1(uk_r), \\
 C_1(u) &= I_1(u) K_0(uk_r) + I_0(uk_r) K_1(u), \quad D_1(u) = -I_1(uk_r) K_1(u) + I_1(u) K_1(uk_r).
 \end{aligned} \tag{2}$$

Note that the resulting system includes functions describing the inner layer inhomogeneity, which can change rapidly. Moreover, it contains integrals with both constant and variable limits of integration.

### 3 Mathematical Model in Dimensionless Form

Imagine the resulting dimensional system of integral Eq. (1) as dimensionless system

$$e^*(t^*)D^i(z^*)p^{i*}(z^*, t^*) + \sum_{j=1}^n F^{ij*}(\mathbf{I} - \mathbf{V}^*)p^{j*}(z^*, t^*) = g^{i*}, \quad (3)$$

$$i = 1, 2, \dots, n, \quad -1 \leq z^* \leq 1, \quad t^* \geq 1.$$

The following change of variables and functions is used in this equation ( $i, j = 1, 2, \dots, n$ )

$$\begin{aligned} z^* &= 2\bar{a}_i^{-1}(z - \eta_i), \quad \xi^* = 2\bar{a}_j^{-1}(\xi - \eta_j), \\ t^* &= \tau_{\text{start}}^{-1}t, \quad \tau^* = \tau_{\text{start}}^{-1}\tau, \quad t_{\text{out}}^* = \tau_{\text{start}}^{-1}t_{\text{out}}, \quad \eta^{i*} = 2\bar{a}^{-1}\eta_i, \\ g^{i*} &= 2\bar{a}^{-1}[g_i - (r_{\text{in}} - h)], \quad e^*(t^*) = E_{-1}E_{\text{out}}(t - t_{\text{out}}), \\ D^{i*}(z^*) &= \frac{1}{E_{-1}E_{\text{in}}(z)} \frac{1 - \nu_{\text{in}}^2(z)}{1 - \nu_{\text{out}}^2} \frac{h}{\bar{a}_i}, \quad p^{i*}(z^*, t^*) = \frac{2p_i(z, t)}{E_{\text{out}}(t - \tau_{\text{out}})} (1 - \nu_{\text{out}}^2) \frac{\bar{a}_i}{\bar{a}}, \\ F^{ij*}y(z^*) &= \int_{-1}^1 y(\xi^*)F^{ij}(z^*, \xi^*)d\xi^*, \quad \mathbf{V}^*y(t^*) = \int_1^{t^*} y(\tau^*)V^*(t^*, \tau^*)d\tau^*, \\ F^{ij}(z^*, \xi^*) &= \pi^{-1}F_c(r_{\text{in}}^{-1}(z - \zeta)), \quad V^*(t^*, \tau^*) = \tau_0V_{\text{out}}(t - t_{\text{out}}, \tau - t_{\text{out}}). \end{aligned} \quad (4)$$

Here,  $\mathbf{I}$  is identity operator;  $\eta_i = 0.5(a_i + b_i)$  is the midpoint of the  $i$ th insert;  $\bar{a}_i = b_i - a_i$  is its width,  $\bar{a} = \min_{i=1,2,\dots,n} \bar{a}_i$ , and  $E_{-1}$  is dimensional modulus; it can be calculated, for example, as  $E_{-1} = 1/E_{\text{out}}(0)$ . Note that  $\mathbf{V}^*$  is Volterra integral operator and  $F^{ij*}$  are Frenholm integral operators.

For convenience, we present system (3) in operator form

$$e^*(t^*)\mathbf{D}^*(z^*)\mathbf{p}^*(z^*, t^*) + \mathbf{F}^*(\mathbf{I} - \mathbf{V}^*)\mathbf{p}^*(z^*, t^*) = \mathbf{g}^*, \quad z^* \in [-1, 1], \quad t^* \geq 1. \quad (5)$$

Here

$$\begin{aligned} \mathbf{p}^*(z^*, t^*) &= \begin{pmatrix} p^{1*}(z^*, t^*) \\ p^{2*}(z^*, t^*) \\ \vdots \\ p^{n*}(z^*, t^*) \end{pmatrix}, \quad \mathbf{F}^* = \begin{pmatrix} F^{11*} & F^{12*} & \dots & F^{1n*} \\ F^{21*} & F^{22*} & \dots & F^{2n*} \\ \vdots & \vdots & \ddots & \vdots \\ F^{n1*} & F^{n2*} & \dots & F^{nn*} \end{pmatrix}, \\ \mathbf{g}^* &= \begin{pmatrix} g^{1*} \\ g^{2*} \\ \vdots \\ g^{n*} \end{pmatrix}, \quad \mathbf{D}^*(z^*) = \begin{pmatrix} D^1(z^*) & 0 & \dots & 0 \\ 0 & D^2(z^*) & \dots & 0 \\ \vdots & \vdots & \ddots & \vdots \\ 0 & 0 & \dots & D^n(z^*) \end{pmatrix}. \end{aligned} \quad (6)$$

$\mathbf{F}^*$  is Frenholm integral operator with Hilbert–Schmidt kernel (Goursat).

In the resulting Eq. (3), the  $\mathbf{p}^*(z^*, t^*)$  vector function is to be determined. It is related to the dimensional functions  $p_i(z, t)$  describing contact pressures by the ratios (4).

It is two main problems in Eq. (6):

- (1) functions  $D^i(z^*)$  can be rapidly changing (they connect with layer properties)
- (2) equation includes operators of different types (Volterra and Fredholm).

## 4 Solution of the Problem

If in Eq. (6) of work (Kazakov and Parshin 2019), we assume that  $\boldsymbol{\alpha}(t) \equiv 0$ ,  $\mathbf{g}(x) \equiv 0$ ,  $\delta(t) = \text{const}$ , then we get equation similar to Eq. (5) from this work. Moreover, the properties and asymptotics of the kernels included in the operators of the corresponding equations are similar. Therefore, the approach to constructing a solution will be similar to that described in Kazakov and Parshin (2019). Next, we describe the main provisions of this approach.

First of all, it is necessary to present the desired function in a special form

$$\mathbf{p}^*(z^*, t^*) = \mathbf{D}^{-1/2*}(z^*) \cdot \mathbf{P}^*(z^*, t^*) \quad (7)$$

where  $\mathbf{D}^{-1/2*}(z^*)$  is diagonal matrix on the diagonal of which the functions  $1/\sqrt{D^1(z^*)}$ ,  $1/\sqrt{D^2(z^*)}$ , ...,  $1/\sqrt{D^n(z^*)}$  are located,  $\mathbf{P}^*(z^*, t^*)$  is new unknown function. In this case, the operator equation is transformed in the form

$$e^*(t^*)\mathbf{P}^*(z^*, t^*) + \tilde{\mathbf{F}}^*(\mathbf{I} - \mathbf{V}^*)\mathbf{P}^*(z^*, t^*) = \mathbf{D}^{-1/2*}\mathbf{g}^*, \quad -1 \leq z^* \leq 1, \quad t^* \geq 1. \quad (8)$$

Here,  $\tilde{\mathbf{F}}^*$  is new Fredholm operator. The properties of the kernel of this operator are the same as the properties of the kernel of the original operator  $\mathbf{F}^*$ .

Secondly, it is necessary to use a special orthonormal basis constructed using orthogonalization of the following system of linearly independent functions

$$\mathbf{i}^1/\sqrt{D^1(z^*)}, z^*\mathbf{i}^1/\sqrt{D^1(z^*)}, (z^*)^2\mathbf{i}^1/\sqrt{D^1(z^*)}, \dots, \mathbf{i}^2/\sqrt{D^2(z^*)}, z^*\mathbf{i}^2/\sqrt{D^2(z^*)}, (z^*)^2\mathbf{i}^2/\sqrt{D^2(z^*)}, \dots, \mathbf{i}^n/\sqrt{D^n(z^*)}, z^*\mathbf{i}^n/\sqrt{D^n(z^*)}, (z^*)^2\mathbf{i}^n/\sqrt{D^n(z^*)}, \dots,$$

where  $\mathbf{i}^i$  is orthonormal basis with the  $i$ th unit coordinate. This basis can be obtained by formulas (Szegő 1959)

$$\mathbf{q}_k^i(z^*) = \frac{q_k^{i\circ}(z^*)}{\sqrt{D^i(z^*)}} \mathbf{i}^i, \quad q_k^{i\circ}(z^*) = \frac{1}{\sqrt{\delta_{k-1,i} \delta_{k,i}}} \begin{vmatrix} I_{0,i} & I_{1,i} & \cdots & I_{k,i} \\ I_{1,i} & I_{2,i} & \cdots & I_{k+1,i} \\ \vdots & \vdots & \ddots & \vdots \\ 1 & z^* & \cdots & (z^*)^k \end{vmatrix},$$

$$I_{k,i} = \int_{-1}^1 \frac{(\xi^*)^k}{D^i(\xi^*)} d\xi^*, \quad \delta_{-1,i} = 1, \quad \delta_{k,i} = \begin{vmatrix} I_{0,i} & I_{1,i} & \cdots & I_{k,i} \\ I_{1,i} & J_{2,i} & \cdots & I_{k+1,i} \\ \vdots & \vdots & \ddots & \vdots \\ I_{k,i} & I_{k+1,i} & \cdots & I_{2k,i} \end{vmatrix}.$$

Thirdly, it is necessary to find the eigenvector functions  $\psi_k(z^*)$  ( $k = 0, 1, 2, \dots$ ) of the operator  $\tilde{F}^*$ :

$$\tilde{F}^* \psi_k(z^*) = \gamma_k \psi_k(z^*),$$

where  $\gamma_k$  is eigenvalues of operator  $\tilde{F}^*$ . Vector functions  $\psi_k(z^*)$  are linear combination of basis functions  $\mathbf{q}_k^i(z^*)$ , i.e.,

$$\psi_k(z^*) = \sum_{m=0}^{\infty} \psi_{km}^i \mathbf{q}_m^i(z^*).$$

If we represent function  $P^*(z^*, t^*)$  as a series

$$P^*(z^*, t^*) = \sum_{k=0}^{\infty} k_k(t^*) \psi_k(z^*),$$

then it is possible to bring the system of Eq. (8) for the functional coefficients of the decomposition of the solution to a diagonal form:

$$\sum_{k=0}^{\infty} [e^*(t^*) k_k(t^*) + (\mathbf{I} - \mathbf{V}^*) \gamma_k k_k(t^*)] \psi_k(z^*) = \mathbf{D}^{-1/2} \mathbf{g}^*, \tag{9}$$

$$-1 \leq z^* \leq 1, \quad t^* \geq 1.$$

After that, it is necessary to decompose the right part of (9) according to the basic functions  $\psi_k(z^*)$  and equate the coefficients on the left and on the right with the corresponding basic functions  $\psi_k(z^*)$ .

Applying the above approach, we obtain the final formulas for the desired dimensionless functions:

$$p^{i*}(z^*, t^*) = \frac{1}{D^i(z^*)} \sum_{k=0}^{\infty} k_k(t^*) \sum_{m=0}^{\infty} \psi_{km}^i q_m^{i\circ}(z^*),$$

$$i = 1, 2, \dots, n, \quad -1 \leq z^* \leq 1, \quad t^* \geq 1, \tag{10}$$

where

$$k_k(t^*) = (\mathbf{I} + \mathbf{V}_k) \frac{\sum_{i=1}^n \psi_{k0}^i \sqrt{I_{0,i}} \delta^{i*}}{\gamma_k + e^*(t^*)},$$

$$\mathbf{V}_k y(t^*) = \int_1^{t^*} y(\tau^*) \mathbf{V}_k^*(t^*, \tau^*) d\tau^*, \quad I_{k,i} = \int_{-1}^1 \frac{(\xi^*)^k}{D^i(\xi^*)} d\xi^*, \quad \delta_{-1,i} = 1,$$

$$q_k^{i\circ}(z^*) = \frac{1}{\sqrt{\delta_{k-1,i} \delta_{k,i}}} \begin{vmatrix} I_{0,i} & I_{1,i} & \cdots & I_{k,i} \\ I_{1,i} & I_{2,i} & \cdots & I_{k+1,i} \\ \vdots & \vdots & \ddots & \vdots \\ 1 & z^* & \cdots & (z^*)^k \end{vmatrix},$$

$$\delta_{k,i} = \begin{vmatrix} I_{0,i} & I_{1,i} & \cdots & I_{k,i} \\ I_{1,i} & I_{2,i} & \cdots & J_{k+1,i} \\ \vdots & \vdots & \ddots & \vdots \\ I_{k,i} & I_{k+1,i} & \cdots & I_{2k,i} \end{vmatrix},$$

$$i = 1, 2, \dots, n, \quad k = 0, 1, 2, \dots, \quad -1 \leq z^* \leq 1, \quad t^* \geq 1, \tag{11}$$

in which kernels  $V_k(t^*, \tau^*)$  are the resolvents of the  $V^*(t^*, \tau^*)\gamma_k/[\gamma_k + e^*(t^*)]$ ; parameters  $\gamma_k$  and  $\psi_{km}^i$  can be found from solution of the spectral problem

$$\sum_{j=1}^n \sum_{l=0}^{\infty} \psi_{km}^j F_{ml}^{ij} = \psi_{km}^i \gamma_k, \quad i = 1, 2, \dots, n, \quad k, m = 0, 1, 2, \dots, \tag{12}$$

and  $K_{ml}^{ij}$  are calculated by the expression

$$F_{ml}^{ij} = \int_{-1}^1 \int_{-1}^1 \frac{F^{ij}(z^*, \xi^*) q_m^{i\circ}(z^*) q_l^{j\circ}(\xi^*)}{D^i(z^*) D^j(\xi^*)} dz^* d\xi^*, \quad i, j = 1, 2, \dots, n,$$

$$m, l = 0, 1, 2, \dots \tag{13}$$

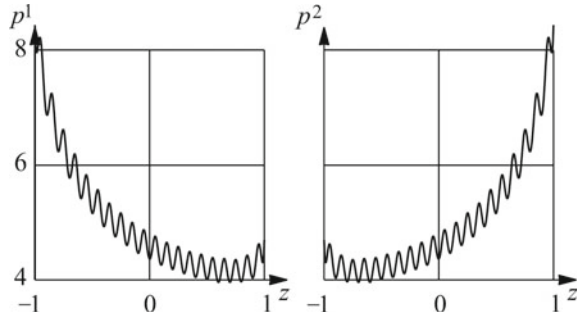
Formulas (4) and (6) allow us to obtain dimensional contact stresses from expression (10):

$$p^i(z, t) = [1 - v_{in}(z)]^{-1} E_{in}(z) \sum_{k=0}^{\infty} \tilde{k}_k(t) \sum_{m=0}^{\infty} q_m^{i\circ} \left( \frac{2z - (a_i + b_i)}{b_i - a_i} \right) \psi_{km}^i,$$

$$i = 1, 2, \dots, n, \quad a_i \leq z \leq b_i, \quad t \geq \tau_0, \tag{14}$$



**Fig. 2** Contact pressures in interaction regions



where

$$\tilde{k}_k(t) = 0.5E_{-1}E_{out}(t - \tau_{out})h^{-1}\bar{a}k_k(\tau_0^{-1}t), \quad k = 0, 1, 2, \dots, \quad t \geq \tau_0. \quad (15)$$

In the obtained expressions (10) and (14), the functions  $\tilde{k}_k(t)$ , and  $q_m^{i\circ}(z^*)$  are continuous and smooth, and the functions associated with the variable properties of the inner layer and their combinations are highlighted by separate multipliers.

## 5 Conclusions

Due to the representation of the solution in the form (14), in which the functions describing the properties of the coating are allocated in a separate multiplier, it becomes possible to perform efficient calculations even when the inhomogeneity of the inner layer is described by a rapidly changing or discontinuous function. Example of contact stresses distributions for such a case presented in Fig. 2. There is considered a case when two inserts that are not far from each other are placed in a cylinder, inhomogeneous coating of which is described by the functions  $D^1(z) = D^2(z) = 0.01(1 - 0.05\cos(2\pi z))$ .

Thus, a solution has been constructed to take into account the influence of the rheological properties of the pipe, the inhomogeneity of its layers and the proximity of inserts on the distribution of contact pressures.

**Acknowledgements** The study was supported by the Government program (contract #AAAA-A20-120011690132-4).

## References

- Arutyunyan, N.Kh.: Some Questions in the Creep Theory. Gostekhizdat, Moscow–Leningrad (1927) (in Russian) (1952)
- Arutyunyan, N.Kh., Manzhairov, A.V.: Contact Problems of the Theory of Creep. Izdat. NAN RA, Erevan (1999) (in Russian)
- Goursat, E.: Cours d'Analyse Mathématique, Tome III. Intégrales Infiniment Voisines; Équations aux Dérivées Partielles du Second Order; Équations Intégrales; Calcul des Variations. Gauthier–Villars, Paris
- Kazakov, K.E.: Contact between a regular system of punches and a layered foundation with consideration of complex surface shapes. AIP Conf. Proc. **2053**, 040041 (2018). <https://doi.org/10.1063/1.5084479>
- Kazakov, K.E., Kurdina, S.P.: Multiple contact problem for bodies with nonuniform coatings of variable thickness and regular systems of punches with complex base shape. J. Phys: Conf. Ser. **1203**, 012019 (2019). <https://doi.org/10.1088/1742-6596/1203/1/012019>
- Kazakov, K.E., Parshin, D.A.: On the indentation of a system of punches into a layered foundation. Eng. Lett. **27**(1), 251–255 (2019)
- Manzhairov, A.V., Chernysh, V.A.: Contact problem for a layered inhomogeneous aging cylinder reinforced by a rigid ring. J. Appl. Mech. Tech. Phys. **31**, 894–900 (1990). <https://doi.org/10.1007/BF00854204>
- Parshin, D.A.: Technological controlling the contact pressure onto a cylindrical substrate from a coating being formed additively on its outer surface. AIP Conf. Proc. **2340**, 040005 (2021). <https://doi.org/10.1063/5.0047838>
- Parshin, D.A., Manzhairov, A.V.: The mechanical problems on additive manufacturing of viscoelastic solids with integral conditions on a surface increasing in the growth process. J. Phys: Conf. Ser. **991**, 012063 (2018). <https://doi.org/10.1088/1742-6596/991/1/012063>
- Szegő, G.: Orthogonal Polynomials. American Mathematical Society, Providence (1959)

# Failure Modes of Skull Bone of a Dog Head Under Impact Loading



Reda M. Othman , M. A. Hassan , and Wael M. Khierldeen 

## 1 Introduction

Many pets and wild animal subject to accidents that cause either skull or brain damage. Brain injuries are devastating and, unfortunately, often fatal. There are both primary brain injuries that are the result of a direct insult to the pets' brain, and secondary brain injuries that occur following the primary brain injury. Secondary brain injuries may include bleeding from a brain blood vessel or swelling of brain tissue. In animal as well as in human the soft tissue of the brain is surrounded and protected with the skull casing, so it is considered the main line of defense for the brain soft tissue from any external head trauma. Traumatic brain injuries (TBI) and skull fractures have serious ramifications (Iboaya et al. 2019); both may lead to permanent disability, mental infirmity, and even death especially in old pets and human patients (Peloso et al. 2003; Syring et al. 2001). Mechanically, skull fractures arise from dynamic impact load such as falling from a height, car accident, and violent interactions. Therefore, studying the skull bone behavior under dynamic impact load is essential to understand the mechanisms of fracture to develop tolerance criteria and to provide fundamental data to mathematical analogs such as the finite element model this will help to improve the design consideration of safety systems

---

R. M. Othman · W. M. Khierldeen (✉)

Department of Mechanical Engineering Faculty of Engineering, Assut University, Assut 71516, Egypt

e-mail: [wael.khaireldin@ejust.edu.eg](mailto:wael.khaireldin@ejust.edu.eg)

M. A. Hassan

Materials Science and Engineering Department, Egypt-Japan University of Science and Technology, New Borg El Arab, Egypt

W. M. Khierldeen

Industrial and Manufacturing Engineering Department, Egypt-Japan University of Science and Technology, New Borg El Arab, Egypt

for pets especially domesticated animals like dogs, donkeys, and horses. The biomechanical characteristics of skull fracture have been studied widely (Distriquin et al. 2020; Nahum and Melvin 2002). Some important mechanical parameters have been discussed such as force, sectional elastic modulus, energy absorbed, shear stress, acceleration deformation, and bending stress. It was found that velocity, strain rate, sampling position and inter cranial variation all have a marked effect on some of the mechanical parameters (Jennett and MacMillan 1981). Simon R. et al., used a clinical coma scale modified from the Glasgow Coma Scale used for humans to predict outcomes of dog head trauma resulted from many different events, including motor vehicle accidents, bites, kicks, or penetrating injuries such as gunshot wounds (Platt et al. 2001). S. Chocron et al., studied Cortical bone tensile mechanical properties at quasistatic and high rates ( $\sim 300 \text{ s}^{-1}$ ) were determined ex vivo using the right femurs of 12 female baboons from different using split Hopkinson pressure bar technique. They found that the dynamic strength results of baboon bones increase slightly with respect to quasistatic results (Chocron et al. 2012). However, despite all efforts done to characterize the skull fracture parameters, there is a shortage in data describing skull crack behavior, how it propagates, and skull fracture patterns (Motherway et al. 2009; Delye et al. 2007). In this paper, the effect of in vivo dog head trauma under dynamic loading and at high strain rates using SHPB is presented, the fractography fractures skulls is used with aid of CT scan and Postmortem analysis to make a complete understand of the three types of skull fracture (depressed, fisher, and compound elevated skull fractures). Baladi Egyptian dogs' specie were used in the test as they are wild tough species with strong bone structure (the samples was taken from street dog that was about to killed by the local authorities). Baladi dogs are the original sight hounds of the Middle East, descendants of the Egyptian Saluki, and Pharaoh Hounds.

## 2 Dog Head Structure and Testing Method

### 2.1 Overview of Dog Head Anatomy

Dog head skull is a complicated structure formed from several bones arranged and connected together by interconnecting joints which called sutures as shown in Fig. 1a. Skull bones are separated into two groups forming cranial and facial bones which have a slightly different bone thicknesses and densities from dog to dog, The dog head (cranium) constructs from multilayers as shown in Fig. 1b, it can be ordered from the outside to inside as follow, the scalp, muscles, skull, meninges, and then the brain. The temporal muscles which surround the flat and Cranium bones varied in thickness. Then the periosteum which is a fibrous membrane attaches to the skull bone and is responsible for bone healing after injury. This study focused on the cranial bones, which form the cranial cavity and houses the brain, two important parts of the cranial bone are the frontal and the parietal bones, both form the upper casing for

the brain, and are made mainly from flat bones. The flat bone consists of three layers in which the outer and inner layers are compact dense cortical bones. However, the former layer is thicker than the latter, while the middle layer (spongy, cancellous or trabecular bone-diploe) is sandwiched between the previous two layers (Kaminski et al. 2019), but near the sagittal crest line there is not diploe.

Test preparation. Six clinically healthy adult (same age) male dogs were used for this study. All animals have been checked clinically before the experiments, none of the animals showed medical problems or neurological disorders. The animals were housed in a clean, dry individual cage with food and water available 24 hs/day. The

**Fig. 1** **a** Dog skull anatomy, **b** cross section in frontal bone describing the 3 main layers

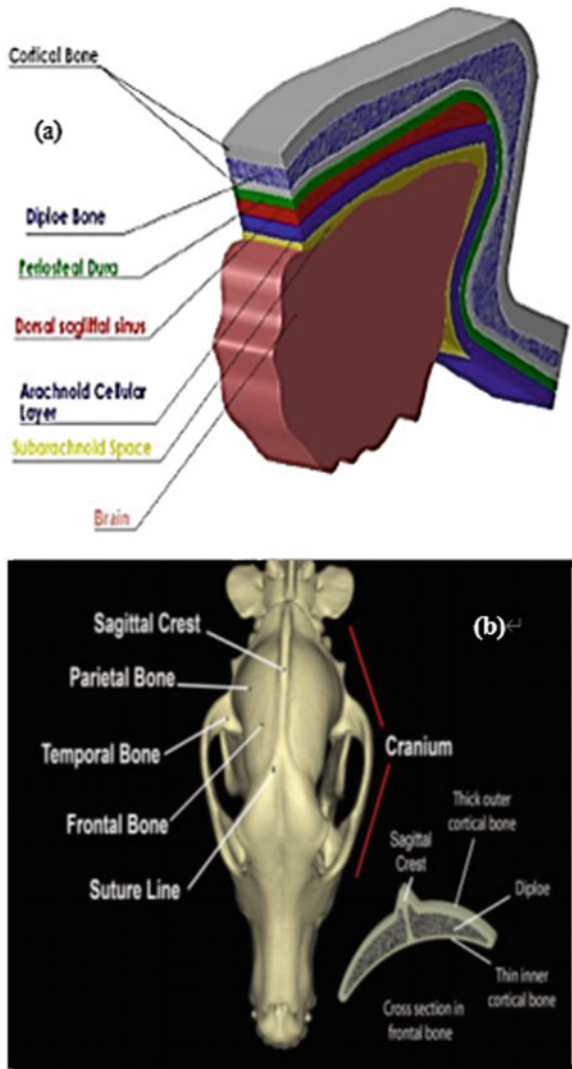


**Table 1** Tested dogs' data

| No. | Head circumference (mm) | Skull cranium circumferences (mm) | Bone density impact site (mg/cm <sup>3</sup> ) | Bone density cranial vault (HU) (mg/cm <sup>3</sup> ) | Bone thickness impact site (mm) | Temporal muscle thickness impact site (mm) |
|-----|-------------------------|-----------------------------------|--|---|---------------------------------|--|
| 1   | 335.2                   | 230.1                             | 980  | 1005  | 4.88                            | 10   |
| 2   | 339.21                  | 222.18                            | 1122   | 1037  | 5.1                             | 5.62                                       |
| 3   | 371.43                  | 214.88                            | 932.98   | 1000.5  | 6.06                            | 6.74                                       |
| 4   | 394.54                  | 240                               | 919.22   | 924.28  | 4.44                            | 16.22                                      |
| 5   | 375.94                  | 199.89                            | 994.5  | 1007.6  | 6.05                            | 8.96                                       |
| 6   | 356.24                  | 235.51                            | 849.52   | 920   | 6.2                             | 11.82                                      |

experimental study was executed according to the roles of the ethical Committee of the Faculty of Veterinary Medicine, Assuit University, Egypt. Food was withheld 12 h before the experiment and water for four hours before. General anesthesia using diazepam (...mg/kg) followed by ketamine (5.0 mg/kg, IM) and xylazine HCl (1.0 mg/kg, IM). Pretest computed tomography (CT) images were taken to identify the head and skull bone properties as listed in Table 1, Hounsfield unit, mg/cm<sup>3</sup> (is a quantitative scale for describing radiodensity) is used in CT scans to measure in order to determine the cranial vault.

## 2.2 Impact Test Apparatus

For imitating the accident rate of loading, a SHPB apparatus was used in this study. SHPB provides a controllable impact force informant where an accurate measurement for load, striking speed and displacement can be measured in few microseconds and high Strain rate. The system consists of a striker bar fired through gas gun in which the firing pressure can be controlled to obtain different striker bar impact speeds. A modified viscoelastic Hopkinson pressure bars (Poly methyl methacrylate PMMA acrylate) are used to compensate for the tested soft tissues (low impedance materials) for low noise and smooth curves (Phan-Thien et al. 1997; Theodorakopoulos 2015). The dog head was fixed in position by means of head holder fixation mechanism to ensure that the bare directed to the frontal side of the skull. The head was positioned between the incident and transmitted bars and when the striker bar hit the incident bar a compression wave double the length of the striker bar generate and propagate through the incident bar as shown in Fig. 2a. Two strain gage stations were attached to the middle of the incident and transmitted bars to record the three strain waves signals namely,  $\varepsilon_1(t)$ ,  $\varepsilon_r(t)$ , and  $\varepsilon_t(t)$  which are the incident, reflected and transmitted strain waves, respectively. The strain gage station attached on the incident and transmitted bars consists of a Wheatstone bridge with four strain gages. When this wave

reached the specimen part it reflects through the incident bar and the remaining wave splatted into two parts one consumed in the specimen and the other transmitted to the supporting transmitted bar which was found to be too small to be considered as shown in Fig. 2b.

The equations of the one direction wave propagation were used to calculate the load and displacement affecting the specimen using the strain signals recorded at the strain gage station positioned in the middle of the two bars after correcting the dispersion and attenuation effect as shown in Fig. 2c (Othman et al. 2016).

The adult dog skull layer consists of two flat compact bones and a spongy cancellous bone in the middle called the diploe. Bone thickness is not uniform throughout

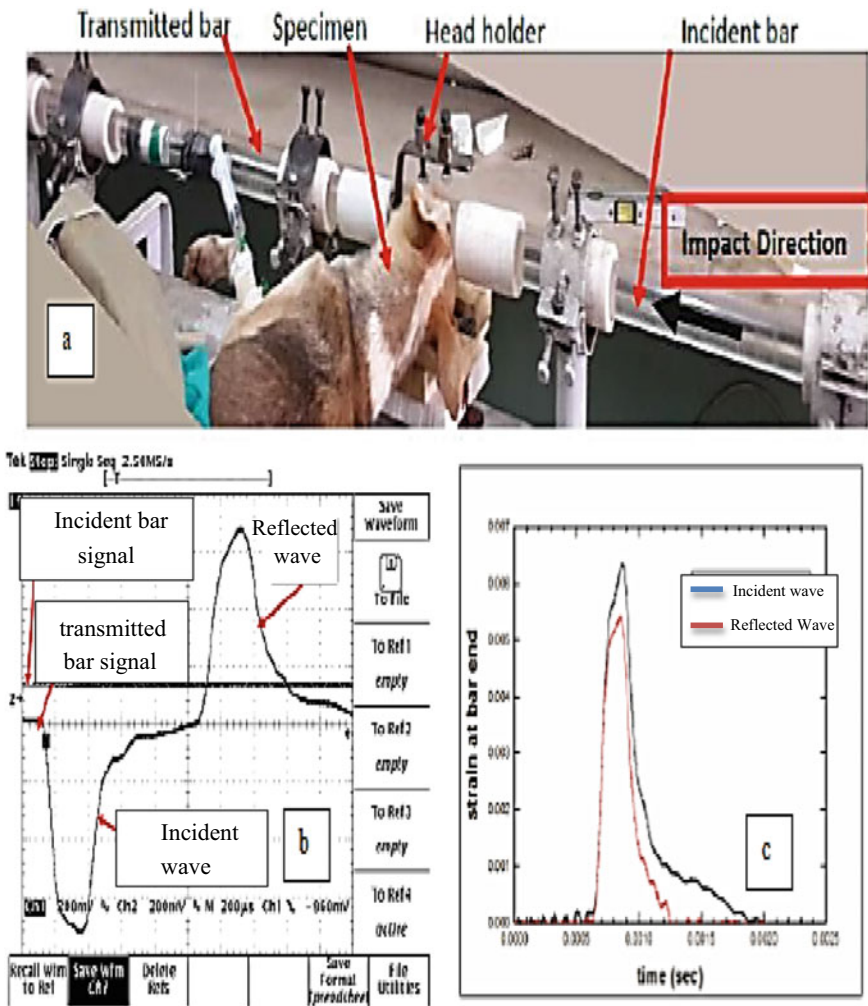
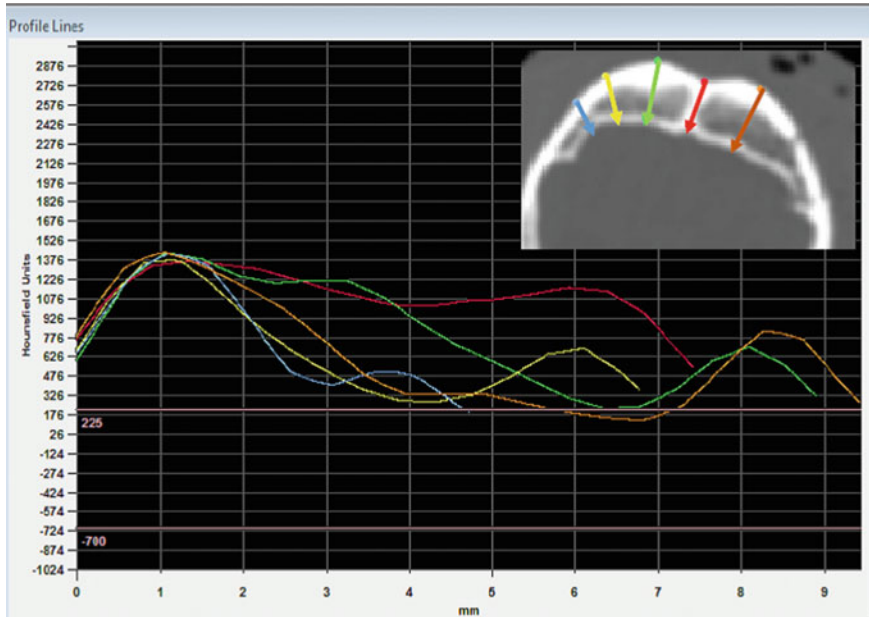


Fig. 2 a Setup of the impact test, b output signal and c processed signal



**Fig. 3** The thickness of diploe layer for dog skull at frontal bone

the skull as can be seen in the plot of Fig. 3. It can be noted that the red line refers to the sagittal line where there is not diploe at this position (only dense cortical bone). All previous data collected using Mimics software.

The equations of the one direction wave propagation were used to calculate the load and displacement affecting the specimen using the strain signals recorded at the strain gage station positioned in the middle of the two bars after correcting the dispersion and attenuation effect as shown in Fig. 2c (Othman et al. 2016).

The adult dog skull layer consists of two flat compact bones and a spongy cancellous bone in the middle called the diploe. Bone thickness is not uniform throughout the skull as can be seen in the plot of Fig. 3. It can be noted that the red line refers to the sagittal line where there is not diploe at this position (only dense cortical bone). All previous data collected using Mimics software.

Sex progressive values of impact forces were directed to the frontal site of the skull ranged from 2 to 12 kN to obtain the mechanical response of the skull bone under dynamic load. Each tested dog was scanned within 15 min from the test using CT scan, and with the aid of post-mortem analysis to represent the fracture surface tomography.



### 3 Results

The test output data showed the regularity of the behavior of the skull bone and the impact loading where the gradual of the fracture topography was agreed with the gradually increased impact loading. Dog 1 produced no significant data, while 2 tests (dogs 2 and 3) showed only subcutaneous emphysema without any fracture. Three different types of fracture were presented of the other three tests (dogs 3, 4, and 6) depressed fracture, depressed fissure fracture, and multiple depressed fracture with compound elevated skull fracture. Dogs (5, 6) showed brain injury that brain laceration, intracerebral air. There was a significant correlation between impact forces, impact velocity, impact site from sagittal crest bone, bone thickness, and the fracture behavior the load–displacement test for the dogs from 2 to 5 are shown in Fig. 4

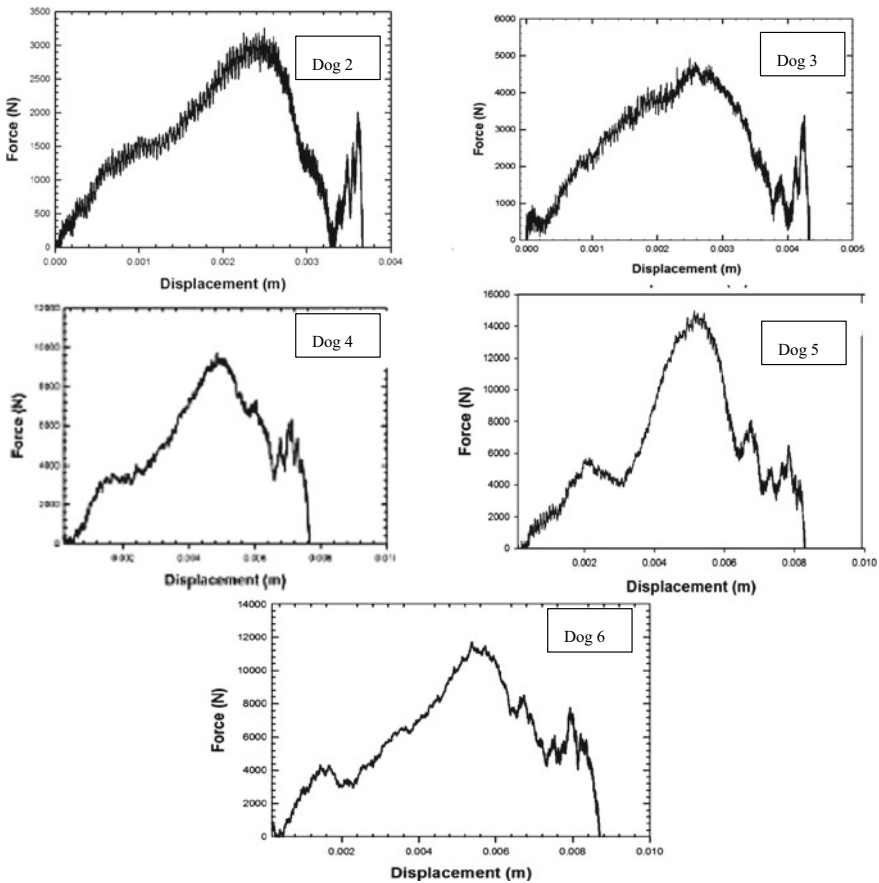


Fig. 4 Load–displacement curves for tested dogs

### 3.1 Discussion

The dog frontal skull bone may be considered as a flat slab without any columns or beam intersect. The critical element in this test is that in a direct contact to the impactor and the disk around it, because of the concentration of shear stress that is generated in the connection zone, and due to the skull bone punching risk. At the moment when the punching occurs, the disk element of bone physically separate from one another, which significantly disturbs the balance of the system formed by these elements. The force distribution model can be represented by a disk loaded in the center through a cylindrical bar, where the force transmitted from the disk center to disk outer boundary causing bending stress and shear stress at boundary. This model shows a potential of shear failure accompanied by conical shear zone attempted at the disk center as shown in Fig. 5a.

However, the skull bone is a nonhomogeneous, multilayers composite organ, consisting of two phases fluid and solid that is classified into two materials organic (softer) and inorganic or mineral which give bones their hard structure. The softer element protects the stiff one from brittle cracking, while the other stiff element stops the soft one from yielding [15 m]. To illustrate this process a more focus analysis

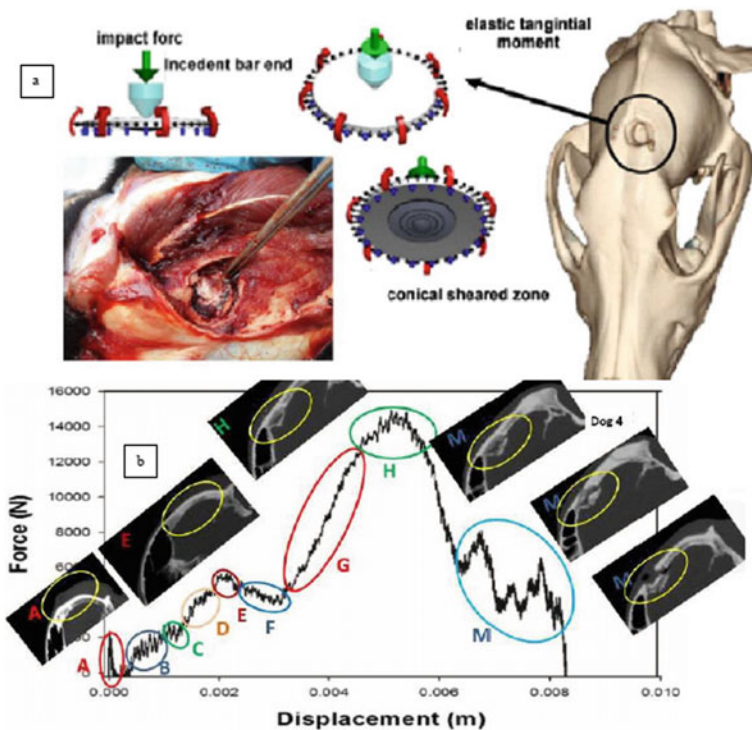


Fig. 5 Dog 4 **a** fracture model, and **b** load–displacement curve with the CT of the various

of dog (4) which recorded a depressed fracture in which one or more fragments of bone may press inward on the brain, damaging the brain. The brain may be exposed to the outside. From the force displacement curve Fig. 4b, it is noted that the first zone (A) refers to the scalp tissue deformed until reached the muscles. Second zone (B) began with the elastic of its tissue.

At (C) the muscles began to be deformed plastically (yielding of plastic deformation) from (E) followed by sudden drop after the first peak which is due to starting the muscles failure and its tissues layer were fully compacted but not completely damaged. Then the curve rising again to the second peak passing with (G) with single phase slope line due to uniform material (cortical) near sagittal line, which represent the elasticity of bone to the maximum load which acting directly to the bone causing starting of formation of the sheared cone, which mean that the bone stating to lose its punching resistance at the curve peak (H), then sudden drop which mean that after initial fracture the load carrying capacity of the skull bone drops. Then the following peaks (M) represent the crack propagation cross the skull bone layers in 3D directions. The same pattern can be identified for the dogs 5, 6.

## 4 Conclusion

Three types of Skull fractures (depressed fracture, depressed fissure fracture, and multiple depressed with compound elevated skull fracture) have been observed. The fracture behavior was found to be dependent on several parameters such as bone density, impact site, and impact force magnitude. In addition, the composition of the bone layers plays the main role of crack behavior versus impact dynamic load due to the mechanical properties of the combination of cancellous and cortical bone layers. The impact wave propagation dependable on the structure of the head skull layer thickness and mechanical properties.

## References

- Allan Gunnarsson, C., Alexander, S.L., Weerasooriya, T.: Mechanical response and fracture of human skull to indent loading. In: International Proceedings of the Society for Experimental Mechanics Series. pp. 3–44 Springer Cham (2019)
- Chocron, S., Nicolella, D., Nicholls, A.E., Bredbenner, T., Havill L.: Dynamic testing of old and young baboon cortical bone with numerical validation. *Eur. Phys. J. Conf.* **26** (2012). <https://doi.org/10.1051/epjconf/20122603004>
- Delye, H., Verschueren, P., Depreitere, B., Verpoest, I., Berckmans, D., Vander Sloten, J., Van Der Perre, G., Goffin, J.: Biomechanics of frontal skull fracture. *J. Neurotrauma* **24**(10), 1576–1586 (2007)
- Distriquin, Y., Vital, J.-M., Ella, B.: Biomechanical analysis of skull trauma and opportunity in neuroradiology interpretation to explain the post-concussion syndrome: literature review and case studies presentation. *Eur. Radiol. Exp.* **4**(66) (2020). <https://doi.org/10.1186/s41747-020-00194-x> open access

- Iboaya, A., Harris, J.L., Arickx, A., Nudo, R.J.: Models of traumatic brain injury in aged animals. A clinical perspective. *Neurorehabilitation Neural Repair* **33**(12), 975–988 (2019)
- Jennett, B., MacMillan, R.: Epidemiology of head injury. *Br. Med. J. (Clin. Res. Ed.)* **282**(6258), 101–104 (1981)
- Kaminski, J., Waller, B.M., Diogo, R., Hartstone-Rose, A., Burrows, A.M.: Evolution of facial muscle anatomy in dogs. *PNAS* **116**(29), 14677–14681 (2019)
- Motherway, J.A., Verschuere, P., Van der Perre, G., Vander Sloten, J., Gilchrist, M.D.: The mechanical properties of cranial bone: the effect of loading rate and cranial sampling position. *J. Biomech.* **42**(13), 2129–2135 (2009)
- Nahum, A.M., Melvin, J.W.: *Accidental Injury Biomechanics and Prevention*, 2nd edn. Springer, New York (2002)
- Othman, R.M., Khier, W.M., Naser, A.A.: Experimental study for dispersion and attenuation correction in viscoelastic split Hopkinson pressure bar arrangement. *JES. J. Eng. Sci.* **44**(5), 566–576 (2016)
- Peloso, P.M., von Holst, H., Kleiven, S.: The epidemiology of head injuries in Sweden from 1987 to 2000. *Inj. Control Saf. Promot.* **10**(3), 173–180 (2003)
- Phan-Thien, N., Bilston, L.E., Liu, Z.: Linear viscoelastic properties of bovine brain tissue in shear. *Biorheology* **34**(6), 377–385 (1997)
- Platt, S.R., Radaelli, S.T., McDonnell, J.J.: The prognostic value of the modified Glasgow Coma scale in head trauma in dogs. *J. Vet. Intern. Med.* **15**(6), 581–584 (2001)
- Syring, R.S., Otto, C.M., Drobotz, K.J.: Hyperglycemia in dogs and cats with head trauma: 122 cases (1997–1999). *J. Am. Vet. Med. Assoc.* **218**(7) (2001). <https://doi.org/10.2460/javma.2001.218.1124>
- Theodorakopoulos, I.D.: Determination of the useful frequency for the calculation of the attenuation coefficient and phase velocity in a viscoelastic Hopkinson pressure bar. *Int. Appl. Mech.* **51**(3), 360–368 (2015)

# Seismic Retrofit of RC Building with Elastic Stage of Buckling-Restrain Braces



Thanawat Thipprapan, Amphon Jarasjarungkiat, Panumas Saingam, and Arthit Petchsasithon

## 1 Introduction

Over the past half-century, an earthquake is a natural disaster that affects serious damage to life and property. After the Mao Lao earthquake, much of the damage was observed in reinforced concrete (RC) structures, as presented in Lukkunaprasit et al. (2014). Therefore, seismic design and detailing requirements for buildings have considerably improved. In Thailand, Ministerial Regulations about Load, Resistance, Durability of the building, and Ground supporting buildings in Earthquake-Resistance has been published in 2021 (Ministry of Interior 2021).

Many existing RC buildings in Thailand should be retrofitted because the country has historically been considered to have a low seismic hazard, and the majority of current existing RC buildings were not designed with seismic resistance. If an earthquake occurs, the existing RC buildings may not be able to withstand earthquakes, which has a high risk of being unable to withstand earthquakes because the structure is not detailed the reinforcing rebar has sufficient toughness to resist earthquakes (Lukkunaprasit et al. 2014).

At present, there are various methods of strengthening reinforced concrete buildings to resist earthquakes, including the extension of the column cross-section or the use of Carbon-Fiber Reinforced Polymer (CFRP) (Triantafillou 1998). Another method is to install a shear wall (Canbay et al. 2003), which limits drift and ensures that the mainframe remains elastic, but imposes large floor accelerations.

Seismic retrofit of RC buildings with energy dissipation devices is an innovative method to develop seismic resistance of the buildings (Saingam et al. 2020, 2021). Buckling-restrained brace (BRB) is a seismic device, composed of a tapered, energy-dissipating steel core encased in an axially de-coupled restrainer, which is

---

T. Thipprapan · A. Jarasjarungkiat · P. Saingam (✉) · A. Petchsasithon  
Department of Civil Engineering, School of Engineering, King Mongkut's Institute of Technology  
Ladkrabang, Bangkok 10520, Thailand  
e-mail: [panumas.sa@kmitl.ac.th](mailto:panumas.sa@kmitl.ac.th)

separated by a debonding interface (Takeuchi 2018). BRB components are shown in Fig. 1. The features of BRBs are withstanding compressive stress without lateral buckling and being able to dissipate seismic energy that resulting in the building can withstand earthquakes safely (Panyakapo and Pongpimonpat 2014). BRBs consist of the following components: steel core (Fig. 2.), unbonding material, encasing material, and outer tube. As for the steel core, there are various cross-sections such as Flat Bar, T-Bar, or Cross, which at this point is the area that allows for yielding. The size of the cross-section will be reduced and will be set to be in the middle of the length of BRBs. The outer tube is defined as having higher strength than the maximum tensile strength of the steel core according to American Institute of Steel Construction Incorporation requirements (American Institute of Steel Construction Incorporation requirements 2012).

This article presents the seismic strengthening of a RC building with BRBs to improve the force resistance system of the existing RC buildings. The elastic stage of the seismic retrofit of RC buildings with BRB is investigated. A 4-story RC building is used as an example building. The results of the bare existing RC building are compared to the retrofitted building to verify the presented seismic retrofit application.

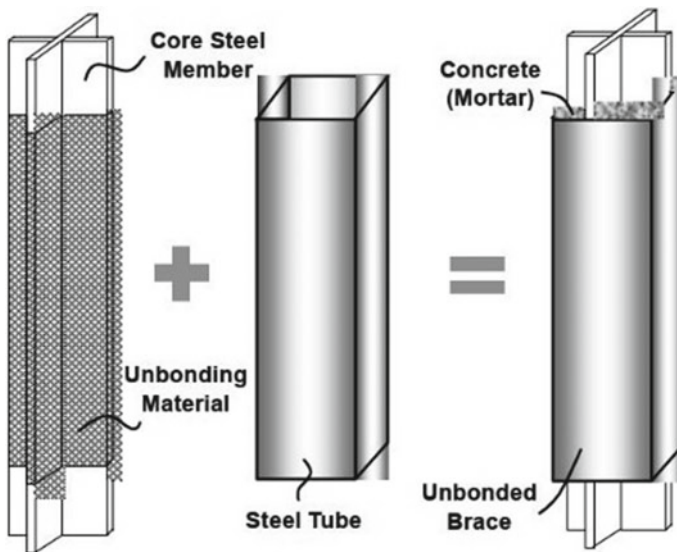


Fig. 1 Schematic of buckling-restrained brace (BRB or unbonded brace, UB) (Lai and Tsai 2002)

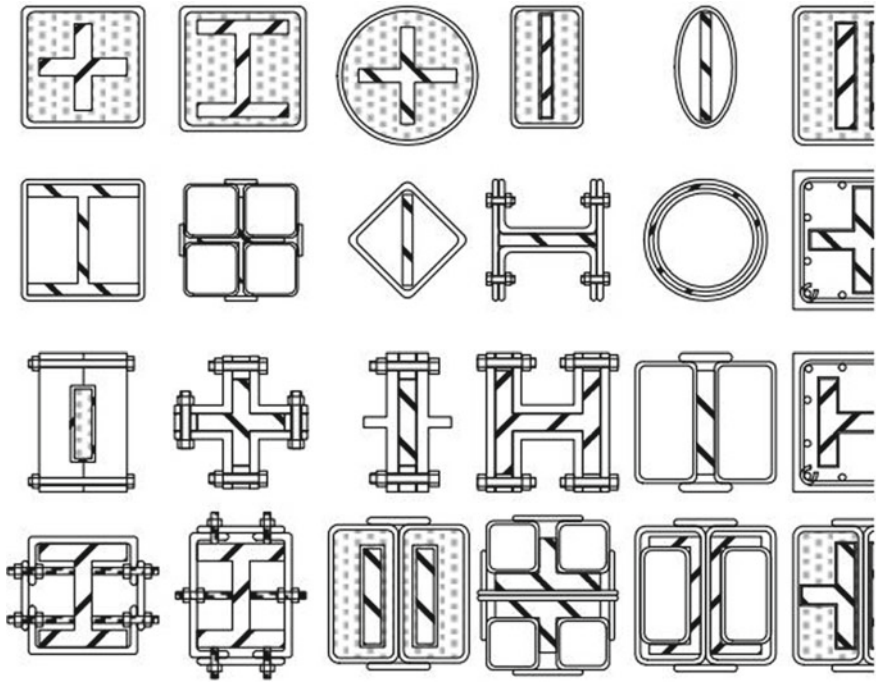


Fig. 2 Typical types of buckling-restrained (Lai and Tsai 2002)

## 2 Seismic Evaluation for Existing RC Building

This study proposes a simple method to retrofit RC buildings with BRBs. A 4-story school reinforced concrete building in Thailand is selected as a target building. This building was designed and constructed before the Ministerial Regulations, Load, Resistance, Durability of the building, and Ground supporting buildings in Earthquake-Resistance of 2021 (Ministry of Interior 2021). This affects that several buildings, which were not designed to withstand earthquakes, are required to improve their seismic performance. Therefore, this building had to be inspected to know the ability to resist earthquakes and know the point of risk of failure or failure from the earthquake, and able to strengthen at the right point.

The aforementioned building was modeled to be located in Mueang District, Chiang Mai Province. The target area is classified as a possible area where the building may be affected in terms of strength and a high degree of stability in the presence of seismic vibrations. For the analysis, the model was simulated using the MIDAS GEN program (User and’s Guide for MIDAS, Gen manual, Getting Started, Verification Examples 1989).

The target 4-story RC school building is shown in Fig. 3. The 1<sup>st</sup> floor is open-air and the 2<sup>nd</sup> to 4<sup>th</sup> floors have infill walls all around. The 1<sup>st</sup> floor has a height of 4.50 m and the 2<sup>nd</sup>–4<sup>th</sup> floor has a height of 3.50 m per floor. The steel roof has a height



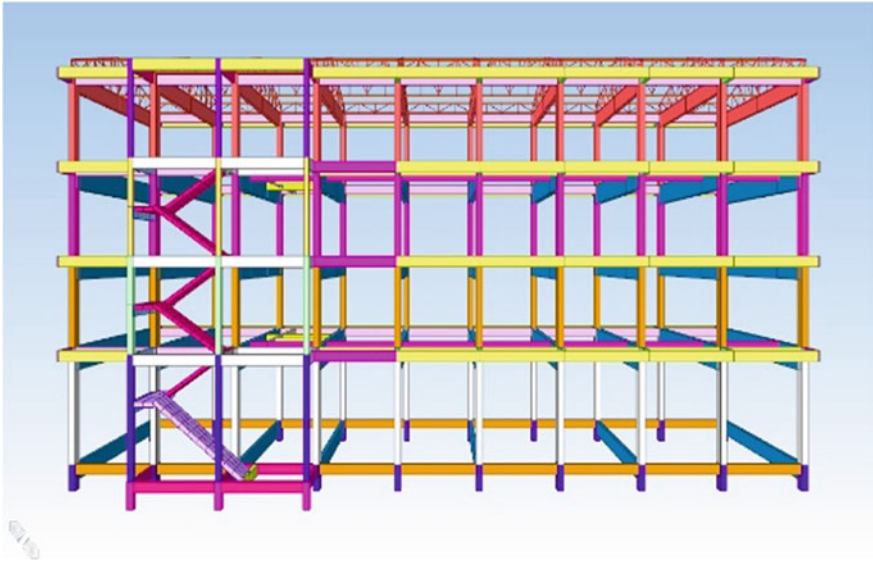


**Fig. 3** Model existing building

of 1.70 m, a building width of 10 m, and a length of 40 m. Material characteristics considered for modeling and analysis are  $f_c' = 240$  ksc for grade concrete and SD40 ( $f_y = 4000$  ksc) for grade steel rebars. The equivalent static forces based on the newest seismic design code (Ministry of Interior 2021) are applied to the target school building. The results indicated that the 1<sup>st</sup> floor is a soft story and has a high risk of being unable to withstand earthquakes. The detailed discussion will be presented in the following sections.

### 3 Results of Seismic Evaluation for Existing RC Building

From the inspection of earthquake resistance, it was found that this building was unable to withstand earthquakes. Ultimate compressive strength of columns on the 1<sup>st</sup> to the 3<sup>rd</sup> floor = 1477 kN, 898 kN and 439 kN, respectively. But nominal compressive strength of columns on the 1<sup>st</sup> to the 3<sup>rd</sup> floor = 737 kN, 709 kN and 368 kN, respectively. Failure will occur on columns from the 1<sup>st</sup> floor to the 3<sup>rd</sup> floor as a result of compressive strength (P) being insufficient. The lateral displacement in the X-axis has a displacement of 48.93 mm.  $> H/500 = 30$  mm., as shown in Fig. 4, and a lateral displacement in the Y-axis has a displacement value of 30.93 mm.  $> H/500 = 30$  mm., as shown in Fig. 5, which the lateral displacement is greater than the standard specified.

It can be indicated that this school building has insufficient seismic strength and stiffness of the building. Therefore, this study introduced the seismic retrofit of the



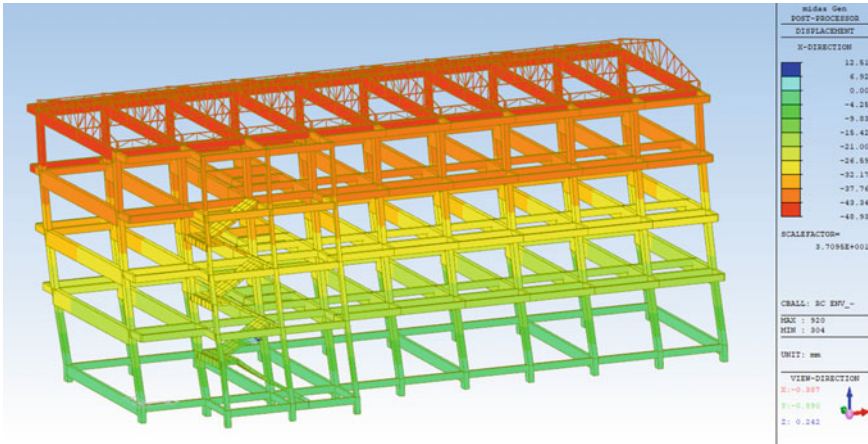


Fig. 4 The lateral displacement in the X-axis

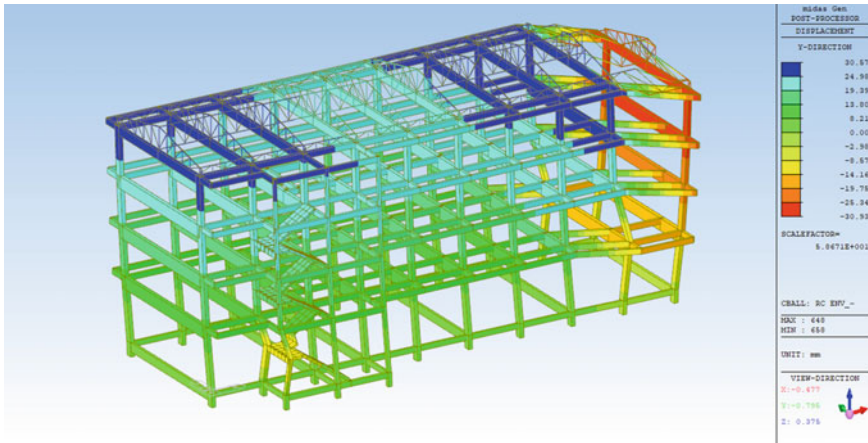


Fig. 5 The lateral displacement in the Y-axis

target buildings with BRBs, which improve in terms of resistance, increase stiffness and increase the damping of buildings.

#### 4 Retrofit Existing RC Building with Buckling-Restrained Braces

BRBs have several appealing qualities that are regularly considered for retrofitting projects. Seismic retrofit is frequently challenging to implement while maintaining

continuous occupancy, and they frequently have a negative impact on the appearance of the building (Takeuchi 2018).

From the inspection of the existing building structure, it was aware of the necessity that the building's resistance was needed to be strengthened. Then, the strength of the BRB is required to do the seismic retrofit. The strength of 275 kN was selected based on the local research by Prof. Dr. Pennueng Wanichchai (Wararuksajja et al. 2020). Then, quantified the number of BRBs on each floor. It is determined by the excess strength of the columns of each floor divided by the strength of one BRB.

Sum of excess strength of columns on the 1<sup>st</sup> floor = 3019.78 kN. The required number of BRBs is 10.98 braces. Arrange the symmetry to obtain the desired amount at 12 braces.

Sum of excess strength of columns on the 2<sup>nd</sup> floor = 281.82 kN. The required number of BRBs is 1.02 braces. Arrange the symmetry to obtain the desired amount at 2 braces.

Sum of excess strength of columns on the 3<sup>rd</sup> floor = 374.29 kN. The required number of BRBs is 1.36 sets. Arrange the symmetry to obtain the desired amount at 2 braces.

Once the number of BRB is known, then arrange the position of the BRB because the columns of the 1st floor on the edge of the building are the part that happens failure and to prevent torsion from occurring to the buckling. The position of BRBs on the 1<sup>st</sup> floor will be arranged at the edge of the building on both sides, as shown in Fig. 6.

The position of the BRBs on the 2<sup>nd</sup> and 3<sup>rd</sup> floors are arranged in the same position at the center of the building to prevent torsion from occurring in the building.

When the positioning of the buckling-restrained braces on each floor is complete, the next step is to determine the initial stiffness ( $K_0$ ) in the MIDAS GEN program. The  $K_0$  value is determined from Eqs. (1)–(3).

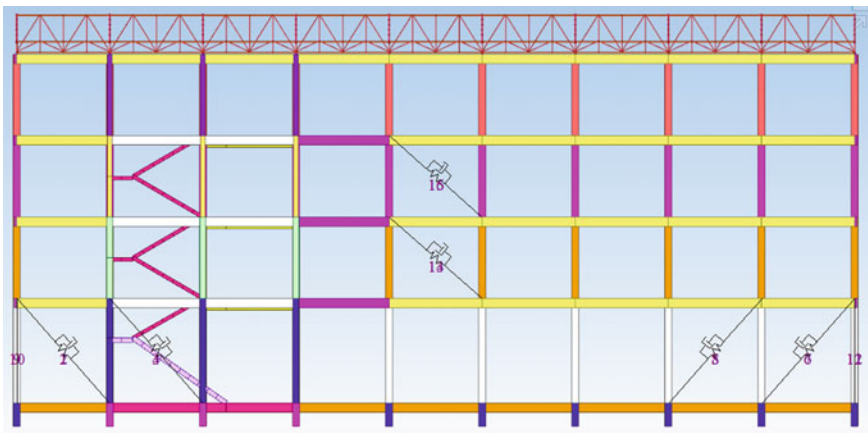


Fig. 6 The position of the buckling-restrained braces

$$K_0 = P / d_y^{\text{BRB}} \quad (1)$$

$$\delta_y^{\text{BRB}} = L^{\text{BRB}} / \theta_{dy} \quad (2)$$

$$L^{\text{BRB}} = \sqrt{(L_{x,y}^2 + H^2)} \quad (3)$$

where  $P$  is the strength of the BRBs (kN),  $\delta_y^{\text{BRB}}$  is the yield displacement at the yield point of the BRBs (m.),  $L^{\text{BRB}}$  is the length of BRBs (m.),  $\theta_{dy}$  is the yield story drift ratio of brb (rad), which is 1/750–1/1000 rad (Takeuchi 2018; Sutcu et al. 2014), in this article choose 1/750 rad because it gives the minimum value of  $K_0$ ,  $L_{x,y}^2$  is the distance between column and column (m.),  $H$  is the height between the floors (m.)  $K_0$  can be calculated and defined post-yield coefficient ( $\alpha_1$ ) as 2% of initial stiffness ( $K_0$ ).

## 5 Results of Seismic Retrofit of RC Building with Buckling-Restrained Braces

The displacements of the before retrofit building's displacements of the  $x$ -axis and  $y$ -axis are shown in Figs. 7 and 9, respectively. The results are only from the elastic stage of structural behavior. When retrofitting the existing RC building with BRBs, the results indicated that the retrofitted building was able to withstand earthquakes because the lateral displacements are smaller than the allowable value of 30 mm. The strength of the column is increased while the lateral displacement values are reduced as shown in Figs. 8 and 10, for the  $x$ -axis and  $y$ -axis, respectively. The results indicated that the roof displacement of the  $x$ -axis and  $y$ -axis are reduced by 44.7% and 24.7%, respectively. This shows the effectiveness of the proposed retrofit strategy.

**Fig. 7** Lateral displacement x-axis before retrofit

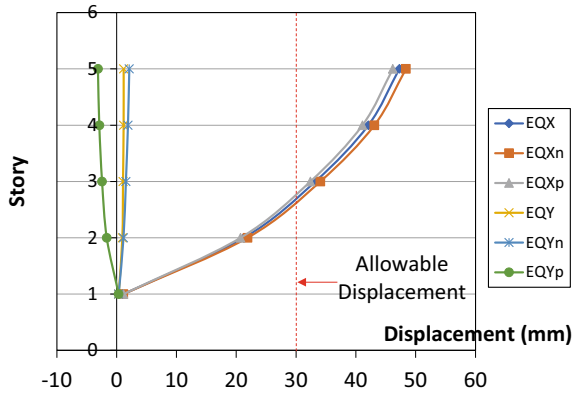


**Fig. 8** Lateral displacement x-axis after retrofitting with BRB

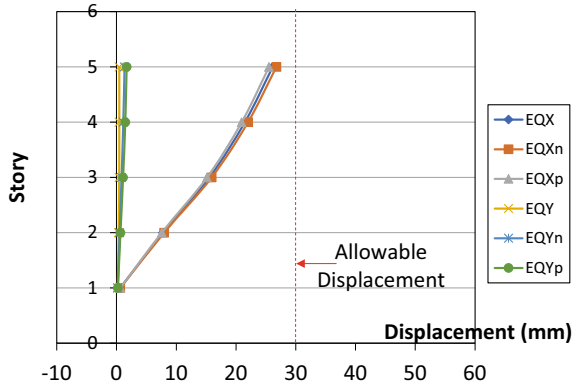


**Fig. 9** Lateral displacement y-axis before retrofit

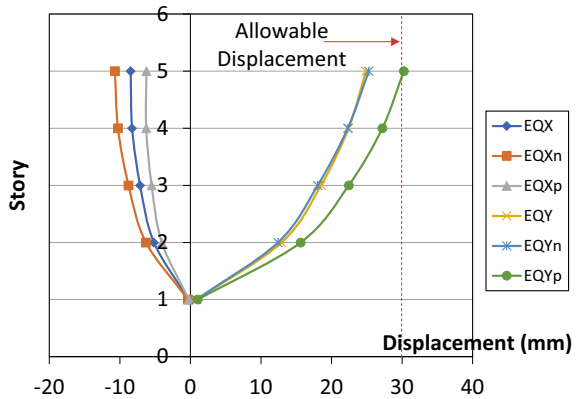
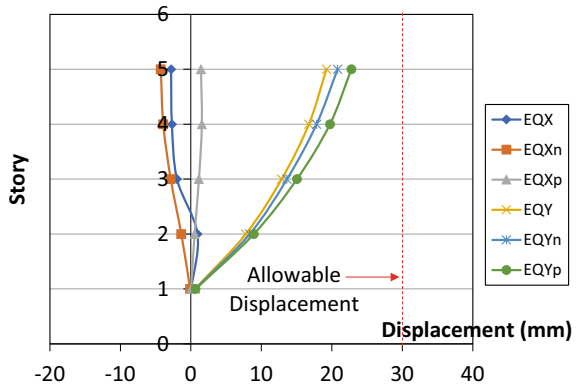


**Fig. 10** Lateral displacement y-axis after retrofitting with BRB



## 6 Conclusion

The seismic retrofit of RC buildings with buckling-restrain braces is investigated. The analysis results indicated that the existing RC building cannot withstand the seismic force from the newest seismic design code. There were failures at the column of the structure of the 1st floor to 3rd floor and has a lateral displacement exceeding the standard.

After retrofitting the target RC building with buckling-restrained braces, the results indicated that the retrofitted building was able to withstand earthquakes. The strength of columns is increased and the lateral displacement values are reduced by 24.7–44.7%, respectively. Therefore, the retrofitted building can be resisted future earthquakes. This verified the effectiveness of the introduced retrofit method.

## References

American Institute of Steel Construction Incorporation requirements (2012)

Canbay, E., Ersoy, U., Ozcebe, G.: Contribution of reinforced concrete infills to seismic behavior of structural systems. *ACI Struct. J.* **2003**(100), 637–643 (2003)

Lai J.W., Tsai, K.C.: Research and application of buckling restrained braces in Taiwan. In: National Center for Research on Earthquake Engineering, No.200, Sec. 3, Shanghai Rd., Daan Chiu, Taipei, Taiwan 106, ROC (2002)

Lukkunaprasit, P., Ruangrassamee, A., Boonyatee, T., Chintanapakdee, C., Jankaew, K., Thanasisathit, N., Chandransu, T.: Performance of structures in the Mw 6.1 Mae Lao Earthquake in Thailand on May 5, 2014, and implications for future construction. *J. Earthq. Eng.* **20**, 219–242 (2015)

Ministerial regulations about load, resistance, durability of the building, and ground supporting buildings in Earthquake-Resistance. Ministry of Interior (2021)

Panyakapo, P., Ponpimonpat, P.: In strengthening of reinforced concrete school building with buckling restrained brace (2014)

- Saingam, P., Sutcu, F., Terazawa, Y., Fujishita, K., Lin, P.C., Celik, O.C., Takeuchi, T.: Composite behavior in RC Buildings Retrofitted using Buckling-Restrained Braces with Elastic Steel Frames. *Eng. Struct.* **219**, 110896 (2020)
- Saingam, P., Matsuzaki, R., Nishikawa, K., Sitler, B., Terazawa, Y., Takeuchi, T.: Experimental dynamic characterization of friction brace dampers and application to the seismic retrofit of RC buildings. *Eng. Struct.* **242**, 112545 (2021)
- Sutcu, F., Takeuchi, T., Matsui, R.: In Seismic retrofit design method for RC building using buckling-restrained braces and steel frames (2014)
- Takeuchi, T.: Buckling restrained braces history design and applications. In: 9th international conference on behavior of steel structures in seismic areas Christchurch, New Zealand, Feb 14–16. (2018)
- Triantafillou, T.C.: Shear strengthening of reinforced concrete beams using epoxy-bonded FRP composites. *ACI Structural J.* **95**(2), 107–115 (1998)
- The User 's Guide for MIDAS/Gen manual, Getting Started, Verification Examples (1989)
- Wararuksajja, W., Leelataviwat, S., Warnitchai, P., Bing, L., Tariq, H., Naiyana1, N.: Seismic strengthening of soft-story RC moment frames. In: The 25th National Convention on Civil Engineering, Chonburi, Thailand. July 15–17 (2020)

# Response and Damage Identification by Long-Gauge Strain Sensor of Beam-Like Bridges Under the Loads of Vehicle: A Comparison of the Analytical Model and in Situ Measurement



Pham-Truong Son, Tien Hoang, Denis Duhamel, Gilles Foret, Franziska Schmidt, François-Baptiste Cartiaux, and Véronique Le Corvec

## 1 Introduction

Most bridges in the world have been built in the twentieth century. Hence, bridge assessment and monitoring are necessary. One of the preliminary stages of bridge Structural Health Monitoring (SHM) is to construct a direct model that can predict the behavior of the structure under traffic loads. Many studies have been carried out about this problem: Ichikawa et al. (2000) found the solution of a continuous beam subjected to a moving mass by eigenmodes superposition. Dugush et al. (2002) used infinite polynomial series to describe the mode shapes of a continuous beam with non-uniform section. In another approach, Hoang et al. (2017) used space–time Fourier transform to calculate the dynamic response of a periodically supported beam. Recently, Son et al. (2021) decoupled a continuous cracked beam into several segments. By introducing transfer matrices that connect these segments, the eigenvalue problem has been solved directly.

The presence of structural damage will modify the dynamic behavior of the beam. Many researchers have studied the effect of cracks on the natural frequency of a cantilever beam, and the identification of the location and the magnitude of the cracks (Ostachowicz and Krawczuk 1991; Rizos et al. 1990). However, these methods

---

P.-T. Son (✉) · T. Hoang · D. Duhamel · G. Foret  
Laboratoire Navier, UMR 8205, Ecole Des Ponts ParisTech, Université Gustave Eiffel, CNRS, 6-8  
Avenue Blaise Pascal, Champs-Sur-Marne, France  
e-mail: [truong-son.pham@enpc.fr](mailto:truong-son.pham@enpc.fr)

F. Schmidt  
Université Gustave Eiffel, IFSTTAR/MAST, 14-20 Boulevard Newton, Champs-Sur-Marne,  
France

F.-B. Cartiaux · V. Le Corvec  
OSMOS Group, 37 Rue La Pérouse, Paris, France

require many sensors. A moving load is an excitation which depends not only on time, but also on space. From the response of the beam, we can find out its modal properties such as the natural frequencies, the mode shapes...

Nowadays, bridges can be monitored continuously thanks to advanced technology. Unlike the traditionally electrical strain gauge, a long-gauge optical strand measures the average strain over its length. Hence, it has a higher probability to cover the damage. Moreover, Optical Strand sensors have many advantages such as high-sample strain measurements over long periods, high precision and durability (Cartiaux et al. 2018). The use of these sensors is not only restricted in civil engineering, but also in aviation, pipeline transport (Ignatovich et al. 2013).

This paper presents firstly an analytical method that describes the response of a damaged continuous beam which is subjected to a multi-axle vehicle load. Based on the longitudinal distribution of strain on a simply supported beam, we propose a damage index which can be used to identify and localize the damage. By using this analytical method, a parametric study is carried out to study the dependence of the proposed index to the properties of the damage. Finally, the analytical method is applied to calculate the response of an existing structure, and the results are compared to the real signals obtained during the test.

## 2 Formulation of the Problem

Consider a continuous beam of total length  $L$ , which has  $N_s$  spans. In the general case, we suppose that a damage is located in the  $k$ th span. The damaged span is divided into 3 separated beam segments: the damaged zone of length  $L_e$  and two intact segments which are on the left and on the right of the damaged segment. The initial continuous beam can be modeled as a system of  $N = N_s + 2$  beam segments (Fig. 1). A vehicle of  $M$ -axles passes over the beam with constant velocity  $v$ . Let's denote  $d_i$  the distance between the  $i$ th and  $(i + 1)$ th axle and  $D_{i-1} = \sum_{j=1}^{i-1} d_j$  is the distance between the first axle and the  $i$ th axle ( $i \geq 2$ ).

Assume that the beam follows the Euler–Bernoulli beam theory and has a linear elastic behavior. The governing equation of the  $r$ th beam segment which describes the vertical displacement  $u_r(x_r, t)$  in the local coordinates  $x_r$  is (Svedholm et al. 2016):

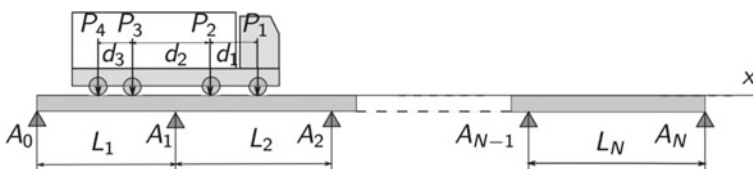


Fig. 1 A continuous beam with  $N$  spans subjected to  $M$  moving loads



$$E_r I \frac{\partial^4 u_r}{\partial x_r^4} + E_r^* I \frac{\partial^5 u_r}{\partial t \partial x_r^4} + c \frac{\partial u_r}{\partial t} + \rho A \frac{\partial^2 u_r}{\partial t^2} = f(x_r, t), 0 \leq x_r \leq L_r \quad (1)$$

where  $E_r I$  is the flexural stiffness,  $\rho$  is the mass density and  $A$  is the cross-sectional area of the beam. In Eq. 1, the familiar term  $c(\partial u_r / \partial t)$  represents the external damping whereas the term  $E_r^* I (\partial^5 u_r / \partial t \partial x_r^4)$  represents the internal damping. The force applied by the vehicle can be expressed by:

$$\begin{aligned} f(x, t) &= P_1 \delta(x - vt) + P_2 \delta(x - vt + D_1) + \dots + P_M \delta(x - vt + D_{M-1}) \\ &= \sum_{i=1}^M P_i \delta(x - vt + D_{i-1}). \end{aligned}$$

where  $\delta(x)$  is the Dirac distribution and  $x$  is the global coordinates.

The solution of the initial equation can be decoupled into two terms: the time-dependent term  $q(t)$  and the mode shapes  $\phi_r(x_r)$ :

$$u_r(x_r, t) = \phi_r(x_r) q(t) \quad (2)$$

Substituting Eq. 2 into Eq. 1, setting  $f(x, t)$  to be zero to obtain the free vibrations and by separating the variables, we have:

$$\frac{\phi_r^{(4)}(x)}{\phi_r(x)} = -\frac{c\dot{q} + \rho A \ddot{q}}{E_r I^* \dot{q} + E_r I q} = \lambda_r^4 \quad (3)$$

### 3 Natural Frequencies and Mode Shapes

From Eq. 3, the mode shapes of the  $r$ th beam segment are the solution of the following differential equation:

$$\frac{d^4 \phi_r(x_r)}{dx_r} - \lambda_r^4 \phi_r(x_r) = 0 \quad (4)$$

where  $\phi_r(x_r)$  is the mode shape of the  $r$ th beam segment. The form of  $\phi_r(x_r)$  can be expressed explicitly as:

$$\phi_r(x_r) = A_r \sin \lambda_r x_r + B_r \cos \lambda_r x_r + C_r \sinh \lambda_r x_r + D_r \cosh \lambda_r x_r \quad (5)$$

### 3.1 Configuration of the Beam

BY the same concept of transfer matrices as introduced by Son et al. (2021), we search the transfer matrix  $M$  such that  $X_r = MX_{r-1}$ . Here  $X_r = [A_r, B_r, C_r, D_r]^T$  is the vector which contains the coefficients of the mode shapes  $\phi_r(x_r)$  for the  $r$ th beam segment. This  $4 \times 4$  matrix ensures the continuity conditions at the intermediate support points and at the interface between the intact segment and the damaged segment.

### 3.2 The Intermediate Supports

The intermediate supports are assumed to be infinitely rigid, so the displacement is blocked at these points. Moreover, the slope of the beam and the bending moment are unchanged across the support. Considering the  $(r - 1)$  th support which is found between the  $(r - 1)$  th span and the  $r$ th span, the above conditions can be written as:

$$\begin{aligned} u_r(0, t) &= u_r(L_r, t) = 0, \\ u'_r(0, t) &= u'_{r-1}(L_{r-1}, t), \\ u''_r(0, t) &= u''_{r-1}(L_{r-1}, t). \end{aligned} \quad (6)$$

We obtain  $S(L_{r-1}, L_r)$  the transfer matrix at the intermediate support, such that:  $X_r = S_{4 \times 4} X_{r-1}$ . This matrix can be expressed as:

$$S_{4 \times 4} = \frac{1}{2} \begin{bmatrix} -\kappa.s + 2\eta.c & -\eta.s - \kappa.c & \kappa.sh + 2\eta.ch & 2\eta.sh + \kappa.ch \\ s & c & -sh & -ch \\ \kappa.s + 2\varepsilon.c & -2\varepsilon.s + \kappa.c & -\kappa.sh + 2\varepsilon.ch & 2\varepsilon.sh + \kappa.ch \\ -s & -c & sh & ch \end{bmatrix} \quad (7)$$

in which:

$$\begin{aligned} s &= \sin \lambda L_{r-1}, c = \cos \lambda L_{r-1}, sh = \sinh \lambda L_{r-1}, ch = \cosh \lambda L_{r-1}, \\ \kappa &= (\cos \lambda L_r - \cosh \lambda L_r) / (\sin \lambda L_r - \sinh \lambda L_r), \\ \eta &= -\sinh \lambda L_r / (\sin \lambda L_r - \sinh \lambda L_r), \varepsilon = 1 - \kappa. \end{aligned}$$

### 3.3 *The Interface Between Intact and Damaged Beam Segments*

In the literature, a crack can be modeled by a spiral spring or by a reduction of the bending stiffness in the concerned zone (Friswell and Penny 2002). In this paper, we use the second model to describe the damage. We denote  $(EI)_1$  and  $L_1$ , respectively, the bending stiffness and the length of the segment located on the left of the interface. By the same way,  $(EI)_2$ ,  $L_2$  are the bending stiffness and the length of the right segment. Across the interface, the traverse displacement, the slope of the beam, the bending moment and the shear force are unchanged. Therefore, the continuity conditions at the interface are:

$$\begin{aligned} u_2(0, t) &= u_1(L_1, t), & u_2'(0, t) &= u_1'(L_1, t), \\ (EI)_2 u_2''(0, t) &= (EI)_1 u_1''(L_1, t), & (EI)_2 u_2'''(0, t) &= (EI)_1 u_1'''(L_1, t). \end{aligned} \quad (8)$$

The transfer matrix at the interface  $T(k, L_1)$  is such that  $X_2 = T(k, L_1)X_1$ :

$$T_{4 \times 4} = \frac{1}{2} \begin{bmatrix} (1+k)/\sqrt{kc} & -(1+k)/\sqrt{ks} & (1-k)/\sqrt{kch} & (1-k)/\sqrt{ksh} \\ (1+k)s & (1+k)c & (1-k)sh & (1-k)ch \\ (1-k)/\sqrt{kc} & -(1-k)/\sqrt{ks} & (1+k)/\sqrt{kch} & (1+k)/\sqrt{ksh} \\ (1-k)s & (1-k)c & (1+k)sh & (1+k)ch \end{bmatrix}$$

in which:

$$k^2 = \frac{(EI)_1}{(EI)_2}, \quad (9)$$

$$s = \sin \lambda_1 L_1, \quad c = \cos \lambda_1 L_1, \quad sh = \sinh \lambda_1 L_1, \quad ch = \cosh \lambda_1 L_1.$$

By assembling all these aforementioned matrices together and taking into account the boundary conditions of the continuous beam, we deduce an eigenvalue problem to solve for  $\omega = \lambda_r^2 \sqrt{E_r I / \rho S}$ , which is the angular frequency of the beam. Once the values of  $\{\omega\}$  are found, by integrating both sides of the initial equation, we solve the same initial differential equation for the general coordinates  $q(t)$ , segment by segment. Finally, by superposition of the modes, we have the analytical solution of the problem.

### 3.4 *Damage Identification Using Distributed Long-Gauge Strain Sensors Method*

For a simply supported beam, it can be shown that the maximum and the area values of the static macro-strain follow a parabolic distribution (Wu et al. 2019). Some

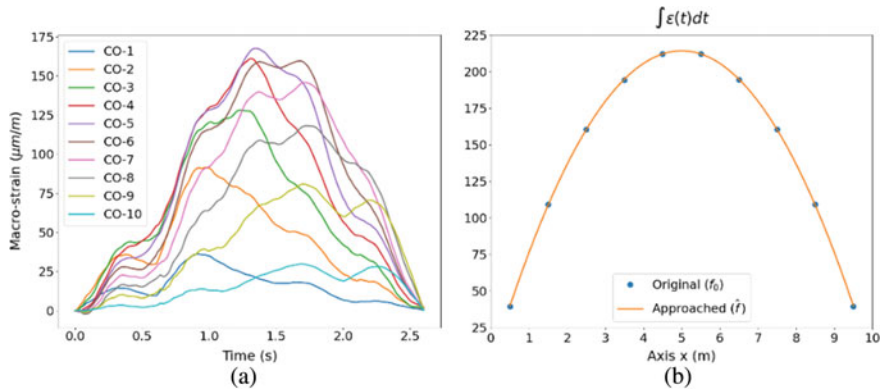


**Fig. 2** Macro-strain time histories of a simply supported beam and the distribution of their area

damage indices based on this property were proposed in Wu et al. (2019); Hong, et al. 2016). Moreover, the parabolic shape of the area values is still correct in case where the total strain is measured by a long-gauge sensor, which is the sum of static and dynamic strain. For illustration, it is supposed that a sequence of 10 Optical Strands sensors of equal length  $l_g = 1$  m is placed under a simply supported beam of 10 m length. The sensors are named as CO-1–CO-10, from left to right. Figure 2a presents the numerical results of total macro-strain time histories obtained by these Optical Strands, subjected to a 2-axle vehicle which passes over the beam at constant speed  $v = 5$  m/s. The front load and the rear load are 1 kN and 2 kN, respectively. The distance between these two loads is 3 m. The beam is made of steel ( $E = 210$  GPa,  $\rho = 7800$  kg/m<sup>3</sup>). The Fig. 2b shows the distribution of the area of these responses. The orange line is the regression parabola  $\hat{f}$ .

We propose a damage index (DI) which measures the relative error between the approached parabola and the measured points:

$$EG = 100 \times \frac{\|f - f_{02}\|}{\|f_{02}\|}. \quad (10)$$

in which:  $\|x\|_2 = \sqrt{x_1^2 + x_2^2 + \dots + x_n^2}$  is the Euclidian norm of vector  $x$ .

In order to localize the damaged zone, we propose an additional criterion, which is based on the above damage index EG. It is calculated by the same way of the criterion EG, but the considered point  $\varepsilon_i$  is excluded:

$$EL_i = EG^i = 100 \times \frac{\|f^i - f_{02}^i\|}{\|f_{02}^i\|} \quad (11)$$

### 3.5 Results

To illustrate the above criteria, we take the same steel beam and same vehicle load as presented on the previous subsection. We create a damaged zone at the center of the beam. The length of the damage varies from 0.5 m to 3.0 m and the reduction of bending stiffness on this zone varies from 0% (intact) to 50%. As a parabola is defined by 3 parameters, at least 4 measure points are required to determine the damage index EG. Hence, to identify and localize the damage, at least 5 measured points are required. In this parametric study, we use 5 Optical Strands with 2 m-length each, covering the whole length of the beam. The response of the beam is calculated by the current analytical model.

Figure 3 presents the dependence of EG as the function of the length and of the reduction of bending stiffness of the damaged zone.

From Fig. 3a, we see that EG varies linearly with  $\Delta(EI)$ . Figure 3b shows that the damage index EG get its maximal value while the length of the damage is equal to 2 m. The relation between EG and the size of the damage is also linear. The global damage index is exceeding 5% for a damaged zone of length 1.5 m and a reduction of bending stiffness  $\Delta E = 10\%$ .

To localize the damage, the local criterion EL is calculated in case the size of the damage is 2 m, for different levels of reduction of bending stiffness. We see that this index EL vanishes at the sensor which corresponds to the damage (Fig. 4). For a damage of  $\Delta E = 10\%$ , the average value of EL is over 4%.

## 4 Application to Bridge Structures

The analytical method is now applied to calculate the strain response of an existing highway overpass in France. This prestressed concrete girder bridge was built in the 1960s. The bridge has 4 spans, where each of those is composed of 10 prestressed concrete beams. The structure has been monitored since 2011 by the Optical Strands sensors of length 1 m (red) and 2 m (blue). Figure 5 shows the instrumented plan of the bridge with the selected sensors. There was a calibration test on the bridge in 2019.

One of the test trucks is a 5-axle of 44 tons. From the first axle, the distances between two consecutive axles are:  $d_1 = 3.8$  m,  $d_2 = 3.0$  m,  $d_3 = d_4 = 1.25$  m. The axle loads  $P_1, P_2, P_3, P_4, P_5$  are, respectively, 6.94 t, 10.62 t, 9.2 t, 8.64 t and 8.16 t. The vehicle passes over the bridge in direction S–N at constant speed 50 km/h, so it enters firstly into the Span 3, then the Span 2. In the analytical model, the bridge is considered as a set of T-beams in parallel. The general cross-section of the T-beam is calculated for its properties (second moment of area, area...). The density of concrete is 2500 kg/m<sup>3</sup> and its Young modulus is 36.6 GPa. Because the forces are also distributed in the transverse direction, a coefficient of 0.14 is taken into account

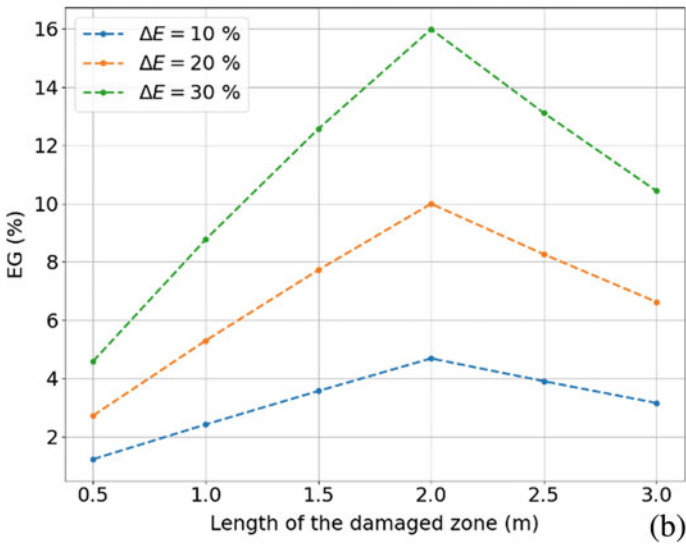
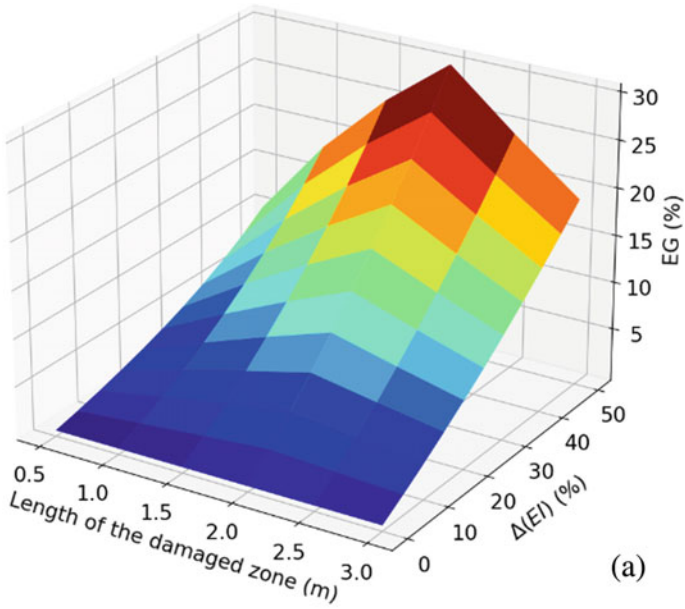


Fig. 3 Damage index EG in function of the properties of damage

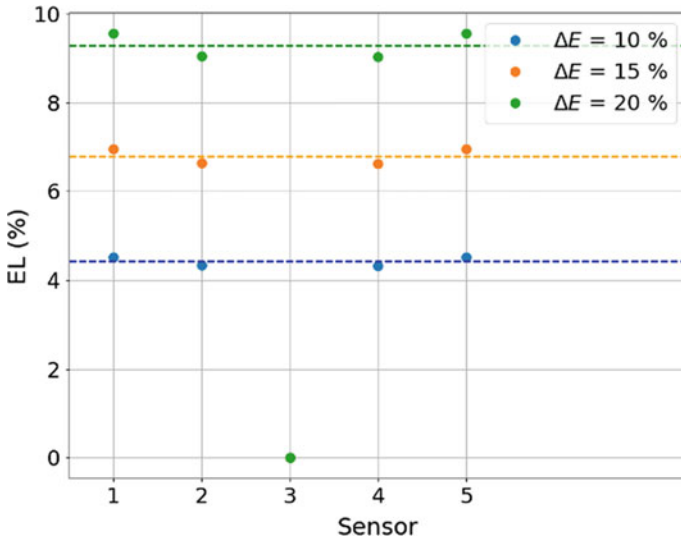


Fig. 4 Local criterion for localizing the damage

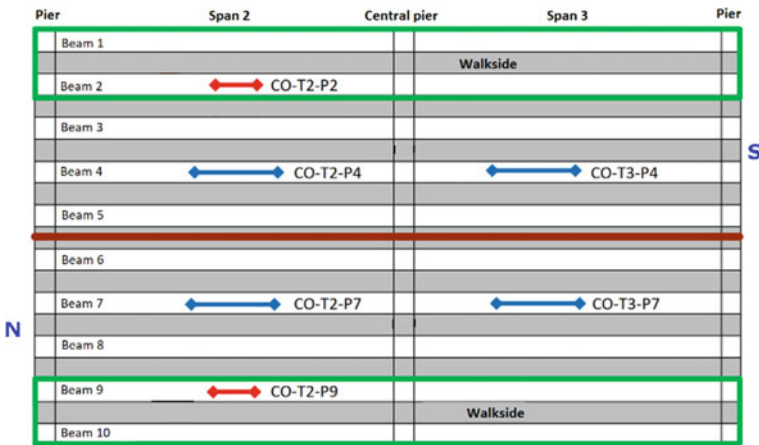


Fig. 5 Instrumentation plan on the central spans of the bridge

for the response of the largest signal. The other signals are re-constructed from the load distribution factor obtained for this girder bridge.

Figure 6 shows the results of the analytical method comparing with the signal obtained from the in situ test. The solid lines present the results calculated by the present analytical method, while the dashed lines are the measured strain during the test. The calculated and measured signals are coherent.

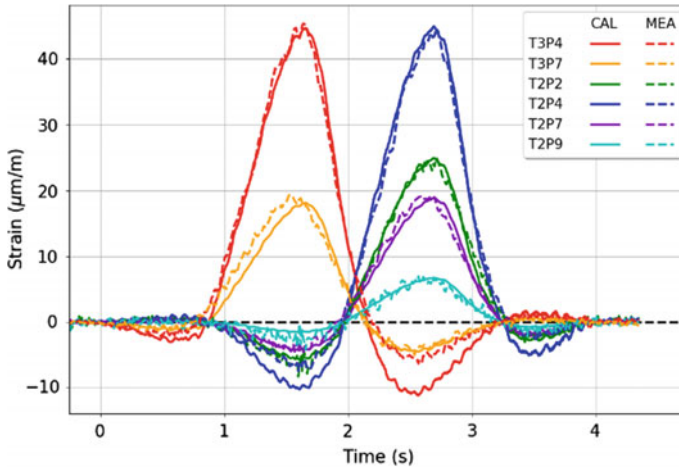


Fig. 6 Comparison of the analytical results and in situ measurement

## 5 Conclusion

The analytical method gives us quickly the dynamic response of the bridge structure. It takes under 10 s to calculate the presented parametric study, whereas the same model calculated by FEM costs more than 15 min in total. From the distribution of the area of strain time history along the beam, the proposed index can detect the presence of a damage and localized its position. The coherence between the simulated results and the real signals gives an opportunity for the analytical method on modeling of the bridge, in order to obtain rapidly the total response of the structure.

**Acknowledgements** This work has been developed in the partnership between OSMOS Group and Ecole des Ponts ParisTech. The supports from the personnel of OSMOS Group are acknowledged as well.

## References

- Cartiaux, F.B., Pelletier, P., Semiao, J.: Traffic and temperature effects monitoring on bridges by optical strands strain sensors, pp. 1–8 (2018)
- Dugush, Y.A., Eisenberger, M.: Vibrations of non-uniform continuous beams un-der moving loads. *J. Sound Vib.* **254**(5), 911–926 (2002)
- Friswell, M.I., Penny, J.E.T.: Crack modeling for structural health monitoring. *Struct. Heal. Monit.* **1**(2), 139–148 (2002)
- Hoang, T., et al.: Calculation of force distribution for a periodically supported beam subjected to moving loads. *J. Sound Vib.* **388**, 327–338 (2017)
- Hong, W. et al.: Strain-based damage-assessment method for bridges under moving vehicular loads using long-gauge strain sensing. *J. Bridg. Eng.* **21**(10) (2016)



- Ichikawa, M., Miyakawa, Y., Matsuda, A.: Vibration analysis of the continuous beam subjected to a moving mass. *J. Sound Vib.* **230**(3), 493–506 (2000)
- Ignatovich, S.R., et al.: Fatigue damage and sensor development for aircraft structural health monitoring. *Theor. Appl. Fract. Mech.* **65**, 23–27 (2013)
- Ostachowicz, W.M., Krawczuk, M.: Analysis of the effect of cracks on the natural frequencies of a cantilever beam. *J. Sound Vib.* **150**(2), 191–201 (1991)
- Rizos, P.F., et al.: Identification of crack location and magnitude in a cantilever beam from the vibration modes. *J. Sound Vib.* **138**(3), 381–388 (1990)
- Son, P.T. et al.: Dynamic response of a cracked multi-span continuous beam subjected to a moving multi-axle vehicle load. In: 10th International Conference on Structural Health Monitoring of Intelligent Infrastructure, SHMII 10, 2021, no. July, pp. 1–8 (2021)
- Svedholm, C., et al.: Vibration of damped uniform beams with general end conditions under moving loads. *Eng. Struct.* **126**, 40–52 (2016)
- Wu, B., et al.: Parametric study of a rapid bridge assessment method using distributed macro-strain influence envelope line. *Mech. Syst. Signal Process.* **120**, 642–663 (2019)

# **Metallic Materials and Corrosion Protection**

# Relation Between Binding Energy, Isothermal Bulk Modulus, and Surface Tension of Liquid Metals



Yu. N. Starodubtsev  and V. S. Tsepelev 

## 1 Introduction

Interatomic (intermolecular) forces (Israelachvili 2011) bind the atoms together and prevent the deformation of the body. The interatomic interaction is characterized by the cohesion energy  $E_{\text{coh}}$  or the energy of atomization (sublimation), which is equal to the energy required for the decomposition of a solid into independent atoms at 0 K. The vacancy formation energy  $E_{\text{vac}}$  can also be a characteristic of interatomic interaction. Vacancy formation energy is the energy required to take an atom from inside the crystal, and to place it on the surface without altering the surface energy of the crystal (Friedel 1964). The binding energies include the melting enthalpy  $\Delta^l_s H_m$  and the evaporation enthalpy  $\Delta^g_l H_b$ , which determine the amount of heat required to melt a solid at the melting point  $T_m$  or to evaporate a liquid at boiling point  $T_b$ . The thermal energy  $RT_m$  and  $RT_b$  at the melting or boiling point is used to compare the strength of interatomic interaction with the destructive effect of thermal motion.

Previously, the relationship between the bulk modulus, surface tension and certain types of binding energies was demonstrated (Kaptay 2008; Iida and Guthrie 2010; Aqra 2014; Keene 1993; Turkdogan 2002). In the present work, we investigated the relationship between various energy quantities characterizing the interatomic bond with the isothermal bulk modulus and surface tension of liquid metals at the melting point. The aim of the work was to find the energy quantities that are most related to the bulk modulus and surface tension.

---

Yu. N. Starodubtsev · V. S. Tsepelev (✉)

Research Center for Physics of Metal Liquids, Ural Federal University, Ekaterinburg, Russia  
e-mail: [v.s.tsepelev@urfu.ru](mailto:v.s.tsepelev@urfu.ru)

Yu. N. Starodubtsev

Gammamet Research and Production Enterprise, Ekaterinburg, Russia

## 2 Initial Data

Data on the cohesion energy  $E_{\text{coh}}$  ( $\text{J}\cdot\text{mol}^{-3}$ ), melting enthalpy  $\Delta H_{\text{m}}$  ( $\text{J}\cdot\text{mol}^{-3}$ ), evaporation enthalpy  $\Delta H_{\text{b}}$  ( $\text{J}\cdot\text{mol}^{-3}$ ), melting point  $T_{\text{m}}$  (K) and boiling point  $T_{\text{b}}$  (K), molar volume  $V_{\text{m}}$  ( $\text{m}^3\cdot\text{mol}^{-1}$ ) was taken from Iida and Guthrie (2015). For the experimental vacancy formation energy  $E_{\text{vac}}$  ( $\text{J}\cdot\text{mol}^{-3}$ ) the values collected in Starodubtsev and Tsepelev 2021a were used. We also used data on the sublimation enthalpy  $\Delta H_{\text{sub}}$  ( $\text{J}\cdot\text{mol}^{-3}$ ) (Garvin 1981), Debye temperature  $\Theta_{\text{D}}$  (K) (Stewart 1983) and surface tension at the melting point  $\gamma_{\text{m}}$  ( $\text{J}\cdot\text{m}^{-2}$ ) (Iida and Guthrie 2015). The isothermal bulk modulus at the melting point  $K_{\text{Tm}}$  ( $\text{J}\cdot\text{m}^{-3}$ ) were taken from Blairs (2007); Marcus (2017). In this work, we analyzed data for alkali, alkaline earth, rare earth, transition metals and metals from 12 to 14 groups of 60 metals in total.

## 3 Results and Discussion

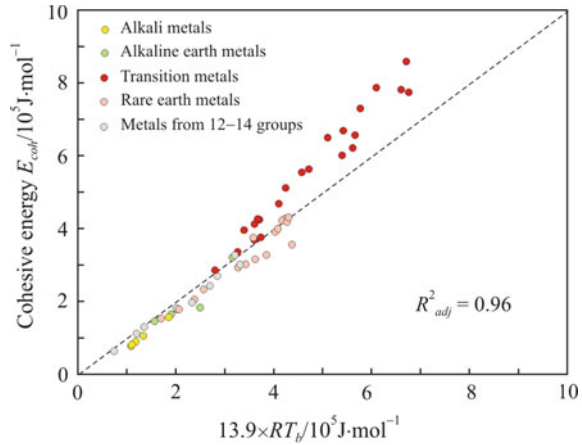
The relationship of different types of the binding energy is presented in Table 1. The numbers without brackets show the ratio of the energy quantity in the column of the table to the energy quantity in the row, which are averages for all 60 metals. The numbers in brackets show the adjusted coefficient of determination  $R^2_{\text{adj}}$ , which characterizes the linear relationship between the energy quantities.

The sublimation enthalpy  $\Delta H_{\text{sub}}$  from solid at temperature 0 K coincides with the cohesive energy  $E_{\text{coh}}$  at 0 K. The  $E_{\text{coh}}/E_{\text{vac}}$  ratio is close to 3 in accordance with early results (Gorecki 1974; Starodubtsev et al. 2020). The  $E_{\text{coh}}$ ,  $\Delta H_{\text{b}}$  and  $RT_{\text{b}}$  quantities, which characterize the decomposition of substance to the monatomic gas, have the highest correlation. The ratio  $\Delta H_{\text{b}}/RT_{\text{b}}$  corresponds to the Trouton's rule, which indicates a significant and almost identical change in entropy  $\Delta S_{\text{b}} = \Delta H_{\text{b}}/T_{\text{b}} = 12R$

**Table 1** Ratios of energy quantities and the coefficients of determination  $R^2_{\text{adj}}$  (in brackets)

|                  | $E_{\text{coh}}$ | $E_{\text{vac}}$ | $RT_{\text{b}}$ | $\Delta H_{\text{b}}$ | $RT_{\text{m}}$ | $\Delta H_{\text{m}}$ |
|------------------|------------------|------------------|-----------------|-----------------------|-----------------|-----------------------|
| $E_{\text{coh}}$ | 1<br>(1)         | 3.1<br>(0.77)    | 13.9<br>(0.96)  | 1.13<br>(0.987)       | 31.4<br>(0.86)  | 29.9<br>(0.83)        |
| $E_{\text{vac}}$ | 0.32<br>(0.77)   | 1<br>(1)         | 5.1<br>(0.73)   | 0.4<br>(0.84)         | 10.1<br>(0.84)  | 9.5<br>(0.85)         |
| $RT_{\text{b}}$  | 0.072<br>(0.96)  | 0.196<br>(0.73)  | 1<br>(1)        | 0.083<br>(0.95)       | 2.31<br>(0.80)  | 2.21<br>(0.65)        |
| $H_{\text{b}}$   | 0.89<br>(0.987)  | 2.51<br>(0.84)   | 12.0<br>(0.95)  | 1<br>(1)              | 28.7<br>(0.85)  | 27.1<br>(0.86)        |
| $RT_{\text{m}}$  | 0.032<br>(0.86)  | 0.1<br>(0.84)    | 0.43<br>(0.80)  | 0.035<br>(0.85)       | 1<br>(1)        | 0.98<br>(0.91)        |
| $H_{\text{m}}$   | 0.035<br>(0.83)  | 0.11<br>(0.85)   | 0.45<br>(0.77)  | 0.037<br>(0.86)       | 1.02<br>(0.91)  | 1<br>(1)              |

**Fig. 1** Relationship between the cohesive energy  $E_{\text{coh}}$  and the  $13.9 \times RT_b$  thermal energy parameter at vaporization point. The dashed line corresponds to the equality  $E_{\text{coh}} = 13.9 \times RT_b$



when a liquid passes into a gas. On the contrary, during melting, the entropy change is insignificant  $\Delta S_m = \Delta H_m/T_m = R$  (Richard's rule).

Figure 1 shows the relationship between the cohesive energy  $E_{\text{coh}}$  and the  $13.9 \times RT_b$  thermal energy parameter at vaporization point. It can be seen that all metals can be divided into two groups: transition metals with a high boiling point and with a faster increase in cohesion energy and all other metals with a lower boiling point.

In (Starodubtsev and Tsepelev 2021b), the kinetic energy of atomic vibrations  $e_k$  (J)

$$e_k = \frac{1}{2} m \omega_D^2 (\alpha a)^2, \quad (1)$$

where  $\omega_D$  is the Debye frequency ( $\text{s}^{-1}$ )

$$\omega_D = \Theta_D \frac{2\pi k_B}{h}, \quad (2)$$

$\Theta_D$  is the Debye temperature (K),  $h$  is the Planck's constant (J·s),  $a$  is the atomic diameter (m),  $m$  is the atomic mass (kg),  $\alpha$  is the relative atomic vibration amplitude,  $\alpha a$  is the absolute vibration amplitude, was compared with thermal energy  $e_{T_m}$  at melting point

$$e_{T_m} = k_B T_m. \quad (3)$$

From the comparison of (1) and (3) we obtain the relative amplitude of atomic vibrations at the melting point

$$\alpha_m = \frac{h}{\pi a \Theta_D} \sqrt{\frac{T_m}{2k_B m}}. \quad (4)$$

For liquid metals at the melting point, the average  $\alpha_m = 0.053$ , and the distance between the centers of neighboring atoms increases by  $0.106a$ . This estimate coincides with Lindemann's melting criterion (Lindemann 1910).

Relative amplitude of atomic vibrations at boiling point

$$\alpha_b = \alpha_m \sqrt{\frac{T_b}{T_m}}. \quad (5)$$

For liquid metals at the boiling point, the average  $\alpha_b = 0.079$ , and the distance between the centers of neighboring atoms increased by  $0.158a$ . Consequently, an increase in the distance between atoms by an average of 50% compared to the melting temperature leads to a complete break in interatomic bonds and decomposition of substance to the monatomic gas.

Dimensional analysis allows us to represent the relationship between the bulk modulus, surface tension and the binding energy as

$$K_{Tm} \propto \frac{E}{a^3 N_A}, \quad (6)$$

$$\gamma_m \propto \frac{E}{a^2 N_A} \quad (7)$$

where  $E$  is the molar binding energy ( $\text{J}\cdot\text{mol}^{-3}$ ),  $N_A$  is Avogadro constant ( $\text{mol}^{-1}$ ). An analysis of relationships (6) and (7) for different molar binding energies showed that the bulk modulus and the surface tension at melting point correlate better with the quantities characterizing the complete breaking of interatomic bonds, i.e., with  $E_{\text{coh}}$ ,  $\Delta H_b$  and  $RT_b$ , rather than with the quantities  $\Delta H_m$  and  $RT_m$ , which characterize the metal state at the melting point. In the future, we will investigate the relationship between the bulk modulus, surface tension and thermal energy at boiling point  $RT_b$ , since the boiling point can be determined most accurately by experimental methods.

Figure 2 shows the relationship between the bulk modulus  $K_{Tm}$  and the volume density of thermal energy at boiling point  $k_B T_b a^{-3}$  multiplied by a factor of 23. This factor is equal to the arithmetic mean for the ratio of  $K_{Tm}$  to  $k_B T_m a^{-3}$  for all metals. A similar relationship for the surface tension at the melting point  $\gamma_m$  and the surface density of thermal energy  $k_B T_b a^{-2}$  is shown in Fig. 3. Figures show a good correlation between the elastic energy density at the melting point and the thermal energy density at the boiling point,  $R^2_{\text{adj}} = 0.86$  and  $0.93$ , respectively. A particularly high correlation is observed for the surface, which atoms can leave at a temperature below the boiling point.

According to (8) and (9), the bulk modulus and surface tension depend on both the atomic size and the boiling point. To evaluate the effect of atomic size, we introduce the reduced quantities, which are related to the unit of thermal energy at the boiling point and are equal to the reciprocal atomic size with exponents 3 and 2, respectively.

**Fig. 2** Relationship between the bulk modulus  $K_{Tm}$  and  $23 \times k_B T_b a^{-3}$  parameter. The dashed line corresponds to the equality  $K_{Tm} = 23 \times k_B T_b a^{-3}$

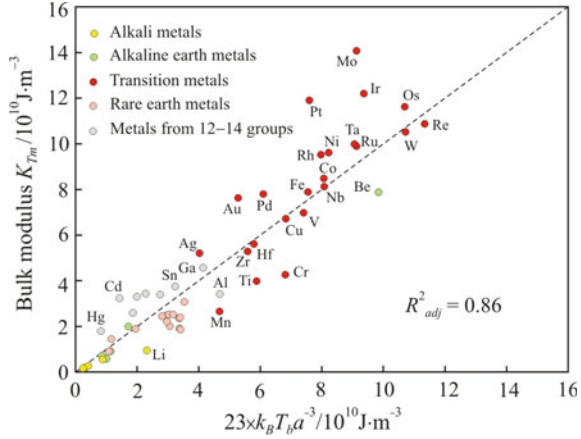
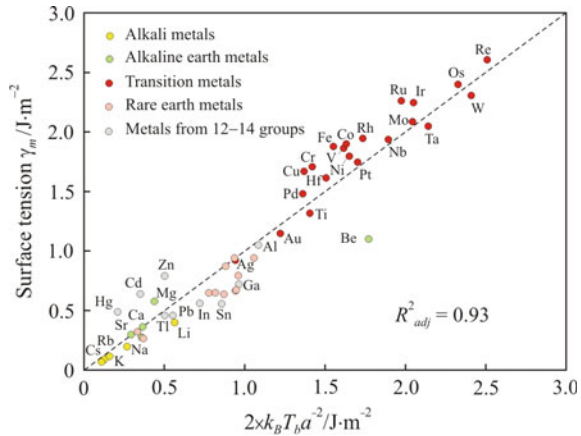


**Fig. 3** Relationship between the surface tension  $\gamma_m$  and  $2 \times k_B T_b a^{-2}$  parameter. The dashed line corresponds to the equality  $\gamma_m = 2 \times k_B T_b a^{-2}$



$$\frac{K_{Tm}}{23k_B T_b} = a^{-3}, \tag{8}$$

$$\frac{\gamma_m}{2k_B T_b} = a^{-2}, \tag{9}$$

Figure 4 shows the relationship of reduced bulk modulus  $K_{Tm} \times (23 \times k_B T_b)^{-1}$  with atomic size parameter  $a^{-3}$ , and Fig. 5 the relationship of reduced surface tension  $\gamma_m \times (2 \times k_B T_b)^{-1}$  with atomic size parameter  $a^{-2}$ . It can be seen that the reduced quantities increase with decreasing the atomic size  $a$ .

Metals Zn, Cd, Hg from group 12, as well as Be in Fig. 5 show the anomalous deviation from the regression line. If these metals are excluded, then the coefficient of determination increases to 0.90. Figure 5 also shows that the slope of the reduced surface tension  $\gamma_m \times (2 \times k_B T_b)^{-1}$  versus  $a^{-2}$  is steeper for transition metals, which

**Fig. 4** Relationship between the reduced bulk modulus  $K_{Tm} \times (23 \times k_B T_b)^{-1}$  and atomic size parameter  $a^{-3}$ . The dashed line corresponds to the equality  $K_{Tm} \times (23 \times k_B T_b)^{-1} = a^{-3}$

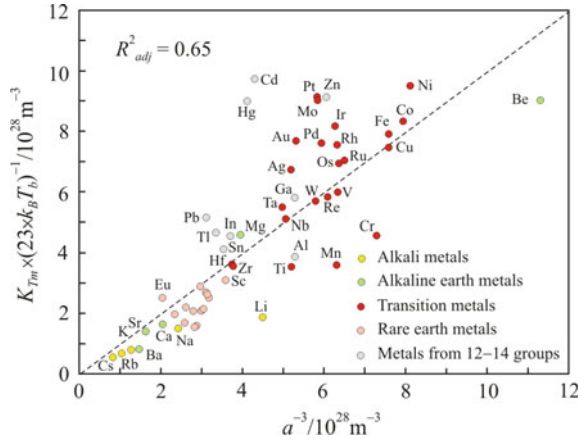
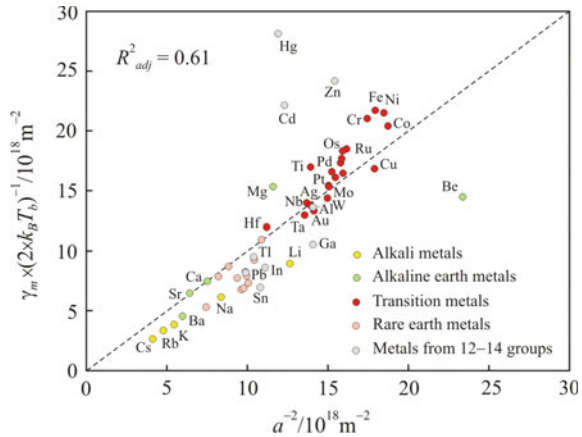


**Fig. 5** Relationship between the reduced surface tension  $\gamma_m \times (2 \times k_B T_b)^{-1}$  and atomic size parameter  $a^{-2}$ . The dashed line corresponds to the equality  $\gamma_m \times (2 \times k_B T_b)^{-1} = a^{-2}$



have the smallest atomic size. Similar patterns, but in a more diffuse form, take place for the reduced bulk modulus.

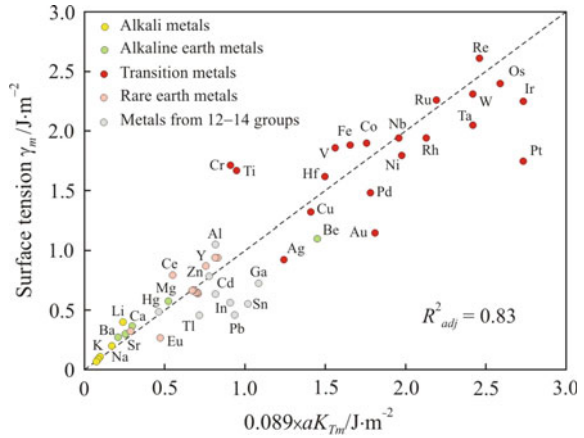
The ratio of  $\gamma_m$  to  $aK_{Tm}$  compares the energy of atoms on the surface and in the bulk and the average ratio for all metals is 0.089. Thus, the energy of atoms in the surface layer of liquid metals at the melting point is approximately 9% of the atomic energy inside the liquid. Figure 6 shows the relationship between the surface tension  $\gamma_m$  and the product of the atomic size by the bulk modulus  $aK_{Tm}$ .

### 4 Conclusion

In this work, we investigated the relationship of various energy quantities characterizing the interatomic bond with the isothermal bulk modulus and surface tension



**Fig. 6** Relationship between the surface tension  $\gamma_m$  and the  $0.089 \times aK_{Tm}$  parameter. The dashed line corresponds to the equality  $\gamma_m = 0.089 \times (aK_{Tm})$



of 60 liquid metals at the melting temperature. It is shown that the isothermal bulk modulus and surface tension at melting point correlate better with the values characterizing the complete breaking of interatomic bonds, i.e., with the cohesive energy  $E_{coh}$ , evaporation enthalpy  $\Delta H_b$ , and thermal energy at the boiling point  $RT_b$ . With the melting enthalpy  $\Delta H_m$  and thermal energy at the melting point  $RT_m$ , which characterize the state of the metal at the melting point, this relationship is weaker. Transition metals are distinguished by a faster increase in the cohesive energy with increasing the boiling point. Decomposition of liquid metals to the monatomic gas occurs when the distance between atoms increases on average by 50% compared to the melting point. The isothermal bulk modulus and surface tension at melting point increase with decreasing atomic size. It is shown that the average energy of atoms in the surface layer of liquid metals at the melting temperature is approximately 9% of the energy in the atomic layer inside the liquid.

**Acknowledgements** The article was made within the framework of state work No. FEUZ-0836-0020.

## References

Aqra, F.: The cohesive energy density and the isothermal compressibility: their relationships with the surface energy. *Phys. B* **446**, 28–31 (2014)

Blairs, S.: Review of data for velocity of sound in pure liquid metals and metalloids. *Int. Mater. Rev.* **52**, 321–344 (2007)

Friedel, J.: *Dislocations*. Pergamon Press, Oxford (1964)

Garvin, D.: Thermodynamic properties of elements. *Bull. Alloy Phase Diagr.* **2**, 261–262 (1981)

Gorecki, T.: Vacancies and changes of physical properties of metals at the melting point. *Z. Metallkunde* **65**, 426–431 (1974)

Iida, T., Guthrie, R.: Performance of a modified Schytil model for the surface tension of liquid metallic elements at their melting point temperatures. *Metall. Mater. Trans. B* **41**, 437–447 (2010)

- Iida, T., Guthrie, R.I.L.: The thermophysical properties of metallic liquids. University Press, Oxford (2015)
- Israelachvili, J.N.: Intermolecular and surface forces. Elsevier, Amsterdam (2011)
- Kaptay, G.: Link between the semi-empirical Andrade and Schytil equations and the statistical-mechanical Born-Green equation for viscosity and surface tension of pure liquid metals. *Metall. Mater. Trans. B* **39**, 387–389 (2008)
- Keene, B.J.: Review of data for the surface tension of pure metals. *Int. Mater. Rev.* **38**, 157–192 (1993)
- Lindemann, F.A.: Über die Berechnung molekularer Eigenfrequenzen. *Phys. z.* **11**, 609–612 (1910)
- Marcus, Y.: On the compressibility of liquid metals. *J. Chem. Thermodyn* **109**, 11–15 (2017)
- Starodubtsev, Yu.N., Tsepelev, V.S., Wu, K.M., Kochetkova, Ye.A., Tsepeleva, N.P.: Vacancy formation energy of metals. *Key Eng. Mater.* **861**, 46–51 (2020)
- Starodubtsev, Yu.N., Tsepelev, V.S.: Vacancy formation energy and kinetic properties of liquid metals. *Key Eng. Mater.* **880**, 43–48 (2021a)
- Starodubtsev, Yu.N., Tsepelev, V.S.: Analysis of the kinematic viscosity and self-diffusion of liquid metals at the melting temperature. *High Temp.* **59**, 192–197 (2021b)
- Stewart, G.R.: Measurement of low temperature specific heat. *Rev. Sci. Instrum.* **54**, 1–11 (1983)
- Turkdogan, E.T.: Thermodynamic and kinetic properties of elements and inorganic compounds relating to the their melting and boiling point temperatures. *Can. Metall. Q.* **41**, 151–162 (2002)

# Corrosion Protection Method with Sacrificial Anode for Steel Members in Boundary with Ground Using Water Swelling Rubber



J. Xu, S. Kainuma, K. Takaki, M. Yang, and T. Tomoda

## 1 Introduction

Many anti-corrosion methods have been applied in steel structures, such as coating and sacrificial anodes cathodic protection (SACP), but they are not continuously reliable in practice. The deterioration of the coating film resulting from hydrolysis and oxidative decomposition is common (Yang et al. 2019). Besides, the quality of the coating cannot be sufficiently secured in edge corners and imperfect areas of connection details.

For some steel structures, corrosion is prone to occur, where the coating is vulnerable to deterioration (Kere and Huang 2019; Jeong et al. 2019). In addition, dew and stagnant water with chloride from antifreeze at the corner of the structure contribute to corrosion of steel members, especially (Cramer et al. 2002). And the localized and uniform corrosion damage of steel members in boundary with ground in an actual bridge is shown in Fig. 1a. Apart from the coating, SACP is the most broadly utilized strategy to diminish corrosion. However, an electrolyte is necessary, so that SACP is preferred for protection for steel structures buried in soil or submerged in water (Tezdogan and Demirel 2014). Its application in a dry environment is still raw and problems exist (Suzumura and Nakamura 2004; Yang et al. 2020).

Recently, S. Kainuma fixed sacrificial anode and fiber sheet with high water absorption and retention properties together, to achieve the anti-corrosion effect for steel plates (Yang et al. 2019, 2020). However, the fiber sheet is difficult to fit with steel members at the corner of the structure tightly over a long period of time. In this study, instead of fiber sheet, water swelling rubber with higher elastic modulus was

---

J. Xu · S. Kainuma (✉) · K. Takaki · M. Yang

Department of Civil Engineering, Faculty of Engineering, Kyushu University, Fukuoka 8190395, Japan

e-mail: [kai@doc.kyushu-u.ac.jp](mailto:kai@doc.kyushu-u.ac.jp)

T. Tomoda

Transportation Division, Nippon Koei Co.,Ltd, Tokyo, Japan

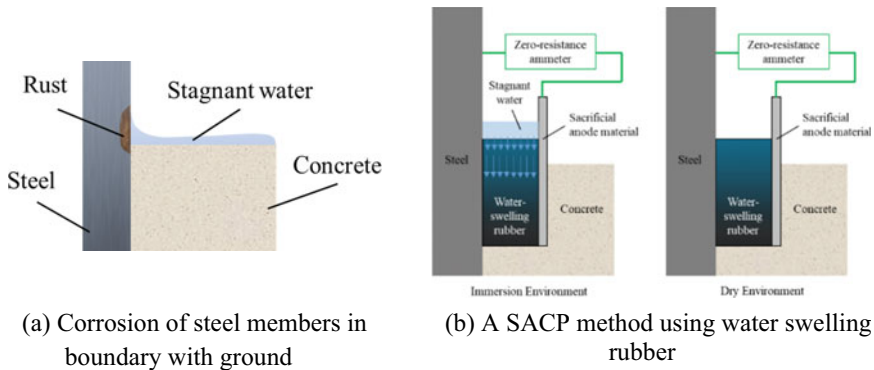


**Fig. 1** A SACP method with water swelling rubber applied in boundary with ground

applied in the SACP system, as shown in Fig. 1b. The water swelling rubber was expected to act as an electrolyte carrier with high absorption and retention capacity to prevent corrosion under different environmental conditions.

## 2 Experiment

### 2.1 CP System

The CP system applied in this study includes a Zn plate and water swelling rubber, which are fixed together and attached to a surface-cleaned steel plate by a peek bolt and an acrylic plate. The steel plate, acting as cathodic material, directly contacts with the rubber and is connected with the Zn plate acting as a sacrificial anode, by lead wires.

The water absorption mechanism of water swelling rubber is shown in Fig. 2. The water-absorbent polymer in the rubber has a network structure, and when the cations in the polymer are dissolved in water, osmotic pressure is generated, so that the rubber can absorb a large amount of water. In the system, the rubber works as an electrolyte carrier to establish the ion flow, so that the effectiveness of the CP system is strongly associated with the absorption and retention properties of the rubber.

### 2.2 Water Absorption and Retention Test

Immersion and drying tests were carried out to evaluate the water absorption and retention properties of the water swelling rubber. The appearance, enlarged view, and properties of the rubber ( $40 \times 40 \times 6$  mm) are presented in Fig. 3 and Table 1,

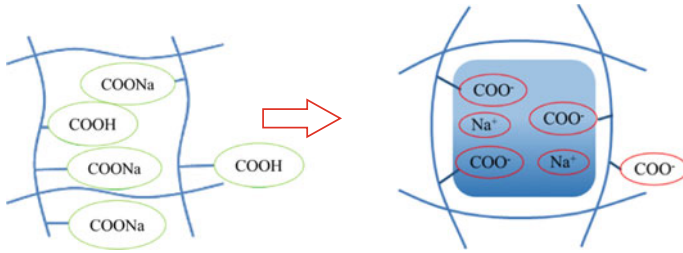


**Fig. 2** Mechanism of superabsorbent polymer

respectively. In the test, the rubber was submerged in distilled water and 0.1, 3.5, and 7.0 mass% NaCl aq electrolytes, respectively. The water retention test was carried out by allowing the rubber swollen in the water absorption test to be exposed in the air, and the changes of weight were measured in the same manner as in the water absorption test. The test conditions for the test are shown in Table 2.

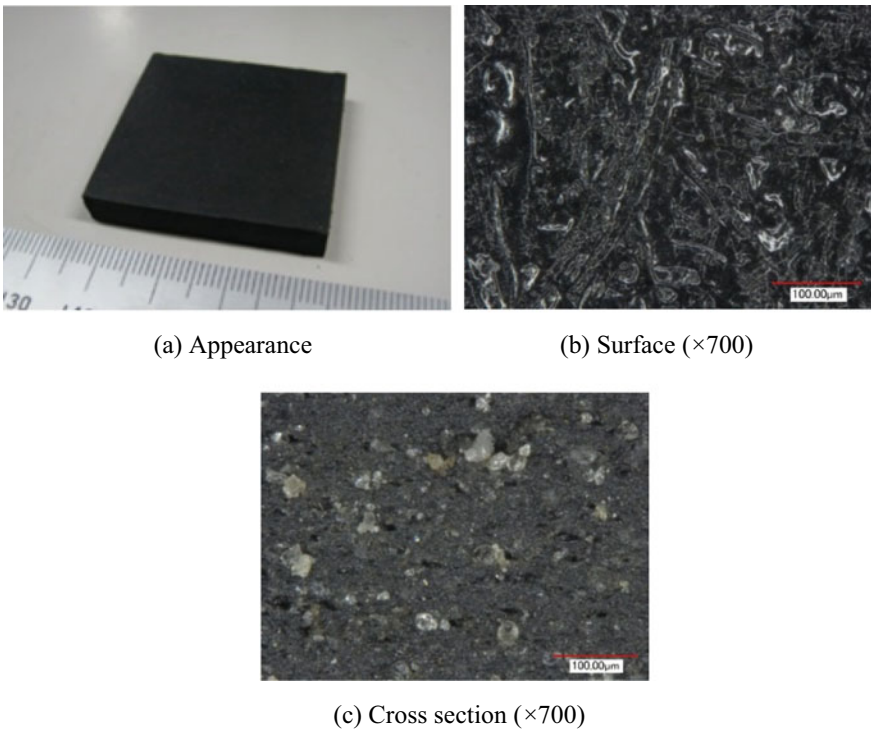


**Fig. 3** Appearance and enlarged view of the water swelling rubber

**Table 1** Properties of water swelling rubber

| Density (kg/dm <sup>3</sup> ) | Modulus of elasticity E(MPa) | Hardness H* | Tensile strength T <sub>B</sub> (MPa) | Stretching H <sub>B</sub> (%) | Volume change rate |
|-------------------------------|------------------------------|-------------|---------------------------------------|-------------------------------|--------------------|
| 1.2                           | 0.65                         | A40±5       | 4.0+                                  | 500+                          | 200+               |
|                               |                              |             |                                       |                               | *JIS K 5253        |

**Table 2** Condition of the water absorption and retention test

| Specimen | Steeping environment | Steeping period | Drying period | Initial weight (g) |
|----------|----------------------|-----------------|---------------|--------------------|
| A        | Distilled water      | 60 days         | 60 days       | 12.09              |
| B        | 3.5mass%NaCl aq      |                 |               | 12.92              |
| C        | 0.1mass%NaCl aq      | 30 days         | –             | 13.09              |
| D        | 7.0mass%NaCl aq      |                 |               | 12.76              |

### 2.3 Electrochemical Test

An electrochemical test was carried out to evaluate the anti-corrosion performance of the CP system, as shown in Fig. 4. A steel plate without a Zn plate was set as a controlled experiment. To simulate the environment of stagnant water and dryness at the steel members in boundary with ground, the tests were conducted in the order of (1) to (3) below. The test piece was placed in a chamber maintained at a temperature of 18° C and a relative humidity of 75%.

#### (1) moist curing (0–120 h)

The measurement was performed by allowing the test piece to stand in a constant temperature and humidity chamber. The measurement period was 120 h.

#### (2) immersion test (0–120 h)

The measurement was performed by immersing the rubber in 3.5 mass% NaCl aq. In addition, one of the rubbers swollen with 1.0 mass% NaNO<sub>2</sub> aq was immersed in the immersion environment of 0.1 mass% NaCl aq. The measurement period was 120 h.

#### (3) moist curing (0–120 h)

The specimen submerged in (2) was taken out and conducted in the same environment as in (1). The measurement period was also 120 hrs.

The anti-corrosion current generated between the anode plate and the steel plate, an external wire was measured and recorded by a nonresistance ammeter. Table 3 shows the electrolytes soaked in the rubber, absorption and drying periods and conditions of immersion environment in the test.

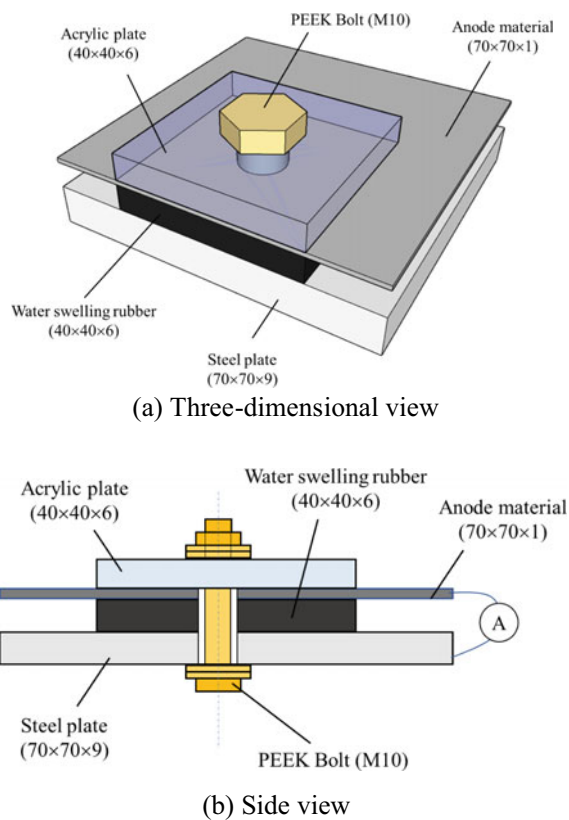


**Fig. 4** Configuration and dimensions of the specimens (unit: mm)

**Table 3** The test condition

| Specimens  | Electrolytes      |                       | Absorption period (day) | Drying period (day) | Immersion environment | Sacrificial anode material |
|------------|-------------------|-----------------------|-------------------------|---------------------|-----------------------|----------------------------|
|            | Electrolyte       | Concentration (mass%) |                         |                     |                       |                            |
| Dew1.0     | NaNO <sub>2</sub> | 1.0                   | 30                      | –                   | 3.5mass% NaCl aq      | Zn plate                   |
| Dew5.0     |                   | 5.0                   |                         |                     |                       |                            |
| Dry1.0     |                   | 1.0                   | 60                      | 40                  |                       |                            |
| Dry5.0     |                   | 5.0                   |                         |                     |                       |                            |
| Dew1.0–0.1 |                   | 1.0                   | 30                      | –                   | 0.1mass% NaCl aq      |                            |
| Dew1.0-X   | 1.0               | 30                    | –                       | 3.5mass% NaCl aq    | –                     |                            |

### 3 Results and Discussion

#### 3.1 Water Absorption and Retention Properties of the Rubber

The time-dependent weight of the rubber in the water absorption and retention test is shown in Fig. 5. The maximum weight of rubber immersed in distilled water is reached about the 40th day, which increases by about 20 g. However, the weight increase of rubber soaked in 3.5 mass% NaCl aq reaches about the 50th day, and the weight increases by about 9 g. In distilled water, the cations of the rubber are more easily dissolved than NaCl aq due to a larger osmotic pressure between the water inside the polymer and the surrounding water. For NaCl aq, the water absorption of rubber increases as the concentration decreases. Since a larger osmotic pressure is generated in 0.1 mass% NaCl aq compared to 3.5 and 7.0 mass% NaCl aq.

The weight of rubber immersed in both the distilled water and 3.5 mass% NaCl aq decreases significantly until about 30 days after the start of drying. However, the weight loss rate of the rubber absorbed with NaCl aq decreases after 30 days, which takes longer to dry than distilled water. It is considered that  $\text{Na}^+$  is less likely to dissociate and the drying rate is lower than that of distilled water due to the affinity of the superabsorbent polymer for  $\text{Na}^+$ . Above all, it is easy for the rubber to absorb the solution with a low ion concentration and retain electrolyte with ion.

In this method, the absorption and retention performance of the rubber, acting as the role to provide the electrolyte, is remarkably affected by the concentration of the immersion solution. If the concentration of the electrolyte that the rubber absorbs is too high or too low, either performance can be significantly reduced. Considering the balance between water absorption and retention performance, it is necessary to select an electrolytic solution with an appropriate concentration.

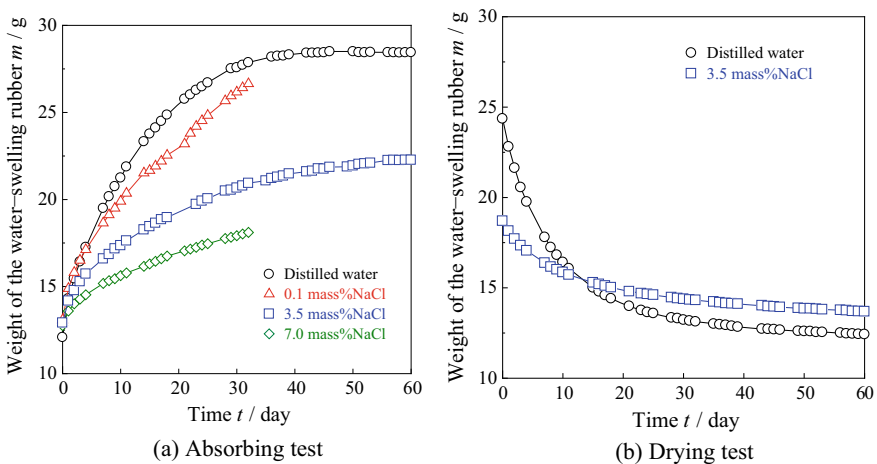
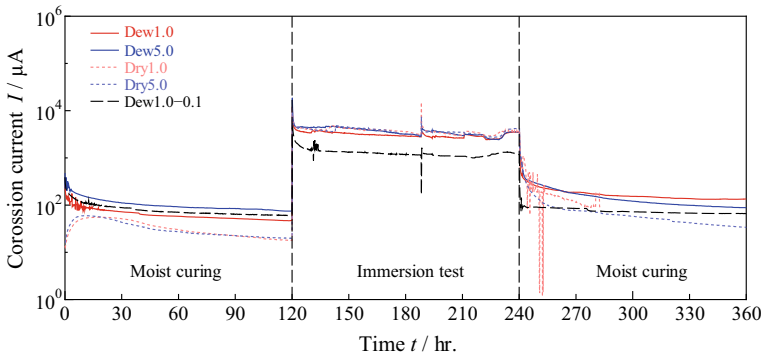


Fig. 5 The time-dependence of weight for the water swelling rubber





**Fig. 6** The time-dependence of corrosion current for specimens

### 3.2 Electrochemical Test Result

The time-dependent variations of the anti-corrosion current according to environmental changes are shown in Fig. 6. In Dry1.0, poor contact of the conductor occurred near 280 h., after that data was lost. The current  $I$  of Dew1.0, Dew5.0, and Dew1.0–0.1 have changed at the same level during 0–120 h. The current  $I$  of Dry1.0 and Dry5.0 with dried rubber have been measured from the start of the test, and the sacrificial anode anti-corrosion effect is exhibited because of a small amount of water in the rubber.

In the immersion environment (120–240 h), the current  $I$  of the specimen immersed in 3.5 mass% NaCl aq is larger than that in Dew 1.0-0.1 immersed in 0.1 mass% NaCl aq, because the corrosion circuit mainly depends on the surrounding immersion environment instead of the electrolyte inside the rubber.

The current  $I$  in the second moist curing (240–360 h.) Shows the same tendency as the first time. The current  $I$  in specimens with the swollen rubber is large, compared to that in Dry 5.0 with dried rubber. Furthermore, the current  $I$  of the specimen remains stable even when the environment changed from a stagnant water environment to a dry environment, resulting from the high water retention performance of the rubber.

The corrosion conditions of steel surface in contact with the rubber after the test are presented in Fig. 7. There is no visible corrosion on the surface of specimens (a–e) and most surface in contact with rubber of specimen (f), which should be attributed to the application of the rubber leading to the dissolved oxygen reduction. The black part at the lower end of the contact surface in Fig. 8f is a rubber deposit, the enlarged view of which is presented in Fig. 8. Corrosion can be observed in the red frame, which results from a gap generated between the rubber and the steel plate due to the shrink of the rubber in moist curing. However, for specimens applied with Zn plate, corrosion does not occur, because the significant effect of SACP can be achieved, despite the occurrence of the void.

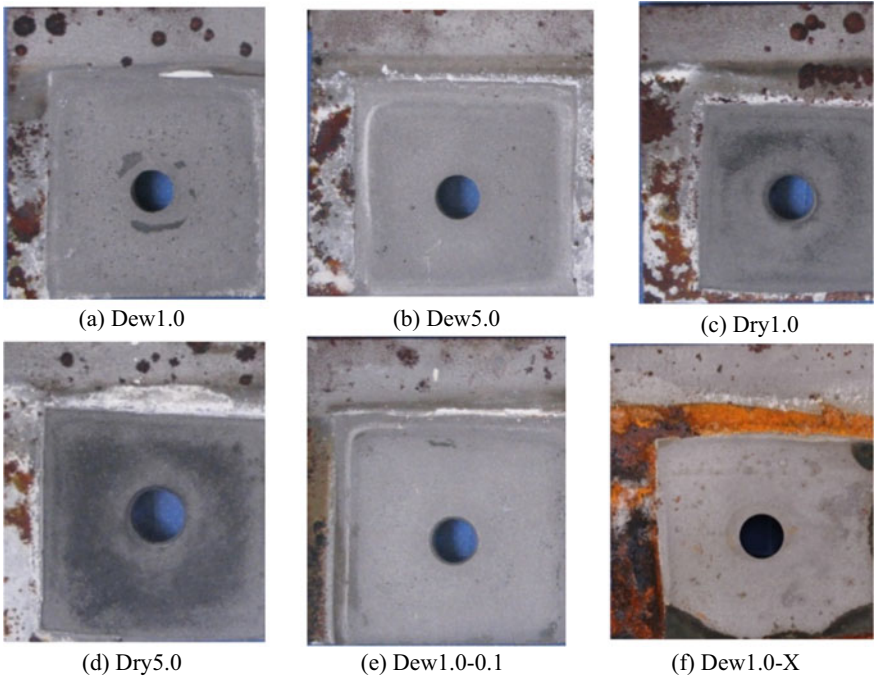
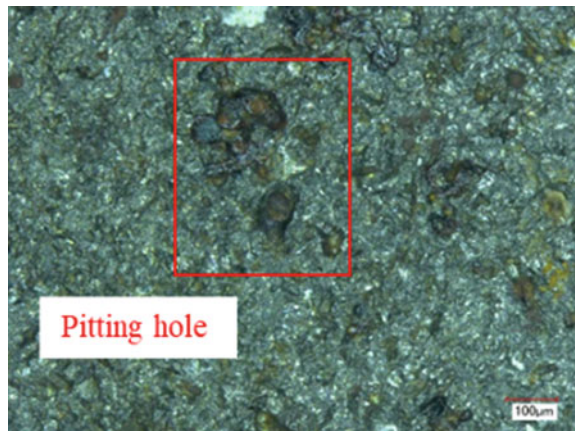


**Fig. 7** Corrosion protection situation of the steel surface after the test

**Fig. 8** Enlarged view of specimen Dew1.0-X. ( $\times 500$ )



## 4 Conclusion

In this study, an anti-corrosion method with water swelling rubber for steel members in boundary with ground was developed and the effectiveness of that was verified.

Water absorption and retention test and electrochemical test were carried out to verify the effectiveness of the water swelling rubber.

- (1) The amount of water absorbed by the rubber increases as the ion concentration of the electrolyte decreases, and the rubber takes more time to dry with the electrolyte concentration inside rubber increasing. An appropriate electrolyte concentration should take both water absorption and retention into consideration.
- (2) If the rubber is not completely dried, the anti-corrosion circuit of the sacrificial anode can be maintained through a small amount of water in the rubber.
- (3) The effect of the sacrificial anode cathodic protection maintains due to the high-water retention performance of the water swelling rubber, despite the environment changing from water immersion to dryness.

## References

- Cramer, S.D., Covino, B.S., Jr., Bullard, S.J., Holcomb, G.R., Russel, J.H., Nelson, F.J., Laylor, H.M., Soltesz, S.M.: *Cement Concr. Compos.* **24**, 101–117 (2002)
- Jeong, Y.S., Kim, M.J., Jeon, S.H., Ahn, J.H.: *J. Korea Inst. Struct. Maint. Insp.* **23**, 75–83 (2019)
- Kere, K.J., Huang, Q.: *J. Bridge Eng.* **24**, 04019007 (2019)
- Suzumura, K., Nakamura, S.: *J. Mater. Civil Eng.* **16**, 1–7 (2004)
- Tezdogan, T., Demirel, Y.K.: *Brodogradnja.* **65**, 49–59 (2014)
- Yang, M., Kainuma, S., Zhuang, S., Ishihara, S.: *Int. J. Electrochem. Sci.* **14**, 9858–9875 (2019)
- Yang, M., Kainuma, S., Ishihara, S., Kaneko, A., Yamauchi, T.: *Const. Build. Mater.* **234**, 117405 (2020)